

Designing polymer-tethered membrane-nanoparticle composites

Mingyang Hu

胡明暘

2013

Department of Physics
Carnegie Mellon University
Pittsburgh, PA

*Submitted in partial fulfillment of the requirements
for the degree of Doctor of Philosophy*

advised by Prof. Markus Deserno

To those whom I love and those who love me

Abstract

This thesis proposes a novel design of nanoparticles for drug delivery. By tethering a bilayer membrane vesicle to a solid nanoparticle core at its center using hydrophilic soft polymers, this structure is expected to exhibit improved stability, narrowed size distribution, and a variety of functionalization possibilities. Various aspects of this design will be examined from a theoretical perspective using physico-chemical knowledge and computer simulations. The aim is to significantly reduce the size of the fairly large parameter space and shed light on experimental protocols for how to effectively assemble such nanoparticles in the laboratory.

To study the properties of this design, coarse-grained molecular simulations are introduced in Chapter 2 as one of the major tools employed in this work, thanks to their computational efficiency and the possibility of obtaining important generic insights of the system being modeled. The general philosophy of coarse-graining (CGing) will be outlined, followed by an introduction to the CG models used in this work. Then, it will be illustrated how to connect length, energy, and time scales in CG simulations to reality. This chapter is concluded by applying the CG concepts and techniques described earlier on to obtain a CG model for PEGylated linker molecules, which is one of the two major components of the system of polymer-tethered nanocomposites studied in this work.

After the second chapter on coarse-graining, this thesis will spend three chapters focusing on either one of the two major components of the system we proposed, namely the polymeric linkers and the lipid bilayers. In Chapter 3, to understand the mechanical properties of the polymer linkers which tether the membrane vesicle to the nanoparticle core, a theoretical model for polymer brushes confined by two concentric spheres will be derived based on single-chain theories and scaling concepts. Using the CG linker model parameterized in Chapter 2, it will be demonstrated that this theoretical polymer model quantitatively predicts the force-extension relation of the polymers. This provides an efficient way to estimate both the size distribution and the stability of the tethered membrane-nanoparticle composites.

Following the chapter on polymers, this thesis will proceed to investigate the other major component in the proposed nanocomposites, namely the lipid membrane. Hence, computational methods to determine the two curvature elastic moduli in Helfrich theory, namely the bending modulus and the Gaussian curvature modulus, will be elaborated upon in the next two chapters. To be more specific, a method to measure the bending modulus by simulating membrane buckles will be proposed and validated in Chapter 4. Compared to other existed ways for measuring the bending modulus, the buckling method will turn out to be computationally efficient, and it can be applied to almost all types of membrane models.

In Chapter 5, a novel method for determining the Gaussian curvature modulus in simulations will be developed. The interplay between the bending energy and the edge tension in the membrane vesiculation process provides an efficient and robust way to pinpoint the Gaussian curvature modulus. As a comparison, another time-honored method to determine this modulus by measuring the lateral stress profile of flat bilayers is discussed. Based on the results measured in this alternative technique, as well as a comparison with the vesiculation protocol, it is argued that the stress profile method in fact fails to produce trustworthy values for the Gaussian curvature modulus. This unexpected result suggests caution when attempting to extract bilayer properties from the stress profile.

The models and knowledge which have been developed in this thesis will then be linked together in Chapter 6. The study of planar polymer-tethered bilayer membranes in this chapter serves as an intermediate step towards the membrane-nanoparticle composites in a spherical geometry. Simulations of the assembly process of tethered bilayers mimicking the rapid solvent exchange and the vesicle fusion protocols are qualitatively consistent with experimental observations found in the literature, supporting the reliability of our CG model. Moreover, the polymer theories discussed in Chapter 3 prove sufficient in semi-quantitatively describing the structural properties of such tethered membranes.

Bringing everything together, this thesis concludes with a study of the polymer-tethered membrane-nanoparticle composites proposed in Chapter 1. Theoretical constraints on the design parameters of this structure are first outlined and tested in simulations, with a major focus on the plausible range of the nanocomposite size. Then, a number of practical aspects regarding such nanocomposites, including their assembly process, solvent conditions, and the effect of the polydispersity in the linker chain lengths, are investigated.

Acknowledgments

In this thesis, the acknowledgments may be the most difficult part for me to write, and it is indeed the last one that I finished. During my years as a PhD student, I have benefited from many people, in one way or another. It is quite a challenge to put my appreciation into these limited words.

First and foremost, I would like to thank my advisor, Markus Deserno, who has educated me in so many different aspects. Since my first year at Carnegie Mellon, when I did a small but interesting project with him for the course Introduction to Research, he has showed me how to become a good scientist through his enthusiasm for research, his broad and solid knowledge of physics, and his care for detail. Moreover, his understanding, kindness, and support have helped me to go through many tough situations. Also, he has exposed me to a great deal of wonderful things in life, such as a witty sense of humor (“They brought a flag...”), many interesting books and movies, and enjoyable food and drinks (*e.g.* Caipirinha and single malts). His dedication to his students and postdocs has made it a very unique environment with strong connections within the group.

Then, I would like to thank the other members of my committee: Michael Bockstaller, Mathias Lösche, and John Nagle. During the past few years, their advice during my annual reviews has pointed me in the correct direction to keep my research on track. Their constructive comments on my thesis made it a much better piece of work. The weekly biophysics group meetings have also enlightened me with interesting topics and knowledge.

Thanks to Markus, I had many opportunities to attend conferences, join workshops, and even have extended visits to a few world-class institutions internationally, for which I was envied by a lot of my friends. The two-month visit to Kurt Kremer’s Theory Group at the Max Planck Institute for Polymer Research in Mainz, Germany, was an impressive experience, in which I learned a lot of science, met many new friends, and (legally) set up my personal driving record of 240 km/h on the autobahn. I also feel fortunate for my three-time visits to Christian Holm’s group at the University of Stuttgart, where I was invited to lecture on our membrane package `mbtools` in ESPResSo and give scientific talks about my own research. In addition, the hospitality of the Kavli Institutes for Theoretical Physics in Santa Barbara and in Beijing, where part of the work in Chapters 4 and 5 was completed, is gratefully acknowledged.

These conference experiences not only have broadened my horizon, but also led to a fruitful collaboration: The MARTINI part of the study on the Gaussian curvature modulus is a joint project with the MARTINI group, which was started by me and Djurre de Jong (the tallest guy I’ve ever had a handshake with) sitting in a tutorial session in Lausanne and discussing back-mapping Cooke membranes into MARTINI. Another appreciated collaboration is the whole nanoparticle project with Roland Faller from UC Davis, Amadeu

Sum from Colorado School of Mines, Richard Gandour and Alan Esker from Virginia Tech, from which my knowledge was extended beyond biophysics.

My life in Pittsburgh wouldn't be as wonderful as it has been if I had not met many dear colleagues and friends here: Tristan Bereau taught me important knowledge and skills with MD simulations when I started here; I've gained a better understanding of physics, computers, and life through the daily discussions with Cem Yolcu; Venky Krishnamani has been a great buddy who not only had many exciting conversations with me on all aspects of life, but also rescued me several times after sport injuries; Patrick Diggins has helped me many times with my English writing, as well as knowledge of sports; Zunjing Wang and Xiaofei Li have become my elder sisters, who always offer me assistance in academic and personal life; Siddharth Shenoy has given me much valuable advice on my career plans. I also want to thank Marilia Cabral, Rebecca Eells, Frank Heinrich, Brian Josey, Zach McDargh, and Xin Wang for many wonderful dinner experiences. On the personal side, I am especially grateful to my "lunch buddy" Muwen Kong, my roommate Mingjiang Zhong, and another good friend Jing Wang for their accompany.

最后，我想感谢我最在乎的人们：一方面是我的家人，尤其是父母以及奶奶，是他们给了我健康的环境，温暖的支持，以及一个不一样的眼界，使我很好地成长；另一方面是我最好的朋友以及一生的爱人，于娅溯，是我们的交往使我能够认识自己，更好地为人处事，更好地生活。我希望将这本文献给他们。

List of Publications

The original content of this thesis has appeared or will appear in the following publications:

Chapters 1, 3, and 7:

M. Hu and M. Deserno, *Designing polymer-tethered membrane-nanoparticle composites for drug delivery*, in preparation.

Chapter 4:

M. Hu, P. Diggins IV and M. Deserno, *Determining the bending modulus of a lipid membrane by simulating buckling*, *The Journal of Chemical Physics* **138** (2013), 214110.

Chapter 5:

M. Hu, M. Deserno, *Determining the Gaussian Curvature Modulus of Lipid Membranes in Simulations*, *Biophysical Journal* **102** (2012), 1403-1410.

M. Hu, D.H. de Jong, S.J. Marrink, and M. Deserno, *Gaussian curvature elasticity determined from global shape transformations and local stress distributions: a comparative study using the MARTINI model*, *Faraday Discussions* **161** (2013), 265-382.

Contents

1	Introduction	1
1.1	Overview: nanoparticles for drug delivery	1
1.1.1	General advantages of nanoparticles for drug delivery	1
1.1.2	Current nanoparticles for biomedical purposes	3
1.1.3	Limitations and challenges	4
1.2	A novel design of nanoparticles for drug delivery	5
1.2.1	Nanoparticle structure	6
1.2.2	Comparative advantages	6
1.2.3	Design objective	7
1.2.4	Preliminary knowledge	7
1.3	Thesis overview	8
2	Coarse-grained modeling	11
2.1	Overview: coarse-grained modeling	11
2.1.1	The need for coarse-graining	11
2.1.2	Building coarse-grained models	13
2.1.3	Limitations	14
2.1.4	Top-down coarse-grained model examples	15
2.1.5	Resolution transformation: back-mapping	19
2.2	Units and scales in coarse-grained simulations	20
2.2.1	Length scales	20
2.2.2	Energy scales	22
2.2.3	Time scales	24
2.3	A coarse-grained model for linker molecules	25
2.3.1	Molecular structure	25
2.3.2	Parameterization	26
3	A theoretical model of the polymers	31
3.1	Introduction	31
3.2	Single-chain stretching	32
3.2.1	Freely jointed chain	32
3.2.2	Worm-like chain	33
3.2.3	Discrete worm-like chain	35
3.2.4	Simulations of single-chain stretching	37

3.3	Scaling theory	38
3.3.1	Blobology	39
3.3.2	Osmotic pressure: theory	40
3.4	Planar brushes	41
3.4.1	Overview: planar brushes	41
3.4.2	Brush height: planar brushes	41
3.4.3	Osmotic pressure: planar brushes	42
3.5	Spherical brushes	43
3.5.1	Overview: spherical brushes	43
3.5.2	Brush height: spherical brushes	43
3.5.3	Osmotic pressure: spherical brushes	45
3.5.4	Compression Results	46
3.5.5	Full-range force-extension relation	47
4	Membrane elasticity I: The bending modulus by buckling	49
4.1	Introduction	49
4.1.1	Helfrich theory	49
4.1.2	Existing methods to measure κ in simulations	50
4.2	Theory	52
4.2.1	Hamiltonian and shape equation	52
4.2.2	Constraints of imposed strain	53
4.2.3	Stress-strain relation	55
4.2.4	Fluctuation corrections	55
4.3	Simulation setup	57
4.4	Results	58
4.4.1	Buckle shape	58
4.4.2	Stress-strain relation	59
4.4.3	Bending modulus	60
4.4.4	Microscopic cutoff	60
4.5	Discussions	61
4.5.1	Advantages	61
4.5.2	Limitations	62
4.5.3	Free energy of buckling	62
4.5.4	Thermodynamics of membrane bending	64
4.6	Outlook	67
5	Membrane elasticity II: the Gaussian curvature modulus	71
5.1	Introduction	71
5.2	Theory	73
5.2.1	The vesiculation process	73
5.2.2	Hamiltonian	74
5.2.3	Determining $\bar{\kappa}$: the splitting probability	75

5.2.4	Stress profile method	78
5.3	Simulation setup	78
5.3.1	Requirements on the system	78
5.3.2	Initial conditions	80
5.3.3	Sampling closure probability and shape anisotropy	81
5.3.4	Other quantities measured	83
5.4	Results	84
5.4.1	Dependence on other parameters	84
5.4.2	Results from the stress profile method	87
5.4.3	Results using MARTINI model	88
5.5	Discussion	91
5.5.1	Notes on the stress profile method	91
5.5.2	Notes on the patch-closure method	92
5.6	Outlook	93
6	Planar tethered bilayer lipid membranes	97
6.1	Introduction	97
6.2	Simulation setup	98
6.2.1	Rapid solvent exchange	99
6.2.2	Vesicle fusion	99
6.3	Results	100
6.3.1	tBLM assembly	100
6.3.2	tBLM height	102
6.3.3	Diffusion constants	104
6.3.4	Destabilization by long linker chains	106
6.4	Discussion	109
7	Polymer-tethered membrane-nanoparticle composites	111
7.1	Generic constraints	111
7.2	Optimal combination of the parameters	112
7.3	Simulation setup	115
7.4	Results	116
7.4.1	Stability of pre-assembled vesicles	116
7.4.2	Assembly	118
7.4.3	Solvent condition	121
7.4.4	Polydispersity	122
7.5	Discussion	125
A	Notes on Data Analysis	129
A.1	Blocking Analysis	129
A.2	Least Square Curve Fitting	131
A.2.1	Linear Least Square Regression	132

Contents

A.2.2 Nonlinear Least Square Regression	133
A.3 Monte Carlo Data Resampling	133
List of Figures	137
List of Tables	139
List of Technical Notes	141
Bibliography	143

1 Introduction

“There’s plenty of room at the bottom.”

— Richard Feynmann [Fey60]

On December 29th 1959, at the annual meeting of the American Physical Society at Caltech, Richard Feynman asked the following question [Fey60]:

“Why cannot we write the entire 24 volumes of the *Encyclopædia Britannica* on the head of a pin?”

He was promoting a field, in which physics on atomistic length scales (“at the bottom”) is studied, “in which little has been done, but in which an enormous amount can be done in principle.” Indeed, a lot has been done since then; today, we can proudly answer “Oh, but *we* can!”¹ This work on nanoscales, later coined as the field of “nanotechnology”, has emerged as one of the most rapidly evolving scientific and engineering endeavors.

So have biomedical sciences.² Naturally, these two areas intersect; many innovations have been made to the manufacture of nanoscale particles for biomedical purposes. Due to the enormously large number of topics in this interdisciplinary area of mathematics, physics, chemistry, biology, pharmacy, material science and engineering, and so on,³ only closely related aspects will be reviewed in this section.⁴

1.1 Overview: nanoparticles for drug delivery

1.1.1 General advantages of nanoparticles for drug delivery

As drug delivery vehicles, artificially designed and produced nanoparticles (NPs), with sizes ranging from several to several hundreds of nanometers, outperform conventional free drug agents in many aspects.

¹The now 31-volume *Encyclopædia* contains approximately 40 million words [EB], which can be estimated as 400 million characters or 400MB (1 Byte/character). In my smartphone, which outsmarts any computer from the 1960’s and yet still fits into my (back) pocket, a micro SD card stores 32GB of data on an area of $11\text{mm} \times 15\text{mm} = 165\text{mm}^2$ [mSD]. So 400MB takes up about 2mm^2 , comparable to the size of the head of a pin.

²“Actually I don’t know any field where they are making more rapid progress than they are in biology today.” — R. Feynmann [Fey60]

³Any perceived innuendo in this non-exhaustive list, pertaining to the purity [Mun] of these disciplines, is strictly imaginary.

⁴Interested readers are kindly referred to the following reviews for more information: [PL03, VRL05, PKH⁺07, DCS08, RSL⁺09, DB12].

One advantage of encapsulating the drug molecules into vehicles is the increase in bioavailability and the protection against premature degradation [AC04, PKH⁺07, PMS12]. For instance, the solubility of hydrophobic drugs which, as the name suggests, do not dissolve well in aqueous environments, can be significantly increase by loading into soluble nanocarriers [Fro83, CGFF11]. Or by means of surface conjugation of hydrophilic polymers such as polyethylene glycol (PEG) [All94, ONK03], nanocarriers enjoy prolonged half-life due to the extra steric repulsions that reduce the opsonization⁵ by serum proteins and the consequent clearance from the circulatory system by the mononuclear phagocyte system [All94, CGFF11, AC13]. Moreover, the complexity of delivering every one of the exponentially growing number of drug variations can be greatly reduced by instead focusing on general characteristics of drug loading and NP delivery.

Drug delivery NPs also obtain another advantage from their sizes, which helps them to overcome certain barriers to arrive at the targeted regions. For example, a general scheme used in “escorting”⁶ drug carriers to tumor tissues is based on NP sizes and the enhanced permeability and retention (EPR) effect observed in various tumor tissues [MM86, Gre10]: Macromolecules in a size range between approximately 10 – 100 nm can escape from the leaky blood vessels supplying the tumor and obtain long duration in the tumor tissue due to the underdeveloped lymphatic drainage [PKH⁺07, DP10]. This specific accumulation of nanocarriers at the tumor tissues both increases the efficacy of drug agents and reduces the toxicity to normal organs.

Moreover, this extra layer of drug delivery vehicles brings in additional possibilities of enhanced functionality, such as the aforementioned long circulation time. One possibility of targeted drug delivery, in addition to the *passive* accumulation due to the EPR effect, is to *actively* target the NPs to special tumor cells by decorating the NP surface with ligands that specifically bind to receptors found mostly on the surface of those tumor cells but rarely on normal cells. Another broadly discussed subfield is the controlled release of drug payloads when certain internal (*e.g.* low pH in lysosomes [LKSP10]) conditions are satisfied and/or external conditions are applied (*e.g.* shining light with a specific range of wavelength for photothermal therapy [DB12]). NPs provide a valuable platform for researchers to extend the functionalities of the administrated agents.

Other advantages of nanoparticles include a large payload (*e.g.* roughly 2000 small interfering RNA as compared to less than ten for antibody conjugates), the ability of containing multiple targeting ligands, the ability of encapsulating multiple drugs, and many more, which are discussed further in a recent informative review by Davis *et al.* [DCS08].

⁵In the process of opsonization, antigens are bound by antibody, which enhances their later binding to phagocytosis cells such as the white blood cell.

⁶One may question the use of the word “escort” here since this delivery process is essentially *passive*. Yet such words are nevertheless being used broadly in the field of drug delivery without much scrutiny. This issue will be brought up again in Section 1.1.3.

1.1.2 Current nanoparticles for biomedical purposes

After a brief overview of some of the advantages of employing nanoparticles for drug delivery, this subsection will continue with a few example NP systems designed for biomedical purposes. Note that there exists a large number of systems in the field, *e.g.* liposomes, drug-polymer conjugates, polymeric micelles [PMS12, DV13]. The number of varieties is also growing quickly. For the focus of this work, only the most relevant ones will be mentioned here.

Liposomes

Liposomes, first developed in 1965 [BSW65], have soon been utilized as drug carriers [Gre73, Gre76a, Gre76b] and become one of the most widely used drug delivery carriers [FC08, AC13]. Since then, the liposomal platform has evolved from simple membrane vesicular systems into complex nanoscale carriers and been used to transport a myriad of therapeutic agents, no matter hydrophilic or hydrophobic [Gre76a], ranging from conventional anticancer drugs to a novel class of genetic drugs (*e.g.* small interfering RNAs or DNA plasmids) [FC08]. Liposomes also have become a clinically established platform since the approval by the US Food and Drug Administration (FDA) of a PEGylated liposome-encapsulated doxorubicin (Doxil[®], Ortho Biotech) for the treatment of HIV-related Kaposi's sarcoma in 1995.

Generally speaking, biocompatibility, biodegradability, and possibilities of surface decorations provided by liposomal systems distinguish them from other NP delivery systems [RSL⁺09, AJK11]. On the other hand, liposomes also suffer from several limitations, including physical and chemical stability, batch-to-batch reproducibility, drug entrapment, and so forth [MBM⁺13].

Lipid-nanoparticle assemblies

In order to mitigate some of the shortcomings of liposome systems, structurally more sophisticated liposome-based NPs have been devised. Some interesting examples are several types of lipid-NP assemblies, including NP-supported lipid membranes [TL07] and core-shell-type lipid-polymer NPs [MBM⁺13], where NPs are coated by bilayer or monolayer membranes, together with liposome-nanoparticle hybrids [AJK11], where NPs are embedded, encapsulated, or conjugated to liposomes. The goal is to combine the advantages of liposomes and those of the NPs. On the one hand, by supporting lipid vesicles with solid colloidal cores, the membranes are stabilized, their morphology is controlled, and the reproducibility is increased [TL07, MBM⁺13]. On the other hand, the encapsulation into biomimetic bilayers improves the biocompatibility of the NPs [AJK11]. Moreover, including NPs in liposomes could also realize multiple functions with the same delivery vehicle [AJK11]. The types of solid NPs examined in this direction include, but are not limited to, silica, magnetic iron oxide, polysaccharide, gold, and solid polymeric particles [TL07, AJK11, MBM⁺13]. One of the remaining challenges concerns the stability of

such composites under different environmental stress conditions [MBM⁺13].

Metal nanoparticles

Along with the field of *delivering* therapeutic drugs, another area in biomedical studies, *diagnosis*, is also experiencing great inputs from NPs, especially metal NPs made of gold or iron oxide. Metal NPs become an attractive option mainly because of their versatility [JMM10]; they can be employed as a stable platform to graft other functional groups, as imaging contrast, and even for magnetic-directed guidance for superparamagnetic iron-oxide NPs [GG05, JMM10]. Compared to polymeric or silica NPs, gold NPs also provide photothermal functions for the possibility of NP-mediated hyperthermia thanks to their enhanced surface plasmon resonance [PB11]. The fabrication of these NPs allows a wide range of sizes ranging from a few to a few hundreds of nanometers with controlled polydispersity [RBMR12]. When combining with other ingredients, such as lipid membranes, these attractive properties of gold and iron oxide NPs have led to many applications as diagnostic and therapeutic agents, some of which have headed to clinical studies approved by the FDA [JMM10, MMFC13].

1.1.3 Limitations and challenges

Unfortunately, although significant progress has been accomplished in this field, certain fundamental limitations and challenges have not yet been successfully addressed, especially concerning the uptake of drug molecules into the desired cells (*e.g.* tumor).⁷

Targeted delivery, as mentioned in Section 1.1.1, mainly relies on the passive EPR effect which permits the extravasation of nanocarriers into the interstitial space of the tumors, and the “active” ligand-receptor specific interactions which ideally would enable the carriers to “home in” on the targets. However, some have argued that such “targeting” is more of a misnomer, since both of the passive and active targeting mainly depends on the *probabilistic* process of escaping through the leaky blood vessels first. [RCF10, Flo12, KLHP12]. As a result, only a small fraction (1 – 10%) of the intravenously injected NPs extravasate and accumulate at the tumor: The majority stay in the circulatory system for a while and end up in the liver and spleen [KLHP12, ATC12].

More importantly, accumulation does not guarantee *uptake* [PC08]. Several uncertainties may lead to limited uptake. For instance, drug-loaded carriers may lose partial or all of their payload on the way to the destination due to their instability [RCF10, KLHP12]. Having escaped from the circulatory system, further diffusion of the vehicles deep into the tumor may be hindered due to the crowded interstitial environment [Jai99, RCF10]. Even worse, the internalization into the cells should not be taken for granted, either; for example, in order to enter the cells, some of the NPs rely on receptor-mediated endocytosis, which is

⁷“There is little use for a carrier that, although highly selective *in vitro*, ends up in phagocytic cells or cannot reach its destination *in vivo*. Since little can be done to influence the target and surroundings, the carrier must be chosen or designed appropriately.”
— Gregory Gregoriadis (1981) [Gre81]

a complicated biological process that involves many factors such as particle size, receptor density and mobility. [TDGBS04, ZLL⁺09, ATC12].

Among these factors, size and shape of the particles impact the biodistribution in almost every step mentioned above [DJHK⁺08]: Only NPs within the allowed size range can extravasate from the leaky vascular walls through the EPR effect [MM86, Gre10]; The diffusion of NPs among the crowded tumor cells is also greatly affected by the size [PWJ⁺09, RCF10, KLHP12]; Early-arrived NPs may physically block the incoming ones and thus cancel the EPR effect [BP11]; Not to mention the paramount dependence of NP size and shape in the endocytosis process [OKS⁺04, CGC06, CC07]. In addition, carefully designing NP size may bring in extra benefits; the depletion of receptors after the endocytosis of NPs around certain optimal size may inhibit certain cell-growth pathways, which leads to apoptosis (programmed cell death) [Fer08].

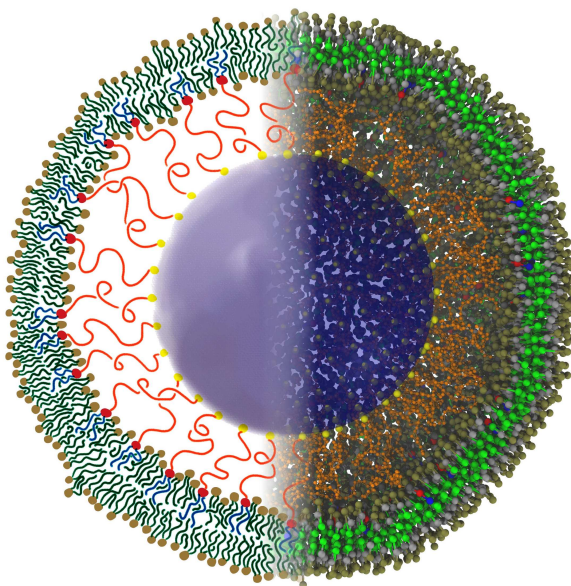


Figure 1.1: A schematic of the proposed polymer-tethered membrane-nanoparticle composite.

1.2 A novel design of nanoparticles for drug delivery

As discussed in the previous section, it will be beneficial to develop a new type of nanoparticles that enables fine-tuning of the size and shape, and maintains stronger particle stability. In this section, such a design of a polymer-tethered membrane-nanoparticle composite will be proposed, followed by the elaboration of its comparative advantages. Then the design

objective will be stated, followed by a short summary of the existing knowledge that will lead the way towards this complex structure.

1.2.1 Nanoparticle structure

The proposed nanoparticle is a polymer-tethered membrane-nanoparticle composite, whose schematic structure is drawn in Figure 1.1. A solid NP core resides at the center, with hydrophilic polymer spacers covalently grafted onto the solid surface *via* their endgroups. The other end of the spacers is conjugated to an amphiphilic molecule which anchors into an enclosing lipid vesicle.

1.2.2 Comparative advantages

This seemingly complex structure is expected to keep most of the attractive functions of its components as discussed in Section 1.1.2, *e.g.* the ability to transport a large number of hydrophobic and/or hydrophilic drugs *via* the liposome and the possibility of magnetic guidance if an iron oxide NP core is chosen.

One direct consequence of combining a liposome with a solid core is the potential of integrating receptor-specific delivery, diagnosis and monitoring, and other advanced functions into one unified delivery platform. For instance, the liposome can encapsulate the therapeutics as usual, while at the same time protect and stabilize the solid core that can be utilized for imaging, diagnosis, and/or even photothermia. Such “theranostic” particles have surfaced as one of the most exciting topics in drug delivery [LKHS10, LAH⁺11, CLLC12, BMT13].

Moreover, this composite should be able to exhibit several more advantageous properties besides those it inherits from its components. An equally important goal for this design is the improvement in mechanical stability. Similar to the lipid-nanoparticle assemblies described in Section 1.1.2, the polymer brush and solid core provides support to the lipid vesicle [TL07, MBM⁺13]. In addition, the presence of those linkers that have been grafted to a colloid surface may 1) assist the NP to survive strong shearing and 2) in case of partial rupture, “heal” the bilayer and save part of the drug payload since the spacer part of the linkers will pull back upon large stretching. In contrast, for common liposomes or lipid-NP assemblies, it would be more difficult to recover from a partial rupture, since the only “healing force” in this case is the membrane’s attempt to reduce the free energy cost of having an open edge (edge tension).

An even more crucial advantage of this design, as will be examined in detail in later chapters, is the size and shape control afforded by the spacers. These polymer chains prefer a certain range of extension, which imposes a constraint on the nanoparticle size. Also, if the polymers have a relatively narrow length distribution, they will alleviate possible shape deformations from a sphere. Increased batch-to-batch reproducibility can be expected as well because the dimensions of the polymer chains and the solid cores can be fabricated with high precision [MBM⁺13].

1.2.3 Design objective

Despite of the strengths outlined above, this polymer-tethered design is unlikely to be a panacea. The paramount obstacle of delivering drug carriers to desired locations, as summarized in Section 1.1.3, still needs to be addressed. Nevertheless, the hope is that by providing a general and robust NP design with a size and shape control, this sophisticated question would become more approachable with the input from other closely related research topics, such as shape- and size-dependent endocytosis [CGC06, CC07] and diffusion in tumor tissues [Jai99, PWJ⁺09].

Note that the description of the structure shown above is a *generic* design without much specificity: the core can be either a gold or an iron oxide NP; the surface chemistry of the endgroups also has options such as a disulfide or thiol bond on gold surfaces; the spacers may be made of PEG, but other biocompatible hydrophilic polymers would also work; the anchors may have one chain like a cholestanol or two like a lipid; and for the lipids there exists a wide spectrum of possibilities. Each individual aspect of the design could expand into a series of independent projects. Yet, they fall out of the scope of this thesis; only general properties, such as particle size, grafting density, and chain length, will be studied here.

This is because the main purpose of this work is *not* to figure out the detailed conditions to synthesize the composites in experiments, due to our lack of expertise in relevant fields, and, more importantly, the very high-dimensional parameter space which almost forbids experimental exploration without supporting theoretical considerations. Instead, we will focus on laying the foundation for experiments by ruling out the unphysical or unfavorable part of the large parameter space from a theoretical and computational perspective. In addition to its academic merits, this effort, hopefully, can significantly reduce the number of random trials in the lab so that time can be saved and economic costs can be lowered [SS08].

1.2.4 Preliminary knowledge

The potential functional improvements of this polymer-tethered membrane-nanoparticle structure originate from a relatively complex design, which might seem to be a serious challenge in fabrication. Fortunately, one does not need to start from scratch; relevant preliminary knowledge and techniques exist for both experiments and theoretical modeling.

Experiments

In addition to those closely related nanoparticles that have been developed already (see Section 1.1.2), this polymer-tethered structure was also inspired by a model membrane system widely used to study membrane-protein interactions: the planar tethered bilayer membrane [WT00, SK01, MVV⁺07, VOR⁺08]. In a planar tethered bilayer system, the membrane is tethered by polymer linkers to a flat substrate surface, allowing a thin layer of water in between. This separation of a few nanometers is a key condition for the inclusion of some proteins into the bilayer and to avoid the unfavorable interactions between integral

proteins and the substrate that immobilize certain membrane proteins. From the study of tBLM systems, valuable knowledge on linker synthesis, endgroup-substrate interactions, membrane-substrate interactions, *etc.*, can be utilized for reference in the current project. More detailed studies about planar tethered bilayer systems using polymer theories and computer simulations will continue in Chapter 3 and 6.

Theoretical knowledge

Complementary to the experimental knowledge and techniques, delivery of drugs has also been studied using mathematical and computational modeling. The early work by Higuchi, in which the release of drug from containing matrices was mathematically modeled by a diffusion process [Hig61], marked the beginning of quantitative modeling of drug release [SS08, Pep13]. Since then, a few categories of models have been studied, including empirical/semi-empirical models at first, and mechanistic models later. The latter describe the systems based on physical and chemical principles and provide more insights [SS08]. Also, thanks to the ongoing increase in computational power, numerical solutions to some complicated problems, such as solving partial differential equations under complex boundary and initial conditions, become more feasible and accurate [SS08].

Advances in computation also enable direct modeling of the drug agents and carriers by molecular dynamic (MD) simulations, where detailed molecular information inaccessible in experiments can be gained [Jor04].⁸ For instance, the interactions between drug molecules and the liposomes containing them have been examined using different models [XA06]. Studies of the properties of many nanocarriers, *e.g.* polymersomes [DOS⁺07b], pH-responsive polymeric micelles [ZYG⁺11], dendrimers [HNPA12, TM12], and translocation of NPs through membranes [DTM12], have also been conducted.

1.3 Thesis overview

Aiming to obtain fundamental knowledge about the proposed membrane-NP structure from a theoretical and computational point of view, and thus providing insights and guidance to experimentalists, the rest of this thesis will proceed in the following manner:

Chapter 2 deals with coarse-grained (CG) modeling, which is essential to our study due to the size and complexity of the system. Some background knowledge about CG modeling is reviewed, followed by the parameterization of a new CG linker model which will be used in later chapters to support our theory for a polymer brush tethered to two concentric shells (Chapter 3) and to study the mesoscopic behaviors of lipid-linker systems (Chapter 6 and 7).

The elastic properties of lipid membranes, one main ingredient in the formulation, are also studied. New methods are developed to measure the two elastic moduli of a membrane, namely the bending modulus that penalizes the increase in mean curvature

⁸One *always* needs to be cautious about the ability to correctly represent the reality with any kind of modeling. More discussions on MD simulation and modeling can be found in the next chapter.

(Chapter 4), and the Gaussian curvature modulus which matters when topological and boundary changes take place (Chapter 5).

Equipped with these prerequisites, planar tethered bilayer membrane systems are then explored as a test case (Chapter 6), before various aspects of our major target, the polymer-tethered membrane-nanoparticle composite, are investigated (Chapter 7).

2 Coarse-grained modeling

“The purpose of computing is insight, not numbers.”

— Richard Hamming [Ham86]

Molecular simulations are a useful tool to bridge the gap between microscopic interactions and macroscopic behaviors, providing complementary information to what is accessible in experiments [vGB90, KM02]. Significant progress has been made in simulating chemical and biological systems, partially acknowledged by the Nobel Prize in Chemistry this year (2013).¹

Molecular simulations, specifically molecular dynamic (MD) simulations, where the time evolution of the system follows the classical equations of motion, play a crucial role in the subject of this thesis, the study of nanoparticle design. Our theoretical considerations about the global system properties, such as stability and particle dimensions, would be more convincing if cross-checked by simulations. In addition, some practical issues regarding the assembly of such NPs will be addressed by further simulations.

For this purpose, it is very important to obtain a reasonable model for our system. Due to its size and complexity, instead of an all atomistic model, where all atoms are explicitly represented,² a coarse-grained (CG) model, where several atoms are combined into one pseudo-atom, will be constructed to reach the length and time scales of interests. In this chapter, relevant background knowledge of CG modeling will be reviewed, followed by the buildup of a CG model for the linker molecules in our system.

2.1 Overview: coarse-grained modeling

This section presents an overview on coarse-grained modeling, with a particular focus on the background knowledge necessary for constructing a CG model of membrane-nanoparticle composites. Many topics covered here are based on a thoughtful review by Noid [Noi13].

2.1.1 The need for coarse-graining

With the help of Moore’s Law, computational limits have been pushed forward by many orders of magnitudes: Before the 1980’s, typical simulations contained roughly 1000 atoms

¹Martin Karplus, Michael Levitt, and Arieh Warshel have been awarded the Prize for their contributions to the “Development of Multiscale Models for Complex Chemical Systems.”

²There is also a type of atomistic models called united-atom models, where atoms within each CH, CH₂ and CH₃ units are combined as a single pseudo-atom. But since all heavy atoms are represented separately, these models are still generally considered as atomistic.

or beads and lasted for about 10 ps [vGB90], whereas the most recent atomistic simulations have stepped into the regimes of tens of millions of atoms for 100 ns (HIV-1 capsid structure [ZPY⁺13]), or tens of thousands of atoms for 1 ms with several repeats (ubiquitin folding [PLLS13]).

Admittedly, these extremely large or long atomistic simulations are tremendous accomplishments in computation. However, the *ability* to run such simulations should not be confused with the reason to do so, which should be aiming for the *insight* [Ham86]. Thus, certain “unnecessary” atomistic details can sometimes be “coarse-grained” out *carefully*, leaving a simpler yet more fundamental part of the system which is represented by a smaller number of interaction “sites” or superatoms and still keeps the *physics*. During this process of selecting the necessary features one wishes to preserve, much insight of the system can be gained [Noi13].

Moreover, characteristic length or time scales of many important biological processes still remain inaccessible to simulations at atomistic resolutions, *e.g.* the self-assembly process of viral capsids [GKDP13]. Among these two scales, the temporal one sometimes poses more serious challenges, unlike the problem of having a very large system size, which can be handled efficiently by simulation techniques such as domain decomposition [BCOY93].³

This happens because, very frequently, the required simulation time grows superlinearly as a function of system size, especially when global conformational changes are of interests, or when thermal undulations need to be sampled [GKDP13]. For instance, for a quasi two-dimensional membrane of length scale L , the number of particles in the simulation scales as L^2 . However, the relaxation time τ of thermal undulation modes depends quartically on L , *i.e.* $\tau \propto L^4$. Thus, the total simulation cost is proportional to L^6 [Des09]. This means a 10 times larger system in linear size requires 1 million times more simulation time! Even with very well-designed parallelization techniques like domain decomposition, the major simulation effort of sampling the fluctuation modes still requires an additional factor of 10^4 ; parallelization does not help to resolve the L^4 problem.

In other words, large systems demand much longer simulation times not only because of the larger number of degrees of freedom, but also due to the longer equilibration time for their larger modes, *e.g.* the thermal undulation modes mentioned above; unable to do so will undermine the validity of the simulation results [vGB90].

In such cases, a simpler CG model can be a useful alternative. Compared to fully atomistic models, their CGed counterparts provide significant improvements in computational efficiency. The decrease in the number of degrees of freedom lowers the cost of force calculations at each integration step, which can be further reduced due to the shorter interaction range resulting from the “averaging” of atoms into coarser sites, and due to the larger integration time step permitted by the smoother interactions [MPTV10]. Moreover, such averaging also flattens energy barriers and lower molecular “friction”, thus leading to faster dynamics.⁴ Overall, CG models can easily gain three or more orders of magnitude

³Domain decomposition, as the name suggests, divides the system into domains of smaller size, and obtains speedup by assigning particles in different domains to separate CPUs for parallel calculations.

⁴Note that this also makes the interpretation of the dynamics in CG simulations more subtle. More on

in computational speedup [FHKvdV09].

2.1.2 Building coarse-grained models

Construction of a particle-based CG model normally takes two steps [Noi13]: Firstly, a CG representation of the system is defined by mapping a detailed chemical structure to a model with lower resolution (*i.e.*, fewer particles); and secondly, the interactions among those particles need to be determined in such a manner that the essential physics is preserved.

Mapping

During the mapping process, particles in the model with higher resolution, or atoms in the chemical structure of the molecules, are grouped together into different CG sites, which are linked together by CG bonds based on the topology of the molecules. The coordinates of these sites will then be calculated based on the coordinates of the atoms in the finer model; the center of mass or geometry of each group is often used.

The choice of such mapping affects accuracy, efficiency, and transferability of the CG model [Noi13]. However, systematic methods of optimizing the mappings are still under research [Noi13]. Some conditions have been proposed to screen the mappings for the physically correct ones [RAG12], but most often, CG mappings still depend on the chemical intuition of the researcher.

Parameterization

Based on the CG representation of a system, a set of appropriate interactions needs to be carefully derived, so that the effects from the eliminated degrees of freedom can be replaced to such an extent that the fundamental physics is intact. For example, when the solvent degrees of freedom are removed from the system, additional effective interactions need to be included to capture the hydrophobic effect.

As the field of CG modeling advances rapidly, a broad range of methods have been studied to obtain optimal sets of CG interactions [Vot09, PK09, SCGH⁺11, Noi13]. Based on whether the CG model is derived from a model of higher resolution, these methods can be categorized into two types: “bottom-up” and “top-down” [FC99, TV05, Noi13]. The former is built on a more detailed “fine-grained” model (*e.g.* an all atomistic model) which provides a good approximation to the real system, while the latter represents the reality by reproducing important phenomena that are observed in experiments on scales accessible to the CG model.

Top-down models can be further divided into two sub-categories: “generic” top-down models and “chemically specific” top-down models [Noi13], depending on, as their names suggest, whether the model can represent specific chemical systems. Generic models normally contain only a small number of interaction sites, exchanging the loss of chemical

this topic will be discussed later in this chapter.

details for efficiency. More importantly, the functional forms of the potentials used in these generic models are relatively simple and contain only a few parameters, which can be varied systematically to match desired system properties on larger scales, such as self-assembly and bending modulus of lipid bilayers [NT01, BB03, Far03, WF05, LS05, CKD05, CD05, Des09]. Chemically specific models also adopt relatively simple functional forms, and their interaction parameters are normally determined to match certain thermodynamic properties measured in experiments, *e.g.* the partition of chemical groups between aqueous and organic solvents [MdVM04, MRY⁺07, MKP⁺08, MT13].⁵

The construction of a CG model for our nanoparticles will follow the generic top-down philosophy, mainly because of the generality of our design.⁶ As emphasized in Section 1.2.3, the objective of this work is to study aspects of the overall design that are not specific to certain chemical implementations. Thus, we will build our model upon general physical principles without chemical specificity, instead of from some fine-grained models of the components of the system which are not yet determined. Main parameters in the model will be tuned so that characteristic length scales (mainly membrane thickness and area per lipid) and mechanical properties (*e.g.* polymer persistence length) are comparable to those found in experiments.

2.1.3 Limitations

Every coin comes with two sides. While coarse-grained modeling generates a significant speedup, it also imposes certain limitations. During the process of integrating out the “unnecessary” degrees of freedom, atomistic details contained in the sub-structure of a CG site re-emerge in the CG model in the form of effective interactions, which, ideally, should compensate for the absence of those details. In this perspective, the multibody potential of mean force (PMF) exactly captures all the physics that got integrated out, thus should be faithfully matched during the CG process. However, it is usually completely impractical to work with it. The resulting uncontrolled approximations that replace it by a much simpler but manageable force field is responsible for many inaccuracies created on the CG level. It is unlikely that all of the properties of the system can simultaneously survive through the coarse-graining process [RAG12]. Certain trade-offs will be faced: Some properties of interest, which will be targeted when optimizing the interactions, can often be reproduced; the rest will be examined after the parameterization, but how well they compare to the real system is generally not known ahead of time. This general problem goes under the label “representability”, which has been called for attentions by many researchers such as Ard Louis [Lou02, JHGL07].

To give an example, in a recent study of CG models of water [WJK09], a structural property, the two-body radial distribution function, was used to parameterize the interac-

⁵Note that, in practice, the difference in the parameterization methods among different types of models (top-down *vs* bottom-up, generic *vs* chemically specific) is not always black-and-white. Recent models often adopt methods with more than a single flavor [Noi13].

⁶Readers who are interested in the methods of building bottom-up models are encouraged to consult the recent comprehensive review by Noid [Noi13].

tions and was reproduced with high accuracy, and, as a consequence, the compressibility is also exactly matched. However, the pressure of the system was *four orders of magnitude* too high. With further corrections that provide reasonable values of the pressure, the thermal compressibility is now significantly compromised. Thus, matching those system properties of interest should be prioritized, at the cost of a lower accuracy on the other properties; a balance among the various properties need to be reached based on the purposes of the simulations.

Moreover, this process of coarse-graining implies that the potential energy of the CG system is essentially an approximation of the potential of mean force (PMF) in the fine-grained model [Noi13], which is a *free* energy function that depends on temperature, pressure, density, and other thermodynamic conditions. This gives rise to the problem of transferability in bottom-up models: a CG model may not behave as well at thermodynamic state points other than the one at which it has been constructed using an atomistic model.

Generic top-down models also have their drawbacks. A major issue is that the reasonable *macroscopic* phenomena a top-down model exhibits are not a validation of its underlying *microscopic* assumptions: right answers might be provided for the wrong reasons [Noi13].

2.1.4 Top-down coarse-grained model examples

A membrane model, namely the Cooke model [CD05, CKD05] will be reviewed here as an example for generic top-down models. Most of the membrane-related part of this thesis relies heavily on the efficiency and flexibility of this model. Another top-down membrane model used in this work, the MARTINI model [MdVM04, MRY⁺07], will also be briefly summarized.

Cooke model

The Cooke model⁷ is a generic top-down membrane model developed by Cooke and Deserno to study mesoscopic membrane physics [CD05, CKD05]. Each lipid is represented by three linearly connected beads/sites (one hydrophilic and two hydrophobic, as shown in Fig. 2.1) in order to, on the one hand, be minimalistic and efficient in design, and on the other hand, produce an approximately physical lipid aspect ratio. The nearest neighbors are connected using finite extensible nonlinear elastic (FENE) bonds:

$$V_{\text{F}}(r) = -\frac{1}{2}k_{\text{F}}r_{\infty}^2 \ln \left[1 - (r/r_{\infty})^2 \right]. \quad (2.1)$$

⁷a.k.a. the 3-bead model, or the *snowman* model (named by Cameron Abrams, Drexel University).

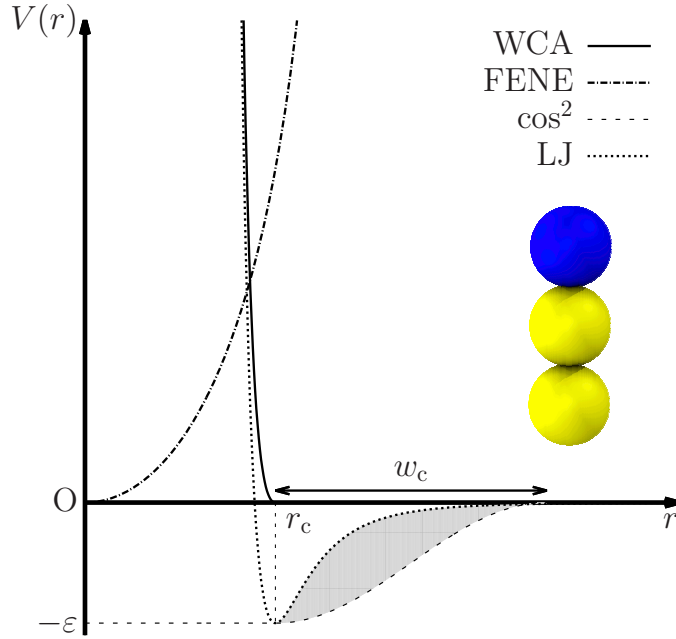


Figure 2.1: The interaction potentials used in the Cooke model. The shaded area emphasizes the enlarged attraction range of the cosine-square potential when compared to a Lennard-Jones potential. A Cooke lipid is shown as inset, with a blue bead for the hydrophilic headgroup and two yellow beads for the hydrophobic tails.

A Weeks-Chandler-Andersen potential (WCA), a truncated and shifted Lennard-Jones potential, is used to describe the excluded volume effect:

$$V_{\text{WCA}}(r) = \begin{cases} 4\epsilon_{\text{LJ}} \left[\left(\frac{r_0}{r}\right)^{12} - \left(\frac{r_0}{r}\right)^6 \right] + \epsilon & , r < 2^{1/6}r_0 \\ 0 & , r \geq 2^{1/6}r_0 \end{cases} \quad (2.2)$$

The length scale r_0 in the WCA potential will be interpreted as the size of the particles. These two potentials Eqs. (2.1) and (2.2) also determine the bond lengths b between a pair of neighbors, which is roughly r_0 .

A harmonic potential between the first and third site within a lipid is implemented to straighten the lipid:

$$V_{\text{harmonic}} = \frac{1}{2}k(r - R_0)^2, \quad (2.3)$$

where equilibrium length R_0 is normally set to $4r_{0,t}$, *i.e.* four times of the tail bead size $r_{0,t}$. This is an approximation to the harmonic *angle* potential, $V_{\text{angle}} = \frac{1}{2}k_{\text{angle}}b^2(\theta - \pi)^2$, where θ is the angle between the two bonds connecting the neighbors and b is the bond length. The main difference is that the former is a two-body potential, which is more

efficient in computation, and more importantly, provides an easy way to calculate the local stress tensor, which will be covered in Chapter 5.

Note that the Cooke model is also an *implicit* solvent model; the hydrophobic effect of the lipid tails is replaced by an effective attraction (from here on referred to as the cosine-square potential):

$$V_{\text{cos}}(r) = \begin{cases} -\epsilon_{\text{cos}} & , \quad r < r_c \\ -\epsilon_{\text{cos}} \cos^2 \frac{\pi(r-r_c)}{2w_c} & , \quad r_c \leq r \leq r_c + w_c \\ 0 & , \quad r > r_c + w_c, \end{cases} \quad (2.4)$$

where ϵ_{cos} and w_c is the depth and width of the attractive potential. $V_{\text{cos}}(r)$ smoothly goes to zero at $r = r_c + w_c$, where in our case $r_c = 2^{1/6} r_0$ is the minimum position of an LJ potential with parameter r_0 . Lennard-Jones, WCA, FENE, and the cosine-square potentials are plotted in Fig. 2.1.

The extended range of the cosine-square potential, tuned by the width w_c , rescues translational entropy and is the key to have a fluid phase in between the gas phase (weak attractions) and the solid phase (strong attractions) in the absence of solvent [CD05].⁸ One can also use w_c to conveniently adjust the bending modulus or the area per lipid of the membrane [CD05].

Another important membrane property is the shape of the lipids, which can also be adjusted in the Cooke model. The *intrinsic curvature* of a lipid, *i.e.* whether to have a shape of a cone, a cylinder, or an inverted cone, can be varied in a straightforward way by changing the size of lipid heads. If lipids with higher *aspect ratio* are needed, then one can try to increase w_c so that the tail region becomes more contracted, or to append another bead to the tail. The former can only change the aspect ratio within a limited range before forcing the membrane into other phases (see the next section), but the phase diagram is known [CKD05, CD05]. The latter offers a larger range of available aspect ratio, yet the phase transition for a membrane which consists of lipids made of four or more beads has not been explored.

In addition to the flexibility described above, the Cooke model is also highly efficient in computation. The speedup originates from mainly three aspects. First, there are only three beads in each lipid, as compared to 138 atoms in an all atomistic DOPC ($\text{C}_{44}\text{H}_{84}\text{NO}_8\text{P}$). Second, solvent is treated implicitly, which significantly saves computation time when the system size increases [Des09]. Third, no many-body interaction potentials, such as angle potential (3-body) or dihedral potential (4-body), are used. Also, thanks to the smooth energy landscape, the dynamics of the system is three orders of magnitude faster, which will be shown later in this chapter.

The intuitiveness, efficiency, and flexibility make this model a very useful tool. For example, when studying membrane macroscopic properties such as the elastic moduli, this model can be utilized as a test ground: Although these properties are lipid specific, the

⁸“...and because of a smart choice of potentials, the solvent (water) can be omitted altogether .” — F. Schmid [Sch09].

fast simulations using the Cooke model provide very short turnaround time for developing general methods, which can then be applied to high resolution lipid models with specificity to save development time [HD06, HBD12, HDD13]. It is also helpful in semiquantitative explorations of phenomenological questions like membrane-mediated protein interactions that are not chemically specific and computationally demanding [RIH⁺07, RD08].

Although the generic design and simple interaction forms of the Cooke model offer many advantages, there are also limitations. First, due to the simplicity of the model, essentially all properties of the membrane depend on model parameters such as w_c in a convoluted way; for instance, it is quite difficult to change the bending modulus without affecting the lipid aspect ratio. Thus, as discussed in the previous subsection, for a generic top-down model like the Cooke model, the choice of model parameters, in this case w_c and others, should focus on reproducing the most relevant system properties given the problem of interest. Second, although the Cooke model behaves reasonably well on mesoscopic scales, microscopic details should not be taken too seriously. An example is the form of the lateral stress profile of a Cooke bilayer, which is unphysical as a direct consequence of the model design.⁹ Third, the absence of water leaves certain problems very challenging to approach using this model. For example, the behavior of lipid vesicles under normal and shear stress cannot be studied easily, because the excluded volume effect of the solvent molecules is not included in the model.

MARTINI model

The MARTINI model is a top-down model with chemical specificity [Noi13, MT13] for lipid membranes [MdVM04, MRY⁺07], peptides and proteins [MKP⁺08], polyethylene glycol [LdVMP09], and other biomolecules [MT13]. In this model, to balance the computational efficiency and the representability, on average four heavy atoms are combined into one of the 18 types of CG particles (“building blocks”), depending on the polarity of the group and the charge they carry. The nonbonded interactions among building blocks are parameterized to reproduce thermodynamic data obtained in experiments, including the free energy of hydration, the free energy of vaporization, and the partition coefficients between water and organic phases. These nonbonded interactions can be transferred across different systems without further parameterizations, making the MARTINI model very easy to use. Thus, it has been applied to investigate a wide range of problems, for instance lipid rafts [RM08] and membrane-protein interactions [LRvdGM10, SJH⁺11]. On the down side, in addition to the general limitations of CG models (resolution, dynamics, entropy, *etc.*), the MARTINI model is also limited in reproducing some structural properties such as the aspect ratio of lipids. This is understandable, since the model is specifically parameterized for thermodynamic properties, but not for structures. A recent review by Marrink and Tieleman [MT13] is recommended for a comprehensive picture of the applications, limitations, and perspectives of the MARTINI model.

⁹The lateral stress profile will be discussed in detail in Chapter 5.

2.1.5 Resolution transformation: back-mapping

As discussed in Section 2.1.1, CG models obtain part of their speedup at the cost of reduction in resolution. When the details matter, it will be of great advantage if one can make use of the efficiency and the fast dynamics offered by CG models to simulate large systems for a long time, and later be able to recover the atomic details lost in the coarse-graining process. This process of “fine-graining” (FGing) is sometimes referred as back-mapping: mapping a CG structure back to a corresponding one with higher resolution. Several different methods have been developed for this purpose, such as Hamiltonian exchange [LZ06], adaptive resolution simulations [PSK08], and multigraining [CG06].

Here, a simple simulated annealing [KGV83] procedure will be outlined, in which a CG configuration can be transformed into a more resolved FG one in three steps [RSG⁺10].¹⁰ The first step is an inverse mapping; the groups of finer atoms are associated with their corresponding CG sites, and are initially placed randomly within a certain distance of the CG sites. Then, in the second step, simulated annealing is conducted. These finer atoms evolve according to their interactions defined by the FG model, with extra restraints on the center of mass of each group so that they stay near the CG site. During this annealing step, system temperature is slowly reduced from a high initial value, so that potential barriers can be overcome. In the last step, the restraints are gradually removed and the system is allowed to relax into the final FG structure.

This back-mapping technique is very useful when the final FG structure is used simply as the initial configuration for a serious simulation on the finer resolution. It is, however, very dangerous to assume that this FG configuration is equilibrated well, and then start to measure system properties, even after an additional relaxation. This is because the CG and FG models normally have different energy landscapes and very different relaxation rates. If for any reason the FG configuration constructed from an equilibrated CG configuration does not reside at the minimum of the FG energy landscape, then the FG system may not be able to reach equilibrium within possible FG simulation time.

To give an example, consider a back-mapping of a lipid vesicle from the Cooke model (CG) to the MARTINI model (FG). If the lipids in the two representations have different aspect ratio, especially if the FG lipids are longer, and thus might overlap after back-mapping, then a simulation after the back-mapping may blow off. If the aspect ratio is matched exactly, there exists another subtle issue. The Cooke lipids have a conveniently high flip-flop rate [CD05],¹¹ so within a short simulation time, the chemical potential of lipids between the inner and outer leaflets will reach equilibrium. When mapped back to the MARTINI model, however, due to the difference in the position of the pivotal plane,¹² the MARTINI configuration may not be in equilibrium. The much lower flip-flop rate

¹⁰There exists one major difference between this simulated annealing method and those three mentioned in the last paragraph: the former is applied to obtain a static structure/configuration, while the latter run on the fly and keep the communications between CG and FG.

¹¹Flip-flop is the behavior of lipids spontaneously move from one leaflet into the other and change their orientation.

¹²The pivotal plane is a surface whose area does not change upon bending.

of MARTINI lipids will then keep the two leaflets in the FG configuration unbalanced throughout the simulation, affecting the study of system properties that are sensitive to the lipid packing.

2.2 Units and scales in coarse-grained simulations

In computer simulations, variables are simply numbers, which do not naturally come with units; one needs to assign meanings to these numbers based on the physics which the computer does not know anything about. In all atomistic models, due to their close relationship with the real chemical systems, such an assignment is normally straightforward. We can simply set up the system in a way that all physical quantities follow a specific set of real units. For instance, by assigning the same numeric values of bond length and energy known from experiment to the bonded interactions in the model, the length and energy values in the simulation automatically imply their units to be, say, Å and kJ/mol. In this manner, interpretation of the numeric values in atomistic simulations has little ambiguity.

This becomes more subtle for CG simulations. After the process of coarse-graining, each interaction site represents a group of real atoms. Many physical quantities, such as particle size and bond properties, no longer have their counterparts in experiments. For CG models with chemical specificity, the assignment of units can still be done based on the mapping which relates the CG particles to real chemical structures. If, for example, the mapping defines the position of each CG particle to be at the center of mass of the real atoms this CG particle represents, then the bond length is simply the distance between the center of mass of the two groups in real molecules, and it inherits its units from the atomistic simulations.

Unfortunately, for generic CG models, this procedure does not work any more. Take the Cooke model as an example: Since a Cooke lipid does not represent any real lipid, it is unclear what real atoms each one of the three CG particles corresponds to. As a result, the meaning of the numeric values requires additional thought.

In this section, we will focus on how to match simulation units with real physical units, and thus understand the numeric values in the Cooke model.

2.2.1 Length scales

In the Cooke model, assign σ to be the intrinsic unit of length. Then, for instance, the Lennard-Jones parameter, r_0 , can be expressed as $r_0 = 1.0\sigma$ instead of the more awkward (but frequently found) claim $\sigma_{LJ} = 1.0$.¹³ Ideally, one wants to match σ to some value measured in experiment, then all lengths in simulation can be translated to real units. However, neither the particle size $r_0 = 1.0\sigma$ nor the approximate bond length $b \approx 1.0\sigma$ has any obvious correspondence for a real lipid. Thus, we need to compare another length

¹³Such an assignment is not necessary, but it makes the following descriptions more clear and precise. Otherwise, imagine saying “ $1 = 1.32\text{ nm}$ ” if σ is not defined.

scale in the Cooke model (in units of σ) to experimental values (maybe in nanometers) instead, so that a conversion from σ to a real unit like nm becomes available.

Find the length scale to match

Membranes are quasi-two-dimensional elastic surfaces with finite thickness. Consequently, there are two other natural length scales that one could use to match to a length scale in experiments: 1) the characteristic length for lipid distance $\sqrt{a_\ell}$ within the two dimensional surface, where a_ℓ is the area per lipid in a monolayer, and 2) the membrane thickness d . Then, the problem becomes which one to choose.

The answer is both and neither. “Neither” is because the aspect ratio $\sqrt{a_\ell}/d$ of a Cooke lipid often does not match that of any common lipid, such as 1,2-dimyristoyl-*sn*-glycero-3-phosphocholine (DMPC) or 1,2 -dipalmitoyl-*sn*-glycero-3-phosphocholine (DPPC). Thus, when one length scale, say the thickness $d \approx 4.5 \sigma$ for $w_c = 1.6 \sigma$, is matched to the distance between the phosphate groups in the two leaflets of a real bilayer, *e.g.* $d = 3.83$ nm for DPPC at 50° [NTN00], then $1 \sigma \approx 0.85$ nm. However, this leaves the other length scale $a_\ell \approx 1.2 \sigma^2 \approx 0.87$ nm², which is about 35% larger than the corresponding experimental value $a_\ell = 0.64$ nm² [NTN00]. Only one of the length scales can be matched.

A better way to solve this problem is to fine-tune the aspect ratio of the Cooke model to the desired experimental value first, and then match both of the length scales. Of course, this careful adjustment only matters when the structural properties of the lipids are of higher priority, *e.g.* when a geometrically more precise NP system is wanted, or if one wants to back-map the CG structure to one with higher resolution. When precise length scale is not required, one can approximate $\sigma \approx 1$ nm.

Fine-tuning the aspect ratio

In order to quantitatively match the lipid aspect ratio, two model parameters, namely the width of the cosine-square potential, w_c , and the temperature $k_B T$, are scanned within the range where the bilayer remains in the fluid phase. Each simulation contains 1000 lipids and runs in an $NP_{xy}T$ ensemble for 10000τ .¹⁴ Area per lipid a_ℓ is obtained from the average box size, and thickness d by the difference in the peak positions of the density profile of the headgroups. Note that, at this time, there is not a unique way to match this head-to-head distance to any thickness in a real bilayer, since what atoms the CG headgroup represents is not specified. However, considering the chemical structure of a real lipid, it seems plausible to match this distance with real distances between phosphate groups in opposite leaflets. The lipid aspect ratio $\sqrt{a_\ell}/d$ is calculated and shown as symbols in Fig. 2.2. In the left panel, where the $\sqrt{a_\ell}/d$ is plotted against w_c , the simulation results at different temperature $k_B T$ fit well to a parabola, suggesting that $\sqrt{a_\ell}/d$ may be fit to a

¹⁴ τ is the intrinsic time unit in the model, which will be discussed later in Subsection 2.2.3.

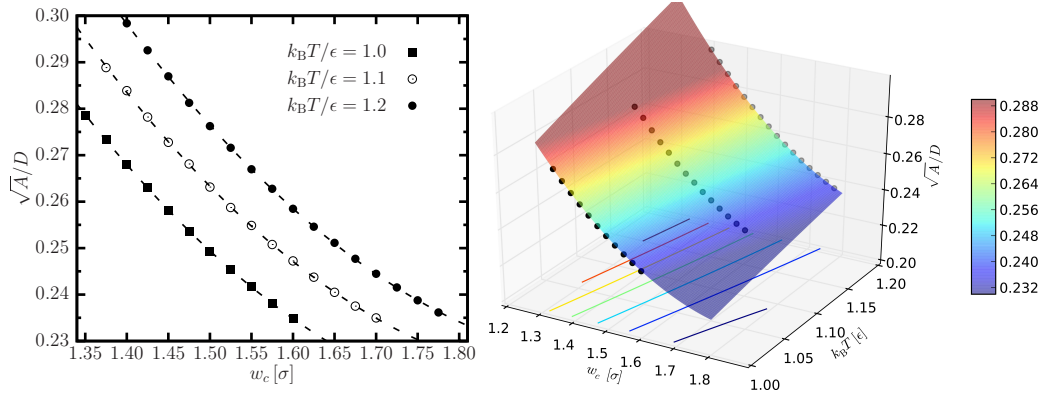


Figure 2.2: Fine-tuning the aspect ratio in the Cooke model. Left, the aspect ratio as a function of w_c . Right, paraboloid fit (Eq. (2.5)) of the aspect ratio as a function of w_c and $k_B T$. The contour lines are projected onto the xy -plane.

a_0	a_1	a_2	a_3	a_4	a_5
0.1948	-0.5804	-0.0438	0.4850	-0.1691	0.4943

Table 2.1: Parameters to tune the aspect ratio in the Cooke model, as defined in Eq. (2.5).

quadratic function in w_c and $k_B T$:

$$z\left(\frac{w_c}{\sigma}, \frac{k_B T}{\epsilon}\right) = a_0 \left(\frac{w_c}{\sigma}\right)^2 + a_1 \frac{w_c}{\sigma} + a_2 \left(\frac{k_B T}{\epsilon}\right)^2 + a_3 \frac{k_B T}{\epsilon} + a_4 \frac{w_c}{\sigma} \frac{k_B T}{\epsilon} + a_5. \quad (2.5)$$

The fit is shown in Fig. 2.2 (right). The fitting parameters are listed in Table 2.1 and can be used later as an empirical formula.

For reference, DPPC (50°), DMPC(30°), and DOPC (30°) (1,2-dioleoyl-*sn*-glycero-3-phosphocholine) exhibit aspect ratios of 0.209, 0.213, and 0.231, respectively (using the area per lipid A and headgroup peak-to-peak distance D_{HH} from Nagle and Tristram-Nagle [NTN00]). Considering the range of w_c and $k_B T$ where the membrane remains liquid, matching $\sqrt{a_\ell}/d$ of the former two using the current Cooke model is not feasible without adding another bead to the tail. In other words, the Cooke model is slightly too short to quantitatively reproduce the aspect ratio of saturated lipids.

2.2.2 Energy scales

Similar to the intrinsic *length* unit σ , determining the meaning of the intrinsic *energy* unit ϵ requires a characteristic energy scale. In the Cooke model, there exist a few energy scales. Since it is normally difficult to stretch a membrane, the bending energy, which is proportional to the bending modulus κ , and the thermal fluctuation $k_B T$ become the

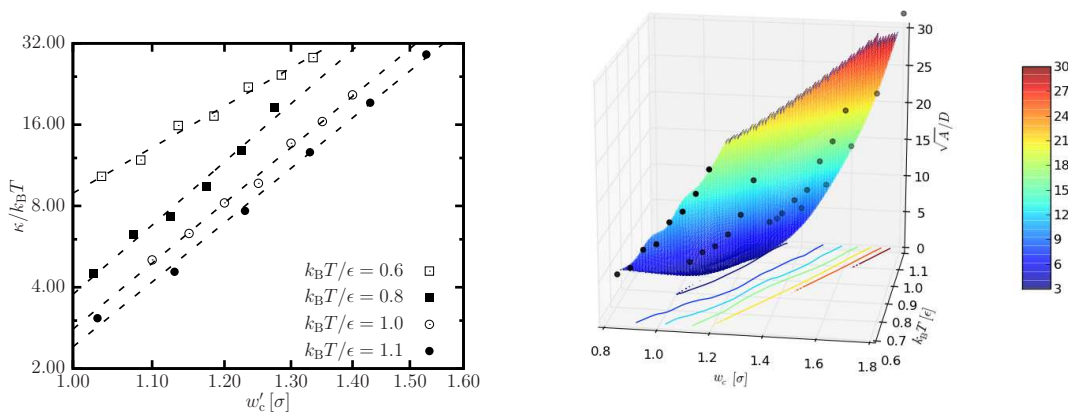


Figure 2.3: Fine-tuning the energy scales in the Cooke model. Left, $\kappa/k_B T$ as a function of w'_c at four different temperatures. The attractive range is shifted by $w'_c = 1 + w_c - w_c^{lg}$, where w_c^{lg} is the w_c at the liquid-gas phase boundary. For the four isotherms, w_c^{lg}/σ is 0.815, 1.025, 1.2, and 1.27, respectively. Right, $\kappa/k_B T$ as a function of w_c and $k_B T$. Note that the surface is an interpolation from the data, not a fit. The contour lines are projected onto the xy -plane.

most relevant energy scales [Des09]. Thus, in order to have a more realistic energy unit, one can first tune the ratio $\kappa/k_B T$ so that this value matches experimental data of a real membrane, and then both $k_B T$ and κ can be directly interpreted in real units.

The dependence of $\kappa/k_B T$ as a function of w_c and $k_B T$ is shown in Fig. 2.3. The data are taken from the original publication of the Cooke model [CD05].¹⁵ The log-log plot on the left suggests an exponential relation between w_c and $\kappa/k_B T$.¹⁶ Due to this more complicated exponential function, $\kappa/k_B T$ is not fit to a 2-variable function of w_c and $k_B T$. Instead, the right panel in Fig. 2.3 shows an interpolated surface using the data points.

It has to be pointed out that, as explained in the parameterization section 2.3.2, spontaneously matching up all system properties with experiments during CGing could be very difficult. This is also seen here. If one wants to obtain a membrane model where both structure and energetics compare quantitatively to experimental data, then both $\sqrt{a_\ell}/d$ and $\kappa/k_B T$ need to be realistic. Unfortunately, the two sets of contour lines, along which either the structural or energy ratio stays constant, are almost parallel to each other on the plane of w_c vs. $k_B T$, as shown in Fig. 2.4. This means that, within the parameter space that corresponds to the correct membrane phase, one may not be able to find an

¹⁵Many thanks to Ira Cooke for keeping the data safe for years and kindly sharing them with me.

¹⁶In the original publication [CD05], three of the isotherms overlapped upon the shift of w_c . However, from some independent measurements, it appears that κ was plotted in unit of ϵ and not $k_B T$, despite what is stated in the original publication.

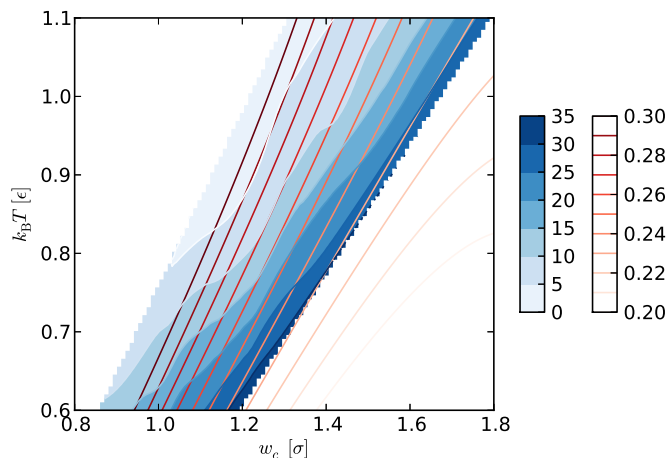


Figure 2.4: Length and energy scales together. The length scale ratio $\sqrt{a_l}/d$ is plotted as red contours, while the energy ratio $\kappa/k_B T$ is shown as different shades of blue.

intersection between one structural curve and another energy curve with the desired values. As a result, one might have to de-emphasize the less important observables.

2.2.3 Time scales

Time scales in CG simulations are more subtle than length and energy scales. On the one hand, there is an intrinsic time unit derived from the units of length σ , energy ϵ , and mass μ . For the Cooke model, as discussed above, $\sigma \approx 1$ nm, $\epsilon \approx k_B T \approx 4.1$ pN · nm. For the mass unit μ , one can take the mass of a real lipid, say DOPC with a molecular mass of 786, divide it by three, and obtain $\mu \approx (786/3)m_p \approx 4 \times 10^{-25}$ kg. Then, the intrinsic time unit τ would be given by

$$\tau = \sqrt{\frac{\mu\sigma^2}{\epsilon}} \approx 10 \text{ ps}. \quad (2.6)$$

However, the dynamics in CG simulations are sped up due to the reduced “friction” and smoothed free energy landscape, as discussed in Section 2.1.1. Consequently, the *effective* time scale which quantifies the evolution of the system could be very different from the one defined in Eq. (2.6) [NLSK04].

This effective time scale can be estimated by matching a dynamical process. But just like for the length scale, there are various choices, for instance, diffusion, flip-flop, or lipid rotation. In the Cooke model, diffusion is normally picked. The diffusion constant is on average $0.01 \sigma^2/\tau$ [CD05]. When compared to the value of lipids in real membranes (on the order of $1 \mu\text{m}^2/\text{s}$ [FW78]), the effective time unit $\tau_{\text{eff}} \approx 10$ ns.

Note that this effective time unit τ_{eff} is 1000 times larger than the intrinsic unit τ , which means that, from the perspective of diffusive motions, the CG dynamics evolve

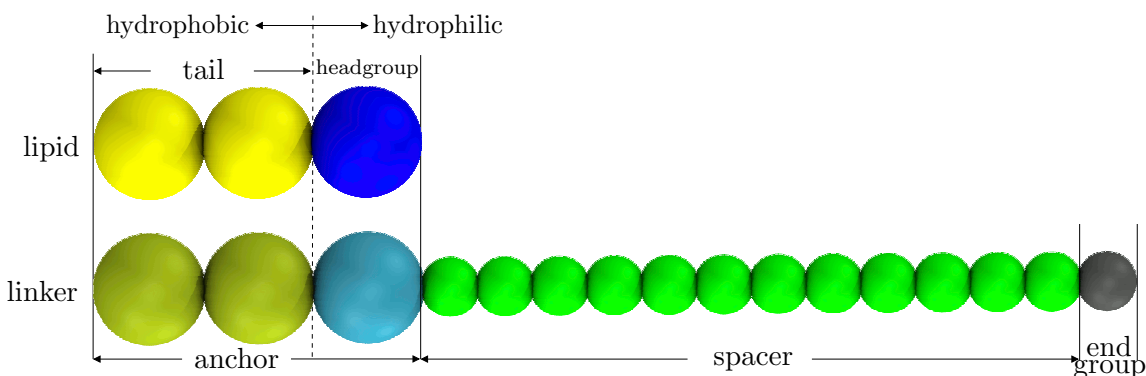


Figure 2.5: Schematics of the CG linker and lipid molecules. The anchor part of the linkers share the same structure with the lipids. Different colors indicate the bead types in simulations.

three orders of magnitude faster. This dynamic speedup leaves some ambiguity in the interpretation of the dynamics in CG models, especially when different parts of the system experience different dynamic speedup [Noi13]. However, it also shows why CG models are a powerful tool to study biochemical processes that happen on longer time scales.

2.3 A coarse-grained model for linker molecules

After a brief review of CG modeling and a discussion of units and scales, it is time to construct our CG model for the membrane-nanoparticle composite.

2.3.1 Molecular structure

As explained previously in this chapter, a generic top-down model will be set up in order to keep the generality of the NP design. Since the Cooke model has been proven to be very successful in simulating mesoscopic membrane phenomena [RIH⁺07, Des09], it is intuitive to design the other major component of the system, *i.e.* the linkers, in a similar and compatible manner.

For simplicity, the amphiphilic anchor part of the linker will be modeled like a Cooke lipid: There will be three beads in an anchor, one head bead (hydrophilic) and two tail beads (hydrophobic), interacting with each other *via* the same interactions that the lipid beads experience. A soft hydrophilic polymer chain, composed by beads of *half* the lipid bead size, is conjugated to the head bead of the anchor on one end, while the other end connects to an endgroup bead of the same size, which will graft the spacer to the NP. A schematic structure of this CG linker is shown in Fig. 2.5 together with a Cooke lipid for comparison. Different colors indicate different bead types in the simulations.

2.3.2 Parameterization

Since the anchor part of the linker experiences the same interactions as the lipids do, there are only two other types of interactions which need to be parameterized, namely the interactions for the spacer beads, and the cross interactions between the spacer beads and the others. Note that the endgroups are set up to be the same as the spacer beads, except that the endgroups may be fixed in simulations when the linkers are supposed to be grafted to surfaces. Thus, no extra parameterization is necessary for the endgroups.

Basic spacer interactions

For the interactions governing the spacer beads, the same functional forms from the lipid interactions are used, *i.e.* FENE for the neighboring bonds, WCA for the excluded volume, harmonic for the angle between two FENE bonds (see Section 2.1.4). However, since the spacers are normally soft polymers like PEG, the size of the spacer beads, $r_{0,s}$, which is its WCA length parameter, will be reduced to half of the lipid bead $r_{0,\ell} = 1\sigma$, *i.e.* $r_{0,s} = 0.5\sigma$. The specific number of this reduction is not unique, but it has to be shorter than the Kuhn length $\ell_K = 2\ell_p$, where ℓ_p is the persistence length of the spacer. The reason to choose $r_{0,s}$ to be half of the lipid bead size $r_{0,\ell}$ is because each lipid has *two* tails, while the polymers only have *single* chains; this difference in bead sizes approximately reflects the difference in chain volume.

With the reduction in size, the balance between the several interaction potentials requires some attention. The WCA potential (Eq. (2.2)) scales naturally with different length scales r_0 , because the distance r between two particles already appears as the ratio r/r_0 . However, this is not the case for the FENE and harmonic interactions; they decrease proportionally with the length scale in the potentials. Thus, in order to maintain the ratio between these two interactions and the WCA, the energy constants for the FENE and harmonic interactions, *i.e.* the “ k ” in Eqs. (2.1) and (2.3), need to be rescaled. Note, the spacers are assumed to be hydrophilic, thus no cosine-square interaction is needed.

As an example of this rescaling, the FENE bonds, Eq. (2.1), between two spacer particles of size $r_{0,s} = 0.5\sigma$, can be rewritten as

$$\begin{aligned} V_F(r) &= -\frac{1}{2}k_F r_\infty^2 \ln \left[1 - (r/r_\infty)^2 \right] \\ &= -\frac{1}{2}(k_F r_{0,s}^2) \left(\frac{r_\infty}{r_{0,s}} \right)^2 \ln \left[1 - \left(\frac{r/r_{0,s}}{r_\infty/r_{0,s}} \right)^2 \right]. \end{aligned} \quad (2.7)$$

In the second formula, all lengths are scaled by the size of the bead. Thus, if the bead size of a polymer were to be reduced to a half of its original value, like in the case of our spacer, then $(k_F \sigma_i^2)$ should remain the same after the change in size, so that the bond length, which is the distance r that corresponds to the minimum of $V_{\text{FENE}} + V_{\text{WCA}}$, can also scale with the bead size. For this reason, the spring constant k_F needs to be amplified by a factor of $(r_{0,\ell}/r_{0,s})^2 = 4$ for the spacer beads.

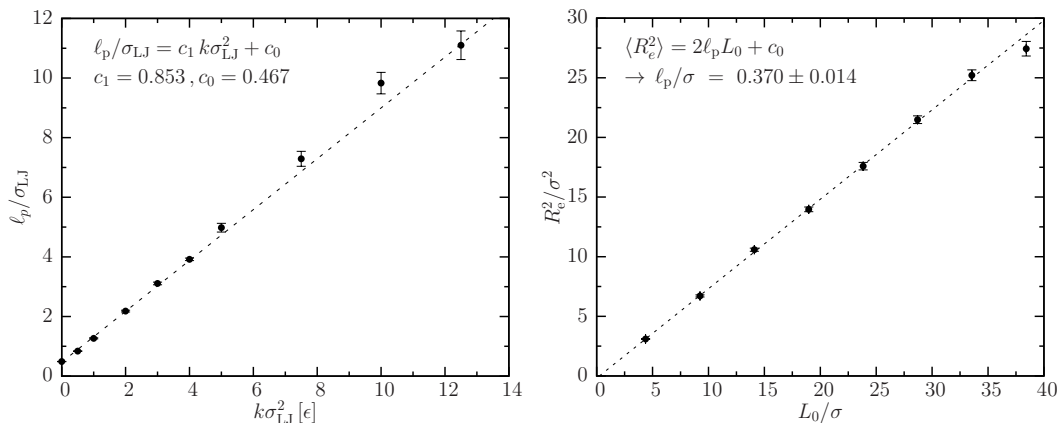


Figure 2.6: Left, the scaled persistence length ℓ_p/r_0 as a function of the spring constant kr_0^2 , where r_0 is the bead size defined by the length scale in the WCA potential. Right, end-to-end distance is measured for polymers of different contour length L_0 when $k = 1.5\epsilon/\sigma^2$, resulting $\ell_p = 0.370 \pm 0.014 \sigma$.

Persistence length of the spacer

Most of the interaction parameters for the spacer beads are easily set up using the scaling argument described above. The next step is the main target in the parameterization: obtaining a spacer with predetermined elastic properties, so that their mechanical response can be tuned to the experimentally relevant situation. For this, the harmonic potential, which connects the next neighbors and straightens the chain, will be scanned in order to study how the persistence length ℓ_p varies with different spring constant k .

The persistence length ℓ_p is measured in the following way. Chains of different degrees of polymerization N (N ranges from 20 to 100, bead size $r_0 = 1.0\sigma$) are simulated at temperature $k_B T/\epsilon = 1.1$ for at least 50000τ .¹⁷ Their end-to-end distance is measured and fit to the following equation [dG79]

$$\langle R_e^2 \rangle = N_a a^2 = L_0 a = 2L_0 \ell_p, \quad (2.8)$$

where N_a is the number of Kuhn segments, $a = 2\ell_p$ is the size of each Kuhn segment, and L_0 is the contour length. Note that, during these simulations, only the nearest neighbors experience the excluded volume interactions, and beads further apart are allowed to overlap, mimicking the Θ -condition in experiments. An set of simulations to measure the value of ℓ_p when $k = 1.5\epsilon/\sigma^2$ is shown in Fig. 2.6 as an example.

The measured ℓ_p , normalized by the bead size r_0 , for a range of spring constants kr_0^2 , is shown in Fig. 2.6. A linear fit to the data shows

$$\ell_p/r_0 = 0.853kr_0^2/\epsilon + 0.467. \quad (2.9)$$

¹⁷Depending on the chain length and spring constant, simulation time may be up to $4 \times 10^5 \tau$. Longer and softer chains are simulated longer to reduce the errors.

Eq. 2.9 shows how to tune the persistence length ℓ_p for chains of any given bead size r_0 .

This linear dependence of ℓ_p on k (with an offset) can also be derived by theory. Assume a really long chain of the above type consists of $N \gg 1$ repeating units, and is arranged into the shape of a complete circle of radius $R = Nb/2\pi$, where b is the bond length. Then each bond occupies an arc angle of $\theta \approx b/R$. The total bending energy from the harmonic bonds will be

$$E_{\text{bend}} = N \cdot \frac{1}{2}kb^2\theta^2 = \frac{N}{2}b^4/R^2. \quad (2.10)$$

At the same time, creating a curvature $K = 1/R$ costs energy E_{curv}

$$E_{\text{curv}} = \oint ds \frac{1}{2}\kappa K^2 = \frac{Nb}{2}\kappa/R^2, \quad (2.11)$$

where $\kappa = k_B T \ell_p$ is the bending modulus of the polymer chain [dG79] (see Technical Note 3.1 for derivation). Putting Eq. (2.10) and Eq. (2.11) together, one has

$$\ell_p = kb^3/k_B T. \quad (2.12)$$

Also considering when $k = 0$, *i.e.* when it's a freely jointed chain, the Kuhn length ℓ_K reduces to the bond length b , giving $\ell_p = \ell_K/2 = b/2$. Adding this offset to Eq. (2.12), plus the fact that $b \approx r_0$, the dependence of ℓ_p on k should be

$$\frac{\ell_p}{r_0} = \frac{1}{k_B T}kr_0^2 + \frac{1}{2}. \quad (2.13)$$

Since $1/k_B T = 1/1.1\epsilon = 0.91/\epsilon$, Eq. (2.9) measured from simulations is in good agreement with this simple theoretical estimation. The small disagreement may be a result of, for instance, ignoring the fluctuation contribution to the persistence length ℓ_p .

Now, the persistence length of the spacer part can be tuned to a realistic value. Since $\ell_p = 0.38$ nm for PEG [MF65, KPK⁺00], the persistence length of the spacer will be fixed to $\ell_p = 0.38\sigma$, assuming $1\sigma = 1$ nm.¹⁸ Using Eq. (2.9) with $r_0 = r_{0,s} = 0.5\sigma$, one derives $k \approx 1.5\epsilon/\sigma^2$. As an independent test, ℓ_p of a system with $r_0 = r_{0,s} = 0.5\sigma$ and $k = 1.5\epsilon/\sigma^2$ is measured, as shown in Fig. 2.6. The measured $\ell_p = 0.370 \pm 0.014\sigma$ is in good agreement with the targeted $\ell_p = 0.38\sigma$. This will be the k for the spacers.

Cross terms between the spacer and the anchor

Having successfully derived the interaction parameters for the spacer beads alone, the cross terms between them and the anchor beads are construct using the Lorentz-Berthelot mixing

¹⁸Note, the ratio σ/nm may be set to a different value later when a more accurate length matching is required, as described in Section 2.2.1, then $\ell_p = 0.38\sigma \neq 0.38$ nm any more. But this is not a real issue, since the persistence length of PEG is only a reference for our generic polymer chain.

Type	WCA		FENE		Harmonic	
	$r_0 [\sigma]$	$\epsilon_{\text{LJ}} [\epsilon]$	$k_{\text{F}} [\epsilon/\sigma^2]$	$R_{\infty} [\sigma]$	$k [\epsilon/\sigma^2]$	$R_0 [\sigma]$
lipid/anchor	1.0 ^a	1.0	30.0	1.5	10.0	4.0
spacer	0.5	1.0	120.0	0.75	1.5	2.0
cross terms	0.75	1.0	53.33 ^b	1.125	17.78 ^b	3.0

^a The $r_{0,\text{h}}$ for the hydrophilic head bead may be varied for different lipid shapes, as demonstrated in Chapter 5. Normally $r_{0,\text{h}} = 0.95\sigma$ will provide a bilayer with little spontaneous monolayer curvature.

^b Only two decimal places are shown here. In simulations, the maximum number of digits allowed by the `float` type is used.

Table 2.2: Interaction parameters for the WCA, the FENE, and the Harmonic potentials. Definitions of the functional forms can be found in Eqs. (2.1)–(2.3).

rule [AT89]: For particles of type A and B, of sizes σ_{A} and σ_{B} respectively, the cross terms are given by

$$\sigma_{\text{AB}} = \frac{\sigma_{\text{A}} + \sigma_{\text{B}}}{2}, \quad (2.14\text{a})$$

$$\epsilon_{\text{AB}} = \sqrt{\epsilon_{\text{A}}\epsilon_{\text{B}}}. \quad (2.14\text{b})$$

As mentioned before, the ϵ_{LJ} 's for the spacer beads and the anchor beads are the same. For the FENE and the harmonic bonds, after $\sigma_{\text{AB}} = (r_{0,\text{a}} + r_{0,\text{s}})/2 = 0.75\sigma$ is calculated, the spring constants were scaled in the same way as shown in Eq. (2.7). All interaction parameters except for the w_{c} used in later simulations, are collected in Tab. 2.2 for reference.

3 A theoretical model of the polymers

In the previous chapter, background knowledge of coarse-grained simulations was reviewed, and a generic model of the membrane-nanoparticle system has been developed. Starting with this chapter, a divide-and-conquer strategy will be applied to the examination of our nanoparticle design. The first ingredient, a tethered polymer brush under confinements, will be studied in this chapter. Lipid membranes, the other ingredient, will be covered in the subsequent two chapters.

3.1 Introduction

The polymeric tethers between the NP core and the surrounding lipid bilayer are the key difference between our NP design and the alternatives discussed in Section 1.1.2. As will be examined later in Chapter 7, most of the benefits of this design can be traced back to the properties of this extra layer of polymer linkers and their interactions with the enclosing membrane.

The polymer spacers in this design behave like a polymer brush confined between two concentric spherical shells, with both of their chain ends either grafted to the NP surface or anchored in the lipid bilayer. Our goal is to quantitatively, or at least semi-quantitatively, understand the brush responses when these confinements are changed, so that the spacer-membrane interactions can be predicted.

Polymers within this brush are subject to a rather complex environment restricting their conformational degrees of freedom. In the hope to simplify the problem, two extreme regimes, namely the large extension regime and the strong compression regime, will be explored separately using polymer theory. In the former regime, the chains are almost fully extended, and thus they experience little inter-molecular interactions and essentially behave like single chains. In the latter regime, the strong compression of the brush creates substantial lateral repulsions between the chains, which lead to a strong radial pressure. Both of these two regimes can be theoretically analyzed using suitable theoretical models. Then, the theories for these two regimes can be combined together and utilized to predict the full-range behaviors, which will be cross-checked using MD simulations. It turns out that this approximated method is accurate enough to predict the response of the polymer brush to variations in radial confinement.

Historically, single chain polymer physics has been studied since the first half of last century, led by the seminal work of Flory [Flo53]. In the 1970's, the scaling concepts proposed by de Gennes created a convenient framework to deal with the complicated many-body problem of polymers in solution [dG79]. Starting from the late 70's and early 80's, thanks

to the advances in both computer hardware and efficient algorithms, molecular simulations of polymers have become a powerful tool to study polymer systems under a great variety of conditions [LW75, EKB82, GK86, Bin02].

After decades of research, a great number of topics in polymer physics have been covered. In this chapter, a small sliver of this, the theoretical basis of single-chain stretching and polymer brushes, will be outlined. Then, these useful tools will be applied to the planar brush system as an example, before being extended to our special spherical geometry and tested by simulations.

3.2 Single-chain stretching

In the large extension regime of the brush, each chain is approximately aligned in parallel to the direction of the external force, while its expansion perpendicular to this direction is very small. The interactions between different chains are therefore negligible: the brush becomes equivalent to many non-interacting single chains.

Remarkably, important details of the force-extension relation for polymers depend quite sensitively on details of the underlying theoretical model, so we need to be very careful to pick the suitable one. In this section, three related models and their predictions for this relation will be briefly reviewed. Their derivations will only be outlined. However, the difference between the models will be emphasized.

3.2.1 Freely jointed chain

The most basic polymer model is the freely jointed chain (FJC). Such a chain consists of a number N of stiff segments, each one of which has the same length b and can freely rotate with respect to its neighboring bonds without any energy penalty. If each segment i is denoted as $\vec{r}_i = b\hat{t}_i$, where \hat{t}_i is a unit direction vector, then the end-to-end distance of the chain is $\mathbf{R}_e = b\sum_i \hat{t}_i$. In the absence of external forces, the mean-squared end-to-end distance $\langle \mathbf{R}_e^2 \rangle$ will be given by

$$\langle \mathbf{R}_e^2 \rangle = b^2 \left\langle \sum_{i,j} \hat{t}_i \cdot \hat{t}_j \right\rangle = Nb^2 = L_0 b, \quad (3.1)$$

where the contour length $L_0 = Nb$. In the second to last step, the fact that the orientations of different segments are uncorrelated, $\langle \hat{t}_i \cdot \hat{t}_j \rangle = \delta_{i,j}$, has been used.

Thus, for a freely jointed chain, the Kuhn length, defined as $\ell_K \equiv \langle \mathbf{R}_e^2 \rangle / L_0$, is the same as the bond length b . Also, the root-mean-squared end-to-end distance $R_e \equiv \langle \mathbf{R}_e^2 \rangle^{1/2}$ is proportional to $N^{1/2}$. For real polymers in better solvents than their Θ -solvents,¹ the

¹ Θ -condition, or Θ -solvent, refers to the situation in which polymer chains behave like *ideal* chains, meaning $R_e \sim N^{1/2}$. It happens at the point when the excluded volume effect, which tries to expand the chain, is balanced by the unfavorable mixing between the polymers and the solvent, which attempts to shrink it.

excluded volume effect makes the chain swollen. In this case, the end-to-end distance is called the Flory radius $R_F = R_e = bN^\nu$, where $\nu \approx 3/5$ is the Flory exponent [Flo53].

If an external force \mathbf{F} in the x -direction acts on one end of the chain, while the other end is fixed, then \mathbf{R}_e also points in the x -direction in equilibrium. The total energy will be $E_{\text{FJC}} = -\mathbf{F} \cdot \mathbf{R}_e = -Fx = -Fb \sum \cos \theta_i$, assuming $\mathbf{R}_e \cdot \hat{\mathbf{x}} = R_e = x$, and $\hat{\mathbf{t}}_i \cdot \hat{\mathbf{x}} = \cos \theta_i$. The partition function can be then calculated as

$$\mathcal{Z} = \int d\Gamma e^{\beta Fx} = \prod_i \int_0^{2\pi} d\phi_i \int_0^\pi d\theta_i \sin \theta_i e^{\beta Fb \cos \theta_i} = \left[4\pi \frac{\sinh \beta Fb}{\beta Fb} \right]^N, \quad (3.2)$$

where $d\Gamma = \prod_i d\hat{\mathbf{t}}_i = \prod_i d\phi_i d\theta_i \sin \theta_i$ and $\beta = 1/k_B T$.

Using Eq. (3.2), the average end-to-end distance $R_e = x$ will be extended to [FK73]:

$$x = \langle R_e \rangle = \frac{1}{\mathcal{Z}} \int d\Gamma x e^{\beta Fx} = \frac{1}{\beta \mathcal{Z}} \frac{d}{dF} \int d\Gamma e^{\beta Fx} = \frac{1}{\beta} \frac{d}{dF} \ln \mathcal{Z} = Nb \mathcal{L}(\beta Fb), \quad (3.3)$$

where $\mathcal{L}(x) = \coth x - 1/x$ is the Langevin function.

In the large force and extension regime, where $\beta Fb \gg 1$, the Langevin function can be approximated as $\mathcal{L}(x) \approx 1 - 1/x$. The force-extension relation for a FJC in this regime is then

$$\frac{x}{L_0} = 1 - \frac{k_B T}{Fb}, \quad (F \gg k_B T/b). \quad (3.4)$$

3.2.2 Worm-like chain

Unfortunately, real polymers are more difficult to describe theoretically, for instance because they have stiffness; two consecutive repeating segments are correlated due to the bending energy that penalizes deviations of the angle between the pair of segments from its relaxed value. Such chains are called worm-like chain (WLC). This correlation introduces a new length scale ℓ_p :

$$\langle \hat{\mathbf{t}}_i \cdot \hat{\mathbf{t}}_j \rangle = \exp\left(-\frac{|i-j|b}{\ell_p}\right). \quad (3.5)$$

This scale ℓ_p is called the *persistence length* of the chain.

As Eq. (3.5) shows, the bond-angle correlation dies off exponentially when two segments i and j are sufficiently far away, *i.e.* when $|i-j| \gg 1$. Thus, when N is large, one can “renormalize” the chain by combining consecutive and correlated segments into one effective Kuhn segment of length ℓ_K , so that different Kuhn segments become essentially independent, and the mean-squared end-to-end distance turns out to be [dG79]

$$\langle \mathbf{R}_e^2 \rangle \equiv \ell_K L_0 = 2\ell_p L_0. \quad (3.6)$$

This is the equation used for the parameterization of our CG linker model (see Eq. (2.8) in Section 2.3.2).

For such *semi-flexible* chains, bending contributes to their Hamiltonian as [Kaw04]

$$E_{\text{bend}} = \frac{\kappa_0}{2} \sum_i |\hat{\mathbf{t}}_i - \hat{\mathbf{t}}_{i+1}|^2 = -\kappa_0 \sum_i \hat{\mathbf{t}}_i \cdot \hat{\mathbf{t}}_{i+1} + \text{const.}, \quad (3.7)$$

where κ_0 is the bending stiffness between two segments of a chain.

Most often, such a system is treated in the *continuum limit*, *i.e.* $b \rightarrow 0$ and $N \rightarrow \infty$, while keeping the contour length L_0 finite. Then, the summation in Eq. (3.7) can be replaced by an integral form

$$\mathcal{H} = \frac{\kappa}{2} \int_0^{L_0} ds \left| \frac{d\hat{\mathbf{t}}(s)}{ds} \right|^2, \quad (3.8)$$

where $\kappa = b\kappa_0$ is the bending modulus, and $\hat{\mathbf{t}}(s) \equiv \frac{d}{ds}\mathbf{r}(s)$ is the tangent vector at an arc length s (measured from one end of the chain). This Hamiltonian is generally referred as the Kratky-Porod Hamiltonian [KP49].

In the presence of an external force \mathbf{F} in the x -direction, the Hamiltonian becomes

$$\mathcal{H} = \int_0^{L_0} ds \left(\frac{\kappa}{2} \left| \frac{d\hat{\mathbf{t}}(s)}{ds} \right|^2 - \mathbf{F} \cdot \hat{\mathbf{t}}(s) \right). \quad (3.9)$$

In the large extension regime, $\hat{\mathbf{t}}$ is roughly parallel to \mathbf{F} . One can decompose the tangent vector $\hat{\mathbf{t}}$ into parallel component \mathbf{t}_{\parallel} and a perpendicular one \mathbf{t}_{\perp} . After Fourier transforming $\mathbf{t}_{\perp} = \int \frac{dq}{2\pi} \tilde{\mathbf{t}}_{\perp}(q) \exp(iqs)$, the Hamiltonian becomes [MS95, Kaw04]:

$$\begin{aligned} \mathcal{H} &\approx \int_0^{L_0} ds \left(\frac{\kappa}{2} \left| \frac{d\mathbf{t}_{\perp}}{ds} \right|^2 + \frac{F}{2} |\mathbf{t}_{\perp}|^2 \right) - FL_0 \\ &= \frac{1}{2} \int \frac{dq}{2\pi} (\kappa q^2 + F) |\tilde{\mathbf{t}}_{\perp}|^2 - FL_0, \end{aligned} \quad (3.10)$$

From the equipartition theorem, $\frac{1}{2}(\kappa q^2 + F) \langle |\tilde{\mathbf{t}}_{\perp}|^2 \rangle = k_{\text{B}}T$, since there are two polarizations. Then the mean square perpendicular component $\langle \mathbf{t}_{\perp}^2 \rangle$ can be calculated as

$$\langle \mathbf{t}_{\perp}^2 \rangle = \int \frac{dq}{2\pi} \langle |\tilde{\mathbf{t}}_{\perp}|^2 \rangle = \int \frac{dq}{2\pi} \frac{2k_{\text{B}}T}{(\kappa q^2 + F)} = \frac{k_{\text{B}}T}{\sqrt{\kappa F}}. \quad (3.11)$$

Now one can calculate the extension $\langle x \rangle / L_0$ as [MS95]

$$\begin{aligned} \langle x \rangle / L_0 &= \frac{1}{L_0} \int_0^{L_0} ds \langle \hat{\mathbf{x}} \cdot \hat{\mathbf{t}} \rangle = \frac{1}{L_0} \int_0^{L_0} ds \langle t_{\parallel} \rangle \approx \frac{1}{L_0} \int_0^{L_0} ds \left(1 - \frac{1}{2} \langle \mathbf{t}_{\perp}^2 \rangle \right) \\ &= 1 - \frac{k_{\text{B}}T}{\sqrt{4F\kappa}} = 1 - \sqrt{\frac{k_{\text{B}}T}{4F\ell_p}}. \end{aligned} \quad (3.15)$$

Technical Note 3.1: Relation between κ and ℓ_p

From Eq. (3.7), the ensemble average of the angle between segment i and $i + 1$ is given by

$$\langle \hat{\mathbf{t}}_i \cdot \hat{\mathbf{t}}_{i+1} \rangle = \langle \cos \theta \rangle = \frac{\int d\Gamma \cos \theta \exp(\beta \kappa_0 \cos \theta)}{\int d\Gamma \exp(\beta \kappa_0 \cos \theta)} = \mathcal{L}(\beta \kappa_0) \approx 1 - \frac{1}{\beta \kappa_0}, \quad (3.12)$$

where $d\Gamma = d\theta d\phi \sin \theta$, assuming $k_B T / \kappa_0 \ll 1$.

Set $j = i + 1$ in Eq. (3.5), one immediately obtains

$$\langle \hat{\mathbf{t}}_i \cdot \hat{\mathbf{t}}_{i+1} \rangle = \exp\left(-\frac{b}{\ell_p}\right) \approx 1 - \frac{b}{\ell_p} \quad \text{for } \frac{b}{\ell_p} \ll 1. \quad (3.13)$$

Comparing the two equations above, it is easy to see that

$$\kappa \equiv b \kappa_0 = k_B T \ell_p. \quad (3.14)$$

In the last step, $\kappa = k_B T \ell_p$ was used (see Technical Note 3.1). Together with the result from the small extension regime, the widely used interpolation equation for the force-extension relation of WLCs by Marko and Siggia is derived [MS95]:

$$\frac{F \ell_p}{k_B T} = \frac{\langle x \rangle}{L_0} + \frac{1}{4(1 - \langle x \rangle / L_0)^2} - \frac{1}{4}. \quad (3.16)$$

Note that a few important assumptions entered this derivation. As clearly shown in the step from Eq. (3.7) to Eq. (3.8), a fundamental assumption is that the chain needs to be in the *continuum* limit, so that the discrete sum can be replaced by an integral. This requirement on continuity was also seen in Eq. (3.13) in Technical Note 3.1. The decay length ℓ_p of the correlation between neighboring segments is assumed to be much larger than the segment size b . In other words, within the “renormalized” effective Kuhn segments of $\ell_K = 2\ell_p$, there have to be enough repeating units of size $b \ll \ell_p$.

3.2.3 Discrete worm-like chain

In their classical study [MS95], Marko and Siggia successfully fitted Eq. (3.16) to the force-extension curves of double-stranded DNA (dsDNA) measured in experiments. This is mainly because, for dsDNA, the requirement of continuity is met beautifully. dsDNA molecules have a persistence length of $\ell_p \sim 50$ nm, which is significantly larger than the dimension of its repeating units (*i.e.* an approximate separation of 0.34 nm between consecutive base pairs) [PKT09].

However, $\ell_p \sim b$ for many polymers which are not that stiff. For example, the repeating segments in polyethylene glycol (PEG) are (C-O-C), whose size can be estimated using the bond length of the three C-O or C-C bonds. Each bond has a length of roughly 1.5 Å [MF65, LdVMP09], so a segment is about 4 Å long. The persistence length is very close to this value: $\ell_p \sim 3.8$ Å [KPK⁺00, LVMJP08].

As will be shown in the next subsection, the WLC model shall not be applied to soft polymers like PEG, due to the discreteness of the chain. Instead, a *discrete* WLC model should be considered. A few independent publications can be found on this topic, including the ones by Rosa *et al.* [RHMM03], and by Toan and Thirumalai [TT10].² Both works discuss the existence of a crossover force F_c , beyond which the discrete WLC behaves essentially like a freely jointed chain which was described in Section 3.2.1. This happens when the external force $F \gg F_c = ck_B T \ell_p / b^2$, where c is a constant around 4, and hence the energy to bend the chain κ/b becomes insignificant compared to the energy from the external force, Fb [RHMM03, TT10], thus the force-extension relation of a FJC, as described by Eq. (3.4), should be recovered.

No significant difference was observed when fitting the two discrete WLC models to results obtained from simulations (see the next subsection). Thus, only the model by Rosa *et al.* will be outlined here, for its derivation is very similar to the one of the WLC model described above.

In the model by Rosa *et al.* [RHMM03], the discrete nature of the chain is considered explicitly; the Hamiltonian of the system is kept in a discrete form, as shown in Eq. (3.7). After adding the contribution from the external force, $-b\mathbf{F} \cdot \sum_i \hat{\mathbf{t}}_i$, to the Hamiltonian, the partition function is calculated as

$$\mathcal{Z} = \int d\Gamma e^{-\beta\mathcal{H}}, \quad (3.17)$$

using the discrete Hamiltonian:

$$\mathcal{H} = -\kappa_0 \sum_i \hat{\mathbf{t}}_i \cdot \hat{\mathbf{t}}_{i+1} - b\mathbf{F} \cdot \sum_i \hat{\mathbf{t}}_i. \quad (3.18)$$

Then the average elongation $\langle x \rangle$ is derived from the partial derivative of the partition function with respect to F :

$$\langle x \rangle = -\frac{1}{\beta} \frac{\partial}{\partial F} \ln \mathcal{Z}. \quad (3.19)$$

In the large extension regime, decompose the direction vectors into parallel and perpendicular components to \mathbf{F} , *i.e.* $\hat{\mathbf{t}} = \mathbf{t}_{\parallel} + \mathbf{t}_{\perp}$, and approximate $|\mathbf{t}_{\parallel}| \approx 1 - \frac{1}{2}\mathbf{t}_{\perp}^2$ again. After this, one eventually arrives at [RHMM03]

$$\begin{aligned} \frac{Fb}{k_B T} = \frac{2\ell_p}{b} & \left[\sqrt{1 + \left(\frac{b}{2\ell_p}\right) \frac{1}{(1-\xi)^2}} - \sqrt{1 + \left(\frac{b}{2\ell_p}\right)} \right] + \\ & \left(3 \frac{1 - \mathcal{L}(\ell_p/b)}{1 + \mathcal{L}(\ell_p/b)} - \frac{b/2\ell_p}{\sqrt{1 + (b/2\ell_p)^2}} \right) \xi, \end{aligned} \quad (3.20)$$

where $\xi = \langle x \rangle / L_0$ is the normalized end-to-end extension. When $\ell_p \gg b$, Eq. (3.16) for the (continuous) WLC is recovered. This condition of $\ell_p \gg b$ signifies the difference between the WLC and the discrete version.

²Surprisingly enough, these works were published no earlier than a decade ago.

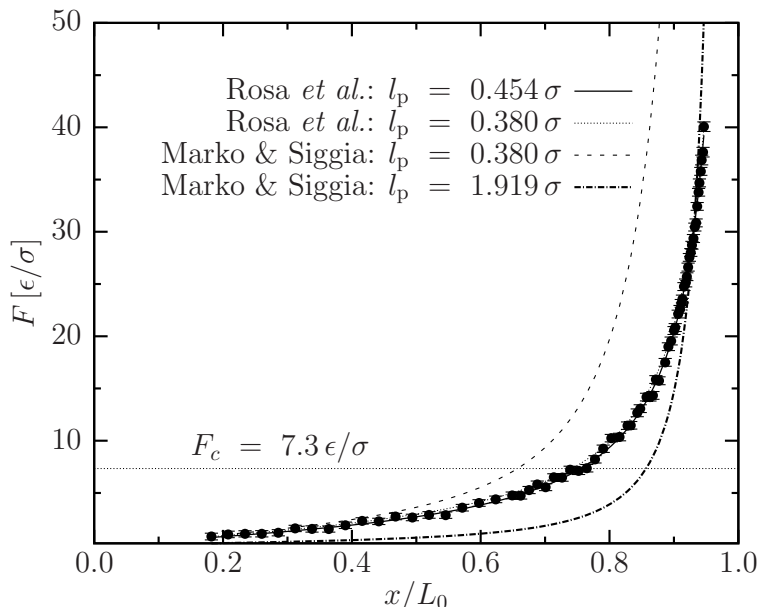


Figure 3.1: Force-extension relation for a single chain of $N = 80$ segments. The solid points are data from simulations. Two curves are overlapped with the data: The solid one is a fit, while the dotted one shows the theoretically predicted force-extension relation with a given $\ell_p = 0.38 \sigma$, both using the discrete WLC Eq. (3.20). The dashed curve is predicted using the WLC Eq. (3.16) with $\ell_p = 0.38 \sigma$, and the dash-dotted curve is a fit using the same equation. The crossover force F_c is shown as a horizontal dotted line.

When the force is large, the normalized end-to-end extension $\xi = \langle x \rangle / L_0 \rightarrow 1$. Then, the leading term in Eq. (3.20) becomes $1/(1 - \xi)$, following the same scaling behavior as a freely jointed chain. In fact, in the large force regime, all models should converge to the FJC model with this scaling of $F \sim 1/(1 - \xi)$ (*c.f.* Eq. (3.4)), since the bending energy κ/b between consecutive segments is overwhelmed by the contribution Fb from the external force [TT10]. The WLC model, however, shows a different scaling of $F \sim 1/(1 - \xi^2)$, as shown in Eq. (3.16). It is this different scaling in the large force regime that made the WLC model inappropriate to be used to describe soft polymers with $\ell_p/b \sim 1$, for which the large force regime is the relevant one.

3.2.4 Simulations of single-chain stretching

In order to select the most relevant polymer model from the three described above, and also to understand the single-chain force-extension behavior of our CG linker model, a set of MD simulations of a single chain was conducted using the spacers parameterized in Section 2.3.2. Each chain contains $N = 80$ segments, with excluded volume turned off

except for the nearest neighbors, since segments in a WLC two steps apart are allowed to overlap. In each specific simulation, the end-to-end distance x is imposed by fixing the end points. Forces acting on the end points were measured. All simulation ran at temperature $k_B T/\epsilon = 1.1$ for 125000τ . The results are shown in Fig. 3.1, together with two theoretically predicted curves and two fits.

Firstly, the curves based on the discrete WLC Eq. (3.20) quantitatively capture the force-extension relation. The fit (solid curve), as well as the parametric plot (thin dotted) with a given $\ell_p = 0.38 \sigma$, show very good agreement with the simulation data. Although the fit results in $\ell_p = 0.454 \sigma$, which is roughly 19% higher than the value $\ell_p \simeq 0.38 \sigma$ that was parameterized and measured based on the end-to-end distance of a free chain (see Section 2.3.2), the agreement from the two curves suggests that the quality of the fit is insensitive to such small variations in the persistence length ℓ_p . Instead, it is the general functional form in the theory that matters.

Secondly, as a comparison, both curves using the continuous WLC model fail to capture the chain behavior over the full range of forces, regardless of whether the persistence length is obtained from fitting to the data, or taken from the parameterization of the model. Since ℓ_p is only a prefactor in the WLC model that simply scales the curve, as shown in Eq. (3.16), the inability to quantitatively reproduce the force-extension curve suggests that the fundamental scaling of the WLC model cannot describe such soft polymers.

Of course, this does not mean that the WLC model is useless. On the contrary, for stiffer polymers like dsDNA, the crossover force $F_c \approx 4k_B T \ell_p / b^2 = 8 \text{ nN}$ is much larger than the value it takes for soft polymers like PEG. Applying forces comparable to F_c may affect the chemical structure of the chains. In the case of dsDNA, the stacking and base-pairing interactions generate a few $k_B T$ per base pair, corresponding to an unstacking force on the order of $10k_B T / \text{nm} \approx 40 \text{ pN}$ [MS95], which is much lower than the crossover force $F_c \approx 8 \text{ nN}$. This means, for the physically relevant range of forces and extensions, bending is the dominant physics, which the WLC model can describe very successfully, but the FJC will inevitably fail, as shown by Marko and Siggia [MS95].

3.3 Scaling theory

Unlike in the large extension regime, where all chains are stretched and essentially separated, in the opposite regime, *i.e.* the large compression regime, chains interact strongly with each other due to the increased density. Such interactions are inherently multibody in nature, which increases the difficulty to solve the problem exactly.

Instead, a method called “scaling theory”, pioneered by de Gennes [dG79], deals with such problems in a mean-field manner. This scaling theory, or a particular manifestation of it known affectionately as “Blobology”, will be reviewed in this section, and then applied to two systems of distinct geometries, namely the planar polymer brush system and the spherical one.

A special note is needed on the notations used in this section. In the literature, when

the scaling theory is introduced and developed, *e.g.* in the works by de Gennes [dG79], only theoretical polymers are discussed. For these polymers, the size of their repeating unit is denoted as the variable a , which is essentially the *Kuhn* length of the chains. The Kuhn length is the most relevant quantity in the scaling theory, for instance when predicting the end-to-end distance of polymer chains, since it is the effective segment size for the random walk of the chains (regardless of their real chemical structures). However, for more realistic polymers, the Kuhn length rarely equals the *monomer* size (of excluded volume), and the difference is especially large for stiff polymers like DNA. Therefore, we will distinguish these two by denoting the size of the Kuhn segment as “ a ”, while referring to the monomer size as “ b ”. The monomer size b coincides with the bond length b between two neighboring monomers used in the previous section. The ratio a/b is of order unity for soft polymers like PEG, but is much larger for stiff chains (*e.g.* $\mathcal{O}(10^2)$ for dsDNA). Notice, we now have two related numbers of segments; the one that counts the number of Kuhn segments will be denoted as N_a , while the other for the monomers will be N_b . N_a and N_b are related by the contour length of the chains, thus $bN_b = aN_a$. N_a will appear more often in the scaling theory, whereas N_b typically shows up when one wants to relate the theory to some real chains.

3.3.1 Blobology

Depending on the average concentration c of the *Kuhn segments*, polymers in good solvent can be found in different regimes. When c is low, they are in the dilute regime where chains behave like single chains on their own. When the concentration is increased to a critical *overlap concentration* c^* , polymers start to feel each other’s presence. At $c = c^*$, the average concentration c is equal to the local concentration of Kuhn segments inside a single chain, *i.e.* the number of Kuhn segments inside a *blob* of size R_F , the Flory radius [Flo53] of a polymer coil in good solvent. Thus,

$$c^* = N_a/R_F^3 = N_a/(aN_a^\nu)^3 = a^{-3}N_a^{1-3\nu} = a^{-3}N_a^{-4/5}, \quad (3.21)$$

where the Flory exponent $\nu \simeq 3/5$ has been used. The volume fraction, $\Phi = ca^3$, of the Kuhn segments at the overlap concentration, is

$$\Phi^* = c^*a^3 = N_a^{-4/5}. \quad (3.22)$$

If Φ increases beyond Φ^* , the polymer solution enters the semi-dilute regime, where the chains are in contact, but not completely packed as in the polymer melt regime, where solvent molecules are expelled from the chains and the polymers take up all of the space with $\Phi = 1$. Thus, in the semi-dilute regime,

$$\Phi^* \ll \Phi \ll 1. \quad (3.23)$$

This semi-dilute regime is where we need to focus on. This is because 1) N_a is normally large, thus Φ^* is low as described by Eq. (3.22), meaning the semi-dilute and melt regimes

cover a big range of relevant systems, and 2) the polymer brush in the semi-dilute regime can provide many desired functions, *e.g.* the existence of solvent (unlike in the melt regime) is required for loading hydrophilic drugs.

The key idea in blobology is to separate *local* interactions, among monomers within a blob of size ξ , from the *global* multi-chain interactions: Monomers within a blob behave as in a self-avoiding walk (SAW), thus the number of Kuhn segments inside a blob, g , is related to the blob size ξ as $g = (\xi/a)^{1/\nu}$. Interactions of the segments from different blobs are represented by the excluded volume effect between blobs. In this way, interactions happening on two length scales are decoupled.

The size of the blobs, ξ , reflects the physics in the system. One example is when a chain is under a *small* external force \mathbf{F} , similar to the situation of a *large* force discussed in the previous section. The blob size is determined by the interplay between the entropy, which favors to explore as many configurations as possible, and the enthalpy by the force applied. The blob size ξ_P in this case, normally referred to as the ‘‘Pincus blobs’’ [Pin76, dG79], is given by $\xi_P = k_B T / F$, which is the blob size ξ at which the tensional enthalpy $F\xi_P$ becomes comparable to the thermal energy $k_B T$. For monomers within this length scale ξ_P , the thermal fluctuations rule, thus SAW behavior is observed; while beyond ξ_P , the force dominates and blobs align along the direction of \mathbf{F} .

The blob size ξ also scales with Φ in the semi-dilute regime. There are two requirements [dG79]. First, at the overlap monomer fraction $\Phi \sim \Phi^*$, $\xi \approx R_F$. Second, with increasing $\Phi > \Phi^*$, because the polymers are largely in contact, ξ should be independent of the degree of polymerization $N_b = \frac{a}{b} N_a$. Assuming ξ follows a power law,

$$\xi = R_F \left(\frac{\Phi^*}{\Phi} \right)^{m_\xi} = a N_a^\nu N_a^{-4m_\xi/5} \Phi^{-m_\xi}. \quad (3.24)$$

Thus, due to the second requirement, $m_\xi = 5\nu/4 \approx 3/4$, leading to

$$\xi \approx a \Phi^{-3/4}. \quad (3.25)$$

3.3.2 Osmotic pressure: theory

Enlightened by the virial expansion, one can expand the osmotic pressure Π as [dG79]

$$\frac{\Pi}{k_B T} = \frac{c}{N_a} + B_2 c^2 + \mathcal{O}(c^3) = \frac{c}{N_a} f_\Pi \left(\frac{c R_F^3}{N_a} \right) = \frac{c}{N_a} f_\Pi \left(\frac{c}{c^*} \right). \quad (3.26)$$

Note that, since c denotes the *Kuhn segment* concentration, c/N_a here is the *molecule* concentration.

The requirement on Π is that it should be independent of N_a when $\Phi > \Phi^*$. This turns out to be a rather strict constraint; in order to cancel out the N_a in the prefactor, the function $f_\Pi(x)$ *must* be a simple power of x :

$$\lim_{x \rightarrow \infty} f_\Pi(x) = \text{const.} \times x^m = \text{const.} \times \left(\frac{\Phi}{\Phi^*} \right)^m = \text{const.} \times \Phi^m N_a^{4m/5}, \quad (3.27)$$

where Eq. (3.22) is used in the last step. Thus, $m = 5/4$. Putting this back into Eq. (3.26), together with $c = \Phi/a^3$, we have

$$\frac{\Pi a^3}{k_B T} = \text{const.} \times \Phi^{m+1} = \text{const.} \times \Phi^{9/4}. \quad (3.28)$$

Combining Eq. (3.25) and (3.28), and ignoring the constant of order unity [dG79], we have

$$\Pi \approx \frac{k_B T}{\xi^3}. \quad (3.29)$$

This means that the osmotic pressure given by the blobs is equal to the energy density determined by the characteristic energy $k_B T$ and the characteristic length ξ .

3.4 Planar brushes

3.4.1 Overview: planar brushes

In this section, the blobology arguments described in the previous section will be applied to a polymer brush in a planar geometry. This system has been investigated using the blobology concepts since the late 1970's by Alexander [Ale77] and de Gennes [dG80, dG87]. Others have studied this system using self-consistent mean-field theory, such as Milner *et al.* [MWC88b, MIL91]. However, we will stay focused on the scaling method for its simplicity and pedagogical implications.

3.4.2 Brush height: planar brushes

In a relaxed brush without external forces, depending on the grafting density Σ (number of molecules per unit area), the chains can either be in the ‘‘mushroom’’ regime, where chains do not overlap and behave like separate globules, or in the ‘‘brush’’ regime, where they do interact with their neighbors [dG80]. Only the semi-dilute ‘‘brush’’ regime will be the topic here for its interesting properties.

In this regime, the distance D between two neighboring grafting points satisfies $D = \Sigma^{-1/2} < R_F$. Thus, in such a planar brush, the chains are laterally confined while being extended in the vertical direction. This lateral confinement limits the blob size to be $\xi_0 = D$.³

Each chain contains a string of blobs of size ξ_0 . The number of Kuhn segments in each blob is $g \approx (D/a)^{5/3}$. So there will be N_a/g blobs per chain, giving a brush height of [dG80]

$$L_{0,\text{pl}} = \frac{N_a}{g} D = \left(\frac{b}{a}\right) N_b a^{5/3} D^{-2/3}. \quad (3.30)$$

³From here on, all quantities with subscript 0 refer to the *uncompressed* state.

Notice that in the last step the number of Kuhn segments, N_a , is replaced by the number of monomers, N_b , with an additional factor of b/a . This is because N_b is often *known*, and thus using it is more convenient.

One issue should be pointed out here regarding the accuracy of these scaling predictions. Studies using self-consistent field (SCF) theory, with more physical constraints on its solutions, have predicted a more realistic concentration profile, which quadratically depends on the vertical position from the substrate and thus is normally referred to as the “parabolic profile” [MWC88a]. The blobology picture, however, implies a step-function-like concentration profile of the monomers, the value of which is equal to the concentration inside each blob and vanishes at the brush height $L_{0,\text{pl}}$. Moreover, shown in the SCF results, the chain ends should also have a broad distribution at different height, even deep inside the brush [MWC88b], which conflicts with the assumption that the ends of the chains remain inside the last blob.

These are valid concerns about regular planar polymer brushes discussed in the literature. However, the polymer brush in our membrane-nanoparticle composite is designed in a slightly different way; each polymer not only has one of its ends grafted to a solid surface, but also has the other end *anchored* into a lipid membrane. So there are no open ends any more, unlike in conventional polymer brushes. For this reason, blobology provides a more realistic model for our special brush than for the ordinary brush it has first been invented for.

3.4.3 Osmotic pressure: planar brushes

If the brush is compressed, then the spacing L between the two parallel planes is reduced from the relaxed $L_{0,\text{pl}}$, and the monomer concentration increases as $\Phi/\Phi_0 = L_{0,\text{pl}}/L$. Using Eq. (3.25), the size of the blobs decreases as

$$\frac{\xi}{\xi_0} = \left(\frac{\Phi}{\Phi_0}\right)^{-3/4} = \left(\frac{L}{L_{0,\text{pl}}}\right)^{3/4}. \quad (3.31)$$

Substitute into Eq. (3.29), the osmotic pressure for a planar polymer brush is derived as [dG79, WP86]⁴

$$\Pi_{\text{pl}} \approx \frac{k_{\text{B}}T}{\xi_0^3} \left(\frac{\Phi}{\Phi_0}\right)^{9/4} = \frac{k_{\text{B}}T}{\xi_0^3} \left(\frac{L_{0,\text{pl}}}{L}\right)^{9/4}, \quad (L < L_{0,\text{pl}}). \quad (3.33)$$

⁴If the elastic energy of the chains is also taken into account, the osmotic pressure for a planar brush becomes [dG87, Isr91]

$$\Pi_{\text{pl}} \approx \frac{k_{\text{B}}T}{\xi_0^3} \left[\left(\frac{L_{0,\text{pl}}}{L}\right)^{9/4} - \left(\frac{L}{L_{0,\text{pl}}}\right)^{3/4} \right], \quad (L < L_{0,\text{pl}}) \quad (3.32)$$

However, the additional elastic term is negligible when $L < L_{0,\text{pl}}$ [WP86].

3.5 Spherical brushes

The discussion on planar brushes in the previous section serves as an example application of the scaling theory reviewed in Section 3.3. For the purpose of understanding the behavior of the brushes in our NPs, we need to move on to a more complicated geometry: a confined space between two concentric spherical shells.

3.5.1 Overview: spherical brushes

One key difference between the spherical and the planar geometry is that because of the geometry the blobs are not all of the same size. As the distance from the center of the sphere increases, more space is available for each chain and thus the blob size ξ increases. From pure geometry, we have $\xi(r)/\xi_{\text{in}} = r/R_{\text{in}}$, where ξ_{in} is the blob size at the inner core, to which the polymers have one end attached, and R_{in} is the radius of the core. If, however, there are only a few layers of blobs due to a short chain length N and the brush height is comparable to the R_{in} as in the case of our NPs, then the brush will behave somewhere between a planar brush and a spherical one.

Two quantities in the result for a planar brush, *i.e.* Eq. (3.33), need to be adapted, namely the uncompressed brush thickness $L_{0,\text{sp}}$ and the dependence of the concentration Φ on the separation L . They will be discussed in the following two subsections.

3.5.2 Brush height: spherical brushes

The first revision to Eq. (3.33) is the relaxed brush height L_0 , since the distance between the neighboring chains depends on their distance to the center of geometry. Two different methods to derive $L_{0,\text{sp}}$ will be compared here.

Blobology Perspective

From the perspective of “Blobology”, each polymer chain consists of a string of blobs, taking up a cone-shape space. In order to derive $L_{0,\text{sp}}$, one needs to figure out the number of blobs per chain, the size of each blob, and then add up the diameters of the blobs.

At the surface of the inner sphere, the blob size $\xi_1 = \Sigma^{-1/2}$. From geometry, the next one will be $\xi_2 = \alpha\xi_1 = \xi_1(1 + \xi_1/R_{\text{in}})$, where the proportionality factor $\alpha \equiv (1 + \xi_1/R_{\text{in}})$. The blob size for the last blob, labeled as ξ_n , is [DC82]

$$\xi_n = \xi_1 \alpha^{n-1} = \xi_1 \left(1 + \frac{\xi_1}{R_{\text{in}}}\right)^{n-1}, \quad (3.34)$$

with the following constraint on the total number of Kuhn segments N_a in a chain:

$$N_a = \sum_{i=1}^n g_n = \sum_{i=1}^n (\xi_i/a)^{5/3} = \sum_{i=1}^n \left[\frac{\xi_1}{a} \alpha^{i-1}\right]^{5/3} = \left(\frac{\xi_1}{a}\right)^{5/3} \sum_{i=1}^n (\alpha^{5/3})^{i-1}. \quad (3.35)$$

Summing up this geometric series and solving for n , one has

$$n = \frac{\log \left\{ 1 + N_a \left(\frac{a}{\xi_1} \right)^{\frac{5}{3}} \left[\left(1 + \frac{\xi_1}{R_{\text{in}}} \right)^{\frac{5}{3}} - 1 \right] \right\}}{\frac{5}{3} \log \left(1 + \frac{\xi_1}{R_{\text{in}}} \right)}. \quad (3.36)$$

Note that there is no need to round up n into an integer, since it appears in the brush height $L_{0,\text{sp}}$ in the form of α^n :

$$L_{0,\text{sp}} = \sum_{i=1}^n \xi_i = \xi_1 \sum_{i=1}^n \alpha^{i-1} = R_{\text{in}} \left\{ 1 + N_a \left(\frac{a}{\xi_1} \right)^{\frac{5}{3}} \left[\left(1 + \frac{\xi_1}{R_{\text{in}}} \right)^{\frac{5}{3}} - 1 \right] \right\}^{\frac{3}{5}} - R_{\text{in}}. \quad (3.37)$$

Again, $N_a = bN_b/a$ is the number of Kuhn segments, whereas N_b is the degree of polymerization.

One can perform two simple sanity checks on this result for the brush height in a spherical geometry. First, when $R_{\text{in}} \rightarrow \infty$, the planar thickness (Eq. (3.30)) is recovered. Second, when the distance between two grafting points is equal to their Flory radius, *i.e.* $\xi_1 = R_{\text{F}} = aN_a^{3/5}$, the chains are barely in contact thus the thickness $L_{0,\text{sp}}$ is equal to the Flory radius R_{F} .

Concentration Perspective

Another way to derive the brush height $L_{0,\text{sp}}$ has been discussed in the literature [DC82, WP86, BM12]. Assuming $\xi(r)/\xi_1 = r/R_{\text{in}}$, Eq. (3.25) gives

$$\Phi(r) = \left(\frac{R_{\text{in}} a}{\xi_1} \right)^{4/3} r^{-4/3}. \quad (3.38)$$

Since the monomer concentration $c(r) = \Phi(r)/a^3$, we can use the constraint of monomer number again [DC82, WP86]:

$$Nf = 4\pi \int_{R_{\text{in}}}^{R_{\text{out}}} dr [c(r) r^2], \quad (3.39)$$

where f is the total number of chains in the brush. Consequently,

$$L_{0,\text{sp}} = R_{\text{out}} - R_{\text{in}} = R_{\text{in}} \left[1 + \frac{5}{3} N_a \frac{a^{5/3}}{\xi_1^{2/3} R_{\text{in}}} \right]^{3/5} - R_{\text{in}}. \quad (3.40)$$

This also satisfies $L_{0,\text{sp}} \rightarrow N_a a^{5/3} \xi_1^{-2/3}$ when $R_{\text{in}} \rightarrow \infty$.

Comparison between the two ways of estimating $L_{0,\text{sp}}$ for a range of ξ_1 (when $N_b = 80$) and N_b (when $f = 103$ and $\xi_1 = 2.8\sigma$) is shown in Fig. 3.2. For the same N_b and ξ_1 , the

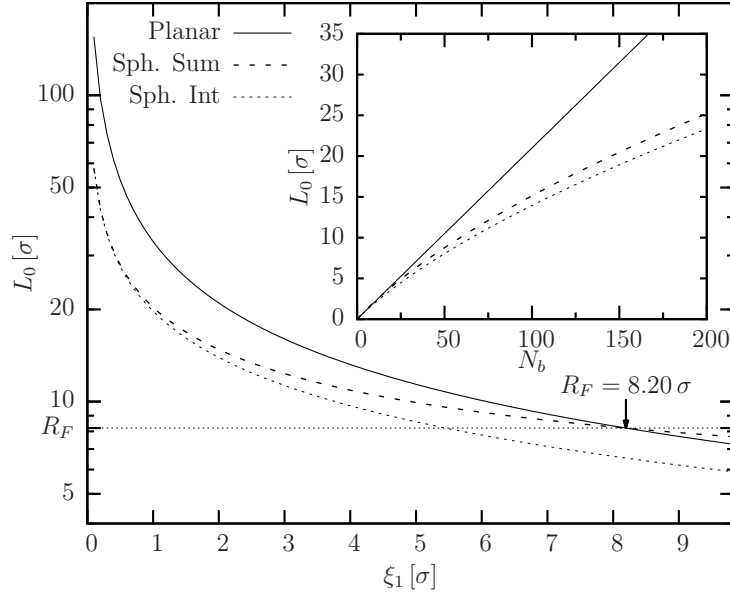


Figure 3.2: Comparison of L_0 predicted by Eq. (3.30) (solid, “Planar”), Eq. (3.37) (dashed, “Sum”), and Eq. (3.40) (dotted, “Int”) as a function of grafting distance ξ_1 (when $N_b = 80$) and N_b (inset, when $f = 103$ and $\xi_1 = 2.8 \sigma$), given $R_{\text{in}} = 8 \sigma$.

value of $L_{0,\text{sp}}$ calculated using both methods are lower than the planar $L_{0,\text{pl}}$, as the chains spread out at larger distance from the substrate. When the grafting density decreases (ξ_1 increases), the brush thickness L_0 predicted by the blob arguments (Eq. (3.30) and (3.37)) reduces to $L_0 = R_F$ when $\xi_1 = R_F$, after which the system enters the mushroom regime. The result from the concentration perspective (Eq. (3.40)) does not capture this requirement. Thus, Eq. (3.37) will be used later to predict the height $L_{0,\text{sp}}$ of a spherical brush.

3.5.3 Osmotic pressure: spherical brushes

The second quantity required to be modified in Eq. (3.33) is the dependence of concentration on the geometry.

$$\Phi(L) = N_a f a^3 / V = \frac{N_a f a^3}{\frac{4\pi}{3} [(R_{\text{in}} + L)^3 - R_{\text{in}}^3]}. \quad (3.41)$$

Thus, analogous to Eq. (3.33) and (3.32), we obtain the osmotic pressure in the spherical geometry ($L < L_{0,\text{sp}}$)

$$\Pi_{\text{sp}} \approx \frac{k_B T}{\xi_0^3} \left(\frac{(R_{\text{in}} + L_{0,\text{sp}})^3 - R_{\text{in}}^3}{(R_{\text{in}} + L)^3 - R_{\text{in}}^3} \right)^{9/4}, \quad (L < L_{0,\text{sp}}). \quad (3.42)$$

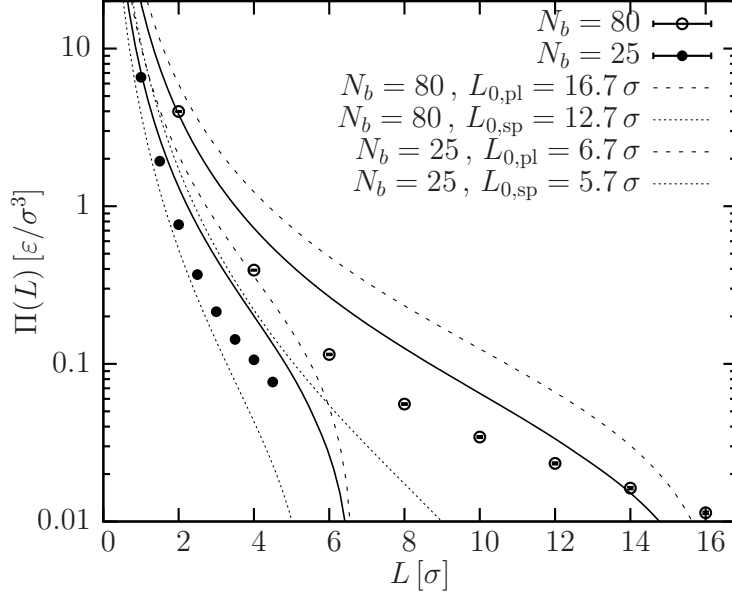


Figure 3.3: The osmotic pressure Π vs the separation L between the two shells, for an example system with parameters $f = 103$, $N_b = 80$, $R_{\text{in}} = 8\sigma$, (open circles), and another system with $f = 80$, $N_b = 25$, $R_{\text{in}} = 5\sigma$, (closed circles). The dashed curves are predicted by the planar case Π_{pl} (Eq. (3.33)), and the dotted curves by the spherical case Π_{sp} (Eq. (3.42)), with L_0 shown in the keys. Solid curves are the average between the planar and spherical predictions.

Here, ξ_0 is the blob size at $L = L_{0,\text{sp}}$, and is not ξ_1 near the inner sphere. In the limit that $R_{\text{in}} \rightarrow \infty$, the planar case (Eq. (3.33)) is recovered.

3.5.4 Compression Results

Two sets of simulations of spherical polymer brushes are conducted. In each simulation, all polymers have one end *grafted* to the inner sphere of radius R_{in} , and the other end *confined* by a stiff harmonic potential to a concentric outer sphere that is L apart from R_{in} . The confined ends of the polymers are allowed to diffuse laterally in the surface of the outer sphere in order to mimic the situation where they are anchored in a fluid lipid bilayer. The osmotic pressure Π is measured by

$$\Pi(L) = \sum_{i=0}^{N_b f} F_r^i / 4\pi(R_{\text{in}} + L)^2, \quad (3.43)$$

where F_r^i is the radial force that monomer i exerts on the outer spherical shell. The monomers interact with the sphere *via* a WCA potential, thus F_r^i is nonzero only if monomer i is close enough to the shell.

The results from the two systems, one with parameters $f = 103$, $N_b = 80$, $R_{\text{in}} = 8\sigma$, (open circles), and the other with $f = 80$, $N_b = 25$, $R_{\text{in}} = 5\sigma$, (closed circles), are shown in Fig. 3.3. *Without* any fitting, both the planar theory (Eq. (3.33), dashed) and the spherical theory (Eq. (3.42), dotted) describe the pressure in a semi-quantitative way. More significantly, the average of the two predicted equations describes the simulation data with a higher accuracy. This empirical improvement may be justified by the fact that $L \sim R_{\text{in}}$, thus the systems are in the crossover regime from the planar geometry to spherical geometry. One can potentially increase the accuracy of the combined prediction by tuning the relative weight between the planar and spherical parts instead of using a simple 50:50 average. But because this weight may be system-dependent, thus a simple average has been used.

Note that when $L \rightarrow L_0$, $\Pi \rightarrow 0$, thus, on the semi-log plot Fig. 3.3, curves diverge at $L = L_0$. However, because in simulations one end of the polymer chains is confined to the outer sphere, there will be forces between the other nonconfined monomers and the sphere even if $L > L_0$. This is why the theoretical curves deviate from the simulations near $L \sim L_0$.

3.5.5 Full-range force-extension relation

Combining the results from the large compression and the large extension regimes together, the force-extension behavior over the whole extension range can be predicted. To be more specific, for the large compression regime, the average of Eq. (3.33) and (3.42) is calculated as the osmotic pressure Π produced by the brush. The repulsive part of the force is the osmotic force averaged over f chains, *i.e.* $\Pi A/f$. For the large extension regime, Eq. (3.20) is utilized for the tensile force due to the chain stretching. The repulsive and tensile forces are then added as the total force per chain, F_{chain} . Fig. 3.4 shows this full-range force-extension curve of a system consisting of $f = 343$ linkers of $N_b = 30$, grafted on a surface of radius $R_{\text{in}} = 11.12\sigma$ (solid curve). A clear crossover from repulsive force to tensile force can be observed as the separation L between the two shells increases.

To cross-check this theoretical brush model, simulation data (open circles) are also presented. For these data, the repulsive force *per chain* is the total osmotic force on the outer sphere (using Eq. (3.43)) divided by the number of chains f . The tensile force (when $R - R_{\text{in}} > L_0$) is the force needed to hold the two ends of each chain at a certain distance. The total force F_{chain} is the sum of the repulsive and tensile forces. As can be seen in Fig. 3.4, our theory describes the simulation data with high accuracy. Note that there is *no* fitting involved: all parameters in the theory are known.

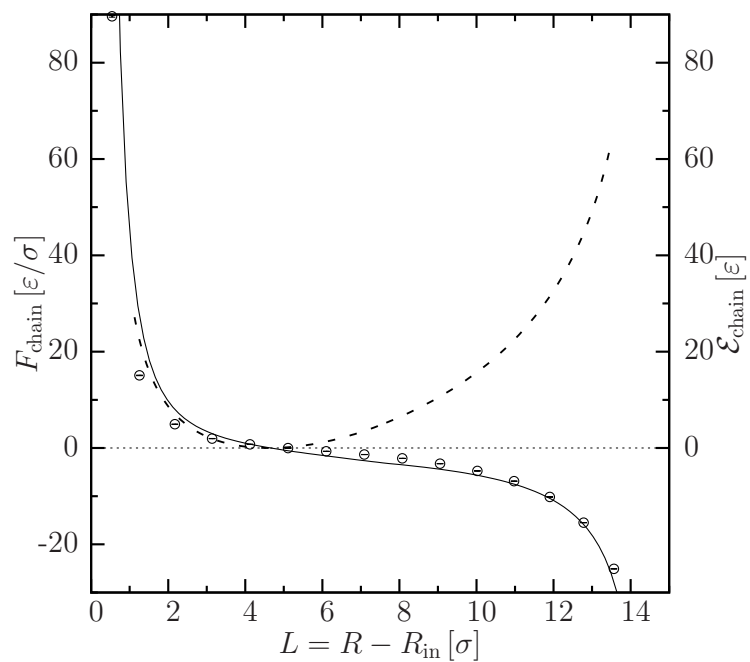


Figure 3.4: Single chain force F_{chain} as a function of separation $L = R - R_{in}$. Data from simulation of a system which consists of $f = 343$ linkers of $N_b = 30$ grafted on a surface of radius $R_{in} = 11.12\sigma$ are shown as open circles. The solid curve is a theoretical prediction as described in the main text. The dashed curve shows the free energy \mathcal{E} of the chain obtained by integrating the force.

4 Membrane elasticity I: The bending modulus by buckling

In the previous chapter, the mechanical properties of the polymer chains in our nanoparticle composites have been investigated. The elastic properties of the other major component of the design, namely the lipid membrane, will be studied in this and the following chapter.

4.1 Introduction

4.1.1 Helfrich theory

In aqueous solutions, lipid molecules spontaneously aggregate into quasi-two-dimensional surfaces, called lipid membranes, whose lateral length scale can be several orders of magnitude larger than their thickness. At length scales only a few times larger than the lipid size, the (free) energy of a membrane surface \mathcal{S} can be quantitatively described by a curvature elastic theory proposed by Helfrich [Hel73]:

$$\mathcal{E}[\mathcal{S}] = \int_{\mathcal{S}} dA \left\{ \frac{1}{2} \kappa (K - K_0)^2 + \bar{\kappa} K_G \right\} + \gamma \oint_{\partial\mathcal{S}} ds, \quad (4.1)$$

where the total curvature $K = K_1 + K_2$ is the sum of the two local principal curvatures K_1 and K_2 , and the Gaussian curvature $K_G = K_1 K_2$ is their product [Car76, Kre91]. In addition to the two corresponding elastic moduli, namely the bending modulus (or the bending rigidity) κ and the Gaussian curvature modulus (or the saddle-splay modulus) $\bar{\kappa}$, two other material parameters enter this expression: first, the spontaneous membrane curvature K_0 , which corresponds to the linear term in this quadratic expansion and quantifies the intrinsic lipid curvature a membrane prefers; and second, the edge tension γ , a free energy cost per unit length of an open edge, where lipids rearrange to minimize their exposure to water. The first integral in Eq. (4.1) extends over the whole surface \mathcal{S} , while the second covers the boundaries $\partial\mathcal{S}$.

Despite its simple form, the Helfrich Hamiltonian Eq. (4.1) is a remarkably accurate model for the physics of fluid lipid membranes and has been successfully applied to a broad range of biological situations, for which it has provided extremely useful descriptions, including the shape transformation of membrane vesicles like red blood cells [DH76, SBL91, NG05], various lipid phases [GCHT85, Lei86, ST93], membrane budding and pearling [JL93, BZM94], and membrane fusion [ZVC93, Sie99, KK02].

If one wishes to apply Helfrich theory, the four material parameters in the Helfrich Hamiltonian need to be known. The spontaneous K_0 normally vanishes for a *bilayer* due

to up-down symmetry, but generally remains nonzero for a *monolayer* [Mar06]. If the two leaflets in the bilayer are *asymmetric*, K_0 can be deduced from the shape of curved regions with opposing K_0 [WHZ12], or from simulating half cylinders [SN11]. The edge tension γ can be determined, both in experiments and in simulations, by studying membrane pores [KSG⁺03, TdOB04b, TdOB04a, WdOEB06]. A method to computationally deduce the first elastic modulus, κ , will be the focus of this chapter, leaving the second modulus $\bar{\kappa}$ for the next chapter.

4.1.2 Existing methods to measure κ in simulations

In simulations, the most widely used method to determine the bending modulus κ is to measure the height undulation spectrum $\langle |h_{\mathbf{q}}|^2 \rangle$ of a flat lipid membrane [GGL99, LE00, MM01, AV02, Far03, MdVM04, WF05, CKD05, CD05, BB05, MNK07, WD10, WPWB11, BBS⁺11, SN11], which is proportional to $1/\kappa q^4$, where q is the wave vector. However, since this method requires sampling of a relatively weak fluctuation signal ($k_{\text{B}}T/\kappa \sim 1/20$) for very long time,¹ in order to obtain accurate statistics, the computational cost is normally high. Moreover, to alleviate contaminations of the signal “leaking in” from the high q regime, where $\langle |h_{\mathbf{q}}|^2 \rangle \propto q^{-2}$ [BBS⁺11], one has to simulate sufficiently large membranes, which substantially increases the simulation cost [Des09] (see also Section 2.1.1). In addition, it is unclear whether the values of κ derived from these weak bending situations can also correctly quantify the membrane elasticity at high curvatures.

Recently, Watson *et al.* proposed to determine the bending modulus κ from the fluctuations of lipid *orientations* [WPWB11], where smaller membranes and shorter simulations suffice since the orientation fluctuations are not only much more local than the height fluctuations, but also relax faster. However, in order to link the *microscopic* lipid orientation to the *macroscopic* membrane bending, one needs a theoretical model that has to make additional assumptions, which may or may not be easily tested (*c.f.* Section 2.1.3).

Both methods mentioned above *passively* observe a membrane’s response to thermal fluctuations. Another type of method employs *active* bending of membranes. Generally speaking, the passive methods receive larger signals, and hence become more efficient, when the material is soft, *i.e.* when its stiffness approximates a few $k_{\text{B}}T$; in contrast, the active methods are more appropriate when the material is stiff ($\kappa \gg k_{\text{B}}T$). Lipid membranes fall between these two regimes; a regular lipid membrane has a bending modulus around $20 k_{\text{B}}T$ [NTN00, Mar06]. Thus, both passive and active methods can be applied.

As an example of an active method of determining κ , inspired by membrane tether pulling experiments [BW89, CDBN05, TB08], Harmandaris and Deserno have deduced κ by simulating cylindrical membrane tethers across periodic boundary conditions, and obtained comparable results with those from height fluctuations [HD06]. In this method, measurements of the tensile force F_z applied to hold the membrane at a certain curvature $1/R$ provide direct access to the bending modulus $\kappa = F_z R/2\pi$. This force is a ground state signal, so that the simulations do not require long equilibration time. One drawback

¹Equilibration time $\tau \sim q^{-3}$ (or $\tau \sim q^{-4}$) in the presence (absence) of solvent [SL93, ZG96].

of this method, however, is that the cylindrical membrane essentially divides the simulation box into two separate compartments, which is fine for implicit lipid models [HD06, AYS08, SN11] like the Cooke model they used, but troublesome for explicit solvent models: It is necessary to equilibrate the chemical potential of the solvent molecules between the two sides, and since on typical simulation time scales the membrane is fairly impermeable to the solvent, this equilibration does not happen automatically. Another potential problem with this method is the asymmetry between the inner and outer membrane leaflets: For lipid models with low flip-flop rate, the two leaflets may not be able to relax their lipid chemical potential during the course of simulations, which then introduces spurious contributions to the force from membrane stretching and compression that are not simple to disentangle from the curvature signal.

Recently, Baoukina *et al.* also simulated membrane tethers using the MARTINI model with explicit solvent [BMT12]. Instead of a *pre-set* cylinder that extends across the periodic boundaries like in the work of Harmandaris and Deserno, in their simulations a flat membrane is actively pulled with an external force to *form* a tether. In this way, the solvent molecules are not separated by the membrane, and therefore the equilibration problem of the solvent is solved. However, the equilibration problem of the lipids could potentially be worse: when using the cylinder method, one can intentionally place different numbers of lipids in the two leaflets, using an estimation based on the cylinder radius and the estimated location of the surface of inextension. As one pulls a tether from an initially *flat* membrane, the two leaflets start with the *same* number of lipids. As the tether grows in length, the area difference between the two leaflets increases. Since this stress is not relaxed by lipid flip-flop on the time scale of the simulations, the associated energy will contribute on top of the bending contribution.

Despite the existence of many methods to determine the bending modulus κ in simulations, existing results are far from consistent, a state of affairs that appears to mirror the situation in experiments [Nag13]. For example, depending on the method employed to analyze the *same* simulation trajectory, by observing either the height undulations or the orientation fluctuations, Watson *et al.* found a factor of two difference in the κ they derived [WPWB11]. Thus, new methods to determine the bending modulus κ , with high accuracy and efficiency, are still needed.

In the rest of this chapter, a new method to determine the bending modulus κ in simulations, originally proposed by Noguchi [Nog11] and subsequently extended by us [HDD13], will be described. In this method, a medium-sized strip of membrane is laterally compressed to form a buckle along its longer edge. At different strains, the restoring forces, which are proportional to κ and caused by this active bending, are measured. This stress-strain relation provides a direct measurement of κ , which turns out to be accurate and computationally efficient. Moreover, this setup solves both aforementioned problems with the solvent and the lipid equilibration. Unless noted otherwise, all derivations and results are based on our publication [HDD13].

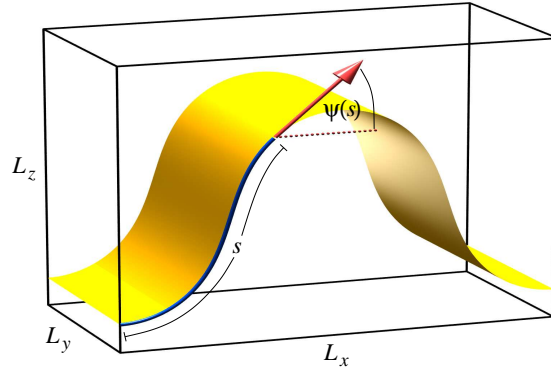


Figure 4.1: Illustration of the geometry of a buckle.

4.2 Theory

4.2.1 Hamiltonian and shape equation

For a membrane in a box of dimensions (L_x, L_y, L_z) , as shown in Fig. 4.1, when its width L_y is limited to about 10 lipid sizes, the buckle exists only along the x -direction; its curvature in the y -direction is negligible. Thus, the Gaussian curvature is essentially zero, and the Gaussian term in the Helfrich Hamiltonian can be neglected.² Also, since there is no open edge due to the periodic boundary conditions, the last term in the Helfrich Hamiltonian, Eq. (4.1), can be dropped as well. This leaves only one term in the Hamiltonian: the term with the total curvature. If the shape of the membrane is parameterized by the angle $\psi(s)$ between the membrane tangent direction and the horizontal direction, as shown in Fig. 4.1, then the Helfrich Hamiltonian can be transformed into

$$\mathcal{E}[\psi] = L_y \int_0^L ds \left\{ \frac{1}{2} \kappa \dot{\psi}^2 + f_x \left[\cos \psi - \frac{L_x}{L} \right] \right\}, \quad (4.2)$$

where $\dot{\psi}$ is the curvature of the membrane, $L \geq L_x$ is the contour length along the buckle, and f_x is an *unknown* Lagrange multiplier for the constraint that the buckle needs to fit into the box along the x -direction.

A simple functional variation shows that $\psi(s)$ satisfies the (Euler-Lagrange) differential equation

$$\ddot{\psi} + \lambda^{-2} \sin \psi = 0 \quad \text{with} \quad \lambda^2 = \frac{\kappa}{f_x}. \quad (4.3)$$

²A deeper reason why we can skip this Gaussian term is that there is no topological or boundary changes in this buckling process. By the virtue of the Gauss-Bonnet Theorem, as introduced in Technical Note 5.1, the integral of the Gaussian term is a constant, and thus does not contribute to the forces.

Multiplying both sides with $\dot{\psi}$ and integrating yields $\frac{1}{2}\dot{\psi}^2 - \lambda^{-2} \cos \psi = \text{const}$. Denoting the angle at the inflection points by ψ_i , the first integral of Eq. (4.3) is

$$\dot{\psi} = \lambda^{-1} \sqrt{2(\cos \psi - \cos \psi_i)} . \quad (4.4)$$

With the boundary condition of $\psi(0) = 0$, the solution of Eq. (4.4) can be solved as $s/\lambda = F[\arcsin(\sqrt{m} \sin \frac{\psi}{2}), m]$, where

$$m \equiv \sin^2 \frac{\psi}{2} \quad (4.5)$$

and $F(x, m)$ is an elliptic integral of the first kind.³ Inverting this solution gives the angle as

$$\psi(s) = 2 \arcsin \{ \sqrt{m} \operatorname{sn} [s/\lambda, m] \} . \quad (4.6)$$

By integrating the cosine and the sine of that angle, one derives a parametric representation of the buckle shape:

$$x(s) = 2\lambda \operatorname{E}[\operatorname{am}[s/\lambda, m], m] - s , \quad (4.7a)$$

$$z(s) = 2\lambda \sqrt{m} (1 - \operatorname{cn}[s/\lambda, m]) . \quad (4.7b)$$

The amplitude $z_a = z(L/4) = 2\lambda\sqrt{m}$, as can be simply read off from Eq. (4.7b).

4.2.2 Constraints of imposed strain

In our solution Eq. (4.7), the parameter $m = \sin^2 \frac{\psi}{2}$ of the elliptic integrals, as well as the characteristic length λ , still need to be fixed for a given geometry.

Utilizing Eq. (4.6) and (4.7a), the boundary conditions

$$\psi(L/4) = \psi_i , \quad \text{and} \quad (4.8a)$$

$$x(L/4) = L_x/4 , \quad (4.8b)$$

can be translated into

$$\frac{L}{4\lambda} = F \left[\frac{\pi}{2}, m \right] = K[m] , \quad \text{and} \quad (4.9a)$$

$$L_x = 8\lambda \operatorname{E}[m] - L . \quad (4.9b)$$

Then the length λ can be eliminated, which gives the relation between the strain γ and the elliptic parameter m as

$$\gamma := \frac{L - L_x}{L} = 2 \left(1 - \frac{\operatorname{E}[m]}{K[m]} \right) . \quad (4.10)$$

³From here, all notations regarding elliptic integrals follow the conventions in Abramowitz and Stegun [AS72].

To invert Eq. (4.10) and obtain an expression for m as a function of γ , we expand m as a power series of γ :

$$m(\gamma) = \sum_{i=1}^{\infty} a_i \gamma^i, \quad (4.11)$$

whose coefficients a_i can be determined by plugging Eq. (4.11) back to Eq. (4.10), expanding both sides in powers of γ , and matching the terms order by order in γ . This results in a coupled system of equations for the coefficients a_i that can be easily solved. The resulting series expansion for $m(\gamma)$ is then found to be

$$m(\gamma) = \gamma - \frac{1}{8}\gamma^2 - \frac{1}{32}\gamma^3 - \frac{11}{1024}\gamma^4 \dots \quad (4.12)$$

The coefficients a_i for terms up to γ^{10} are listed in Table 4.2. Since the accuracy of this expansion is better than 2×10^{-9} for the most relevant range of $\gamma \leq 0.5$, $m(\gamma)$ can be considered as known.

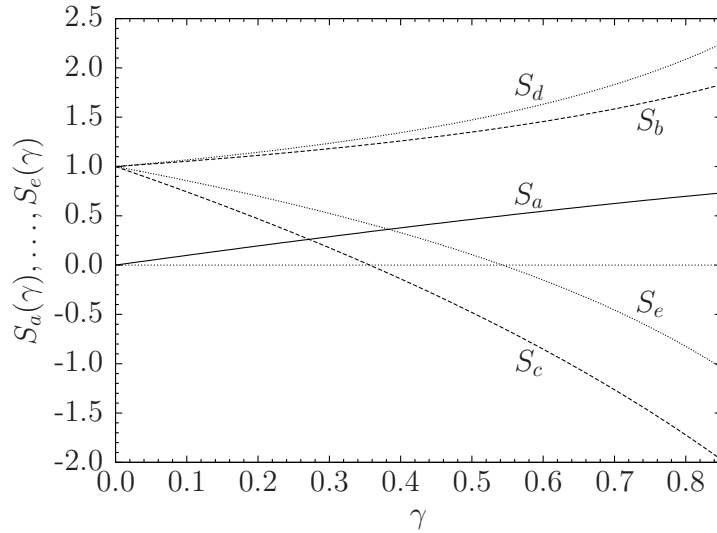


Figure 4.2: Sketch of all five series expansions as a function of γ : $S_a(\gamma) \dots S_e(\gamma)$, with coefficients listed in Table 4.2. Since an ideal buckle overlaps at $\gamma \approx 0.8487$, the current theory no longer applies beyond this value of strain.

4.2.3 Stress-strain relation

Given the relation between the elliptic parameter m and the strain γ , the stress-strain relation can be derived from Eq. (4.9a):

$$f_x(\gamma) = \kappa \left(\frac{4}{L} \text{K}[m(\gamma)] \right)^2 = \kappa \left(\frac{2\pi}{L} \right)^2 \sum_{i=0}^{\infty} b_i \gamma^i \quad (4.13a)$$

$$= \kappa \left(\frac{2\pi}{L} \right)^2 \left[1 + \frac{1}{2}\gamma + \frac{9}{32}\gamma^2 + \frac{21}{128}\gamma^3 \dots \right]. \quad (4.13b)$$

The coefficients b_i of the first eleven terms in Eq. (4.13) can again be found in Table 4.2. An illustration of $S_b(\gamma)$ is shown in Fig. 4.2. The nonzero constant term in Eq. (4.13) indicates a minimum stress is required to create a buckle.

For a *fluid* lipid membrane, a compression in the x -direction will also induce a response in the orthogonal y -direction, contrary to what would be the case for a solid sheet like a piece of paper. In order to derive this, one can first calculate the total energy and then differentiate it with respect to L_y . Inserting Eq. (4.4) and (4.13) into the Hamiltonian Eq. (4.2), one gets the total energy as

$$\mathcal{E} = L_y f_x(L_x - L \cos \psi_i) = f_x A [2m - \gamma] = \kappa (2\pi)^2 \frac{L_y^2}{A} \sum_{i=0}^{\infty} \frac{b_i \gamma^{i+1}}{i+1}, \quad (4.14)$$

where $A = LL_y$ is the total membrane area. Then, the stress in the y -direction can be obtained:

$$f_y(\gamma) = -\frac{1}{L_x} \left(\frac{\partial \mathcal{E}}{\partial L_y} \right)_A = \kappa \frac{L_y}{L_x} \frac{(2\pi)^2}{A} \sum_{i=0}^{\infty} c_i \gamma^i \quad (4.15a)$$

$$= \kappa \frac{(2\pi)^2}{A} \frac{L_y}{L_x} \left[1 - \frac{5}{2}\gamma - \frac{23}{32}\gamma^2 - \frac{39}{128}\gamma^3 \dots \right]. \quad (4.15b)$$

The values of c_i for terms up to order γ^{10} are included in Table 4.2. As shown in Fig. 4.2, the sum $S_c = \sum c_i \gamma^i$ turns *negative* when $\gamma > 0.3567$, meaning the force in the y -direction would become contractile. More interestingly, the membrane has a negative compressibility in the y -direction, since the derivative of this curve is negative everywhere. Also notice that, within a meaningful range of strains, the change in the stress in the y -direction, f_y , is about four times that of the x -direction, f_x .

4.2.4 Fluctuation corrections

The derivations above only account for the ground state response, while the thermal fluctuations are neglected. For real simulations, these fluctuations induce more wrinkles and, consequently, contract the membrane and affect the stresses. In order to mitigate the fluctuations in the y -direction, *i.e.* along the ridge of the buckle, the box size in this dimension

is restricted to be roughly 10 lipid diameters, as shown in Table 4.3. Thus, the major fluctuations only exist in the x -direction, *i.e.* along the buckle. Nevertheless, these affect the stresses in *both* the x - and the y -directions, just as in the case of the ground state stresses.

A careful analysis of the undulations shows that the correction for the force F_x in the x -direction is [HDD13]

$$\delta F_x = L_y \delta f_x = -\frac{3k_B T}{2L} \sum_{i=0}^{\infty} d_i \gamma^i \quad (4.16a)$$

$$= -\frac{3k_B T}{2L} \left[1 + \frac{5}{8}\gamma + \frac{27}{64}\gamma^2 + \frac{295}{1024}\gamma^3 \dots \right], \quad (4.16b)$$

and in the y -direction

$$\delta F_y = -k_B T \frac{L q_c}{2\pi L_y} \left[1 + \frac{3\pi L_y}{L^2 q_c} \sum_{i=0}^{\infty} e_i \gamma^i \right] \quad (4.17a)$$

$$= -k_B T \frac{L}{L_y a} \left[1 + \frac{3L_y a}{2L^2} \left(1 - \frac{11}{8}\gamma - \frac{37}{64}\gamma^2 - \frac{345}{1024}\gamma^3 \dots \right) \right], \quad (4.17b)$$

where the coefficients d_i and e_i again are listed in Table 4.2. The length a appearing in Eq. (4.17) is a *microscopic* cutoff on the order of the membrane thickness.

It is worthwhile to examine the magnitudes of these two corrections. When compared to the ground state forces,

$$\left| \frac{\delta F_x}{F_x} \right| \sim \frac{3}{8\pi^2} \times \frac{L}{L_y} \times \frac{k_B T}{\kappa} \sim 1\% \quad (4.18)$$

$$\left| \frac{\delta F_y}{F_y} \right| \sim \frac{1}{4\pi^2} \times \frac{L^2}{L_y a} \times \frac{k_B T}{\kappa} \sim 5\%. \quad (4.19)$$

In the estimation above, $L \sim 40$ nm, $L_y \sim 8$ nm, $a \sim 5$ nm, and $k_B T/\kappa \sim 1/20$ have been assumed. Real parameters of the systems studied can be found in Tables 4.3. Thus, the y force experiences bigger fluctuation corrections.

To conclude the theoretical basis of the buckling method, one final point should be emphasized regarding the fluctuation corrections Eqs. (4.16) and (4.17). Even though one can use these corrections to analyze the data from simulations, the *practical* impact from thermal fluctuations should not be overlooked; whenever they contribute a significant part of the total signal, extra computation time is required to obtain good statistics. From this perspective, it is recommended to extract the bending modulus κ from the stress measured in the x -direction, where the fluctuation corrections contribute roughly one percent to the total signal, as compared to the 5% in the y -direction. Our simulation results will confirm this expectation.

4.3 Simulation setup

The method to determine κ from simulating membrane buckles has been applied to three membrane models different in resolution and representation of solvent: the generic Cooke model [CKD05, CD05], MARTINI-DMPC [MdVM04, MRY⁺07], and DMPC in the Berger model [BEJ97]. The former two CG models have been described in Section 2.1.4. The last one, the Berger lipid model, is a united-atom model, where all atoms are explicitly represented, except for the hydrogen atoms in CH, CH₂, and CH₃ groups. This model has been shown to successfully reproduce structural and dynamical quantities of phospholipids [LE01, WE06]. System parameters, as well as results from the literatures, are listed in Table 4.3. The systems using the Cooke model are simulated with ESPResSo [LAMH06], while the other two systems are run with GROMACS [HKvdSL08].

Requirements on system dimensions

A couple of requirements on the system size should be considered when setting up the simulations. On the one hand, a smaller membrane speeds up the simulations. On the other hand, a membrane that is too small may give rise to unfavorable finite size effects.

One possible concern is that a small membrane buckle may have an unfavorably high radius of curvature at the buckle’s “turning points” that may push the Helfrich theory to its limit.⁴ This can be estimated using our theory. The highest curvature appears at the maximum and minimum of the buckle. Plugging $\psi(0) = 0$ into Eq. (4.4) yields $\dot{\psi}_{\max} = \dot{\psi}(0) = 2\sqrt{m}/\lambda$. Then, with $m = \sin^2 \frac{\psi}{2}$ and Eq. (4.9a), one can derive the ratio between L and the minimum radius of curvature R_{\min} as

$$\frac{L}{R_{\min}} = 8\sqrt{m(\gamma)}K[m(\gamma)] \quad (4.20a)$$

$$= 4\pi\sqrt{\gamma} \left[1 + \frac{3}{16}\gamma + \frac{39}{512}\gamma^2 + \frac{303}{8192}\gamma^3 \dots \right]. \quad (4.20b)$$

For example, the right-hand-side of the equation above is approximately 10 at a strain $\gamma = 0.5$. If the minimum tolerable radius of curvature is roughly equal to the membrane thickness d , *i.e.* $R_{\min} \approx d \approx 4$ nm, then the membrane length L should be at least 40 nm.

Another concern is about the width L_y of the membrane, along the ridge of the buckle. A small L_y not only reduces the number of lipids one needs to simulate, but, more importantly, suppresses the undulation modes in the y -direction. For this reason the membrane is set to high aspect ratios of L_x/L_y between 5 to 7, and the undulations in the y -direction can then be neglected in our theory. However, reducing L_y too much may create artifacts in simulations due to the periodic boundary conditions. Thus, we have chosen L_y such that there will be roughly ten lipids in the membrane along this direction.

⁴Helfrich theory treats the membrane as an *infinitely thin* two-dimensional surface. However, when the radius of curvature becomes very close to the membrane thickness, this 2D assumption may break down, and then further corrections of higher order terms in the curvatures, such as K^4 , K^2K_G , K_G^2 , and $(\nabla K)^2$ which are quartic in the principal curvatures, are needed [CGS03].

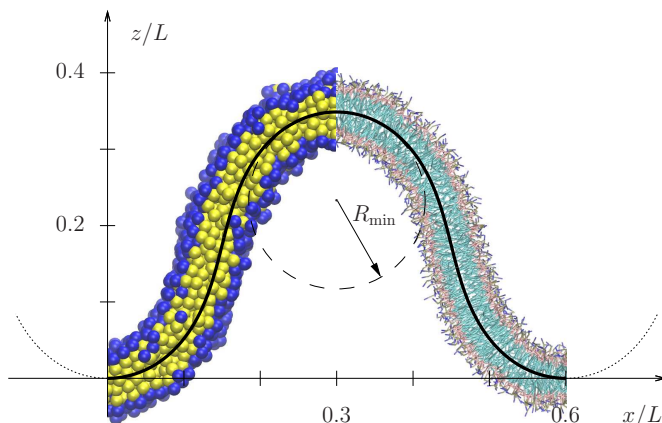


Figure 4.3: Snapshots of two buckled membranes using the Cooke model (left, blue and yellow beads) and the MARTINI model (right, mainly pink and green) at $\gamma = 0.4$, overlaid on the theoretical shape prediction from Eq. (4.7). Even though the agreement between the theory and the simulation snapshots is excellent, it has to be pointed out that the membrane is subject to thermal undulations, thus most of the time its shape will deviate from the predicted one.

Initial configurations

The initial configurations for these three systems were set up in two ways. For the Cooke model and the MARTINI model, a pressure that is a few times larger than the maximum of $F_x/L_y L_z$ was applied in the x -direction, so that the membrane strip was compressed to form a buckle. Various snapshots with different strain γ were taken from this compression trajectory as the initial configurations to measure the stresses f_x and f_y .

This method, however, became computationally expensive for the Berger model, since the higher resolution increased the number of degrees of freedom, and the time step had to be reduced to 1/10 compared to MARTINI. Hence, the initial configurations were created by back-mapping from MARTINI configurations to Berger. The basic principles of back-mapping have been explained in Section 2.1.5. Detailed simulation parameters can be found in the supplementary information of the original paper [HDD13]. The number of lipids in the MARTINI system and the Berger system is not the same because a new set of MARTINI configurations with fewer lipids were specifically created for back-mapping to the Berger level, so that a smaller atomistic system can save some computing time.

4.4 Results

4.4.1 Buckle shape

The very first test of the presented theory is to check whether the the membrane remains as a buckle and its shape indeed follows the prediction from Eq. (4.3). Two example snapshots

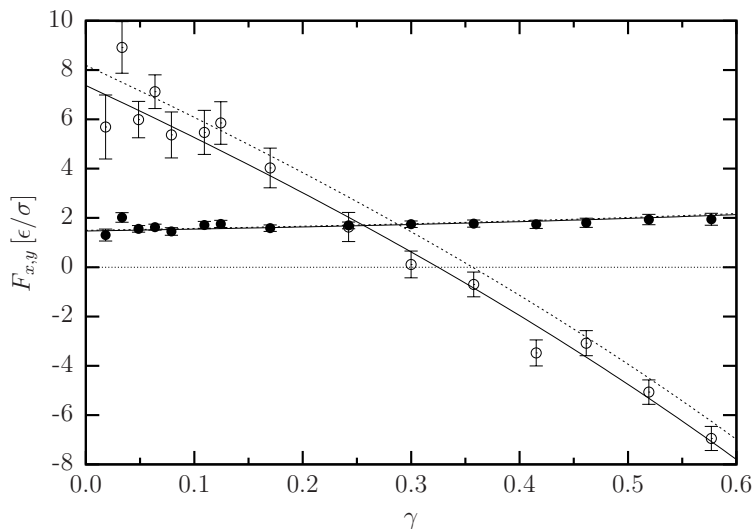


Figure 4.4: The forces in the x -direction (filled circles) and the y -direction (open circles) at strains between $[0, 0.6]$ for a set of simulations using the Cooke model. The solid curves are fits including fluctuation corrections, while the dotted curves have these corrections removed to show their significance.

from simulations using the Cooke model and the MARTINI model are shown in Fig. 4.3. The agreement between the shape in simulations and predicted by theory is excellent. However, as shown in Fig. 1 in Noguchi’s publication [Nog11], buckled membranes fluctuate around the predicted shape. Thus, one needs to select snapshots with a high symmetry before any meaningful comparison can be made.

4.4.2 Stress-strain relation

After cross-checking the shape, the next step is to examine whether the measured stress-strain relations are in agreement with the theory described in Eqs. (4.13) and (4.15). In Fig. 4.4, the forces in the x - and the y -direction are plotted for a buckled membrane using the Cooke model, each with a fit to the theoretical predictions of $F_x + \delta F_x$ and $F_y + \delta F_y$ in Section 4.2. The excellent agreement between the simulation data and the fits shows that our theory predicts very accurately the functional form of the forces, which *cannot* be adjusted by the fitting, since the main fitting parameter κ is merely a scaling factor, and the only other parameter a essentially creates only a downward shift of the curve.

More importantly, Fig. 4.4 also verifies the necessity of the fluctuation corrections in the y -direction, Eq. (4.17b). This correction δF_y lowers the stress-strain curve (from the dashed curve to the solid one), and thus improves the quality of the fit. Without this correction, the curve will *always* go through zero at $\gamma \approx 0.3567$, regardless of the value of κ , as shown in Fig. 4.2. In other words, these simulation data are more compatible with the theory with fluctuation corrections. However, the correction in F_x did not show any

Model	$\kappa_x/k_B T$	$\kappa_y/k_B T$	$a = 2\pi/q_c$	\mathcal{R}
Cooke	12.8 ± 0.4	12.9 ± 0.8	$(7.3 \pm 2.4) \sigma$	5.43 ± 0.12
MARTINI	29.0 ± 1.0	27.7 ± 1.9	$(4.4 \pm 2.1) \text{ nm}$	4.59 ± 0.08
Berger	24.8 ± 0.9	26 ± 11	$(20 \pm 315) \text{ nm}$	4.5 ± 3.0

Table 4.1: Summary of the results found using the buckling method. Here, κ_x and κ_y are the bending modulus as derived from the buckling stress in the x - and y -direction, respectively; a is the value of the microscopic cutoff length in the fluctuation correction δF_y from Eq. (4.17); and \mathcal{R} is the ratio between the (shifted) buckling energy $E_{\text{sim}}(\gamma) - E_0$ measured in the simulation and the buckling free energy $\mathcal{E}(\gamma)$ corresponding to the measured value of κ .

noticeable difference in the fit, confirming our expectation that the force in the y -direction demands more significant corrections (*c.f.* Eq. (4.18)).

4.4.3 Bending modulus

Fitting the stress-strain relation Eqs. (4.13) and (4.15) to the simulation data, one can obtain the bending modulus κ , as collected in Table 4.1. The results for the Cooke and the MARTINI model are also in good agreement with those results published in literatures (*c.f.* the last column in Table 4.3). For the Berger model, our results lie between previous results determined by the height fluctuation method [BBS⁺11] and by the orientation fluctuation method [WPWB11]. Moreover, the values of κ determined from the stresses in the x - and the y -directions are consistent within error bars. However, the errors on κ_x are significantly smaller than those on κ_y . As we have seen, the fluctuation correction plays a more significant role in the y -direction, and we therefore should also expect that fluctuations contribute more thermal noise to our measurements in the κ_y . Thus, we recommend to derive κ from fitting the forces in the x -direction. Note that all errors are obtained by a Monte Carlo resampling of the fits (see Appendix A).

4.4.4 Microscopic cutoff

The last check for the method is to examine the values of the microscopic cutoff $a = 2\pi/q_c$, which is the second fitting parameter used in fitting the y -force. This cutoff a must be introduced to regularize a short wavelength divergence in the integral leading to Eq. (4.17), which reflects the fact that the Helfrich Hamiltonian ceases to be a valid theory for a real membrane at small scales. We therefore expect this cutoff a to be comparable to the length scale at which actual membrane structure beyond Helfrich theory becomes visible, and the most obvious length scale which then comes to mind is the membrane thickness d . As shown in the second last column in Table 4.1, even though the errors on a are relatively large, especially for the Berger model, our results are of the correct order of magnitude. For comparison, the head-to-head thickness of the Cooke membrane is roughly

5σ , and for MARTINI-DMPC it is about 3.5 nm. For the Berger result, the accuracy of the y -forces is insufficient to justify such a fluctuation correction; an error resampling shows q_c approximately follows a Gaussian distribution with its mean very close to zero. As a result, the statistics on $a \propto 1/q_c$ deteriorates badly.

4.5 Discussions

4.5.1 Advantages

In the previous section, the membrane buckling method has been proven to be a reliable way to obtain the bending modulus κ . It also offers several advantages compared to alternative methods.

So far, the most widely used method to determine κ in simulations is to measure the height undulations of a flat bilayer membrane [GGL99, LE00]. As described earlier in Section 4.1.2, this method requires sampling large membranes for a long time to get accurate statistics for the fluctuation signal. As a comparison, the requirements for our buckling method are more manageable: One only needs to simulate a medium size membrane, and the simulation time required by accurate measurements is shorter, since it is an *active* method to measure the *ground state* forces. Although, for the systems studied in this work, several simulations were conducted at different strains γ , only one of them is necessary, because 1) κ is the only fitting parameter in the x -force F_x (Eq. (4.13b)) and 2) more importantly, F_x depends very weakly on γ for the most relevant range of $\gamma \in [0, 0.6]$ (*c.f.* Fig. 4.2), thus a data point at any meaningful γ would work for the fitting. Another simulation at zero tension which provides the free length L of the strip may also be waived, since the error on the value of L is unlikely to affect the result of κ : One can use the known area per lipid and the box size in the y -direction to estimate the membrane length L .

Like the proposed buckling method, simulating cylindrical membrane tethers is also an active method to determine κ [HD06]. Yet, the buckling method improves two drawbacks of the cylinder method that affect its popularity. Both of these two are related to the problems in equilibration: The first one has to do with the balance of solvent molecules *inside* and *outside* the cylinder for explicit solvents models. The second one is the more general difficulty of equating the chemical potential of lipids in the inner and the outer leaflet, which is limited by the slow flip-flop rate in models with relatively high resolution, such as the Berger model. For models like the MARTINI model and the Berger model, one may need to artificially create holes on the cylinder wall to allow solvent exchange and to expedite lipid flip-flop through the pore boundaries. On the contrary, the top and bottom parts of the solvent in the buckling method are connected through the periodic boundary conditions, so the solvent can be equilibrated without any extra efforts. The two leaflets are also up-down symmetric, so lateral diffusion within the same leaflet is enough to balance the monolayer chemical potential.

Watson *et al.* proposed another method to determine κ from analyzing the orientation fluctuations of lipids [WPWB11]. Such methods can be computationally very efficient,

thanks to the short length scale and fast relaxation of the local fluctuations. Even though the buckling method is unlikely to be computationally more efficient, it does not rely on microscopic underpinnings of the Helfrich theory, which one may or may not want to assume. Of course, this is not to disapprove of these microscopic theories, without which one cannot understand the microscopic nature of the membranes.

4.5.2 Limitations

With some of the advantages pointed out, it is also worthwhile considering some potential limitations of the buckling method, mainly regarding the isotropic lateral stress Σ induced by compression. The buckled membrane is created by compression along their longer dimension, *i.e.* the x -direction in our case. A minimum stress is required to form the buckle, as shown in the x -force Eq. (4.13). After the buckle has formed, part of this stress will be released, except for a part [HDD13]:

$$\Sigma = -f_x \cos \psi_i. \quad (4.21)$$

Thus, this isotropic stress vanishes only when $\psi_i = \pi/2$, or equivalently $\gamma \approx 0.543$. Before this strain, Σ remains finite, which may reduce the area per lipid of the membrane, increases its thickness, and consequently affect the apparent κ .

Another more subtle consequence of this finite compressive stress Σ is that it could trigger a phase transition of the membrane. A fluid membrane just above the gel-fluid transition temperature may choose to change into the gel phase upon compression, so that the lipid area can be reduced. Since we keep the box size (an extensive variable) constant, it is likely that only parts of the membrane will transition into the gel phase, thus forming a two-phase system, to which our buckling theory does not apply. Even if the whole piece has become in the gel phase, and our theory still holds, the outcome is not for the original fluid membrane any more. In this case, one also has to pay special attention to any possible defects in the membrane, which will greatly release the stress and provide unrealistically low κ .

4.5.3 Free energy of buckling

Knowing the x -force at various strains γ allows the measurement of the *free* energy $\mathcal{E}(\gamma)$ of the system by integrating F_x with respect to the change in the canonically conjugate variable L_x . This process is essentially a *thermodynamic integration*.

Eq. (4.25) provides a way to calculate the free energy of the buckle $\mathcal{E}(\gamma)$:

$$\mathcal{E}(\gamma) = \int_0^\gamma d\lambda \left\langle \frac{\partial E_{\text{pot}}(\lambda)}{\partial \lambda} \right\rangle, \quad (4.26)$$

where in this case the control parameter λ is the strain γ . The term in the bracket is

$$\frac{\partial E_{\text{pot}}(\gamma)}{\partial \gamma} = \frac{\partial E_{\text{pot}}}{\partial L_x} \frac{\partial L_x}{\partial \gamma} = F_x(\gamma)L, \quad (4.27)$$

Technical Note 4.1: Thermodynamic integration

Assume a system follows a Hamiltonian, which is a function of particle positions and momenta $\{\mathbf{x}_i, \mathbf{p}_i\}$, as well as a control parameter λ :

$$H(\{\mathbf{x}_i, \mathbf{p}_i\}; \lambda) = H_0(\{\mathbf{x}_i, \mathbf{p}_i\}) + U(\{\mathbf{x}_i, \mathbf{p}_i\}; \lambda), \quad (4.22)$$

where i is the index for each individual particle in the system, and only the extra term U contains λ . This parameter λ describes different states of the system, for instance the strain γ of a buckled membrane. Then, the free energy of this system as a function of the parameter λ is given by

$$\mathcal{F}(\lambda) = -\beta^{-1} \ln \mathcal{Z}(\lambda), \quad (4.23a)$$

$$\text{with } \mathcal{Z}(\lambda) = \frac{1}{h^{3N} N!} \int d\{\mathbf{r}_i\} d\{\mathbf{p}_i\} e^{-\beta[H_0(\{\mathbf{x}_i, \mathbf{p}_i\}) + U(\{\mathbf{x}_i, \mathbf{p}_i\}; \lambda)]}, \quad (4.23b)$$

where $\beta = 1/k_B T$, and $d\{\mathbf{r}_i\} d\{\mathbf{p}_i\}$ include all particles.

The free energy changes with λ as

$$\begin{aligned} \frac{\partial \mathcal{F}}{\partial \lambda} &= -\beta^{-1} \frac{1}{\mathcal{Z}(\lambda)} \frac{\partial}{\partial \lambda} \mathcal{Z}(\lambda) \\ &= -\beta^{-1} \frac{1}{\mathcal{Z}(\lambda)} \frac{\partial}{\partial \lambda} \int d\{\mathbf{r}_i\} d\{\mathbf{p}_i\} \left(-\beta \frac{\partial U(\lambda)}{\partial \lambda} \right) e^{-\beta[H_0(\{\mathbf{x}_i, \mathbf{p}_i\}) + U(\{\mathbf{x}_i, \mathbf{p}_i\}; \lambda)]} \\ &= \left\langle \frac{\partial U(\lambda)}{\partial \lambda} \right\rangle_{\lambda}, \end{aligned} \quad (4.24)$$

where $\langle \cdot \rangle_{\lambda}$ denotes thermal averaging over the canonical states belonging to the Hamiltonian $H = H_0 + U(\lambda)$. So the derivative of the free energy with respect to λ is equal to the thermal average of $\partial U / \partial \lambda$. The free energy difference between two states of λ_1 and λ_2 is then

$$\mathcal{F}(\lambda_2) - \mathcal{F}(\lambda_1) = \int_{\lambda_1}^{\lambda_2} d\lambda \left\langle \frac{\partial U(\lambda)}{\partial \lambda} \right\rangle. \quad (4.25)$$

where $F_x = -\partial E_{\text{pot}} / \partial L_x$ and $\partial \gamma / \partial L_x = -1/L$ have been used.⁵ Plugging this back into Eq. (4.26), one obtains the free energy of the buckle:

$$\mathcal{E}(\gamma) = L \int_0^{\gamma} d\lambda \langle F_x(\lambda) \rangle. \quad (4.28)$$

This equation states that one can measure the free energy \mathcal{E} by integrating the thermal average of F_x with respect to $L\gamma = (L - L_x)$.

The measured $\mathcal{E}(\gamma)$ is shown as the open circles in Fig. 4.5. With the value $\kappa = 12.8 k_B T$ measured in simulation, Eq. (4.14) predicts the free energy should be the solid curve, which is in good agreement with the free energy measured by thermodynamic integration *via* Eq. (4.28). So, our theory indeed predicts the *free* energy of a membrane buckle.

⁵Note that this result is not surprising: Since $dF = -S dT + F_x dx + \mu dN$, and T, N remain constant, then $dF = F_x dx = F_x d(L - L_x)$.

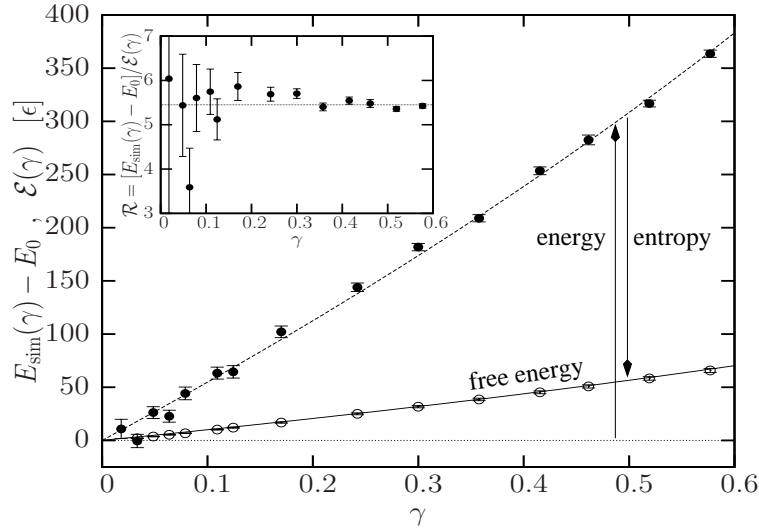


Figure 4.5: The shifted potential energy (filled circles and dashed curve) and the free energy (open circles and solid curve) of a buckled Cooke membrane for strains $\gamma \in [0, 0.6]$. The total potential energy $E_{\text{sim}}(\gamma)$ is measured in simulations and shifted to start from zero. The free energy \mathcal{E} is determined by numerically integrating the x -force F_x , as shown in Eq. (4.28). The solid curve is predicted by our theory of buckled membrane, Eq. (4.14), using the κ obtained from fitting F_x to Eq. (4.13). The dashed curve is the solid curve scaled up with a proportionality factor \mathcal{R} , since the inset suggest that the ratio $\mathcal{R} = (E_{\text{sim}}(\gamma) - E_0)/\mathcal{E}$ is independent of γ .

4.5.4 Thermodynamics of membrane bending

In contrast to the *free energy* $\mathcal{E}(\gamma)$, the *potential energy* E_{sim} in simulations can be extracted directly from the simulation without any additional steps. With a shift such that $E_{\text{sim}}(\gamma = 0) = 0$, this energy $E_{\text{sim}} - E_0$ is also plotted in Fig. 4.5. Maybe unsurprisingly, the energy E_{sim} monotonically increases with γ , since after all energy is being transferred into the system in the form of work done by F_x . And yet, this is a nontrivial statement, since all we know from $dF = F_x dx$ is that the free energy will increase. But that could also mean *lowering* the energy and lowering the entropy even more.

A much more interesting observation is that the *free energy* change \mathcal{E} to buckle the membrane is much lower than the potential energy change $E_{\text{sim}} - E_0$. Since $\mathcal{E} = E - TS$, this means entropy *favours* bending of membranes. As shown in the inset of Fig. 4.5, the ratio between the excess energy $E_{\text{sim}} - E_0$ and the free energy \mathcal{E} , defined as $\mathcal{R} \equiv (E_{\text{sim}}(\gamma) - E_0)/\mathcal{E}(\gamma)$, is essentially a constant, regardless of the value of the strain γ . This constant ratio at varying geometry suggests that we have identified a *material property*. Thus, since the bending modulus κ is the material property which quantifies the *free energy* per unit area per unit squared curvature, a constant \mathcal{R} suggests to decompose the modulus

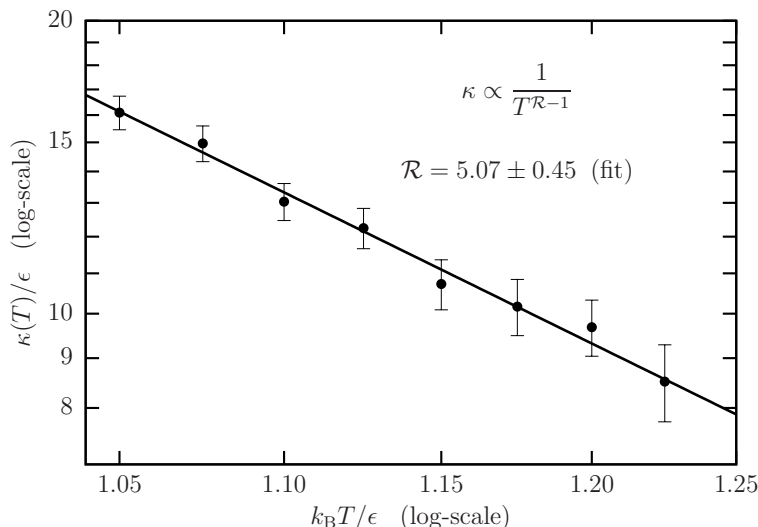


Figure 4.6: The temperature dependence of the bending modulus κ for the Cooke model ($w_c/\sigma = 1.6$). κ is determined using the cylindrical tether method. On this log-log plot, the data is fit to a straight line, giving $\kappa \propto T^{-(\mathcal{R}-1)}$ with $\mathcal{R} = 5.07 \pm 0.45$.

into an enthalpic part κ_E and an entropic part κ_S , *i.e.* $\kappa = \kappa_E - T\kappa_S$, with a constant ratio $\mathcal{R} = \kappa_E/\kappa$ with respect to γ .

The measured values of \mathcal{R} are included in the last column of Table 4.1. Very surprisingly, although the three models studied vary vastly in their resolution, so that the contributions from the degrees of freedom to the entropy could be very different, all three of them show an \mathcal{R} value around 5, meaning the entropy lowers the free energy cost to approximately 20% of the energetic cost required to bend the membrane into a buckle.

Thermodynamics requires $\kappa_S = -\partial\kappa/\partial T$, and consequently $1 - \mathcal{R} = \partial \log \kappa / \partial \log T$. Assuming the value of \mathcal{R} stays constant around a specific temperature T_0 at which one measures κ , the implication of this thermodynamic statement can be very useful: one can extract the bending modulus κ at a neighboring temperature T using the simulation results at T_0 as

$$\kappa(T) = \kappa(T_0) \left(\frac{T_0}{T} \right)^{\mathcal{R}-1}. \quad (4.29)$$

Considering the difficulties of obtaining one reliable measurement of κ at one temperature, Eq. (4.29) is a pleasing bonus.

To test the validity of Eq. (4.29), a set of simulations of a Cooke membrane, with the same parameter of $w_c = 1.6\sigma$, are conducted at a range of temperature T , and the bending modulus κ is measured using the cylinder method [HD06], as mentioned earlier in Section 4.1.2. Results are plotted in Fig. 4.6, which shows that a fit to Eq. (4.29) leads to $\mathcal{R} = 5.07 \pm 0.45$. This agrees well with the value of $\mathcal{R} = 5.43 \pm 0.12$ measured with the

buckling method.

In addition, for all of the three models we studied, the ratio \mathcal{R} is bigger than 1, which according to Eq. (4.29) means that all these membranes soften upon heating. This intuitive observation should not be taken for granted: In experiments, DMPC lipids have been shown to soften upon *cooling* at $T = 300$ K [FPBMM94, MGP⁺97, CKL⁺05], 3 K higher than its main transition temperature $T_{m,DMPC} \approx 297$ K. This is known as “anomalous swelling” in the literatures. The data measured by Chu *et al.* suggests a strongly negative value for \mathcal{R} [CKL⁺05].

The discrepancy between our simulation results and the experiments seems to originate from an overestimation of the transition temperature T_m of the membrane models: The values T_m for MARTINI-DMPC and Berger-DMPC may be lower than values measured in experiments, thus the temperature in our simulations corresponds to some higher temperature in experiments. This may explain why we did not find the anomalous swelling behavior, which experimentally is only observed a few degrees above T_m . High above T_m , membranes do indeed become more flexible when heated. For instance, using the experimental data from Pan *et al.* [PTNKN08], for DOPC between 288 K and 318 K, which is well above its $T_{m,DOPC} \approx 253$ K, we find the ratio $\mathcal{R} \approx 2.8 \pm 0.2$, qualitatively consistent with our results.

In fact, Rodgers *et al.* [RSdM⁺12] find $T_m \approx 274$ K for the MARTINI-DMPC used in this study.⁶ For the Berger-DMPC, no earlier studies have measured its transition temperature T_m . But for a similar DPPC and DSPC (1,2-distearoyl-*sn*-glycero-3-phosphocholine) bilayer, which have 2 and 4 extra CH_2 per tail, the Berger force field is estimated to give values of T_m that are 5 – 6 K lower than those measured in experiments [CK10]. Both observations suggest to compare our results of the MARTINI and the Berger DMPC at 300 K to real DMPC at higher temperatures, where it softens when warmed up, just like we observe.

As discussed in the previous chapter, it is unlikely that a molecular model can correctly reproduce all properties of the target system. Thus, it is not surprising to find that the phase transition temperatures of the MARTINI and even the Berger model are not quite spot on. This indicates some room for improvement of these models, but it is much less disconcerting than the alternative that these models fail to capture some basic membrane thermodynamics. Nevertheless, the buckling method provides not only reliable measurements of the bending modulus κ , but also a probe into the thermodynamics of membranes.

⁶Note that they simulate exactly the same CG lipid model that we also use in the present study, but interpret it as a model for the lipid 1,2-dilauroyl-*sn*-glycero-3-phosphocholine (DLPC), which has two CH_2 units fewer per tail chain than DMPC. This is not a mistake, though, because the resolution of the MARTINI model is not accurate enough to distinguish such a small difference in the atomistic structure.

4.6 Outlook

In this chapter, the buckling method for determining the bending modulus κ of membranes has been introduced and illustrated using three lipid models, namely the generic CG Cooke model, the chemical-specific MARTINI CG model, and the atomistic Berger model. By measuring the force to buckle a membrane as a function of the strain, κ can be reliably determined with good accuracy. The required computation resource is moderate, even for an atomistic model like the Berger model. Moreover, by measuring the potential energy and the free energy separately, it is possible to deduce κ at neighboring temperatures close to the one at which the original simulation has been done.

Based on the advantages of this buckling method, it is reasonable to expect that this method can also be applied to several other types of membrane systems. One important possibility is to measure κ of a membrane in the *gel phase* [DID]. The conventional height fluctuation method cannot be easily employed for a gel membrane because κ is normally several times higher compared to a fluid membrane, and consequently the fluctuation signal will be several times weaker ($\langle |h_{\mathbf{q}}|^2 \rangle \propto 1/\kappa$). However, this is not a problem for the buckling method, as long as the whole membrane is in the gel phase. This is because the buckling method monitors the ground state forces, which are proportional to κ , instead of fluctuation signals. Of course, some difficulties may have to be overcome, such as to keep the high curvature segments from melting or forming defects [NSM⁺12]. One also should restrict to fit only the x -forces, since the behaviors of the y -force mainly depend on the fluidity of the membrane, which is rather different in the gel phase than in the fluid phase. Yet, there is nothing fundamental to invalidate the application of this method to membranes in the gel phase.

i	0	1	2	3	4	5	6	7	8	9	10
a_i	0	1	$-\frac{1}{8}$	$-\frac{1}{32}$	$-\frac{11}{1024}$	$-\frac{17}{4096}$	$-\frac{55}{32768}$	$-\frac{179}{262144}$	$-\frac{9061}{33554432}$	$-\frac{13285}{134217728}$	$-\frac{8093}{268435456}$
b_i	1	$\frac{1}{2}$	$\frac{9}{32}$	$\frac{21}{128}$	$\frac{795}{8192}$	$\frac{945}{16384}$	$\frac{2247}{65536}$	$\frac{42639}{2097152}$	$\frac{6446547}{536870912}$	$\frac{7574715}{1073741824}$	$\frac{70769457}{17179869184}$
c_i	1	$-\frac{5}{2}$	$-\frac{23}{32}$	$-\frac{39}{128}$	$-\frac{1221}{8192}$	$-\frac{1281}{16384}$	$-\frac{2793}{65536}$	$-\frac{49809}{2097152}$	$-\frac{7197933}{536870912}$	$-\frac{8183511}{1073741824}$	$-\frac{74665071}{17179869184}$
d_i	1	$\frac{5}{8}$	$\frac{27}{64}$	$\frac{295}{1024}$	$\frac{1605}{8192}$	$\frac{2163}{16384}$	$\frac{92253}{1048576}$	$\frac{1944495}{33554432}$	$\frac{20252835}{536870912}$	$\frac{104242545}{4294967296}$	$\frac{530346267}{34359738368}$
e_i	1	$-\frac{11}{8}$	$-\frac{37}{64}$	$-\frac{345}{1024}$	$-\frac{1755}{8192}$	$-\frac{2289}{16384}$	$-\frac{95907}{1048576}$	$-\frac{1999953}{33554432}$	$-\frac{20680605}{536870912}$	$-\frac{105867135}{4294967296}$	$-\frac{536173605}{34359738368}$

Table 4.2: Coefficients of γ^i for the five series expansions derived in this chapter. The associated functions are displayed in Fig. 4.2.

Model	lipid	T	$\frac{\text{beads}}{\text{lipid}}$	N_{lipids}	N_{solvent}	L	L_y	$\frac{\kappa}{k_B T}$ [Ref] , method
Cooke	$w_c/\sigma = 1.6$	$1.1 \epsilon/k_B$	3	1344	—	66.75σ	12.0σ	11.7 ± 0.2 [HD06], T 12.5 ± 1 [HD06], HF 12.44 ± 0.26 [HBD12], T
MARTINI	DMPC	300 K	10	1120	$\frac{19\,623}{1 \text{ bead}=4 \text{ H}_2\text{O}}$	46.75 nm	7.1 nm	18 [dOS07a], HF (at 323 K) 36 [BBS ⁺ 11], HF 40.3 [Shk06], HF 40.5 [HJMD13], HF
Berger	DMPC	300 K	46	934	$\frac{47\,896}{\text{(SPC)}}$	39.2 nm	7.1 nm	15.7 [WE09], HF 18 [BBS ⁺ 11], HF 36 [WPWB11], OF

Table 4.3: Summary of the properties of the three lipid models used. Various methods for obtaining κ have been applied in the past, in particular measuring the height fluctuations of a membrane (HF), the orientation fluctuations of the lipids (OF), or the axial force along a tether (T). Note that the work by den Otter and Shkulipa [dOS07a] studied DPPC and not DMPC, but on the CG MARTINI level this difference is insignificant.

5 Membrane elasticity II: the Gaussian curvature modulus

On mesoscopic scales, lipid membranes can be described by the Helfrich theory outlined early in the previous chapter. Two curvature elastic moduli, namely the bending modulus κ and the Gaussian modulus $\bar{\kappa}$, enter Helfrich theory and play important roles. Several methods to determine κ have been described in the previous chapter, including a new protocol which extracts κ from the stress-strain relation of a buckled membrane. The second modulus, $\bar{\kappa}$, is more subtle to investigate. It will be the focus of this chapter.

5.1 Introduction

In Helfrich theory, as described in Section 4.1.1, the (surface) free energy density of a quasi-two-dimensional membrane quadratically depends on the two local principal curvatures, giving two elastic moduli: the bending modulus κ and the Gaussian curvature modulus $\bar{\kappa}$. Because of the Gauss-Bonnet theorem (see Technical Note 5.1), which states that the surface integral of the Gaussian curvature term remains constant if there is no topological or boundary changes [Kre91], this Gaussian term is irrelevant in many processes, *e.g.* in the buckling of a membrane stripe studied in the previous chapter. However, for some other processes, the Gaussian term does play a significant role, hence we need to know the value of this modulus $\bar{\kappa}$. Unfortunately, methods to determine $\bar{\kappa}$ are sparse, again due to the Gauss-Bonnet theorem: one needs to study those processes in which topology and/or boundary vary. Moreover, to derive an accurate value of $\bar{\kappa}$ requires careful control and manipulation mechanisms for the systems of interest, which may be difficult to realize.

The Gauss-Bonnet theorem might offer some peace of mind, considering that $\bar{\kappa}$ only matters if topology or boundary change. However, many biologically relevant processes involve precisely such changes, and hence the contribution from the Gaussian curvature. Such processes include vesicle fusion during transport processes, the remodeling of the Golgi apparatus and endoplasmic reticulum, and endo-/exo-cytosis. For instance, during the process of two vesicles merging into one, the genus g of the topology increases by 1, and consequently the Gaussian terms contributes $-4\pi\bar{\kappa} \approx 240 k_B T$, assuming $\bar{\kappa} \sim -\kappa \sim 20 k_B T$. Even though the energy barrier to reach some intermediate states may be lower than this large energy difference between the initial and final states, and active cell processes like protein-mediated vesicle fusion are fueled by ATP hydrolysis ($\sim 20 k_B T$ per ATP molecule under physiological conditions), the dependence of the intermediate states on $\bar{\kappa}$ is still very important [Sic08]. Hence, an accurate value of $\bar{\kappa}$ is important to studies of such topics.

Technical Note 5.1: Gauss-Bonnet theorem

For a two-dimensional surface \mathcal{S} with boundary $\partial\mathcal{S}$, the Gauss-Bonnet theorem states that [Car76, Kre91]

$$\int_{\mathcal{S}} dA K_G = 4\pi(1 - g) - \int_{\partial\mathcal{S}} ds k_g, \quad (5.1)$$

where K_G is the Gaussian curvature of the surface, k_g the geodesic curvature of the boundary $\partial\mathcal{S}$, and g the genus, *i.e.* the number of “handles”, in the topology. The geodesic curvature k_g is defined as the change in the tangent vector of the curve $\partial\mathcal{S}$ projected on the tangent plane of the surface \mathcal{S} . When the geodesic curvature vanishes everywhere on a curve, this curve is called a “geodesic”, which is as close as one can get to a straight line on a curved surface. If, in the processes of interest, the boundary $\int ds k_g$ and the topology g remain constant, then the right hand side of the equation is a constant. Therefore, the integral of the Gaussian curvature is constant.

Despite the significance of $\bar{\kappa}$ for many interesting membrane-related problems, much less is known about the values of $\bar{\kappa}$ compared to the bending modulus κ . Theoretically, the stability of planar *bilayers* requires the *elastic ratio* $\bar{\kappa}/\kappa \in (-2, 0)$ [Hel94]. If one is willing to make the assumption that changes in the splay of a lipid in one direction can be relaxed to some extent by a change in the orthogonal direction, then the elastic ratio between *monolayer* moduli can be further restricted to $-1 \leq \bar{\kappa}_m/\kappa_m \leq 0$ [TKS98]. The bilayer $\bar{\kappa}$, however, is not simply twice the monolayer value $\bar{\kappa}_m$, unlike what is the case for the bending modulus $\kappa = 2\kappa_m$: connecting the two Gaussian moduli requires the introduction of two further microscopic quantities, namely the lipid spontaneous curvature K_{0m} and the distance z_0 between bilayer midplane and the surface of inextension (defined as the surface within the monolayer where the surface area stays constant upon bending). One then finds the following relation [Hel81, Hel94, SKBS⁺90, SK04, Mar06]:

$$\bar{\kappa} = 2(\bar{\kappa}_m - 2z_0 K_{0m} \kappa_m). \quad (5.2)$$

In other words, $\bar{\kappa} \neq 2\bar{\kappa}_m$, since the monolayer lipid curvature K_{0m} and the distance between the bilayer midplane and the surface of inextension z_0 are generally nonzero.

Experimentally, only a handful of results about $\bar{\kappa}$ are available in the literature, most of which are based on examining membrane phase transitions between the lamellar phase and some inverted phases [TKS98, Sie06, Sie08]. Most of these results are collected in Table 1 of Hu *et al.* [HBD12]. The majority of this small number of studies [TKS98, SK04, Sie06, Sie08] report a *monolayer* elastic ratio $\bar{\kappa}_m/\kappa_m \in (-0.95, -0.70)$. Two other studies [LSH86, BDWJ05] found the *bilayer* ratio $\bar{\kappa}/\kappa \sim -0.9$.¹ In simulations, however, reliable methods to determine $\bar{\kappa}$ with high accuracy are still needed.

In this chapter, we describe our new method to measure the bilayer Gaussian modulus $\bar{\kappa}$ in simulations. The vesiculation process of a circular patch of membrane is investigated,

¹Baumgart *et al.* [BDWJ05] did not measure $\bar{\kappa}$ directly, but $\Delta\bar{\kappa}$ between the gel and fluid phases instead. If one assumes that the ratio $\bar{\kappa}/\kappa$ in both phases is the same, then one gets -0.9 for the bilayer elastic ratio.

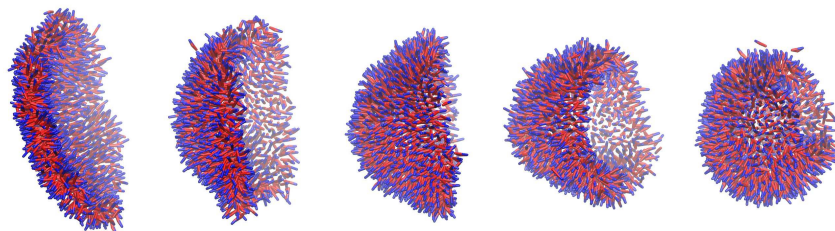


Figure 5.1: Example snapshots of a vesiculation process of a Cooke membrane containing 1400 lipids.

in which the boundary would vary.² As we will show, this method provides accurate measurements of $\bar{\kappa}$ with a moderate requirement on computational resources. Another existing method to obtain $\bar{\kappa}$, namely the stress profile method, is also studied for comparison. We will show that this second strategy, the only one which so far has been used semi-routinely in the literature, produces physically implausible results that are also at odds with our method.

5.2 Theory

5.2.1 The vesiculation process

Our method of determining the Gaussian curvature modulus $\bar{\kappa}$ is based on the vesiculation process of lipid membranes, in which a flat membrane patch spontaneously curves and closes up into a complete lipid vesicle. A sequence of simulation snapshots of this process is shown in Fig. 5.1.

Essentially, this vesiculation process is an interplay between the excess free energy at the open edge of the membrane patch, and the energetic cost to bend it into a vesicle [Hel74, Fro83, BR92]. The former increases linearly with the circumference of the patch, hence prefers to close up the membrane to eliminate the open boundary; while the latter increases with membrane curvature, but is (as long as the final vesicle is spherical) capped by the constant $4\pi(2\kappa + \bar{\kappa})$, regardless of the membrane size. Consequently, beyond a critical size when these two energy contribution balance each other, the edge energy outweighs the bending energy of a vesicle, hence the membrane will vesiculate in order to reduce its total energy [Hel74, Fro83, BR92].

Helfrich studied this process nearly forty years ago when trying to predict the size of lipid vesicles formed by ultra-sonication [Hel74]. In his *one-page* paper, the Gaussian modulus is *neglected*, so that the transition from the flat initial state to the final vesicle state can be quantitatively characterized by the Helfrich Hamiltonian (see Eq. (4.1) in

²The topology of the membrane also changes once it closes up. But this is not directly relevant to our analysis.

the previous chapter). With some knowledge of the other material parameters from experiments and other sources,³ his prediction on the size of the final vesicles agrees pretty well with experimental observations. If, conversely, one wants to *determine* the Gaussian curvature modulus $\bar{\kappa}$, one can turn Helfrich's argument around and look for information of the final vesicle size, or better, quantitative informations about the characteristics of this vesiculation transition.

5.2.2 Hamiltonian

Consider a membrane of area $A = 4\pi R^2$, where R is the radius of the final closed vesicle. If that membrane is still an open patch, and if that patch remains axisymmetric and takes the shape of a spherical cap with radius $1/c$ during the vesiculation process, its total energy according to Eq. (4.1) is [Hel73, Hel74, Fro83, BR92]:

$$\mathcal{E} = E_{\text{bend}} + E_{\text{edge}} = 4\pi(2\kappa + \bar{\kappa})R^2c^2 + 4\pi\gamma R\sqrt{1 - R^2c^2}. \quad (5.3)$$

Subtracting from \mathcal{E} the energy of the flat state, $\mathcal{E}_{\text{flat}} = 4\pi\gamma R$, and normalizing by the energy of a spherical vesicle, $\mathcal{E}_{\text{ves}} = 4\pi(2\kappa + \bar{\kappa})R$, the scaled excess (free) energy $\Delta\tilde{\mathcal{E}}$ of such a curved patch is [HBD12]

$$\Delta\tilde{\mathcal{E}}(x, \xi) \equiv \frac{\mathcal{E} - \mathcal{E}_{\text{flat}}}{\mathcal{E}_{\text{ves}}} = x + \xi [\sqrt{1 - x} - 1], \quad (5.4)$$

where we have defined the scaled (squared) curvature x and a material parameter ξ as:

$$x = (Rc)^2, \quad \xi = \frac{\gamma R}{2\kappa + \bar{\kappa}}, \quad \text{and} \quad R = \sqrt{\frac{A}{4\pi}}. \quad (5.5)$$

The reaction coordinate x ranges from 0 (flat state) to 1 (final vesicle of radius R).

Notice that four material properties, namely the two elastic moduli κ and $\bar{\kappa}$, the edge tension γ , and the membrane size R , are combined into one *single* dimensionless parameter ξ , which completely determines the functional shape of the energy $\Delta\tilde{\mathcal{E}}(x, \xi)$ (see the inset of Fig. 5.2). For $\xi < 1$, the planar state is the global energy minimum, thus a patch would remain flat. At $\xi = 1$, the planar state and the vesicle state share the same energy. For larger values of ξ , the vesicle state becomes the global minimum. However, for $1 < \xi < 2$ there exists a barrier between the two “endpoint” states, located at $x^* = 1 - (\xi/2)^2$ with a barrier height $\Delta\tilde{\mathcal{E}}^* = (1 - \xi/2)^2$. Given that all the other three parameters can be separately measured, $\bar{\kappa}$ can be deduced if one can obtain information about the barrier, such as x^* or $\Delta\tilde{\mathcal{E}}^*$, or in fact the full shape of the transition free energy $\Delta\tilde{\mathcal{E}}(x, \xi)$.

A few remarks about our application of the Helfrich Hamiltonian to this vesiculation process are in order. First of all, our theory is a ground state theory, meaning that thermal fluctuations are not included. For this to be a reasonable approximation, the system size

³Helfrich guessed the edge tension γ based on a suggestion from P. G. de Gennes [Hel74].

needs to be carefully considered, as will be discussed later. Second, the patch has been assumed to follow an axisymmetric and spherical shape, which may not hold at some parts of the membrane, such as at the edge. However, the results presented later will confirm that our simple theory based on these assumptions fits our simulation data. Third, since the lipids can easily swap between the two leaflets by moving around the open edge, their chemical potential and the area difference between the leaflets is in fact equilibrated.

5.2.3 Determining $\bar{\kappa}$: the splitting probability

In order to obtain $\bar{\kappa}$, some information about the functional form of the barrier $\Delta\tilde{\mathcal{E}}$ is required. One possibility is to directly measure this (free) energy curve, *e.g.* using the thermodynamic integration method described in Technical Note 4.1, and then fit Eq. (5.4) to it. However, free energy calculations can be complicated and time-consuming. So instead, the patch-closure probability $P(x)$ will be sampled in simulations, which means that we will measure the probability of finding a membrane that starts with a scaled curvature x and eventually closes up into a vesicle. This is inspired by the intuition that, at the top of the barrier, at $x = x^* = 1 - (\xi/2)^2$, this probability $P(x^*)$ will be approximately $1/2$.⁴ Thus, if one can locate x^* by measuring $P(x)$, then ξ can be calculated, which provides $\bar{\kappa} = \xi/\gamma R - 2\kappa$.

In fact, this probability of patch-closure as a function of x can be *analytically* calculated as the *splitting probability* in a one-dimensional diffusive process [vK07], which describes the probability of reaching one adsorbing end of the diffusion range (here $x = 1$) before the other one (here $x = 0$). With $\Delta\tilde{\mathcal{E}}(x, \xi)$ being the diffusion barrier, this splitting probability is given by [vK07]

$$P_{\xi, \tilde{D}}(x) = \frac{\int_0^x dy e^{\Delta\tilde{\mathcal{E}}(y, \xi)/\tilde{D}}}{\int_0^1 dy e^{\Delta\tilde{\mathcal{E}}(y, \xi)/\tilde{D}}}, \quad (5.6)$$

where \tilde{D} is an effective diffusion constant. Due to the simple functional form of $\Delta\tilde{\mathcal{E}}(x, \xi)$, Eq. (5.6) can actually be evaluated analytically, yielding [HBD12]

$$P_{\xi, \tilde{D}}(x) = \frac{2\sqrt{\tilde{D}} A(x) + \sqrt{\pi} \xi B [C + D(x)]}{2\sqrt{\tilde{D}} A(1) + \sqrt{\pi} \xi B [C + D(1)]}, \quad (5.7)$$

⁴ $P(x)$ is not strictly symmetric on both sides of x^* , since the potential barrier $\Delta\tilde{\mathcal{E}}(x, \xi)$ is not.

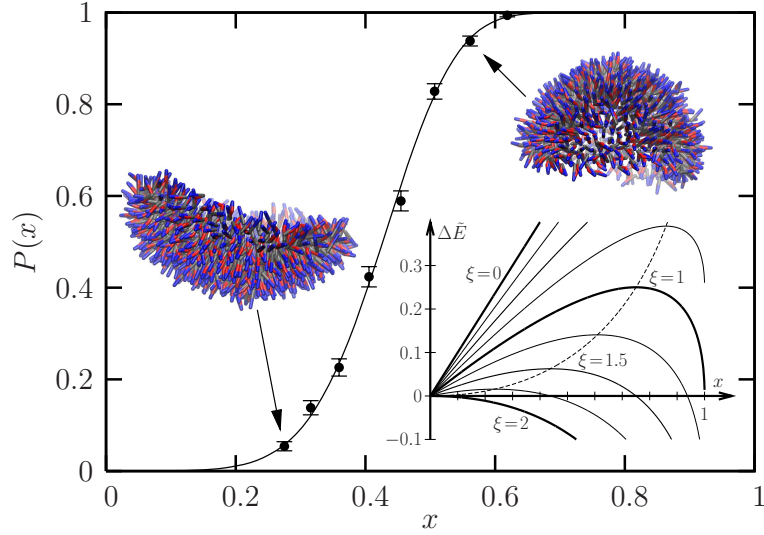


Figure 5.2: The probability of patch-closure $P(x)$ for System 1 in Table 5.1. Snapshots of two initial configurations with different initial curvatures ($x = 0.28$ and $x = 0.56$) are included. Inset: The functional form of the energy barrier $\Delta\tilde{\mathcal{E}}$ at different ξ .

where abbreviations are defined as

$$A(x) = \exp\left\{\frac{\xi}{\tilde{D}}\right\} - \exp\left\{\frac{x + \xi\sqrt{1-x}}{\tilde{D}}\right\}, \quad (5.8a)$$

$$B = \exp\left\{\frac{4 + \xi^2}{4\tilde{D}}\right\}, \quad (5.8b)$$

$$C = \operatorname{erf}\left\{\frac{\xi - 2}{2\sqrt{\tilde{D}}}\right\}, \quad (5.8c)$$

$$D(x) = \operatorname{erf}\left\{\frac{2\sqrt{1-x} - \xi}{2\sqrt{\tilde{D}}}\right\}. \quad (5.8d)$$

In summary, the procedure to derive $\bar{\kappa}$ is the following: First, create initial configurations of curved axisymmetric membrane patches of (squared, scaled) curvature x ; Second, repeatedly simulate the evolution of these patches and thereby measure their probability $P(x)$ of closing up into vesicles; Third and last, fit Eq. (5.7) to the $P(x)$ sampled in simulations with two fitting parameters ξ and \tilde{D} . From there, determine $\bar{\kappa}$ from ξ , using the definition of ξ in Eq. (5.5).

To illustrate the applicability of our procedure, and the resulting high-quality fit, Fig. 5.2 shows the patch-closure probability $P(x)$ determined from one of the Cooke systems studied (System 1 in Table 5.1, plotted as solid circles) and its corresponding fit (solid

curve). Since each simulation is essentially a Bernoulli trial with the flat state and the vesicle state as its outcomes, the number of vesicles found follows a binomial distribution. Its parameter $P(x)$ can be estimated as the ratio between the number of vesicles $N_{\text{vesicle}}(x)$ and the total number of simulations $N_{\text{sim}}(x)$. The error on the estimated $P(x)$ is then $\sigma_P = \sqrt{P(x)[1 - P(x)]/N_{\text{sim}}}$. A fit using Eq. (5.6) provides $\xi = 1.503 \pm 0.003$; the statistical error on ξ is merely 0.2%. Note that, these errors σ_P are “honest”: on average a third of the points are outside the error bar. More importantly, the excellent quality of the fit confirms that in simulations the membrane indeed follows the reaction coordinates assumed in our theory, *i.e.* during the closing process the cap remains axisymmetric and thus can be characterized by a single reaction coordinate x .

Let us conclude with a few remarks on this procedure of pinning the value of $\bar{\kappa}$ using the patch-closure probability $P(x)$.

First, the reason why it is possible to measure $P(x)$ and skip the free energy calculation of $\Delta\tilde{\mathcal{E}}$ is because the complete “reaction pathway” is *assumed* and *controllable*: At every point along the pathway, the membrane patch approximately maintains the shape of a spherical cap with a varying curvature x . More importantly, such pre-curved states can be readily created in simulations on demand. Without either, this procedure would not work.

Second, it is worthwhile to emphasize that the splitting probability in Eq. (5.6) is *not* the equilibrium probability of finding the patch in the vesicle state, which would be the Boltzmann factor of the vesicle state. We could of course also have chosen to approach this problem from an equilibrium point of view and for instance determine the ratio between the Boltzmann factors at the end points. However, since the barrier tends to be *many* $k_B T$, any naive sampling would quickly have gotten stuck in a formidable barrier crossing problem, in which the crossing rates are exponentially suppressed. Then, we would have had to amend the simulations by additional speed-up tricks, such as forward flux sampling [DBCC98] and transition path sampling [AFtW06]. In contrast, the $P(x)$ employed here is essentially the first-passage probability of a non-equilibrium barrier-crossing problem starting from different initial positions along the barrier, the most relevant of which are close to the barrier in terms of $k_B T$. This saves the time to wait for *passive* crossing events by simply *starting* the system up the barrier, close to the maximum, and then letting go. Note that this first-passage probability is also what is easily measured in simulations: once it is “clear” that the patch will form a vesicle or flatten up, this simulation is stopped, and its result is counted into $P(x)$.

Third, the Hamiltonian Eq. (5.4) does not include the excluded volume and hydrodynamic effects of the solvent. Hydrodynamics will indeed change the dynamical behavior of our system. However, as long as the dynamics along the reaction coordinate remains diffusive, our theory should still apply (maybe with a different effective diffusion constant \tilde{D}). In fact, hydrodynamics indeed would make the patch more spherical [NG06], and thus follow more closely along the reaction coordinate. Moreover, the complicated hydrodynamics at the pore when the membrane is about to close up also is irrelevant, since the destiny of the patch is already decided before the vesicle completes (see more details in Section 5.3.3). The most relevant states of the patch are those around the top of the potential barrier, in

which the membrane states will be set up to half-closed, or at least not “almost-closed”, to avoid the high curvature corrections in Helfrich theory.

Fourth and last, fitting with the exponentials $A(x)$ and B in Eq. (5.7) may be numerically unstable when \tilde{D} is really small. In that case, one can divide the numerator and the denominator in Eq. (5.7) by a common factor of $\exp(\xi/\tilde{D})$ and proceed with fitting to the new formula.

5.2.4 Stress profile method

In the literature, another method to determine the Gaussian curvature modulus $\bar{\kappa}$ is the so-called stress profile method, which connects $\bar{\kappa}$ with the lateral stress profile $\Sigma_0(z)$ of a flat and tension-less bilayer. By expanding the energetic cost to deform a *thin continuum* elastic sheet and mapping it to the Helfrich Hamiltonian, the lateral stress Σ , the product of *monolayer* bending modulus κ_m and spontaneous curvature K_{0m} , and the *monolayer* Gaussian curvature modulus $\bar{\kappa}_m$ are given by [Hel81, SKBS⁺90, GK92, GZ92, Hel94, Mar06]

$$\frac{1}{2}\Sigma = \int_0^\infty dz \Sigma_0(z) , \quad (5.9a)$$

$$-\kappa_m K_{0m} = \int_0^\infty dz \Sigma_0(z)(z - z_0) , \quad (5.9b)$$

$$\bar{\kappa}_m = \int_0^\infty dz \Sigma_0(z)(z - z_0)^2 , \quad (5.9c)$$

where z_0 , which we already have encountered in Eq. (5.2), is the distance from the bilayer midplane to the surface of inextension of each monolayer. Note that in the case of zero surface tension, $\Sigma = \int dz \Sigma_0(z) = 0$, Eq. (5.9b) is independent of z_0 , meaning $\kappa_m K_{0m}$ can be determined without the knowledge of z_0 . Similar to the monolayer version in Eq. (5.9c), the bilayer Gaussian modulus $\bar{\kappa}$ is given by the second moment of $\Sigma_0(z)$ as

$$\bar{\kappa} = \int_{-\infty}^\infty dz \Sigma_0(z) z^2 . \quad (5.10)$$

Observe that combining Eqs. (5.9a), (5.9c), and (5.10), at zero tension, is a way to derive Eq. (5.10).

5.3 Simulation setup

A few aspects of the implementation of the patch-closure method need to be elaborated before the results can be presented.

5.3.1 Requirements on the system

As explained in the previous section, our method relies on sampling the probability $P(x)$ of membrane patches folding into vesicles. For both the planar state and the vesicle state

to occur a significant number of times, a barrier is needed in between, which requires $1 < \xi < 2$. Thus, from the definition of ξ in Eq. (5.5),

$$1 < \frac{\gamma R}{2\kappa + \bar{\kappa}} = \frac{R}{\ell} < 2, \quad (5.11)$$

where the characteristic length ℓ of a given membrane is defined as

$$\ell \equiv \frac{2\kappa + \bar{\kappa}}{\gamma}. \quad (5.12)$$

Then, Eq. (5.11) means the patch size R should be in the range of $(\ell, 2\ell)$.

Since $\ell < 2\ell$ is true when $\ell > 0$, and the latter holds because $-2\kappa < \bar{\kappa} < 0$ implies $2\kappa + \bar{\kappa} > 0$, these two limits on R described in Eq. (5.11) can always be satisfied by an appropriate choice of patch size R . However, when other constraints are also considered, the requirements on the system size may turn out to be rather restrictive. On the one hand, R , which is the radius of the final closed vesicle, should not be too small; otherwise the curvature of the membrane is too large for the quadratic Helfrich theory used here. For this reason, we (somewhat optimistically) require this radius to be larger than the membrane thickness, *i.e.* $R > d$. This requirement would become a problem when ℓ is small due to weak bending moduli $2\kappa + \bar{\kappa}$ or a strong edge tension γ . On the other hand, R cannot be too large, either; the undulations of the patch should not make a significant contribution to the system since our method is a ground state theory. This requirement may become problematic when the patch is stiff or the edge tension is weak.

On top of these requirements explained above, for the barrier which separates the flat state and the vesicle state on the free energy landscape (Eq. (5.4)), one may also want its height to be at least a few times higher than the thermal energy. This will make the transition of $P(x)$, from the “low state” of small initial x which favors the planar state to the “high state” of large initial x that is more likely to end up with the vesicle state, sharper, and thus the error on ξ can be smaller. If we denote the barrier height as $\alpha k_B T$, where $\alpha \sim 5$, then this requires the patch size R to satisfy

$$R \lesssim 2\ell \left[1 + \frac{1}{2} \sqrt{\frac{\alpha k_B T}{\pi(2\kappa + \bar{\kappa})}} \right]^{-1}. \quad (5.13)$$

Assuming $2\kappa + \bar{\kappa} \simeq \kappa \simeq 20 k_B T$ and $\alpha = 5$, one gets $R \leq 1.75 \ell$. Or if $2\kappa + \bar{\kappa} \simeq \kappa \simeq 13 k_B T$, as in the Cooke model, $\alpha = 5$ gives $R \leq 1.70 \ell$. Both are not far from the upper bound in Eq. (5.11).

In short, when considering the systems to which the patch-closure method will be applied, one should have these requirements mentioned above in mind, and one has to be somewhat lucky that these can actually be satisfied. For the Cooke systems we studied (see Table 5.1 for system parameters), ℓ ranges from 0.75 to 1.5 times the membrane thickness. The value of ξ measured for these systems ranges from 1.4 to 1.7, satisfying all requirements above. Although the radius of the final vesicle is less than twice the membrane thickness,

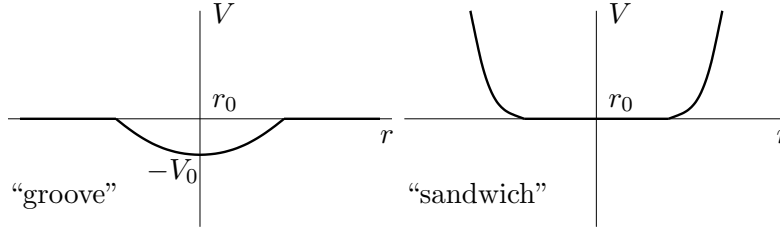


Figure 5.3: Sketches of the “groove” and the “sandwich” constraints used to maintain the initial curvature of the membrane patches.

Helfrich theory seems to hold at this high curvature [HD06], especially if we are mostly interested in half-closed vesicles ($x \sim 1/2$). The MARTINI system has a slightly smaller $\xi = R/\ell \approx 1.36$ in order to save some simulation time.

5.3.2 Initial conditions

When setting up the pre-curved patches, the same number of lipids is initially placed in the two leaflets for simplicity. Due to the opposite sign of their curvatures, the inner leaflet is compressed, while the outer is stretched. However, the lipid chemical potential of the two leaflets needs to be balanced. For this, the membrane is constrained by an external potential of a spherical shape to maintain the preset bilayer curvature, but this potential is chosen such that the lipids are allowed to laterally diffuse within the bilayer and move around at the open edge. Then, after the two layers are equilibrated, this external constraint is removed and the membrane patch evolves freely towards either of the two endpoint states.

For the simulations with the Cooke model, we used the molecular dynamics package ESPResSo [LAMH06]. This external potential is implemented as a “groove” constraint, which harmonically constrains the radial distance r of the last tail bead of each lipid around the desired radius $r_0 = 1/c$. Its functional form is:

$$V_{\text{groove}}(r) = \begin{cases} V_0 \left[\left(\frac{r - r_0}{d} \right)^2 - 1 \right] & , \quad |r - r_0| < d \\ 0 & , \quad \text{otherwise,} \end{cases} \quad (5.14)$$

where the depth of this potential is $V_0 = 0.5\epsilon$, and the maximum range is $d = 1.5\sigma$. A sketch of this “groove” is shown in Fig. 5.3. Each patch is given 100τ to equilibrate, after which this potential is turned off and the patch is released.

The simulations using the MARTINI model are slightly more complicated. The initial curved caps are generated by backmapping, which has been explained in Section 2.1.5, from the Cooke configurations equilibrated using the procedures described above. Then the membrane is “sandwiched”, but not squeezed as shown in Fig. 5.3, between two soft

Technical Note 5.2: Shape anisotropy indexes

The relative shape anisotropy index κ_s^2 is based on the eigenvalues of the gyration tensor \mathbf{S} , which is defined as

$$\mathbf{S} = \frac{1}{N} \sum_{i=1}^N (\mathbf{r}_i - \mathbf{r}_{\text{cm}}) \otimes (\mathbf{r}_i - \mathbf{r}_{\text{cm}}), \quad (5.15)$$

where \mathbf{r}_i is the position of the i th particle of relevance, $\mathbf{r}_{\text{cm}} = \frac{1}{N} \sum_{i=1}^N \mathbf{r}_i$ is the center of mass, and the sums loop over all such particles in the simulation.

Following Theodorou and Suter [TS85], if one arranges the eigenvalues of \mathbf{S} in ascending order, *i.e.* $\lambda_1^2 \leq \lambda_2^2 \leq \lambda_3^2$, the *radius of gyration* R_g^2 , then the *asphericity* b , the *acylindricity* c , and the *relative shape anisotropy* κ_s^2 are given by:

$$R_g^2 = \lambda_1^2 + \lambda_2^2 + \lambda_3^2, \quad (5.16a)$$

$$b = \lambda_3^2 - \frac{1}{2}(\lambda_1^2 + \lambda_2^2), \quad (5.16b)$$

$$c = \lambda_2^2 - \lambda_1^2, \quad (5.16c)$$

$$\kappa_s^2 = \frac{b^2 + \frac{3}{4}c^2}{R_g^4}. \quad (5.16d)$$

spheres to allow for further equilibration while its curvature is maintained. The two spherical walls interact with only the lipids, but not the water molecules, *via* a WCA potential. This is implemented with the Mean Field Force Approximation boundary (MFFA) approach [RMM08]. It is also worthwhile to point out that the “groove” might not be an appropriate choice for MARTINI: Recall that MARTINI lipids have *two* tails, then the groove would bias *both* tail ends towards the midplane, which is not necessarily typical, since many conformations are possible in which one tail is stretched towards the middle but the other tail wiggles up. This “sandwich” avoids this bias.

5.3.3 Sampling closure probability and shape anisotropy

Another important technical aspect of the simulation setup concerns the procedure to sample the patch-closure probability $P(x)$. The value of that probability is calculated as the number of vesicles formed divided by the total number of trials.

For each simulation, it is better to monitor the evolution of the system in order to decide if an endpoint state, either the flat state or the vesicle state, has been reached, then this simulation can be stopped. This is preferable to using some pre-determined run-time: if, on the one hand, the fixed run-time is too short, then it is insufficient for the patch to evolve; if, on the other hand, the run-time is too long, then computational resource is wasted.

In order to obtain good statistics on $P(x)$, at least 200 simulations are conducted for each initial curvature x when using the Cooke model, and normally 8 different x will be sampled for each membrane system studied, as listed in Table 5.1. This large number of

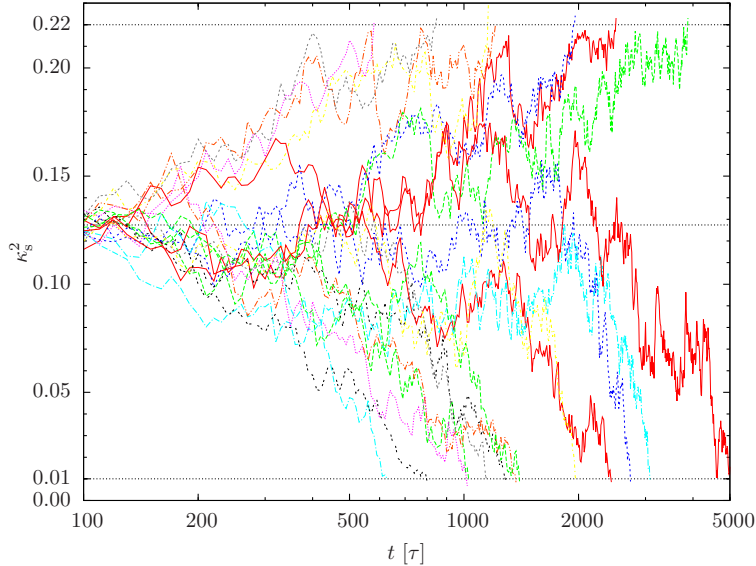


Figure 5.4: Time-evolution of the relative shape anisotropy κ_s^2 for 20 randomly chosen simulations of System 1, initially constrained to $x = 0.456$ for 100τ and then released. As shown in Fig. 5.2, the measured closure probability $P(x)$ here is roughly 60%, consistent with the fact that 13 out of 20 simulations close up into vesicles.

simulations poses a computational question of how to *automatically* stop a simulation if either the flat or the vesicle state has been reached. One solution is to automatically monitor the state of the membrane shape. Ideally, one can simply use the reaction coordinate x . However, it is not easy to calculate given the coordinates of the lipids. So a *relative shape anisotropy* index κ_s^2 [TS85] is used instead. This index is defined in Technical Note 5.2.

For a perfect and complete sphere, $\kappa_s^2 = 0$. For an infinitely thin circular disk, $\kappa_s^2 = \frac{1}{4}$. Of course, the membrane patches do not belong to any one of these ideal cases due to both their nonzero thickness and the thermal fluctuations. Through careful “experimentation”, we found that $\kappa_s^2 < 0.01$ is enough to label the patch as in the vesicle state, while $\kappa_s^2 > 0.22$ indicates it becomes a flat disk. Note that the precise value of the cutoff at the flat end and the vesicle end does not matter so much, since at these two ends the system diffuses in a potential that is strongly biased to either end. As long as the barrier is large enough, it becomes exponentially unlikely that a trajectory that is very close to the end still completely changes its mind. Hence, the precise cutoff is not that important.

As an example, the time evolution of κ_s^2 for twenty pre-curved membrane patches is plotted in Fig. 5.4 for System 1 in Table 5.1. These patches are initially constrained at $x = 0.456$ (or $\kappa_s^2 \sim 0.125$) for 100τ , using the procedure described in the previous subsection, and then let go. One finds 13 out of 20 close up into vesicles, consistent with the $P(x) \approx 0.6$ shown in Fig. 5.2. Note that, from only 20 trajectories, a difference of more

than an order of magnitude in closure time can already be seen, which supports the need to automate the termination of the simulations. Moreover, the plot also demonstrates the diffusive behavior assumed in Section 5.2.3.

For the simulations of Cooke membranes, this analysis of shape anisotropy is implemented in the MD package ESPResSo [LAMH06]. For the MARTINI simulations, no such analysis is available with GROMACS [HKvdSL08] on the fly; thus a standalone Python script is used to monitor the κ_s^2 based on the last frame in the MD trajectory.

5.3.4 Other quantities measured

In order to obtain $\bar{\kappa}$, several other physical quantities are required and thus need to be measured separately in independent simulations.

Bending modulus κ

When using the Cooke model, κ is measured using the cylindrical membrane tether method by Harmandaris and Deserno [HD06], as mentioned in the previous chapter.⁵ For each system studied, five cylinder simulations are conducted at different radius that are comparable to the radius of the caps that will be simulated for $\bar{\kappa}$, and then the resulting values of κ are averaged. For the study using the MARTINI model, two different methods are employed to determine κ , namely the height fluctuation method and the buckling method, both have been described in the previous chapter.

Edge tension γ

A simple simulation setup is used to measure the edge tension γ . A stripe of flat membrane is placed in the simulation box in the xy -plane, and it extends infinitely through the periodic boundary condition in only one of the two directions, *e.g.* in the y -direction. In the x -direction, its width does not cover the box, so *two* open edges are present. Then the stress in all three directions is measured, and γ is given by

$$\gamma = -\frac{1}{2} \left[P_{yy} - \frac{1}{2}(P_{xx} + P_{zz}) \right] L_x L_z, \quad (5.17)$$

where P_{ii} is the pressure in the i -direction for $i = x, y, z$ (Notice that pressure and stress differ by a minus sign), L_x and L_z are the box dimensions in the two directions along which the stripe does *not* periodically connect. Note that Eq. (5.17) is valid for systems with or without solvent. In the latter case, the pressure in the x - and z - directions are simply zero.

⁵Of course, the buckling method described in the previous chapter could have been employed as well; but it so happens that this part of the thesis historically precedes the buckling work. However, since Chapter 4 shows that for the Cooke model cylinders and buckles are both efficient and lead to the same results, it does not matter which one we actually used.

Membrane size R

The area $A = 4\pi R^2$ of a *spherical* cap is estimated based on the area per lipid a_ℓ of a *flat* tensionless bilayer, which is measured in a few simulations of 1000 lipids in the $NP_{||}L_{\perp}T$ ensemble and averaged. This estimation ignores the area difference in the inner and outer leaflet for a curved patch. But since the curvature of the caps are moderate, this error in the membrane size A , and consequently in the radius of the closed vesicle R , is insignificant. Moreover, it turns out that the previous two parameters κ and γ contribute to the major part of the error on ξ , and thus on $\bar{\kappa}$. Thus, no further corrections about the curvature effect on A is necessary.

5.4 Results

5.4.1 Dependence on other parameters

Twelve different systems are studied using the generic CG Cooke model. The reasons to start our study with a generic CG model are twofold: First, the curvature elastic properties in the Helfrich theory are macroscopic observables, and it is worthwhile to check how universal these properties are (*e.g.*, the elastic ratio $\bar{\kappa}/\kappa$ and its dependence on lipid curvature). Second, the Cooke model is computationally efficient to allow us to study a wide range of specific situations with excellent statistics, which we will use to support the soundness of our underlying analysis.

These systems vary in the number of lipids, elastic properties, and spontaneous curvature, as listed in Table 5.1. The elastic properties, mainly the bending modulus κ and the edge tension γ , are tuned by changing the attraction range w_c in the Cooke model described in Section 2.1.4. The spontaneous curvature is adjusted by changing the size of the head bead, b , of each lipid.

In general, all of the systems show a *bilayer* elastic ratio of $\bar{\kappa}/\kappa \approx -0.95 \pm 0.1$, in good agreement with the scarcely available experiment results of $\bar{\kappa}/\kappa \approx -0.9 \pm 0.38$ [BDWJ05], and also within the more restricted theoretical range of $-1 \leq \bar{\kappa}/\kappa \leq 0$ for *monolayers* [TKS98]. However, as we have seen in the introduction, the connection between the monolayer ratio, which is better studied experimentally, and the bilayer ratio we measured in simulations, requires additional microscopic inputs, namely the spontaneous lipid curvature K_{0m} and the surface of inextension z_0 , which will be examined soon. Before that, two more observations are worth pointing out.

Dependence on membrane size

First, three different system sizes are studied among System 1-3 and 4-6 at two different values for the bending modulus κ . In each case, the elastic ratio $|\bar{\kappa}/\kappa|$ seems to slightly increase for smaller systems. This is conceivable since the curvature of the final vesicle is more substantial for smaller system, thus the higher order curvature corrections in Helfrich

theory would become more important. However, the difference in $\bar{\kappa}/\kappa$ between these measurements is insignificant within statistical errors obtained from Monte Carlo resampling of the fit. Thus, we will ignore it in the following analysis and use the average from the three sizes instead.

Dependence on bending modulus κ

Second, across System 1-3, 4-6, and 7, the effect of bending modulus κ on the elastic ratio is examined. By setting w_c to different values while keeping the head size b fixed, the value of κ is lowered to roughly $10 k_B T$ in System 7 ($w_c = 1.55 \sigma$), or increased to approximately $18 k_B T$ in System 4-6 ($w_c = 1.7 \sigma$), from the commonly quoted value of $12.5 k_B T$ (System 1-3, $w_c = 1.6 \sigma$). Even though κ is changed by about 80%, the elastic ratio is different only by several percents. There is a weak trend that $|\bar{\kappa}/\kappa|$ decreases as the membrane becomes stiffer. Our tentative explanation for this phenomenon is the following: increasing w_c not only reduces the area per lipid, but also reduces the *degree* to which the membrane can be compressed further. This corresponds to a larger Poisson ratio ν in simple continuum theory [LL86], which can vary within the range of $\nu \in [-1, 0.5]$. Recall that within thin plate theory $\bar{\kappa}/\kappa = \nu - 1$ [LL86], thus the less “compressible” a membrane is, the higher its Poisson ratio is, and thus the less negative the elastic ratio $\bar{\kappa}/\kappa$, in accord with our observations here. However, this argument cannot be made more quantitative, since membranes are not homogeneous and isotropic continuum materials. So it is better to stop at this semi-quantitative level.

Dependence on lipid curvature K_{0m}

As described in Eq. (5.2), the dependence of $\bar{\kappa}$ on the lipid curvature K_{0m} is nontrivial. To study this, the size of the head bead, b , is changed in Systems 1-3, 8, 9, 10, 11, and 12, such that $b/\sigma \in \{0.92, 0.935, 0.95, 0.965, 0.98, 1.0\}$. As shown in Fig. 5.5, the elastic ratio varies by $\sim 17\%$ over this range, while the change in κ is merely 5% (see Table 5.1). To connect b and K_{0m} , a simply geometric model, shown as the inset in Fig. 5.5, is employed. This model suggests that the spontaneous lipid curvature $K_{0m} = \alpha/R_0 \simeq \alpha(b/b_t - 1)/2\sigma$, using the fact that $b \simeq b_t \simeq 1\sigma$, where b and b_t are the size of the head and tail beads, respectively. The prefactor α would be 2 if only geometry mattered, but it would be smaller if the entropy of lipid tail-bending fluctuations are included. Thus, we expect $1 \leq \alpha \leq 2$, and the value of α will be estimated given the value of z_0 measured independently. Plugging this geometric model into Eq. (5.2) yields

$$\frac{\bar{\kappa}}{\kappa} = \left(\frac{\bar{\kappa}_m}{\kappa_m} + \frac{\alpha z_0}{\sigma} \right) - \left(\frac{\alpha z_0}{b_t} \right) \frac{b}{\sigma} \stackrel{\text{fit}}{=} (0.69 \pm 1.49) - (1.71 \mp 1.56) \frac{b}{\sigma}, \quad (5.18)$$

where the second part of the equation is obtained by fitting to the data (straight line in Fig. 5.5). Note that the errors of the fit are strongly anti-correlated.

In addition to confirming the linear relation between the elastic ratio $\bar{\kappa}/\kappa$ and the spontaneous curvature K_{0m} , the fit above also provides additional information regarding

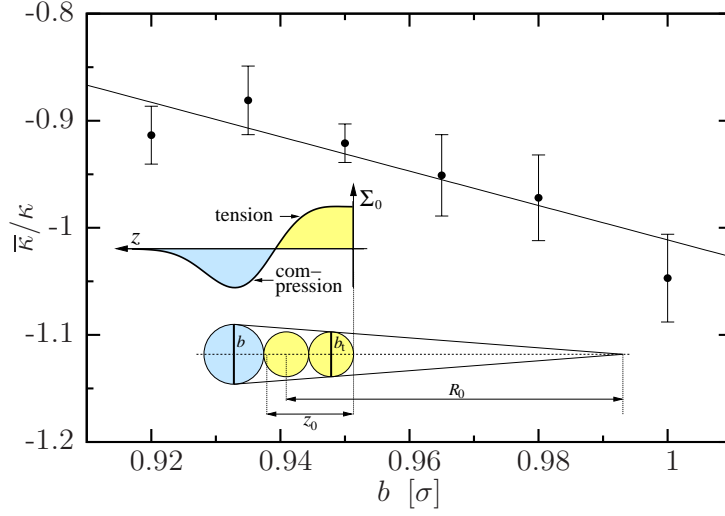


Figure 5.5: Elastic ratio $\bar{\kappa}/\kappa$ as a function of lipid head size b for $w_c = 1.6\sigma$ (System 1-3, 8, 9, 10, 11, and 12 in Table 5.1). A straight line is fit to the data (solid line). Inset: Definition of the distance to the surface of inextension, z_0 ; the bead size b for the head and b_t for the tails; and the geometric curvature radius $R_0 \simeq 2\sigma/(b/b_t - 1)$. A sketch of the lateral stress profile $\Sigma_0(z)$ for the Cooke model is also included.

the membrane elasticity and structure. First, the monolayer elastic ratio can also be estimated, if one is willing to make two more assumptions: 1) b/b_t predominantly affects K_0 but not the monolayer elastic ratio $\bar{\kappa}_m/\kappa_m$; and 2) the effective size for the tail bead is $b_t = 0.95\sigma$ for a Cooke lipid, *i.e.* when $b = 0.95\sigma$ the spontaneous curvature of a Cooke membrane is zero. The former is supported by the observation that, for monomethylated 1,2-dioleoyl-*sn*-glycero-3-phosphoethanolamine (DOPE-Me), the spontaneous curvature K_{0m} varies by roughly 13% from 55° to 90° [SK04, Sie06], whereas the value of $\bar{\kappa}_m/\kappa_m$ barely changes [Sie08]. The latter is plausible because in the Cooke model the lipid tails attract each other due to the cohesion, while the heads only repel, thus the effective tail size is slightly smaller than the head [CKD05, CD05]. With these two assumptions, Eq. (5.18) gives $\alpha z_0 \approx (1.63 \pm 1.48)\sigma$ and the monolayer elastic ratio $\bar{\kappa}_m/\kappa_m \approx -0.93 \pm 0.03$. The large error on the product αz_0 is because the slope of the fit is difficult to pinpoint. In contrast, the statistical error for $\bar{\kappa}_m/\kappa_m$ is very small, for the reason that the strong anti-correlated errors in slope and intercept cancel each other. If we allow the *real* head size b to be somewhere between 0.92σ and 0.98σ , then a more realistic estimation of $\bar{\kappa}_m/\kappa_m$ is -0.93 ± 0.05 , which is compatible with experiment measurements for DOPE-Me, DOPE, and DOPC [SK04, Sie06, Sie08].

The second additional piece of knowledge involves the lipid spontaneous curvature K_{0m} . From the fit in Eq. (5.18), the prefactor $\alpha = (1.71 \pm 1.56)b_t/z_0 \approx (1.1 \pm 1.0)$,

using $b_t = 0.95\sigma$, and $z_0 \approx 1.5\sigma$.⁶ Following this, K_{0m} can be estimated as $K_{0m} \approx 1.1(b/b_t - 1)/2\sigma \in (-0.017, 0.029)\sigma^{-1}$ for the range of b studied, which approximately corresponds to $K_{0m} \in (-0.017, 0.029)\text{ nm}^{-1}$ using the rule of thumb mapping of $\sigma \approx 1\text{ nm}$. Compared to experimental results, this range is on the same order of magnitude with the K_{0m} of some lipids that form planar bilayers, such as DPPC and 1-palmitoyl,2-oleoyl-*sn*-glycero-3-phosphocholine (POPC) [KHRP13], and is an order of magnitude lower than the K_{0m} for some more curved lipids, such as 1,2-dioleoyl-*sn*-glycero-3-phosphoethanolamine (DOPE) and 1,2-dioleoyl-*sn*-glycero-3-phospho-L-serine (DOPS), which tend to form inverse hexagonal phase H_{II} [Mar06]. Of course, due to the large uncertainty on α and the generic essence of the Cooke model, the resulting $K_{0,m}$ should not be overinterpreted.

Despite the low resolution of the Cooke model, this semi-quantitative agreement between our simulations and experiments on the elastic ratio $\bar{\kappa}_m/\kappa_m$ and K_{0m} has deep meanings: Firstly, it supports our assumption that the curvature dependence of $\bar{\kappa}$ on K_{0m} is universal and does not require any more sophisticated underlying microscopic lipid structure (which is probably missing in the Cooke model), since the Helfrich theory is a macroscopic description of lipid membranes without any chemical specificity. Secondly, this study of the subtle dependence of $\bar{\kappa}/\kappa$ on the other parameters is possible only because our patch-closure method is able to determine $\bar{\kappa}$ with such high accuracy to distinguish a difference of approximately a few percents in $\bar{\kappa}/\kappa$.

5.4.2 Results from the stress profile method

Another, potentially easier way, to derive the Gaussian curvature modulus $\bar{\kappa}$ is by calculating the second moment of the lateral stress profile of a tensionless flat membrane, as described in Section 5.2.4. For the Cooke membrane with $w_c = 1.6\sigma$, the stress profile $\Sigma_0(z)$ is measured using the Irving-Kirkwood method [IK50]. Both ESPResSo [LAMH06] and GROMACS [HKvdSL08] are used to cross-check the accuracy of the calculated $\Sigma_0(z)$, and their results are identical. Without any assumption about z_0 , Eq. (5.9b) gives $\kappa_m K_{0m} \simeq 3.75 k_B T/\sigma$, while Eq. (5.10) results in $\bar{\kappa} \simeq -21.7 k_B T$. Using $\kappa_m = \kappa/2 = 6.22 k_B T$ for this system, the former suggests that the spontaneous curvature $K_{0m} \simeq 0.67\sigma^{-1}$, a extremely large value given the fact these lipids would like to form planar bilayers; the latter shows an unusual, yet still permissible, elastic ratio $\bar{\kappa}/\kappa \simeq -1.7$. If one assumes the stress profile will also provide the same monolayer $\bar{\kappa}_m \simeq -0.93\kappa_m = -5.8 k_B T$ measured by the patch closure method, then Eq. (5.9c) requires a very small $z_0 \simeq 0.68\sigma$, which is less than one third of the monolayer thickness away from the bilayer midplane. If a separately measured $z_0 \approx 1.6\sigma$ is used, then the monolayer $\bar{\kappa}_m$ becomes positive. All these results are neither plausible nor in agreement with our patch closure data and, in fact, experiments. Therefore, this stress profile method to derive the material parameters is, if possible at all, not as straightforward as one would hope.

⁶For the surface of inextension, independent simulations of cylindrical, spherical, and buckled membranes suggest that $z_0 \approx 1.5\sigma$ (from personal communication with Wang and Deserno).

5.4.3 Results using MARTINI model

The stress profile method fails to provide meaningful results of the elastic properties of the Cooke membrane. It is unclear whether the stress profile method or the Cooke model should be blamed for these implausible results. It is true that the stress profiles of Cooke membranes are completely unphysical due to the fact that the hydrophobic interaction is replaced by an effective attraction among the tails, as sketched in the inset of Fig. 5.5. However, the results from the patch-closure method are in agreement with theoretical expectations and experiment measurements, which suggests that the Cooke model is able to reproduce fundamental physics of lipid membrane to a large extent. Moreover, nothing in the derivation of Eq. (5.9) and (5.10) needs to make any assumptions about the “physicalness” of $\Sigma_0(z)$. Thus, it is worthwhile to apply both methods to a more resolved lipid model to figure out the causes of the discrepancy between the results from the two methods.

Moreover, the study using the Cooke model proves that our patch-closure method is highly efficient. Since this efficiency does not rely on any specific properties of this model (such as its implicit solvent nature), it is possible to apply our method to a more resolved CG model. Although several lipid CG models are available at a higher resolution than the Cooke model, we choose to use the MARTINI model again, due to its wide range of successful applications and the potential benefits to the community with some additional information about this model.

Patch-closure results

The procedure of the patch-closure method as described above is applied to a MARTINI DMPC membrane consisting of 1200 lipids. Since the MARTINI-DMPC membrane size we chose is on the small side in the optimal range discussed in Section 5.3.1, the energy barrier between the two endpoints is large ($\sim 50k_B T$). This leads to a sharp transition in the closure probability $P(x)$, allowing us to reduce the sample size at each initial x to be 60 without losing accuracy of the final results. This is a substantially smaller number compared to the 200–500 times for the Cooke model. However, as we will discuss in the next section, this saving in computation effort is unlikely to increase the final error on the measured $\bar{\kappa}$, since its major contribution stems from the measurements of κ and γ . The cutoff range for the relative shape anisotropy index (see Section 5.3.3) is slightly adjusted to $\kappa_s^2 < 0.008$ for the vesicle state and $\kappa_s^2 > 0.21$ for the flat state.

From these simulations, we measured $\bar{\kappa}/\kappa = -1.04 \pm 0.03$, as listed in Table 5.1 with the other material parameters. This result is in line with the $\bar{\kappa}/\kappa \in (-1.05, -0.85)$ measured using the Cooke model. Also consider the fact that DMPC lipids have shorter tails than DPPC, which has a slight positive spontaneous curvature [KHRP13], thus a positive spontaneous curvature K_{0m} is plausible for DMPC. This leads to a more negative elastic ratio of $\bar{\kappa}/\kappa \sim -1$, as expected according to Eq. (5.2).

The monolayer elastic ratio can again be estimated using Eq. (5.2), if further microscopic assumptions are made. For the spontaneous curvature K_{0m} , a recent experimental

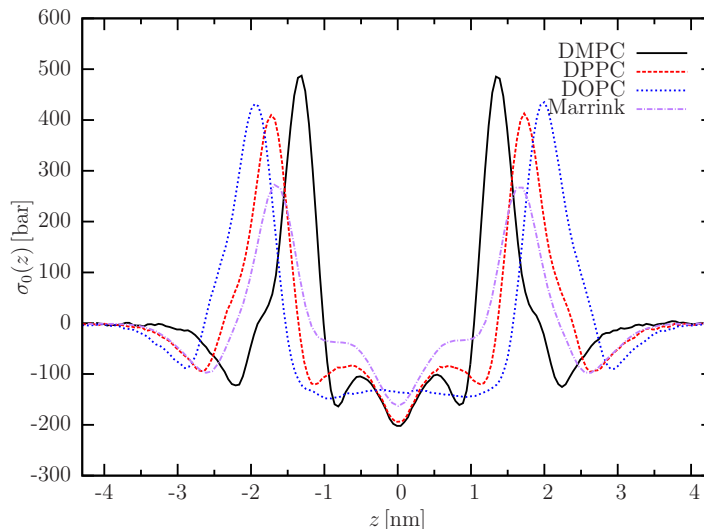


Figure 5.6: MARTINI model lateral stress profiles $\Sigma_0(z)$ of DMPC (solid, black), DPPC (dashed, red), and DOPC (dotted, blue) bilayer of 256 lipids (DMPC and DOPC at 300 K, DPPC at 323 K). The original stress profile by Marrink *et al.* [MRM05] for 512 DPPC lipids at 323 K is shown as the purple dash-dotted curve.

study, which employs small-angle X-ray scattering of mixture lipids that form H_{II} -phase, reported a $K_{0m} = +0.068 \pm 0.032 \text{ nm}^{-1}$ for DPPC [KHRP13]. Since DMPC has two fewer CH_2 groups in each chain, and both PC lipids contain saturated chains, DMPC's K_{0m} is expected to be slightly more positive, roughly in the range of $(0.05, 0.10) \text{ nm}^{-1}$. The value of z_0 , however, is less obvious. It is generally believed to approximately locate at the hydrophilic-hydrophobic interface of a monolayer. Given the thickness of DMPC is 3.53 nm [KLC⁺05], it is plausible that $z_0 \in (1.0, 1.5) \text{ nm}$, which is roughly 55%-85% of the monolayer thickness away from the bilayer center. These two assumptions together gives $2K_{0m}z_0 \in (0.1, 0.3)$, leading to a monolayer ratio $\bar{\kappa}_m/\kappa_m \simeq -0.84 \pm 0.10$, in accord with the experiment range.

Stress profile results

As an alternative way of determining $\bar{\kappa}$, the lateral stress profile of MARTINI DMPC membranes is also calculated using a special version of GROMACS designed for calculations of the 3D local stress tensor [GL98, ORL⁺09], as shown in Fig. 5.6.

For all stress profiles measured, a negative valley at the bilayer center is observed, indicating a repulsion (negative stress) between the lipid tails. At $z \approx 1.5 \dots 2.0 \text{ nm}$, a significant peak of a height of several hundred bars can be seen, showing the strong surface tension created at the hydrophilic-hydrophobic interface. Then, another repulsive region for the head groups dips down to roughly 100 bars, before the profile vanishes 3 to 4 nm away

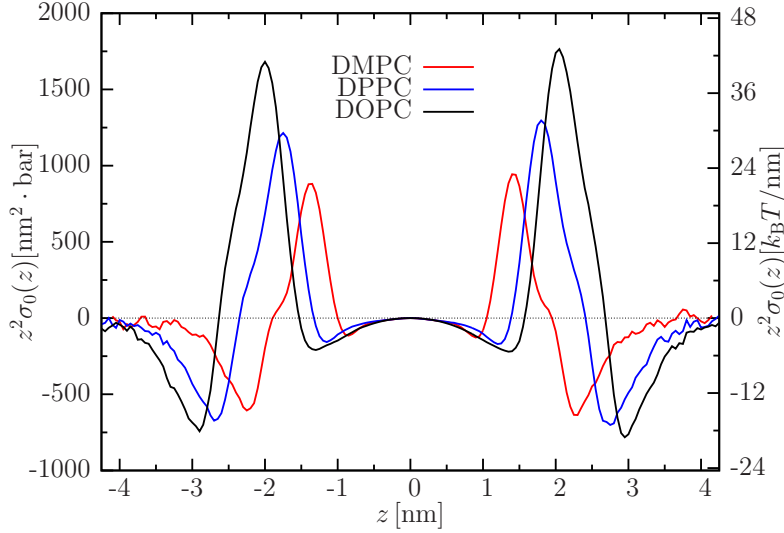


Figure 5.7: The integrand of the second moment, $z^2 \Sigma_0(z)$, of DMPC (black), DPPC (red), and DOPC (blue) bilayer of 256 lipids (DMPC and DOPC at 300 K, DPPC at 323 K). In all three MARTINI cases, $z^2 \Sigma_0(z)$ approaches zero at sufficiently large z .

from the midplane. The general features of these profiles are consistent with the results in literature, including those ones from fully atomistic simulations [ORKV07, OV10].

Several additional simulations are conducted to cross-check the validity of our simulation results, as listed in Table 5.2. To test for the finite size effect, three systems (System 1-3) of 128, 256, and 512 lipids were simulated. Although the profile is widened due to the more extensive fluctuations in larger system, the moments that we need are not affected.⁷ Thus, all other systems were chosen to contain 256 lipids, in order to balance between efficiency and potential finite size effect. Then, the hydration level is also shown to have little effect on the results, when comparing System 2 and 4. In addition to DMPC, MARTINI DPPC and DOPC are also simulated for comparison (System 5-7). Finally, with the concern about the quality of the stress profiles far away from the bilayer center, where the noise is likely to heavily contribute to the second moment, the integrand of the second moment, $z^2 \cdot \Sigma_0(z)$, is plotted in Fig. 5.7. For all these three PC membranes, this quantity approaches zero when $z \geq 4$ nm, showing that the noise in the profiles is well controlled and will not affect the result of the second moment.

Applying Eqs. (5.9) and (5.10), the surface tension Σ , the monolayer spontaneous curvature K_{0m} , and the bilayer elastic ratio $\bar{\kappa}/\kappa$ are calculated. All results can be found in Table 5.2.⁸ For all three types of PC lipids studied, the values of K_{0m} are significantly

⁷Interested readers can find a simple proof of this statement in the publication of Hu *et al.* [HJMD13].

⁸For the bending modulus κ , the value of $\kappa = 16.6 \times 10^{-20}$ J measured using the height undulation method is used for all systems for simplicity. Note that using more accurate values of κ , *e.g.* by applying the

shifted towards the negative side, comparing to experimental results of $+0.068 \pm 0.032 \text{ nm}^{-1}$ for DPPC and $-0.091 \pm 0.008 \text{ nm}^{-1}$ for DOPC [KHRP13]; for DMPC and DPPC the results are even different by a minus sign. More importantly, the calculated bilayer elastic ratio $\bar{\kappa}/\kappa$ are either barely negative (for DMPC) or actually positive (for DPPC and DOPC). The latter means the lamellar phase becomes unstable [Hel94], in contrary to the fact that these MARTINI-PC lipids tend to form perfectly stable planar bilayers. Thus, our results indicate that the stress profile method fails to provide physically meaningful results also for MARTINI-lipids.

5.5 Discussion

5.5.1 Notes on the stress profile method

Since it is computationally more efficient (smaller systems, very few simulations) than the patch-closure method we propose, it is quite disappointing to find that the stress profile method fails to measure the Helfrich elastic parameters, namely the spontaneous lipid curvature K_{0m} and the bilayer and monolayer Gaussian curvature moduli $\bar{\kappa}$ and $\bar{\kappa}_m$.

In recent years, the stress profile method has been implemented in several studies to study K_{0m} and $\bar{\kappa}$, using CG lipid models [MRM05, OHSE08, OME10, OE11, HJMD13] or atomistic models [ORKV07, OV10]. As collected in Table 3 of [HJMD13], one finds that 1) the results for K_{0m} tend to be too negative compared to the values found in experiments; 2) the monolayer ratio $\bar{\kappa}_m/\kappa_m$ is normally between -0.5 and 0; although they are physically permissible, but disagree with the range of (-0.95,-0.75) measured in experiments; and 3) the bilayer ratio $\bar{\kappa}/\kappa$ then becomes less negative or even positive (*c.f.* Eq. (5.2)). This breakdown of the stress profile method is then unlikely due to the imperfect nature of the CG models we used.

In fact, our stress profile simulations using the the generic CG Cooke model and the high-resolution CG MARTINI model show errors in two *opposite* directions: while $\bar{\kappa}/\kappa$ for the Cooke model is an implausibly negative value of -1.7 , it is unreasonably large for the MARTINI model: -0.05 for DMPC and even *positive* for DPPC and DOPC, which indicates the lamellar phase is not stable any more. Since the MARTINI model seems to be able to represent realistic lipid curvatures [FM11], it may not be the loss of local details in the CG models that is to blame, but rather be the intrinsic neglect of local correlations in the continuum theory which leads to Eqs. (5.9) and (5.10). Such local correlations would affect the free energy and hence the stress distribution. In addition, the derivation relies on the *continuum* nature of the theory [Hel81, Hel94, HJMD13], while membranes are inhomogeneous across their normal direction [GK92]. Also, in this continuum theory, local correlations are neglected, but they affect the free energy and hence the stress distribution. Oversteegen and Leermakers have pointed out that additional thermodynamic

buckling method or by measuring each type of lipid separately, will not change the quality of the argument here, since it won't affect the sign of the results.

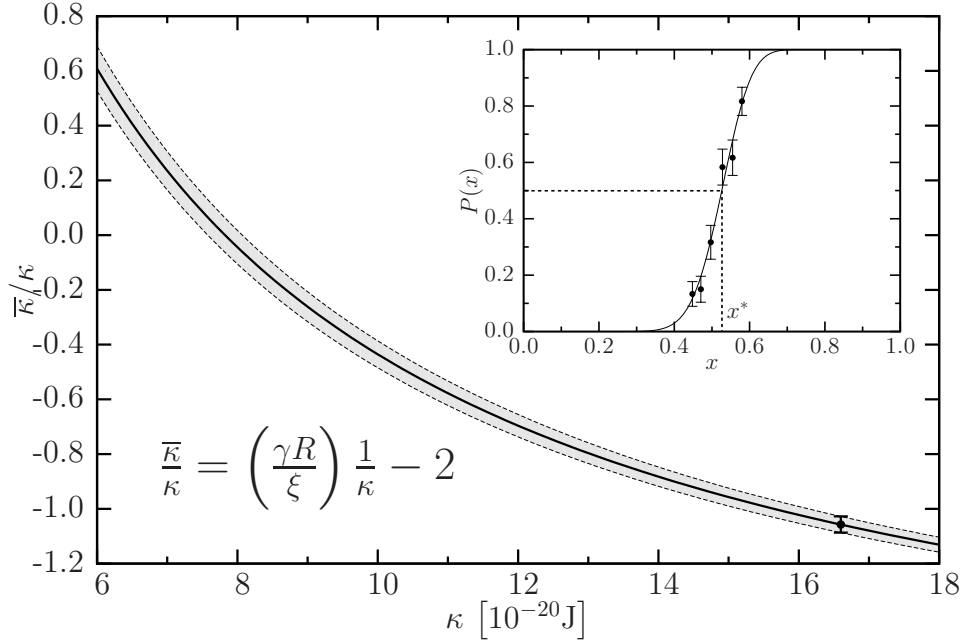


Figure 5.8: The bilayer elastic ratio $\bar{\kappa}/\kappa$ of MARTINI-DMPC as a function of the value of κ used in the analysis (solid curve). The values of ξ , γ , and R listed in Table 5.1 are used. The dashed curves indicate the estimated error on $\bar{\kappa}/\kappa$ assuming the relative error σ_κ/κ stays constant over the range of κ plotted. Inset: the patch-closure probability $P(x)$ (dots) and a fit using Eq. (5.6).

derivatives should be included into the stress profile moments to determine elastic constants of membranes [OL00], which are generally not present in standard derivations.

Thus, even though the stress profile method has existed for more than three decades since the early work by Helfrich [Hel81], it is still unclear whether it can be applied to determine membrane elastic parameters.

5.5.2 Notes on the patch-closure method

On the contrary, the patch-closure method is proven to be a reliable and accurate way to determine the Gaussian curvature modulus $\bar{\kappa}$, assuming other material parameters, namely the bending modulus κ , the edge tension γ , and the membrane size A are known with high precision through other independent measurements.

Unfortunately, sometimes these prerequisites are not determined as accurately as one would like. It is especially true for κ , as discussed in the previous chapter. In fact, what the patch-closure really measures with excellent accuracy is the combination of the two elastic moduli, $2\kappa + \bar{\kappa} = \gamma R/\xi$, since ξ and R on the right-hand-side can be determined with an error of much less than 1 percent, and γ measured by simulating ribbons normally

contains a couple percents of error (see Table 5.1). This means the major contribution to the error in $\bar{\kappa}$ is from κ .

To illustrate this idea, given the values of ξ , γ , and R measured for the MARTINI-DMPC membrane we studied, the bilayer elastic ratio is calculated as a function of κ

$$\frac{\bar{\kappa}}{\kappa} = \left(\frac{\gamma R}{\xi} \right) \frac{1}{\kappa} - 2. \quad (5.19)$$

As shown in Fig. 5.8, the value of $\kappa = 16.6 \times 10^{-20}$ J measured from the height undulations leads to $\bar{\kappa}/\kappa = -1.04$. If the result using the buckling method, $\kappa = 29 k_B T \simeq 12 \times 10^{-20}$ J, is given as the input, then our patch-closure method predicts $\bar{\kappa}/\kappa \simeq -0.7$. Both of the numbers above are consistent with expectations based on experiments and theoretical knowledge. A more dramatic example is when one takes certain values of κ measured in experiments: if $\kappa < 8 \times 10^{-20}$ J, which is within the range of experiment results collected by Marsh [Mar06], the bilayer elastic ratio becomes positive and the planar bilayer state is no longer stable. However, since we have no guarantee that MARTINI DMPC actually reproduces the experimentally known elastic parameters, it is inconsistent to take a value $2\kappa + \bar{\kappa}$ determined via MARTINI and extract $\bar{\kappa}$ by using the value of κ from experiments.

This strong dependence of the resulting $\bar{\kappa}$ on the input value of κ is somewhat unfortunate, given the fact that we can pinpoint ξ with an excellent accuracy of less than 1% statistical error, while the disagreement on κ is still significant (see the discussion in Section 4.1.2). However, this does not weaken the applicability of the patch-closure method; the accurate result of $2\kappa + \bar{\kappa} = \gamma R/\xi$ as a whole is useful due to its natural appearance as $4\pi(2\kappa + \bar{\kappa})$, which is the Helfrich energy of a complete membrane vesicle. In fact, the combination $2\kappa + \bar{\kappa}$ occurs frequently, so accurately knowing its value is useful.

5.6 Outlook

When all prerequisite parameters are available, the patch-closure method has turned out to be very efficient when applied to CG models even with relatively high resolution, such as the MARTINI model. Each one of these simulations contains approximately 75000 particles, and simulates at about 200 ns per day using a current cluster node with 8 CPUs. Thus, a total of roughly 400 simulations can be finished in a month, given 10 cluster nodes. The total clock time can be further reduced if more computational resources are available, since the process of sampling $P(x)$ can be trivially parallelized. At this cost, it is affordable to explore more complex membrane systems using the versatility of the MARTINI model, such as a whole spectrum of lipids.

A possibility to further improve the patch-closure method is to measure $\bar{\kappa}$ *in equilibrium*, instead of in a *dynamic* process of patch closure. This may reduce the total number of simulations needed, because the sampling of probabilistic processes is eliminated. For this purpose, the thermodynamic integration method, as described in Technical Note 4.1, could be a good candidate to employ. A direct problem to solve, then, is 1) to come up

with the correct reaction coordinate λ to describe the system state, such as the reduced curvature x or the relative shape anisotropy κ_s^2 ; and 2) to include an additional potential energy $U(\lambda)$ into the total Hamiltonian, which confines the system to stay in state λ . For the two intuitive reaction coordinates mentioned, *i.e.* x and κ_s^2 , it is unclear yet how to implement the corresponding $U(\lambda)$. It is important to realize that the biasing potential $U(\lambda)$ really should be a function of the reaction coordinate only, because otherwise its contribution to the free energy of the system cannot be easily disentangled from the free energy of the unconstrained system at the given value of λ .

#	N_{lipid}	R [σ]	$N_x N_s$	b [σ]	w_c [σ]	γ [$k_B T / \sigma$]	ξ	ℓ [σ]	κ [$k_B T$]	$-\bar{\kappa}$ [$k_B T$]	$-\bar{\kappa} / \kappa$
1	900	6.57	8 500	0.95	1.6	3.043 ± 0.060	1.503 ± 0.003	4.371 ± 0.009	12.44 ± 0.26	11.59 ± 0.57	0.93 ± 0.03
2	1000	6.92	8 500	0.95	1.6	3.043 ± 0.060	1.568 ± 0.003	4.413 ± 0.008	12.44 ± 0.26	11.46 ± 0.57	0.92 ± 0.03
3	1100	7.26	11 500	0.95	1.6	3.043 ± 0.060	1.631 ± 0.003	4.451 ± 0.008	12.44 ± 0.26	11.34 ± 0.58	0.91 ± 0.03
4	900	6.38	8 500	0.95	1.7	4.558 ± 0.061	1.439 ± 0.002	4.434 ± 0.006	18.36 ± 0.29	16.51 ± 0.65	0.90 ± 0.02
5	1000	6.72	8 500	0.95	1.7	4.558 ± 0.061	1.477 ± 0.002	4.550 ± 0.006	18.36 ± 0.29	15.97 ± 0.65	0.87 ± 0.02
6	1100	7.05	8 500	0.95	1.7	4.558 ± 0.061	1.534 ± 0.002	4.596 ± 0.006	18.36 ± 0.29	15.77 ± 0.65	0.86 ± 0.02
7	900	6.67	8 250	0.95	1.55	2.478 ± 0.054	1.541 ± 0.004	4.328 ± 0.011	10.10 ± 0.32	9.46 ± 0.68	0.94 ± 0.04
8	720	5.76	8 250	0.92	1.6	3.767 ± 0.054	1.703 ± 0.004	3.382 ± 0.008	11.72 ± 0.23	10.71 ± 0.50	0.91 ± 0.03
9	740	5.90	8 250	0.935	1.6	3.495 ± 0.058	1.559 ± 0.004	3.784 ± 0.010	11.82 ± 0.27	10.42 ± 0.59	0.88 ± 0.03
10	1050	7.16	8 200	0.965	1.6	2.676 ± 0.057	1.469 ± 0.005	4.874 ± 0.017	12.43 ± 0.36	11.81 ± 0.78	0.95 ± 0.04
11	1430	8.44	8 250	0.98	1.6	2.208 ± 0.045	1.529 ± 0.005	5.520 ± 0.018	11.87 ± 0.40	11.54 ± 0.83	0.97 ± 0.04
12	1660	9.23	8 200	1.00	1.6	1.657 ± 0.048	1.407 ± 0.006	6.560 ± 0.028	11.41 ± 0.37	11.95 ± 0.80	1.05 ± 0.04

	N_{lipid}	R [nm]	$N_x N_s$	γ [pN]	ξ	ℓ [nm]	κ [$k_B T$]	$-\bar{\kappa}$ [$k_B T$]	$-\bar{\kappa} / \kappa$
MARTINI	1200	5.33	6 60	40.49 ± 0.34	1.359 ± 0.004	3.92 ± 0.01	40.5 ± 1.2	42.2 ± 0.2	1.04 ± 0.03

- #: system index of the Cooke membranes;
 N_{lipid} : number of lipids;
 R : radius of the vesicle if the patch closes (the error is much less than 1%);
 N_x : number of different x -values investigated for each system;
 N_s : number of folding simulations for each value of x ;
 b : diameter of lipid head bead in the Cooke model;
 w_c : attractive range of the interaction potential in the Cooke model;
 γ : edge tension measured by simulating membrane ribbons;
 ξ : parameter in the energy barrier from Eq. 5.4, determined by fitting the closing up probabilities via Eq. 5.6;
 ℓ : characteristic length defined as $\ell \equiv (2\kappa + \bar{\kappa}) / \gamma = R / \xi$;
 κ : bending modulus, determined through simulating tethers [HD06] for the Cooke membranes, and height undulations [GGL99, BBS⁺11] for the MARTINI system;
 $\bar{\kappa}$: Gaussian curvature modulus, inferred from ξ , κ , γ , and R .

Table 5.1: List of all simulated systems

#	Lipid	$N_{\text{lipid}} \frac{4N_{\text{water}}}{N_{\text{lipid}}}$	T [K]	Σ [$\frac{\text{mN}}{\text{m}}$]	$K_{0\text{m}}$ [nm^{-1}]	$\bar{\kappa}/\kappa$
1	DMPC	128 46	300	0.43 ± 0.09	-0.077 ± 0.001	-0.045 ± 0.004
2	DMPC	256 46	300	0.09 ± 0.08	-0.070 ± 0.001	-0.053 ± 0.003
3	DMPC	512 52	300	-0.17 ± 0.05	-0.067 ± 0.001	-0.061 ± 0.003
4	DMPC	256 79	300	0.02 ± 0.06	-0.063 ± 0.001	-0.074 ± 0.003
5	DPPC	256 42	300	0.08 ± 0.08	-0.141 ± 0.001	0.116 ± 0.004
6	DPPC	256 42	323	0.12 ± 0.08	-0.146 ± 0.001	0.135 ± 0.004
7	DOPC	256 41	300	0.14 ± 0.08	-0.246 ± 0.001	0.481 ± 0.004

N_{lipid} : number of lipids in the bilayer;

N_{water} : number of CG water molecule, which is equivalent to 4 real water molecules;

T : temperature;

Σ : the zeroth moment of the bilayer stress profile, which equals the surface tension;

$K_{0\text{m}}$: lipid spontaneous curvature, calculated using Eq. (5.9b), with $\kappa_{\text{m}} = \kappa/2 = 8.3 \times 10^{-20}$ J from height undulation analysis;

$\bar{\kappa}/\kappa$: bilayer elastic ratio.

All error bars come from MC resampling of the original stress profiles (see Appendix A). Note that: 1) κ is assumed to be same for DMPC, DPPC, and DOPC, 2) MARTINI DPPC membranes remain in the fluid phase at 300 K.[MRM05]

Table 5.2: Elastic parameters of some MARTINI membranes obtained using the stress profile method.

6 Planar tethered bilayer lipid membranes

After developing a generic CG model for the linker/tether molecules (Chapter 2), and learning about the two major components of our membrane-nanoparticle composites, namely the polymers (Chapter 3) and the lipid membranes (Chapter 4 and 5), it is time to combine these aspects. In this chapter, planar tethered bilayer membranes, a model membrane system, will be studied, which serves as an intermediate step towards our tethered nanoparticles in a curved geometry.

6.1 Introduction

Cell membranes are complicated systems consisting of a large number of components, including different types of lipids, membrane proteins, and carbohydrates. As a consequence of this complexity, model membrane systems with much simpler but controlled constituents are developed to study membrane properties, such as lipid vesicles, black lipid membranes, and solid supported/tethered bilayers. Among these, supported bilayer lipid membranes [TM85, Sac96] are model systems where a bilayer membrane *physically adsorbs* to a (normally hydrophilic) solid surface. This stabilizes the membrane and enables a host of surface-sensitive characterization techniques. An important example of this asymmetry between the two leaflets is the fact that, due to the interactions between the proximal leaflet and the substrate, the lipid diffusion in the proximal leaflet of a supported bilayer is severely hindered [PSH⁺06]; also, the study of membrane-protein interactions is compromised, for instance because the limited (less than 10 Å [TM85, KKO⁺96]) layer of water underneath the bilayer prohibits the incorporation of transmembrane proteins having any appreciable portion outside the bilayer on both sides, or because the interaction with the substrate immobilizes the protein [PST91, SGB96].

To alleviate these limitations on the study of membrane-protein interactions, tethered bilayer lipid membranes (tBLM) have been developed [CBMK⁺97, WT00, SK01, NPL⁺02, TS05, MVV⁺07]. In these systems, the bilayer membrane is lifted from the substrate by a layer of polymers, which are chemically linked to some of the lipids in the proximal leaflet on the one end, and covalently grafted to the substrate on the other end. This layer of polymer-lipid conjugates, hereafter referred to as *tethers*, allows a nanometer-thick sub-membrane water reservoir [MVV⁺07]. Consequently, tBLMs can be employed to examine membrane-protein interactions for a much larger class of transmembrane proteins.

While the distal leaflet purely consists of lipid molecules, the proximal leaflet of tBLMs can be composed of different fractions of tether molecules and lipids. The tethers can be diluted by “backfillers”, such as β -mercaptoethanol (β -ME), which take up binding sites on

the substrate that would otherwise be occupied by another tether molecule, thereby leaving space for free lipids to reside in the proximal leaflet. This type of sparsely tethered bilayer lipid membrane (stBLM) significantly increase the volume fraction of the solvent in the sub-membrane region [MVV⁺07], which can be highly desirable when studying membrane proteins.

Tethered bilayer lipid membranes are normally prepared in two steps: First, a self-assembled monolayer (SAM) of tethers, or a tether and backfiller mixture for stBLMs, is prepared on the substrate, utilizing the strong chemisorption between the tethers' end-groups and the substrate; Second, the bilayer is completed by adding lipids. The second step can be realized either by the "rapid solvent exchange" method [CBMK⁺97, MVV⁺07] or by vesicle fusion [BM84, LCC00, RBB06]. In the former process, a SAM is incubated with lipids in some organic solution in which the lipids are soluble, followed by a rapid exchange of the organic phase by aqueous buffer. The lipids then precipitate onto the SAM to form a tBLM. For the latter, giant unilamellar vesicles (GUVs) fuse with the SAM, which is hydrophobically terminated, rupture, and complete the bilayer. The tBLMs formed by rapid solvent exchange typically exhibit a superior electrical resistance [RBMC⁺98, MVV⁺07] and a lower defect density [MVV⁺07], while those prepared by vesicle fusion permit a more precise control of their lipid composition (in the case of mixtures), since they inherit this composition without much change from that of the progenitor GUVs [Goh13].

In this chapter, properties of tBLMs will be studied using our CG model containing Cooke lipids [CKD05, CD05] and the linkers newly parameterized in Chapter 2. The significance of this study is twofold: first, we will test whether our CG model can successfully reproduce the behaviors of this well-studied tethered system; and second, we will examine how various factors affect physical characteristics of *planar* tBLMs, *e.g.* the grafting density, polymer chain length, and bilayer assembly. With a better understanding of our model and tethered membrane systems, we can then proceed to the final chapter towards the polymer-tethered membrane-nanoparticle composites in the relevant but more difficult *spherical* geometry.

6.2 Simulation setup

Similar to the experimental procedure, a monolayer of tethers is first deposited onto a surface within the simulation box. To mimic the randomness in this self-assembly step of the monolayer, the endgroup of each tether is randomly placed on the bottom plane of the box. This is essentially a Poisson distribution, but amended by the additional constraint that a minimum distance of 0.5σ (which equals to the size of a tether bead) is enforced between any pairs. Different from experiments, all tethers are fully extended at the start of each simulation. The lipids are then introduced in two different ways: a simple implicit solvent mimic of rapid solvent exchange, or vesicle fusion.

6.2.1 Rapid solvent exchange

In experiments using the “rapid” solvent exchange protocol to form tBLMs, the replacement of the organic solvent with an aqueous buffer happens on a time scale of several seconds [MVV⁺07, HNV⁺09], which is a really slow process in simulations and is beyond what we can simulate.¹ Hence, a “poor man’s” version of this rapid solvent exchange protocol is employed in simulations. Remember that, in our CG model, solvents are *implicitly* represented, thus they enter the physics of our system only by determining effective interactions between the degrees of freedom that are explicitly represented. So before the simulation begins, lipids are randomly distributed inside the box, which mimics their state in organic solvents (in which they dissolve). When the simulation starts, the lipids begin to attract each other and the lipidic anchor part of the tethers due to the hydrophobic effect, as if the solvent has been replaced by aqueous buffer. Of course, one can emulate the (in fact) *gradual* solvent exchange in multiple steps, in which the strength of the effective attraction among hydrophobic groups is increased incrementally. But in practice, we have not seen any difference in the resulting structure of the tBLMs. Thus, for simplicity, we will turn on the attraction due to solvent in one go. Note that this is not terribly surprising if one only monitors equilibrium properties, which should not depend on the history. But the production of a tBLM via “rapid” solvent exchange is a dynamic process, and it is conceivable that the final state is some kinetically trapped structure. In that case, one needs to change the solvent condition in a more gentle manner.

6.2.2 Vesicle fusion

In the case of vesicle fusion, a unilamellar vesicle is placed on top of the SAM. To make sure the vesicle gets in contact with the SAM without being explicitly placed there, a DPD thermostat is used since it conserves momentum,² and the vesicle is given a “moderate” initial velocity of $v_0 = 0.01 \sigma/\tau$ perpendicularly towards to the SAM, which is approximately 1% of the speed of sound $v_{\text{sound}} \sim \sqrt{k_B T/\mu} \sim 1\sigma/\tau$.³ In terms of the total kinetic energy E_k , a vesicle of 2000 lipids will have $E_k = \frac{1}{2}(3 \times 2000 \mu)(0.01 \sigma/\tau)^2 \simeq 0.3 k_B T$, verifying that the vesicle approaches the SAM with a moderate velocity—in the sense that this extra energy will not be thermodynamically relevant.

¹The time scales in CG simulations have been discussed in Section 2.2.3.

²In the DPD thermostat, the noise force in the equation of motion is added in pairs of the same magnitude but opposite directions, so that at any given integration step, the total momentum is conserved. In contrast, in the Langevin thermostat, the noise terms simply are white noise, hence the particles cannot maintain an inertial drift velocity.

³If the approximate length scale and *dynamic* time scale of this model discussed in Section 2.2 are used, then this velocity can be mapped to $v_0 \approx 0.01 (1 \text{ nm})/(10 \text{ ns}) = 10^{-3} \text{ m/s}$. The difference between the two mappings is a consequence of the dynamical speedup of the CG model, but it does not change the fact that v_0 is moderate.

6.3 Results

After initial configurations are generated, simulations are conducted in the NVT ensemble, at $k_B T/\epsilon = 1.1$. The Langevin thermostat is used for simulations following the mimic of the rapid solvent exchange procedure, while the DPD thermostat is employed in those of vesicle fusion. Two repulsive walls cover the top and bottom of the simulation box to stop particles from moving across the periodic boundaries in the vertical z -direction. In contrast, particles can move freely in the horizontal xy -direction across the boundaries. The size of the box in the horizontal directions is set in such a way that the area of the box is equal to the area of a pure Cooke bilayer membranes if all of the tethers were to be replaced by lipids. The size in the vertical direction is chosen to be large enough to contain all macroscopic structures, such as the polymer brush and the vesicle in the case of vesicle fusion.

6.3.1 tBLM assembly

Rapid solvent exchange

Fig. 6.1 shows a sequence of snapshots from an example rapid solvent exchange simulation, which contains 300 tethers of 12 subunits and 700 lipids. These lipids are randomly placed in the box before the simulation starts (Fig. 6.1 A), after which they aggregate into small pieces of bilayers (Fig. 6.1 B). Some of these patches form with the anchor of the tethers, others, which contain only lipids in the bulk, gradually merge with the tethers (Fig. 6.1 C). Eventually, the tBLM is completed (Fig. 6.1 D).

Vesicle fusion

The vesicle fusion process is also simulated, as shown in Fig. 6.2. A lipid vesicle containing 1792 lipids is placed above a SAM made of 768 tethers (and also 12 subunits, as in the case of rapid solvent exchange) (Fig. 6.2 A). Since the vesicle is given an initial velocity of $v_0 = 0.01 \sigma/\tau$, it approaches the SAM and induces (hemi)fusion: The outer leaflet of the vesicle ruptures at the boundary of the contact area with the SAM, part of its lipids merge with the SAM as the proximal leaflet, while the rest slide on top of the SAM and form the distal leaflet (Fig. 6.2 B). Then a pore forms in the vesicle bilayer near the contact site, and the rest of the vesicle becomes a bilayer patch attached to the tBLM (Fig. 6.2 C). This dangling piece merges into the tBLM at the end (Fig. 6.2 D).

This process of vesicle fusion shows a number of similarities with the one described in the experimental study by Goh *et al.*, which studied the hemifusion process of vesicles adsorbing onto SAMs by observing fluorescently labeled GUVs in video microscopy [ZTD⁺12]. In their experiments, these authors covered the hydrophilic glass substrate with a monolayer of octadecyltri chlorosilane to form a hydrophobic monolayer, which induces the hemifusion with the lipid vesicle. They also see a spread of the outer leaflet upon fusion, which increases the stress in the vesicle bilayer and leads to membrane rupture near the

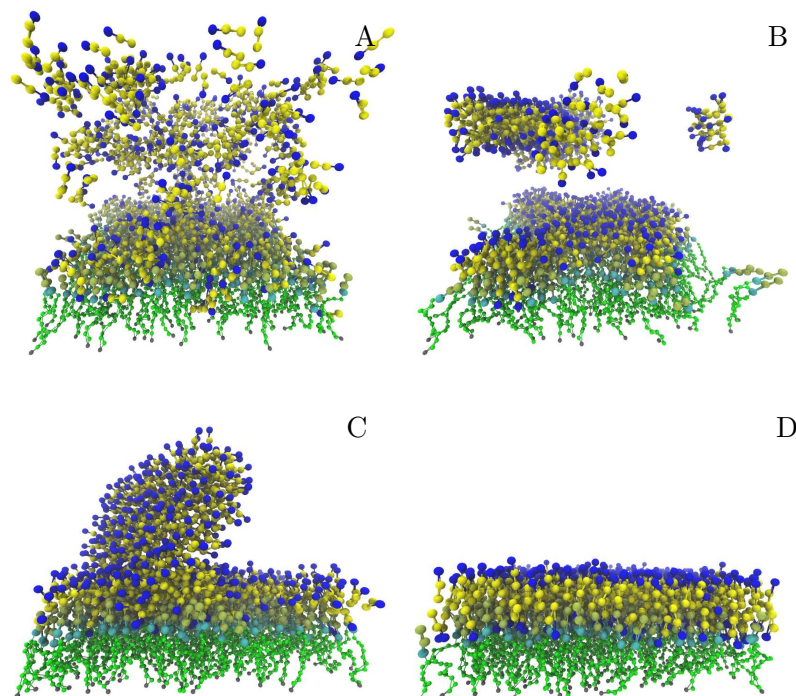


Figure 6.1: Snapshots of a tBLM, which consists of 300 tethers of 12 subunits and 700 lipids, formed using the rapid solvent exchange protocol. A, initially the lipids are randomly distributed in the box. B, when the simulation starts, the lipids begin to aggregate into patches in the bulk or on the SAM. C, the patch in the bulk “fuses” with the SAM, and D, completes the tBLM.

contact site, accompanied by the ejection of vesicle contents and fusion of the lipids from both leaflets.

Despite the great similarity, a few differences do exist. The first important one is that their SAM is much larger than the surface area that the lipids in the vesicle are able to cover; while in our case, the size of the box is set up to accommodate all lipids without any excess area. Thus, we did not see any depleted region (beyond the vesicle patch or at the center of the fusion site). The second difference is related to the fact that there is no solvent present in our CG model. As a consequence, the membrane vesicle is not subjected to a volume constraint due to the enclosed solvent, which in the experimental situation creates additional lateral stress in the lipid bilayer due to the Young-Laplace relation between pressure and tension, and thereby presumably also affects the manner and timing of when the rupture will happen. Nevertheless, since ultimately our goal is not studying vesicle fusion at a quantitative level, or in fact elucidating the formation dynamics of a tBLM, we did not devote more time to investigations of this protocol of preparing a tBLM.

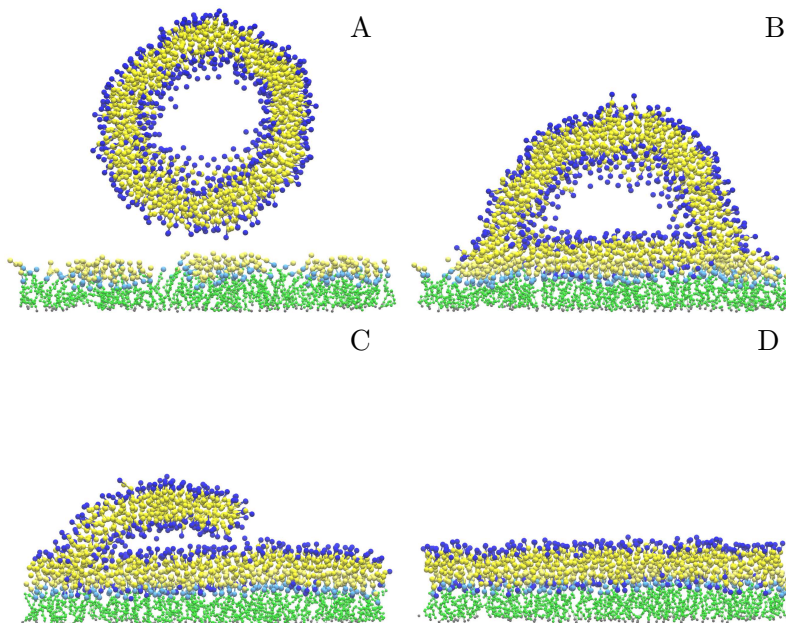


Figure 6.2: Snapshots of a tBLM formed by vesicle fusion, which consists of 768 tethers of 12 subunits and 1792 lipids. Only a thin slice of the system is shown for clarity. A, initially the lipid vesicle hovers above the SAM. B, The outer leaflet of the vesicle ruptures at the peripheral, spreads, and starts to merge with the SAM. C, both leaflets of the vesicle ruptures. D, tBLM has formed. [I'm still experimenting with the colors...]

6.3.2 tBLM height

After the brief study of the assembly of tBLMs, let us now examine their properties. The first important quantity is the height $H(\phi)$ of the tethered bilayer as a function of the mole fraction of the tethers, $\phi \equiv N_{\text{tether}}/N_{\text{total}}$, where N_{tether} and N_{total} are the number of tethers and the total number of lipids and tethers, respectively. The higher ϕ is, the more crowded the submembrane region is, and the tether chains would become more stretched. This is very similar to the brush height of a planar polymer brush, as analyzed in Section 3.4.2. The slight difference is that, unlike in a regular brush, the chain ends here in the tethered bilayer need to stay within the membrane. But, fortunately, this is very close to the assumption made by the blobology analysis, in which the chain ends locate within the last blobs away from the substrate. Thus, we will test whether the blobology prediction about the brush height, namely Eq. (3.4.2), can correctly describe the tether height $H(\phi)$ measured in our simulations.

For a brush of $f = N_{\text{tether}}$ chains in a box of size $L_x = L_y = L$, the average distance

D between two grafting sites is given by

$$D(\phi) = \sqrt{\frac{L_x L_y}{f(\phi)}} = \frac{L}{\sqrt{\phi N_{\text{total}}}}. \quad (6.1)$$

Then the brush height in Eq. (3.30) becomes

$$\begin{aligned} H(\phi) &= \frac{b}{a} N_b a^{1/\nu} [D(\phi)]^{1-1/\nu} \\ &= \frac{b}{a} N_b L \left(\frac{a}{L}\right)^{1/\nu} (\phi N_{\text{total}})^{(1/\nu-1)/2}, \text{ for } D(\phi) < R_F = a N_a^\nu, \end{aligned} \quad (6.2)$$

where N_a is the number of Kuhn segments, N_b is the number of monomers per chain, a is the Kuhn length, $b \simeq 0.5\sigma$ is the monomer size, and a general Flory exponent ν is used instead of the specific value $\nu = 3/5$, the approximate value for real chains discussed in Chapter 3. The condition in Eq. (6.2) arises because this prediction only works when the tethers are in the brush regime.

In a set of simulations of tethered bilayers (formed by “rapid solvent exchange”), a total of $N_{\text{total}} = 360$ molecules are included into a box of size $(15, 15, 60)\sigma$. The mole fraction ϕ of the tether is varied from 0.05 to 0.40. Each tether contains $N_b = 100$ monomers of size $b \simeq 0.5\sigma$. The Kuhn length $a \simeq 0.76\sigma$, giving a Flory radius of $R_F = a N_a^\nu = a N_b^\nu (b/a)^\nu \simeq 9.37\sigma$ if $\nu \simeq 0.6$. For the most sparsely tethered bilayer, *i.e.* when $\phi = 0.05$, Eq. (6.1) shows that the distance D between two chains is $D(\phi = 0.05) = L/\sqrt{\phi N_{\text{total}}} \simeq 3.53\sigma < R_F$. Thus, this tethered bilayer is always in the brush regime, and its height $H(\phi)$ can be compared to the theoretical prediction Eq. (6.2).

The simulation results for the height of the tethered bilayers, as measured by the vertical positions of the end bead of the spacer part, are shown in Fig. 6.3. A fit using Eq. (6.2) with a and ν as fitting parameters yields $\nu = 0.5809 \pm 0.0005$ and $a/\sigma = 0.515 \pm 0.001$ (error derived from Monte Carlo resampling, as described in Appendix A.3). The former is very close to the approximated Flory exponent of $\nu = 0.6$ that is commonly used, and even closer to the exponent $\nu = 0.588 \pm 0.001$ calculated using field theory and renormalization group [LGZJ77].⁴ Although the Kuhn length a is different from the parameterized value of $a \simeq 0.76\sigma$, it is on the same order of magnitude. Remember that the scaling theory is relatively accurate only in the prediction of the scaling exponents; any factors of order unity are ignored.

Thus, our simulation data confirm that the blobology calculation leading to Eqs. (3.4.2) and (6.2) can be utilized to semi-quantitatively predict the brush height of planar tethered bilayer membranes.

⁴The statistical error on our result is very small. However, the systematic errors are not yet included: only a finite-size system is measured, while the field theory result is for systems in the thermodynamic limits. Thus, this somewhat disconcertingly good value for the random walk scaling exponent is therefore most likely fortuitous.

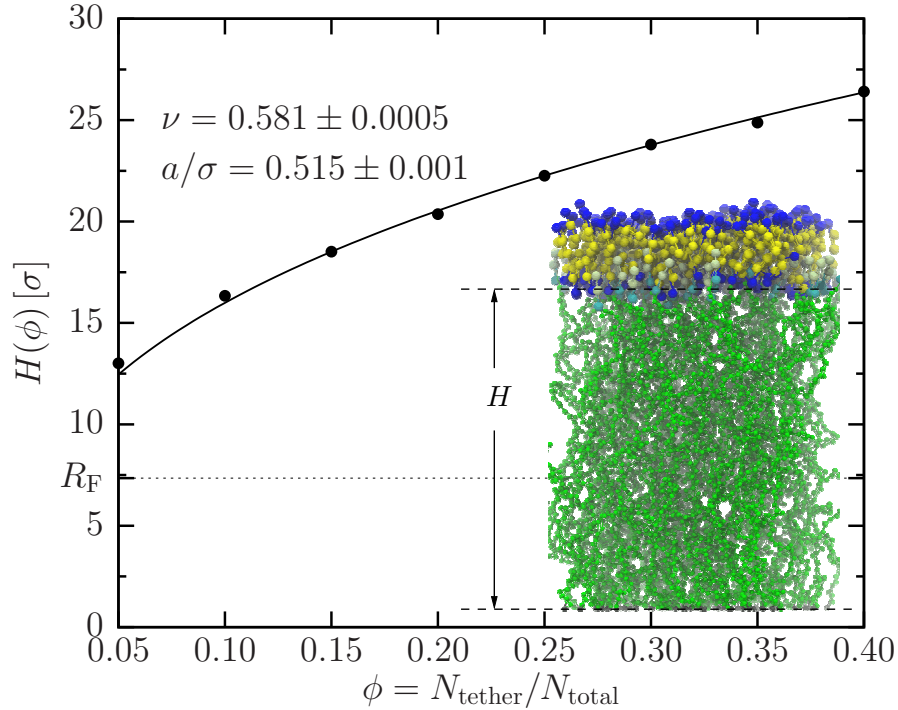


Figure 6.3: The height of the tethered bilayer, $H(\phi)$, as a function of the mole fraction ϕ of the tethers. Each system, which contains a total of $N_{\text{total}} = 360$ lipids and tethers in a box of $(15, 15, 60) \sigma$, is formed using rapid solvent exchange. Simulation data are shown as solid circles, with blocked errors smaller than the size of the symbol. The solid curve is a fit to the data using Eq. (6.2), giving a Flory exponent of $\nu = 0.5809 \pm 0.0005$ and Kuhn length $a/\sigma = 0.515 \pm 0.001$.

6.3.3 Diffusion constants

The coexistence of the tethers and the bilayer also affects the behavior of the bilayer. As mentioned in the introduction, one of the key improvements of the tBLM, especially the stBLM, over supported bilayers is the mobility of the lipids in the proximal leaflet due to the much weakened interaction between this leaflet and the substrate. Thus, it is meaningful to examine the fluidity of the tBLMs.

In a set of simulations containing $N_{\text{total}} = 1000$ molecules in a box of $(25, 25, 25) \sigma$, the mean-squared displacement $\langle d^2 \rangle$ of the lipids within the two leaflets is measured separately every time interval of $\delta t = 5 \tau \simeq 50$ ns, and the mole fraction ϕ of the 12-mer tethers is varied between 2.5% and 50%. After confirming the system is in the normal diffusion regime, the diffusion constant D is calculated as

$$D = \frac{\langle d^2 \rangle}{4\delta t}. \quad (6.3)$$

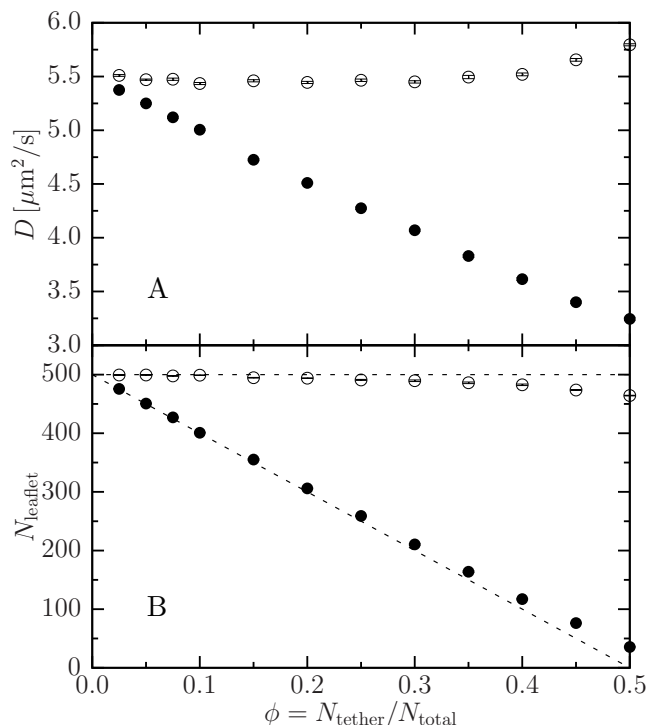


Figure 6.4: A, diffusion constants of lipids, D , in the proximal (solid) and distal (open) leaflet. Units are mapped using $1\sigma = 1\text{ nm}$ and $1\tau = 10\text{ ns}$. B, the number of lipids N_{tether} in the proximal (solid) and distal (open) leaflet. The two dashed lines are guide lines of $N_{\text{tether}} = 500$ and $N_{\text{tether}} = 500 - 1000\phi$, the latter shows the number of lipids in the proximal leaflet if the total number of molecules in both leaflets is the same.

The measured lipid diffusion constant D is plotted in Fig. 6.4 A. On the one hand, for the lipids in the proximal leaflet (solid circles), D decreases linearly as the mole fraction ϕ of the tethers increases, showing how the presence of less mobile tethers can slow down the lipids around them. Compared to free lipids in the distal leaflet, a decrease of approximately 40% in the diffusion constant is found. On the other hand, the lipid diffusion constant in the distal leaflet stays almost constant, except a slight increase when $\phi \rightarrow 1/2$, *i.e.* when the proximal leaflet is almost exclusively occupied by tethers. This small increase in D is likely due to a decrease in the number of lipids in the distal leaflet, as shown in Fig. 6.4 B. When N_{tethers} increases as $\phi \rightarrow 1/2$, it is entropically favorable for some the lipids in the distal leaflet to flip-flop into the proximal one, since the tether anchors are less mobile and thus effectively the “free area” in the proximal leaflet for lipids to diffuse is larger. As a result, the total number of molecules in the proximal leaflet will exceed the number in the distal one. The lipids in the distal leaflet then enjoy a larger area per lipid, and hence diffuse faster.

We should mention that the phenomenon of decreasing fluidity of lipids in the proximal leaflet due to an increase in the tether number is also observed in experiments using fluorescence correlation spectroscopy. Shenoy *et al.* [SMF⁺10] separately measured the diffusion constant of lipids in the two leaflets and found a decrease in the diffusivity in the proximal leaflet as the tether density increases. However, these authors found that the effect is more pronounced than what our simulations show: At a tether density of tether: β -ME=30:70, which is much smaller than the the largest fraction in our simulation, the diffusion constant of lipids in the proximal leaflet decreased by approximately 70%. In their study, the diffusion constant of lipids in the distal leaflet is measured using a densely tethered bilayer with barely any lipids in the proximal leaflet, so that the major part of the fluorescent signal comes from the distal leaflet; the diffusivity in the proximal layer is determined by quenching the distal leaflet by adding potassium iodide to the bulk solution. Our results are qualitatively in line with the experiment measurements of Shenoy *et al.* in that an increasing amount of tethers does slow down the lipids in the proximal leaflet. However, because of the loss of atomistic degrees of freedom during the coarse-graining process, there is no reason to expect such a generic model to quantitatively reproduce changes in dynamic properties.

6.3.4 Destabilization by long linker chains

One additional type of tether-membrane interaction studied using our CG model is the destabilization of a membrane caused by long tether chains. This effect could potentially lead to complications when one considers creating polymer-tethered membrane-nanoparticle composites by first mixing lipids with tethers to form membranes with anchored tethers, and then let the tethers grab onto nanoparticles and wrap the membrane around it. Before one starts such a setup, it is necessary to figure out whether the membrane with anchored tethers is actually stable.

For this purpose, tether anchors are implanted into a pre-assembled lipid bilayer on both sides. The simulation box is allowed to adjust in the horizontal directions where the membrane spans the box, in such a way that the bilayer is under zero lateral tension. Tethers with three different degrees of polymerization, N_b , are simulated, where $N_b = 30, 40,$ and 60 . For each chain length N_b , the mole fraction ϕ of the tethers is scanned. The final state of the polymer-anchored membranes in each simulation is plotted in Fig. 6.5.

As can be seen, given a chain length N_b , the bilayer will disintegrate as the fraction ϕ of the tethers increases beyond a critical limit. Longer chains lead to a smaller critical limit, which means they are more effective in destroying the bilayer. The resulting structure is similar to connected worm-like micelles, which is shown in the inset of Fig. 6.5. Our observation is qualitatively in agreement with a simulation study done by Liu and Faller using the MARTINI model for lipids and tether-lipids [LF12]. They have found pores in the membrane when the tether length and density is sufficiently high.

Thus, our simulations indicate that there exists a critical chain length and tether fraction for free-standing membranes with anchored tethers, beyond which the tethers

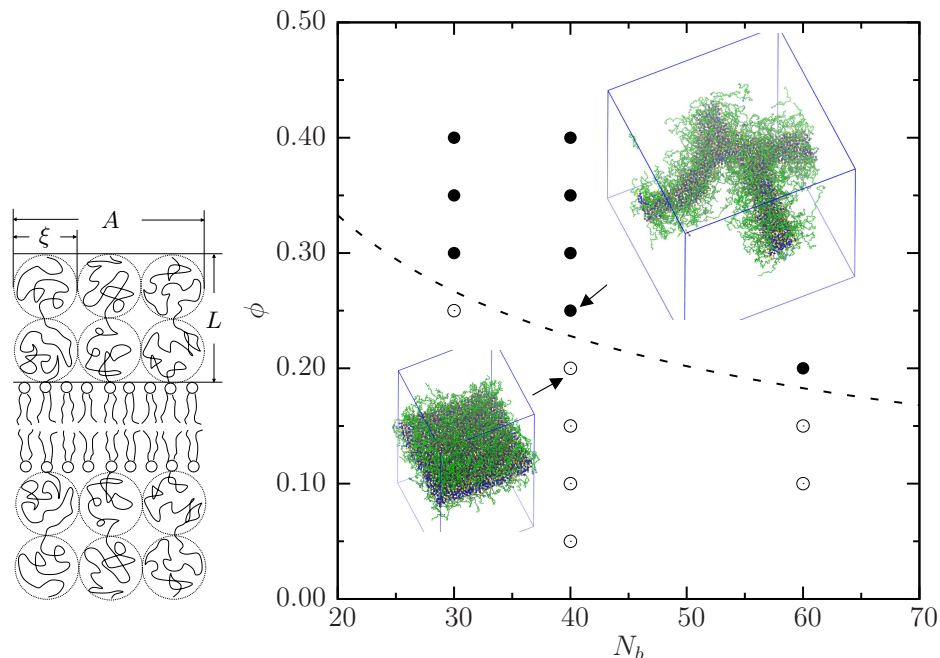


Figure 6.5: Destabilization of membranes due to anchored tethers when the degree of polymerization N_b and the mole fraction $\phi = N_{\text{tether}}/N_{\text{total}}$ of the tethers are changed. Open circles denote the bilayer is stable throughout simulations, while closed circles mean that the membrane is ruptured by the tethers. The stability boundary (dashed curve) is predicted using Eq. (6.10) with a manually chosen $\alpha = 1.1$ to fit the data. Snapshots of the final state of two systems, namely $N_b = 40, \phi = 0.20$ (stable) and $N_b = 40, \phi = 0.25$ (ruptured), are shown as examples. A schematic side view of the system setup is also shown on the left, with A being the total area of the bilayer, ξ the blob size, and L the brush height.

will tear the bilayer apart and form worm-like micelles. This destabilization of polymer-decorated bilayer is probably driven by the entropy of the free tether chains: The presence of the membrane limits the free volume which an anchored tether chain can occupy and form random structures. Hence, the longer the chains are, the more entropy they gain by changing the planar bilayer into a cylindrical “worm”, since the chain enjoys more space at the open edges of a membrane or in a worm-like micelle. The driving force towards higher entropy exerts physical stress on the membrane within which the chains are anchored, and this eventually ruptures the bilayer.

This destabilization can be semi-quantitatively understood using the scaling concepts described in Section 3.3.1. A schematic picture of the system is shown as the inset in Fig. 6.5. Assume a complete planar bilayer covers a surface area of A , and a fraction ϕ of the N_ℓ lipids are conjugated to polymer chains of degree of polymerization N_b , which form two planar polymer brushes of height L on both sides of the bilayer. Denoting the total number of polymer chains as f , the distance D between two neighboring chains, and the

blob size ξ , are then $D = \xi = \sqrt{2A/f}$. In this geometry, the number of Kuhn segments within a blob is $g = (\xi/a)^{1/\nu}$, where a is the Kuhn length, and ν is the Flory exponent. Hence, the total free energy of the brush, E_{brush} , can be estimated as the total number of blobs, $N_a f/g$, times the free energy per blob, $k_B T$, up to a constant α of order unity [dG79]:

$$\begin{aligned} \frac{E_{\text{brush}}(A)}{k_B T} &= \alpha f \frac{N_a}{g} = \alpha N_a f \left(\frac{a}{\xi}\right)^{1/\nu} = \alpha N_a f a^{1/\nu} \left(\sqrt{\frac{f}{2A}}\right)^{1/\nu} \\ &= \alpha \frac{f^{1+1/2\nu}}{2^{1/2\nu}} N_a a^{1/\nu} A^{-1/2\nu}. \end{aligned} \quad (6.4)$$

Since increasing the surface area A reduces E_{brush} , the polymer chains tend to expand the membrane into which they anchor.

However, it costs energy to stretch a membrane: To quadratic order in strain $s \equiv (A - A_0)/A_0$, where A_0 is the area under zero tension, the free energy cost to stretch the membrane, E_{stretch} , is given by

$$E_{\text{stretch}} = \frac{1}{2} K_A \frac{(A - A_0)^2}{A_0}, \quad (6.5)$$

where K_A is the area-stretching modulus, which is roughly $19\epsilon/\sigma^2$ for the Cooke membrane at standard parameters [Des09]. Thus, a free bilayer will prefer the tensionless area A_0 to minimize the stretching free energy E_{stretch} , while the polymers would like to increase the surface area to reduce their free energy due to the crowding. The equilibrium area A^* is then determined by the balance of these two contributions as

$$0 \stackrel{!}{=} \left. \frac{\partial E_{\text{brush}} + E_{\text{stretch}}}{\partial A} \right|_{A^*} = \alpha \frac{k_B T}{2^{1/2\nu}} \left(\frac{f}{A^*}\right)^{1+1/2\nu} N_a a^{1/\nu} \left(-\frac{1}{2\nu}\right) + K_A \frac{A^* - A_0}{A_0}. \quad (6.6)$$

This equation can be simplified as

$$\alpha N_a a^{1/\nu} \frac{k_B T}{\nu} \left(\frac{f}{2A_0(1+s^*)}\right)^{1+1/2\nu} = K_A s^*. \quad (6.7)$$

However, the membrane cannot be stretched beyond a critical strain $s_c = (A_c - A_0)/A_0$ before it ruptures. For the Cooke membrane previous work has found $s_c \approx 9\%$ [CD05, Des09]. When the equilibrium strain s^* obtained from Eq. (6.7) exceeds this critical strain s_c , the membrane ruptures, which gives the following condition for the stability limit:

$$\alpha N_a a^{1/\nu} \frac{k_B T}{\nu} \Sigma_0^{1+1/2\nu} = K_A s_c (1 + s_c)^{1+1/2\nu} \stackrel{s_c \ll 1}{\simeq} K_A s_c, \quad (6.8)$$

where $\Sigma_0 = f/2A_0$ is the grafting density before the membrane expands (the factor of 2 originates from the fact that there are two brushes on both sides of the membrane). The mole fraction of the tethers ϕ is related to Σ_0 as

$$\phi = \frac{f}{f + N_\ell} \approx \frac{f}{2A_0/a\ell_0} = \Sigma_0 a\ell_0 \quad (6.9)$$

where $a_{\ell 0}$ is the area per lipid in the unstressed bilayer. Plugging Eq. (6.9) into Eq. (6.8), one derives the relation between the mole fraction ϕ of the tethers and the degree of polymerization $N_b = aN_a/b$ at the stability boundary as

$$\phi = \left[\frac{\nu s_c}{\alpha} \frac{a}{b} \left(\frac{\sqrt{a_{\ell 0}}}{a} \right)^{1/\nu} \frac{a_{\ell 0} K_A}{k_B T} \frac{1}{N_b} \right]^{\frac{1}{1+1/2\nu}}. \quad (6.10)$$

This predicted stability boundary is plotted in Fig. 6.5, with $\nu = 3/5$, and a handpicked $\alpha = 1.1$ to fit the data. This value of α confirms the assumption in Eq. (6.4) that α is indeed of order unity.

Therefore, if trying to assemble the proposed polymer-tethered membrane-nanoparticle composites by letting membranes with anchored tethers wrap around the NP cores, one has to keep in mind that tether chains that are too long or too dense can destabilize the bilayer. The stability boundary can be predicted using Eq. (6.10), up to a factor of order unity.

6.4 Discussion

In this chapter, we have shown that the CG model we parameterized in Chapter 2 is able to qualitatively reproduce many important behaviors of a model membrane system, namely the tethered bilayer lipid membranes. These behaviors are closely relevant to our study of the polymer-tethered membrane-NP complexes. In our model, lipids can self-assemble on a self-aggregated monolayer *via* the rapid solvent exchange or the vesicle fusion procedures. Moreover, the polymer theories derived in Chapter 3 are found to semi-quantitatively, or even quantitatively, predict properties of the tethers, such as the brush height and their ability to destabilize the membrane in which they anchor. With the proven ability of our model to represent a relatively well-understood model tethered system, and the verified applicability of the relevant polymer theories, the newly-proposed nanocomposites can be studied in the next chapter.

7 Polymer-tethered membrane-nanoparticle composites

In the previous chapter, planar tethered bilayers have been investigated using the generic CG model parameterized in Chapter 2 and the scaling concepts discussed in Chapter 3. As demonstrated, our CG model captures many important aspects of polymer-tethered membrane systems, and the theory of “blobology” is able to semi-quantitatively describe the behavior of the polymer brush in such systems. Equipped with these powerful tools, we can finally move on to study the polymer-tethered membrane-nanoparticle composites which we have been expecting to enter the stage ever since they have been promised in Chapter 1. Their spherical geometry around the NP core naturally raises additional complications compared to planar tBLMs. Our goal is, as explained in the first chapter, to address many generic problems in such a design from a theoretical and simulational perspective without getting involved in discussions about specific chemical implementations. By considering theoretical constraints from geometry and material properties, the enormously large parameter space can be effectively reduced to a physically plausible subspace of much smaller volume. It is the hope of this author that the guiding principles developed in this thesis will help to both shorten the time and reduce economic costs for any endeavors to assemble such NPs in the lab with one’s preferred specific realizations.

7.1 Generic constraints

Fundamental physical principles limit the combination of design parameters from which one can choose, regardless of the chemical specificity of the components in the systems. Such constraints include the maximum number of tethers allowed on the surface of the solid core, and optionally the minimum number of them if one plans to wrap an assembled membrane around the NP core with grafted tethers.

Maximum grafting density

One “hard” limitation is the maximum grafting density, Σ_{\max} , on the surface of the solid core, which is mainly dictated by the surface area, a_{linker} , of the endgroups of the linkers when chemically adsorbed to the surface. Ignoring all the interactions among the linkers *except* for the excluded volume effect, the grafting density Σ is bounded from above by Σ_{\max} as

$$\Sigma \leq \Sigma_{\max} = 1/a_{\text{linker}} . \quad (7.1)$$

We assume the Σ can be tuned *down* from this maximum value by placing “backfillers” on the core surface, as seen in the case of planar tethered bilayer membranes [RBMC⁺98, MVV⁺07, HNV⁺09]. Thus, given a solid core of a fixed radius R_{core} , the maximum amount of linkers in the structure is then $4\pi R_{\text{core}}^2 \Sigma_{\text{max}}$.

Minimum grafting density (optional)

Depending on the assembly process, additional requirements on the minimum grafting density may arise. During assembly, if one needs to wrap the membrane around the solid core and linkers, the free energy gain from inserting anchors into the inner leaflet must compensate the energy cost of bending the membrane [Hel73, Hel74]. If ϵ_{ins} is the free energy gained by inserting a single lipid anchor into the membrane, then the total free energy of insertion is given by $E_{\text{ins}} = \epsilon_{\text{ins}} 4\pi R_{\text{core}}^2 \Sigma$, while the total bending energy is of course $E_{\text{bend}} = 4\pi(2\kappa + \bar{\kappa})$, assuming that the final membrane is spherical. Requiring that insertion must pay for bending leads to the inequality

$$\Sigma \geq \Sigma_{\text{min}}^{(1)} = \frac{2\kappa + \bar{\kappa}}{\epsilon_{\text{ins}}} \frac{1}{R_{\text{core}}^2}. \quad (7.2)$$

When the membrane is stiff, or when the solid core is small, or the free energy of insertion per anchor is small, a larger grafting density is required to curve the membrane.

A second lower bound on the grafting density stems from the experience gained over many years from working with planar tethered bilayer membranes. In order to keep a planar tBLM nicely tethered to the substrate, the anchor:lipid ratio should stay roughly above $1 : n \approx 1 : 10$ [MVV⁺07]. In the spherical case, even though it is unlikely for the anchors to detach from a vesicle formed around them, it may still require a minimum anchoring density during the wrapping process. Because of the spherical geometry, this constraint on the anchoring density at the *membrane vesicle* is translated in terms of the grafting density on the *core surface* as

$$\Sigma \geq \Sigma_{\text{min}}^{(2)} = \frac{1}{na_{\ell}} \left(\frac{R_{\text{ves}}}{R_{\text{core}}} \right)^2, \quad (7.3)$$

where $n \approx 10$, a_{ℓ} is the area per lipid, and R_{ves} is the radius of the membrane vesicle.

To stay on the safe side, one may take the larger value from Eqs. 7.2 and 7.3 as the lower bound for the grafting density: $\Sigma \geq \Sigma_{\text{min}} = \max\{\Sigma_{\text{min}}^{(1)}, \Sigma_{\text{min}}^{(2)}\}$. Note that 1) both constraints are optional if wrapping is not part of the assembly process, and 2) these two conditions become the same when the total insertion free energy E_{ins} is equal to the bending energy E_{bend} of the vesicle.

7.2 Optimal combination of the parameters

So far, the important interplay between these linkers and the enclosing membrane vesicle has not been discussed, which introduces additional requirements on the parameter set of the system.

Recall that the simple theoretical model for spherical polymer brushes developed in Chapter 3, which is based on scaling concepts and single-chain theories, could quantitatively predict the full force-extension relation of the brush. Although the crossover regime between the strong compression and the strong stretching regime is not very accurately described (due to some of the simplifying assumptions made in the model), it provides a straightforward estimate of the relaxed position of the chains given other material parameters.

This ability to predict the response of the polymer brush to the stresses resulting from its confinement between the membrane vesicle and the solid core is of great importance, since it is reasonable to assume that this brush behavior will determine the possible range of the NP size, which in turn affects the uptake of the nanocarriers in many different ways (see the discussion in Section 1.1.3). On the one hand, if the vesicle size is too small, then the polymer chains are strongly compressed, and pores might form in the membrane because the osmotic pressure created by the chains will induce a large Young-Laplace tension in the lipid bilayer. Once this tension exceeds the rupture tension (or comes close), the stability of the vesicle is at risk. If, on the other hand, the vesicle is too large, then the linkers are strongly stretched, the energy in the chains increases, the vesicle may be deformed, and eventually some anchors will be pulled out from the bilayer. Therefore, if the NPs are allowed to choose their preferred structures during the assembly process, then they should arrive at a radius at which the polymer linkers are neither compressed nor stretched. Note that, in reality, this simple reasoning would not hold if kinetic issues prevent the system from reaching thermodynamic equilibrium. These two limits of the NP size will now be examined.

For convenience, when discussing the polymer chains, the *interface radius*, which quantifies the average radial position of the polymer-membrane interface between the last polymer bead and the head bead of the anchor, will be denoted as r . The volume between the radius of the solid core, R_{core} , and this interface radius r will be the space which the polymer chains can occupy. The value of r is related to the vesicle radius R_{ves} (the radius of the bilayer midplane) through the *bilayer* thickness d as

$$R_{\text{ves}} = r + \frac{d}{2}. \quad (7.4)$$

We need to distinguish R_{ves} and r because the *monolayer* thickness $d/2$ is not necessarily very small compared to the chain extension $r - R_{\text{core}}$ (which is also the separation between the inner leaflet and the core surface). In simulations, the values for R_{ves} , d , and r can be very easily determined from the radial distribution profiles of the membrane beads.

Minimum vesicle size

The polymer chains between the solid core and the lipid vesicle serves as a cushion when the vesicle is compressed, which poses a lower bound on the radius of the vesicle, $R_{\text{ves, min}} = r_{\text{min}} + d/2$.

The osmotic pressure Π from the polymer brush will induce a surface tension σ in the lipid membrane according to the Young-Laplace relation $\sigma(r) = \Pi(r)r/2$. When the interface radius r decreases below r_{\min} , the induced surface tension σ will exceed the rupture tension σ_{rup} of the membrane, which will lead to pore formation and potentially the loss of drug payload.¹

This osmotic pressure Π can be semi-quantitatively predicted using the scaling theory described in Section 3.5.3. Adapting Eq. (3.42) with the current notations, Π is given by

$$\Pi(r) \approx \frac{k_{\text{B}}T}{\xi_0^3} \left(\frac{\Phi(r)}{\Phi_0} \right)^{9/4} = \frac{k_{\text{B}}T}{\xi_0^3} \left(\frac{r_0^3 - R_{\text{core}}^3}{r^3 - R_{\text{core}}^3} \right)^{9/4}, \quad \text{for } r < r_0. \quad (7.5)$$

Here, Φ is the monomer volume fraction, and $k_{\text{B}}T$ is the thermal energy. The subscript 0 denotes the *relaxed* reference state: r_0 is the radius of the polymer-membrane interface at which the linkers are relaxed, and $\xi_0 = (r_0/R_{\text{core}})/\sqrt{\Sigma}$ is the average distance between two chains at the surface of $r = r_0$. When the vesicle size R_{ves} is reduced, the concentration Φ increases, and the pressure Π increases with a larger exponent. Thus, as R_{ves} decreases, the stress σ in the membrane increases, until the membrane rupture tension is reached; the lower bound on the vesicle size, $R_{\text{ves, min}}$, is given by the solution of the following equation:

$$\sigma(r_{\min}) = \Pi(r_{\min})r_{\min}/2 = \sigma_{\text{rup}}. \quad (7.6)$$

For an example system described later, we will show this minimum vesicle radius as a dotted vertical line in Fig. 7.1.

Maximum vesicle size

There also exists an upper bound on the vesicle size, $R_{\text{ves, max}} = r_{\text{max}} + d/2$. The linker chains are subject to a tensile stress when they are stretched by an increased vesicle size R_{ves} beyond their relaxed length, before reaching a point when the hydrophobic anchors are pulled out from the membrane. Since this happens when the chains are in the large extension regime, their force-extension relation can be approximated by the single-chain theories discussed in Section 3.2 (assuming the persistence length ℓ_{p} and the degree of polymerization N of the polymers are known). For each chain, the excess energy due to pulling, \mathcal{E} , can be calculated by integrating the force-extension relation. When \mathcal{E} accumulates beyond the (free) energy of insertion ϵ_{ins} of an anchor into the membrane, some chains will be pulled out. For a regular fluid membrane, the maximum vesicle size $R_{\text{ves, max}}$ is then determined by the solution of the following equation:

$$\mathcal{E}(r_{\text{max}}) = \epsilon_{\text{ins}} \simeq 10 \dots 20 k_{\text{B}}T. \quad (7.7)$$

Again, this maximum vesicle radius will be shown as a dotted vertical line in Fig. 7.1 for illustration.

¹In real life, $\sigma_{\text{rup}} = \text{a few } \frac{\text{mN}}{\text{m}}$.

A comprehensive view

As argued above, the various parameters in the design of this polymer-tethered membrane-nanoparticle composite are entangled due to the theoretical constraints derived above. Thus, depending on which parameter is the limiting factor, or which parameter needs to be optimized, one may have to adjust the other parameters accordingly. For instance, if there is no backfiller available to dilute the tethers on the core surface, then the grafting density is presumably close to Σ_{\max} . If now the size of the final nanocomposites needs to be within a certain range (*e.g.* in order to pass through the leaky blood vessels in the tumor issue), then, with one fewer “knob” of Σ to tune, one can only try to pick an appropriate combination of the core size R_{core} and the chain length N of the linkers. Or if, in some other cases, one hopes the nanocomposites could be more resilient to deformation due to external pressures, meaning the particles can recover from larger deformation without their membranes being ruptured, then one should lower the grafting density or pick softer polymer linkers to lower the induced osmotic pressure by compression (see Section 3.5.3).

7.3 Simulation setup

In order to support our theoretical considerations elaborated in the previous sections, several sets of MD simulations are conducted, using our generic lipid and tether model. Although these simulations differ in many aspects of their setup, depending on which purpose they serve, they still share several common aspects that will be outlined in this section.

The first common aspect concerns the interactions between the different particles in the system. For simplicity, the lipidic anchors of the linkers share their parameters with the Cooke lipids. With the conventional temperature $k_{\text{B}}T/\epsilon = 1.1$ for the Cooke model, the attraction range w_c in the cosine-square potential between any two hydrophobic particles, irrespective of whether they are lipid tails or anchors, is slightly changed to $w_c = 1.72\sigma$, so that the aspect ratio of the lipids and anchors can closely match the ratio of real DOPC. If this aspect ratio of DOPC lipids is used as the reference for the mapping of length scales, then $1\text{ nm} \simeq 1.236\sigma$. The mapped real units will be used for a more intuitive picture of the systems. The details of how to tune the aspect ratio of the lipids in our model have been discussed in Section 2.2.1.

The second common aspect in all systems involves how the solid core is realized. Because the size of the core (several to a few tens of nanometers in diameter) is normally an order of magnitude larger than the size of a linker bead (roughly half a nanometer), it is (for purely technical reasons) computationally more expensive to represent the NP core with a real bead.² Instead, the core is implemented as a **constraint** in simulations, which

²The reason is that — at least within the earlier version of ESPResSo used for this study — the largest interaction range sets the interaction cutoff for *all* pair forces, and this is inconvenient because the number of pair interactions one needs to consider increases super-linearly with respect to the interaction range. More advanced MD packages circumvent this problem by using different interaction ranges for different

is fixed at the center of the box and repels all other particles *via* a WCA potential.

Thirdly, with this “pseudo core”, the endgroups of the linkers, which are supposed to be covalently linked to the core, are simply fixed in simulations onto its surface. Note that these grafting sites are placed on a lattice with a roughly equal distance between the nearest neighbors, so that this underlying assumption in the blobology theory is satisfied. A more realistic setup with randomly distributed grafting sites may slightly affect the results, but this has not been tested yet. However, we suspect that the effects of a slightly uneven distribution is comparable to the effects that result from a polydispersity of the polymer chain length, which will be discussed in the next section.

7.4 Results

7.4.1 Stability of pre-assembled vesicles

In Section 7.2, our theoretical polymer model predicts that the optimal size of our nanocarriers will be approximately the radius at which their polymer linkers are relaxed: being too small or too large will destabilize the membrane vesicle or the tether anchors. This relaxed position of the polymers can be predicted by our theoretical model of spherical brushes, as explained in Section 3.5.5.

An example force-extension curve for a polymer brush is shown in Fig. 7.1 for a system with $R_{\text{core}} = 9.0$ nm and $f = 342$ linker chains, each of length $N = 30$, monomer size $a \simeq 0.4$ nm, and persistence length $\ell_p \simeq 0.32$ nm. The measured average force *per chain*, $F(r)$, black dots, our theoretically predicted $F(r)$, dashed red curve, and the free energy accumulated in the chain, $\mathcal{E}(r)$, solid blue curve, are plotted against the interface radius r . Given this curve, the minimum and maximum radius R_{ves} of a *mechanically stable* nanocomposite can be calculated: Plugging in $\sigma_{\text{rup}} \approx 5$ pN/nm, Eq. (7.6) gives $r_{\text{min}} \approx 11.6$ nm, or equivalently $R_{\text{ves, min}} \approx 11.6$ nm + $d/2$. Below this radius, the pressure from the polymers will very likely rupture the membrane. On the opposite side, assuming the free energy of insertion of a lipid is around $15 k_B T$, then the solution of Eq. (7.7) is $r_{\text{max}} \approx 17.0$ nm, above which vesicle deformations may occur, and anchors may be pulled out from the bilayer. The *optimal* vesicle size, $R_{\text{ves, 0}} = r_0 + d/2$, at which $F(r_0) = 0$, is $r_0 \approx 12.4$ nm. Note that the left cutoff happens at a fairly low $\mathcal{E}(r)$, while the right cutoff has a much larger $\mathcal{E}(r)$. The reason is that the left cutoff is a collective effect of *all* chains pushing against the membrane vesicle, while the right cutoff looks at the pull-out of a *single* chain.

To test our statement on NP sizes, membrane vesicles of four different sizes are assembled around the aforementioned spherical polymer brush, whose interface radii r are indicated by the arrows in Fig. 7.1. The number of lipids in each vesicle is approximated separately for the two leaflets, based on their own *monolayer* radii and the area per lipid of a flat bilayer. Based on the simple reasoning above, these four systems would behave in

particle types. Luckily, this is not a big problem here, because it is not in fact necessary to represent the NP core as an actual degree of freedom.

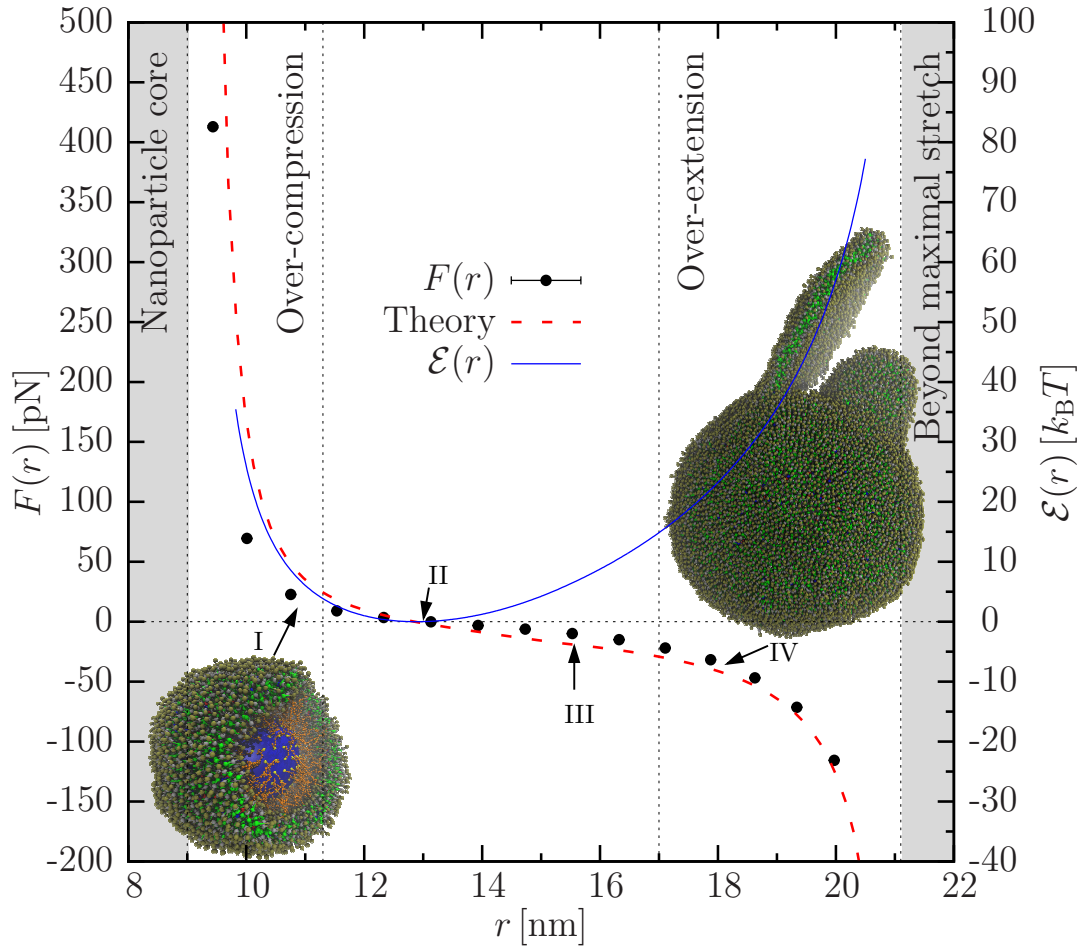


Figure 7.1: The force-extension curve (red dashed) for a single polymer chain in the example system described in the main text, predicted by our theoretical model for spherical brushes. The horizontal axis is the interface radius r , the vertical axis on the left is the average force *per chain*, $F(r)$, and the vertical axis on the right is the free energy per chain, $\mathcal{E}(r)$ (blue), obtained by integrating $-F(r)dr$. The solid circles are the forces measured in simulations of the brush constrained by two concentric repulsive shells. Note that the repulsive (positive) force diverges at the core surface ($r = 9.0$ nm, shaded), while the contractile force (negative) diverges when the chains are fully extended ($r = 21.1$ nm, shaded). The predicted range of a physically viable vesicle size, *i.e.* $r_{\min} \simeq 11.6$ nm predicted by Eq. (7.6) and $r_{\max} \simeq 17.0$ nm by Eq. (7.7), is indicated by two vertical dotted lines. Two snapshots of an overly small vesicle (brush over-compressed) and an overly large vesicle (brush over-extended) show examples of how the polymers can destabilize and deform the enclosing membrane vesicle.

the following different ways: System I includes the smallest lipid vesicle, and is expected to be in the regime that chains repel so strongly that the membrane will be ruptured; System II contains a vesicle whose radius is almost optimal to keep the polymer linkers relaxed; System III is larger, but still within the permissible range; The last system, System IV, is even larger so that the chains are stretched so much that some of them may be pulled out.

Indeed, huge membrane pores are found in System I, while Systems II and III remain stable throughout the simulation time, backing up our theoretical considerations of the minimum vesicle size $R_{\text{ves, min}}$. However, System IV shows some unexpected behavior: All chains together can pull the vesicle inwards so strongly that they force it to assume a smaller radius. Since a smaller vesicle needs fewer lipids, the chains thus collectively force the vesicle to shed lipids. This unexpected behavior stems from the assumption in our constraint of the maximum vesicle radius $R_{\text{ves, max}}$, in which only single-chain pull-outs have been considered as the consequence of over-stretching the brush. But our simulations show that the collective deforming effect of these polymer chains on the membrane will step in earlier than the pull-outs.

7.4.2 Assembly

The polymer brush in our nanocomposites prefers a range of vesicle sizes, outside of which it may deform or rupture the vesicle. However, if the vesicular membrane is in contact with a lipid “reservoir” and is allowed to adjust the number of lipids it contains (and thus its surface area), then our theory predicts that it is most likely to lead to assembled vesicles with their linkers roughly relaxed. To enable the system to choose its own size, and also to test a potential procedure to assemble such composites in experiments, a set of simulations are conducted in a way which is analogous to the rapid solvent exchange method for the planar tethered bilayers covered in the previous chapter.

In the current setup, the self-assembled monolayer (SAM) is the “lawn” of linkers that have their endgroup fixed around the solid core. The lipids in a good organic solvent are again mimicked by randomly placing them in the simulation box. After the “replacement” of the solvent, which is simply enacted by turning on the effective hydrophobic interactions, the development of the system is observed. Note that the total number of lipids in the simulations is approximately twice the number in a vesicle of the optimal size, so that the membrane has the possibility to be (at most $\sqrt{2}$ times) larger than the predicted optimal size.

As shown in Fig. 7.2 with a sequence of snapshots from such a simulation (System V), this assembly process is indeed reminiscent of the rapid solvent exchange method to prepare tBLMs pictured in Fig. 6.1. Once the hydrophobic attraction becomes effective, lipids aggregate into membrane patches in the bulk and around the SAM. After the merge of patches with the SAM and clipping off the excess lipids, a complete membrane vesicle forms with polymer tethers linking it to the solid core.

From our theoretical analysis of the polymer brush, the optimal size of the membrane vesicle would be $R_{\text{ves}} = r_0 + d/2$, at which these linkers are relaxed. To test this, the

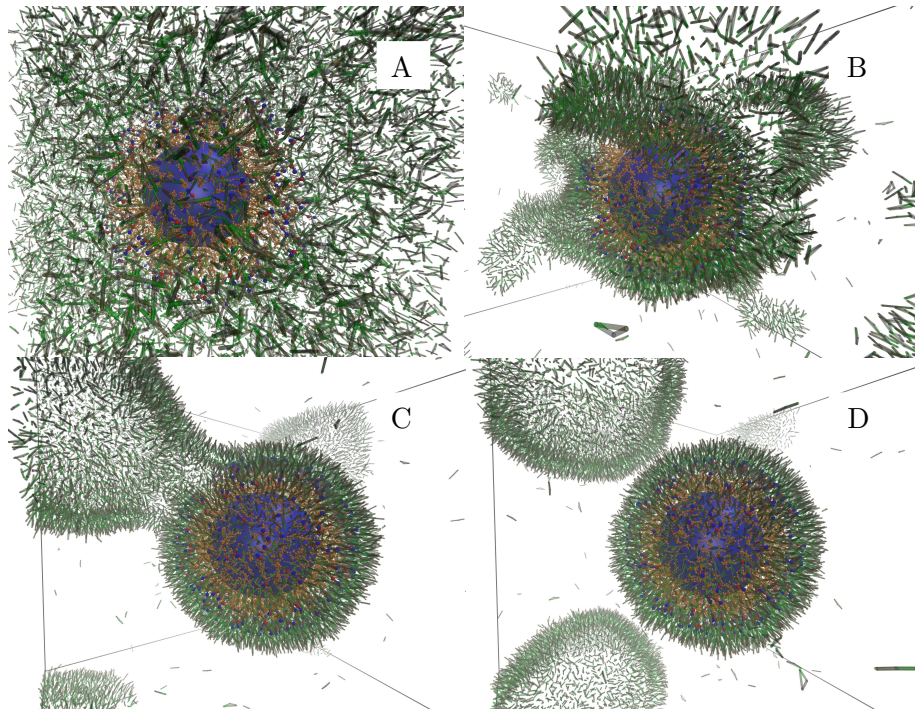


Figure 7.2: A sequence of snapshots of the assembly of System V. Lipids are rendered as semi-transparent licorices so that the linkers and the core are more visible. A, the initial random configuration of the lipids. B, lipids start to aggregate into membrane patches. C, excess lipids bud out from the vesicle. D, the final structure.

radial distribution profile of the particles in this assembled nanocomposite is measured, as shown in Fig. 7.3. The interface radius r of this assembled structure is measured to be $r \approx 14.3$ nm, showing a separation of roughly 5 nm between the vesicle and the solid core. Admittedly, compared to the predicted value of $r_0 \approx 12.4$ nm, the measured value of r is approximately 2 nm larger. However, as shown in Fig. 7.1, the free energy per chain, \mathcal{E} , is rather flat in this range of r : at $r \approx 14.3$ nm, the increase in the free energy *per polymer chain* is around $5k_B T$, which is safely below the free energy of insertion $\epsilon_{\text{ins}} \approx 15k_B T$. Hence, the anchors can remain inside the bilayer.

In fact, it is the interface radius r_0 preferred by the *linkers* that the polymer theory predicts. The *lipids*, however, may choose to form a larger vesicle to lower their free energy: Including one single lipid into the bilayer will lower the free energy by $\epsilon_{\text{ins}} \sim 15k_B T$, while merging a membrane patch into the vesicle also can reduce the free energy by removing open edge. Thus, it is plausible that the vesicle would slightly swell, as we have seen in our simulations. On the other hand, this swelling of the vesicle will inevitably stretch the tethers and increase the free energy of the brush. But notice, the lipids do not pay for this directly; instead, the tethers do. The additional pulling from the tethers increases the

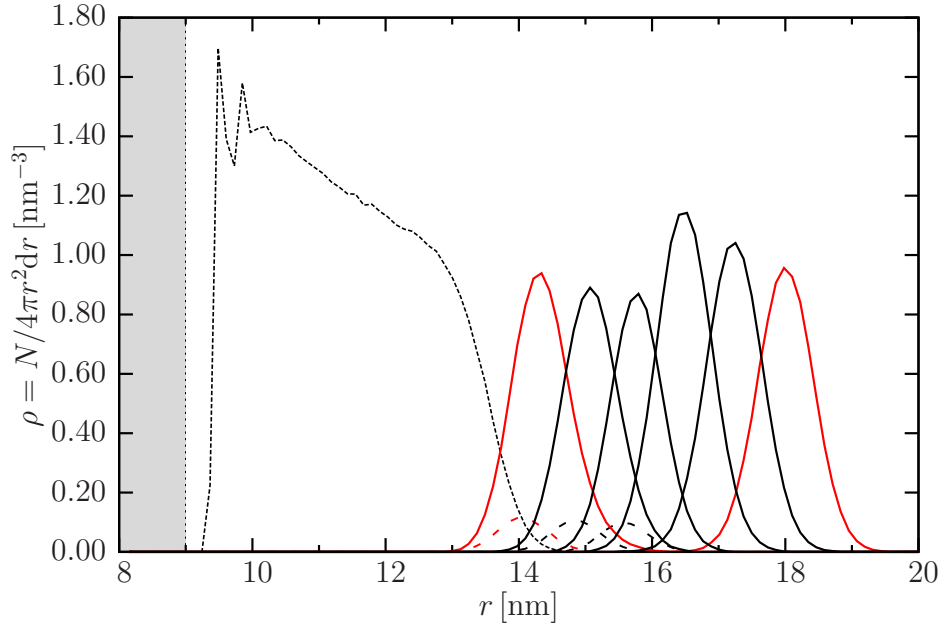


Figure 7.3: Radial distribution profile of System V. The horizontal axis is the interface distance r , and the vertical one is the density of particles, defined as $\rho = N(r)/4\pi r^2 dr$, at a radial distance r from the center. Solid and dashed curves denote lipids and tether anchors, respectively. Red and black curves stand for the head and the two tail beads. The polymer spacer is shown as the dotted curve. A vertical line separates the solid core (shaded) from the rest at $R_{\text{core}} = 9$ nm.

surface stress in the bilayer, hence would cost energy. But since the lipids easily outnumber the tethers by one order of magnitude, the cost *per lipid* could be very bearable. In the extreme scenario when the free energy accumulated per chain is sufficiently high, these chains will induce membrane deformation, followed by possible pullout of the anchors, which defeats our purpose of tethering the membrane vesicle to the solid nanoparticle core.

Another important observation from several assembly simulations is the possibility that the nanocomposite may be kinetically trapped in states with a higher free energy. For instance, if a large patch of membrane is adsorbed onto the tethers while the membrane vesicle is almost complete, then a part of this patch may end up dangling outside the vesicle as an attachment for a really long time. This is because, on the one hand, the amount of the free energy the vesicle lowers by including all these extra lipids into the vesicle (thus eliminating the open edge) may not suffice to compensate for the cost to significantly expand a membrane under tension; on the other hand, the patch may not be able to detach either, since exposing open edges also increases the free energy.

Of course, getting trapped in these intermediate states may not be a real issue in experiments, since the available time scale is much longer than what is achievable in simu-

lations. Without additional experimental knowledge it is unclear whether one can simply wait for the system to evolve towards its free energy minimum or whether additional measures would have to be taken, such as creating shear forces through extrusion, or mildly sonicating the system. Moreover, we neither intend to invalidate this potential assembly procedure, nor do we at the present state aim to find practical solutions to the problem of dangling bilayer patches, using our CG model. Our purpose is to point out the possibilities one may overlook, based on the events observed in simulations.

7.4.3 Solvent condition

In addition to the problem of having undesirable membrane attachments on the surface of the tethered vesicle, the existence of empty lipid vesicles formed by excess lipids (as shown in Fig. 7.2) also raise the practical question of how to separate the membrane-nanoparticles from these empty vesicles, considering that the size of such self-assembled lipid vesicles (tens of nanometers, as first predicted in the work by Helfrich [Hel74]) are comparable to the vesicles with a core inside.

One conceptually possible method to alleviate both of these problems at the same time is to change the quality of the solvent where the assembly will take place. It is conceivable that with a very carefully chosen range of lipid concentration, which is slightly below the lipid's critical micelle concentration (CMC),³ the translational entropy of being a free lipid would only slightly outweigh the free energy decrease of grouping hydrophobic parts together and forming aggregates. Thus, the lipids in the bulk would remain in a random configuration. However, near the surface of the solid core with grafted tethers, it could be entropically more beneficial for the lipids to assemble into a bilayer with the anchors, since the anchors have already lost most of their translational entropy. If such a range of lipid concentration exists, then one can filter away the stray lipids and small aggregates in the bulk easily, and collect mostly the membrane-coated nanoparticles. One may concern about the extremely low CMC for lipids in *water*: for instance, the values of the CMC for the PC lipids discussed in previous chapters are on the order of nM [Mar13]. However, we can choose to use a much *better solvent*, for example good organic solvent like ethanol, in which the lipid CMC is orders of magnitude higher. This not only significantly increases the probability of lipids arriving at the NP surface (which linearly depends on the lipid concentration), but also shifted the chemical potential balance between the lipids in the bulk (logarithmically depending on the lipid concentration) and the lipids around the NP towards the latter. In addition, under such solvent conditions it could be conceivable that the exchange of lipids between membranes and the bulk reservoir, or between two membranes, will be facilitated, such that the system may escape more quickly from some intermediate states.

We have indeed found a small range of solvent condition under which the above scenario is observed. A system consisting of 508 linkers of length $N = 10$ and roughly 10800 lipids

³The CMC (critical micelle concentration) is the concentration beyond which the lipids in solution will start to form micelles.

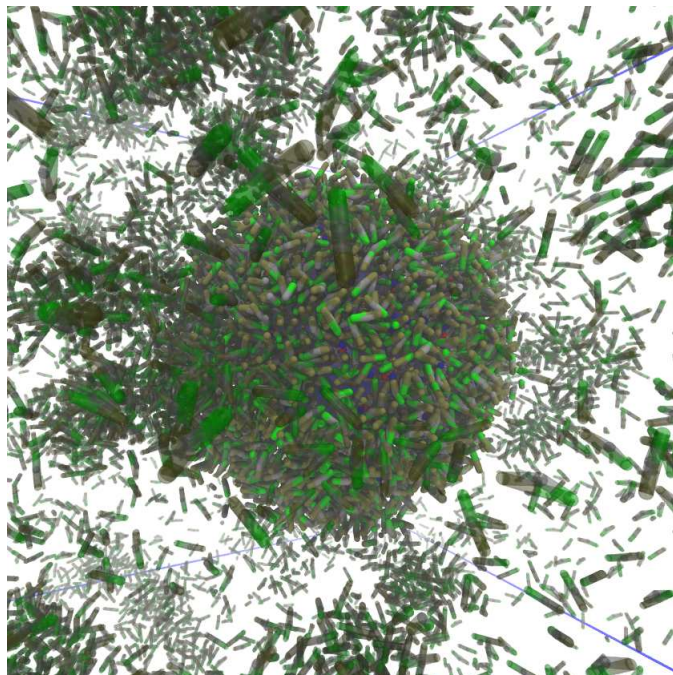


Figure 7.4: Under a carefully chosen solvent quality condition, lipids in the bulk remain randomly distributed, while a bilayer forms with the help of the tether anchors near the surface of the core. Stray lipids are rendered as transparent, so that the molecules around the NP core are better visible. The system contains 508 10-mer linkers and approximately 10800 lipids. The strength of the cosine-square attraction is reduced to 55% of its normal level in an aqueous solution.

is simulated under different solvent quality conditions that are systematically varied by increasing the depth ϵ of the cosine-square potential (see Eq. (2.4), from 0 to its normal value of 1). As shown in Fig. 7.4, when the attraction strength is lowered to 55% of its normally used value, lipids starts to cover the NP core, without any significant aggregation happening in the bulk. Relating the quantitative information from these simulations to experimental systems is probably difficult due to the generic nature of our CG model. But the observation that a range of such solvent condition does exist in simulation suggests that it may be worthwhile looking for the experimental analogue of this condition when one tries to assemble such nanocomposites in experiments.

7.4.4 Polydispersity

So far, only monodisperse polymeric linkers have been considered. This situation is surely easiest to treat in theory, but it usually requires substantial experimental effort. Hence, it is also worthwhile to look into the effects of polydispersity in the chain length. Intuitively speaking, if the chains have a wide distribution in length, then they will prefer different

chain extensions, and thus respond differently to the confinement from the membrane vesicle: the shorter chains are under tension so they *pull* on the bilayer, while the longer ones are compressed and hence *push* on the membrane. This could lead to, for instance, local deformations of the bilayer they anchor into. These “crumbled” vesicles with nonuniformly distributed stress inside may exhibit a compromised mechanical stability. In the extreme case, one can imagine that the chains belonging to the short end of the length distribution function simply pull out of the vesicle, especially if their immediate neighbors happen to be long chains. Such effects would cause an uneven tethering density and presumably lead to other undesired results.

In this subsection, the effects of polydispersity in the tether chains is examined. The distribution of the chain length is assumed to follow the two-parameter Schulz distribution with parameters b and α [RMG96]:

$$W(N) = \frac{\alpha^{b+1} N^b}{\Gamma(b+1)} \exp(-\alpha N), \quad (7.8)$$

where $W(N)$ is the mass distribution function of chains with a degree of polymerization N , and Γ denotes the gamma-function. $W(N)$ is related to the degree of polymerization distribution function, $F(N)$, by

$$W(N) = \frac{NF(N)}{\sum_{N=1}^{\infty} NF(N)}. \quad (7.9)$$

Using Eqs. (7.8) and (7.9), $F(N)$ can be expressed as

$$F(N) = \frac{\alpha^b x^{b-1}}{\Gamma(b)} \exp(-\alpha N). \quad (7.10)$$

The two parameters b and α are related to the number (\overline{N}_n) and weight (\overline{N}_w) averaged chain length as [RMG96]

$$\overline{N}_n = \frac{b}{\alpha} \quad (7.11)$$

$$\text{and} \quad \overline{N}_w = \frac{b+1}{\alpha}, \quad (7.12)$$

respectively. Then the *polydispersity index* (PDI), defined as the the ratio of $\overline{N}_w/\overline{N}_n$, is

$$\text{PDI} = \frac{\overline{N}_w}{\overline{N}_n} = \frac{b+1}{b} = 1 + \frac{1}{b}. \quad (7.13)$$

We have simulated four polydisperse systems that are similar to System V discussed previously in Section 7.4.2, with a PDI of 1.05, 1.1, 1.2, and 1.5, respectively. The PDI of each system determines the parameter b in the Schultz distribution *via* Eq. (7.13). The other parameter α is then determined by Eq. (7.11) to keep the number averaged chain

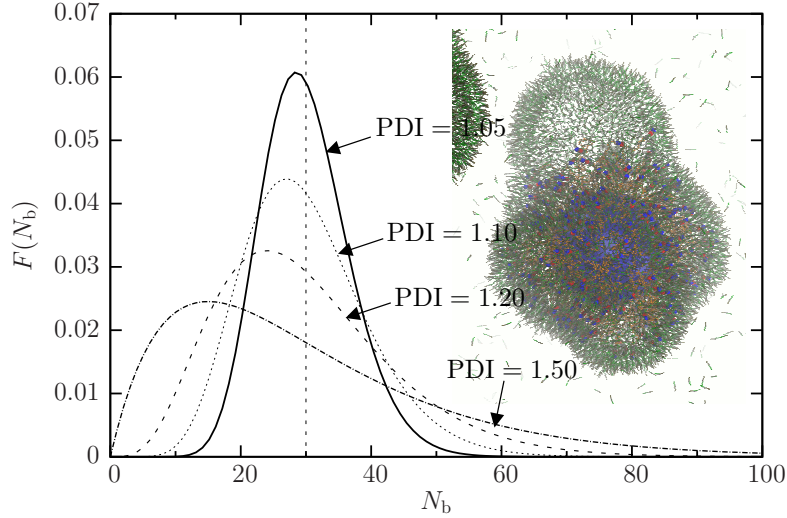


Figure 7.5: Schultz (number) distribution function, $F(N_b)$, as a function of the degree of polymerization N_b , for PDIs equal to 1.05 (solid), 1.10 (thin dotted), 1.20 (dashed), and 1.50 (dash-dotted), respectively. The number averaged degree of polymerization $\bar{N}_n = 30$ is the same in all four cases and is indicated as a vertical dashed line. For the systems with a PDI of 1.20 and 1.50 (shown as inset), the final membrane around the NP is “crumpled” with bulges, where no tethers (drawn as small orange beads connected to a large red-blue anchor) are anchored to.

length $\bar{N}_n = 30$, comparable to $N = 30$ which we used in the monodisperse System V. The amount of tethers of various length are set roughly to the same $f = 342$; a slight deviation of 1 or 2 in f may be caused by the rounding error when applying the distribution function Eq. (7.10). The frequency distribution function $F(N)$ of these four systems is plotted in Fig. 7.5. Notice that, as the PDI increases, the distribution function becomes not just broader but also less symmetric with respect to \bar{N}_n ; shorter chains show up more frequently.

As discussed in the previous subsection, the tether-membrane system may be trapped in some intermediate states, such as states that have a small amount of excess lipids attached to the outside of the bilayer. One potential method to facilitate the escape from such states is by increasing the exchange of lipids with the bulk environment or with other floating membrane patches, which can be realized by adjusting the solvent condition. Thus, all these four systems are initially simulated with a weakened hydrophobic attraction (*c.f.* Section 7.4.3). If a complete vesicle forms around the NP core, then the solvent condition is tuned back to its regular level in water, followed by measurements of the equilibrium properties of the system. Of course, the area per lipid depends on the effective attraction used to represent the hydrophobic interaction. Thus, it is conceivable that if a nice bilayer forms around the relaxed tethers in a carefully chosen solvent quality condition, then switching to an aqueous solvent will contract the bilayer and consequently compress the

polymers.

Among the four polydisperse systems, the desired membrane-nanoparticle composite is found in the two systems with a lower PDI of 1.05 and 1.10; the radial distribution profile of the particles resembles the one measured for the monodisperse System V (which has been shown in Fig. 7.3). The lipids in the other two systems with a PDI of 1.20 and 1.50, however, fail to form a nice membrane vesicle anchored around tethers. Instead, a crumbled vesicle with a few large bulges is observed, with no tethers anchoring to the inside of the bulges. An example snapshots of a system with a PDI of 1.50 is shown as the inset in Fig. 7.5. These “defects” in the vesicle do not disappear throughout the entire simulation time, suggesting that these two systems are indeed stuck — at least in the simulations, but conceivably the same might happen for experimental systems. Observation of the tethers near these bulges shows that the alternation of randomly distributed long and short chains seems to limit the impact of the polymer brush on the vesicle.

7.5 Discussion

In this concluding chapter, we have studied a few important aspects of the proposed membrane-nanoparticle composites. First, by simulating pre-assembled nanoparticles with vesicles of different sizes, we verified that our theoretical model for polymer brushes in a spherical geometry can be applied to semi-quantitatively predict the force-extension response of the tether chains in the composites. This helps us to estimate the range of vesicle sizes in which the interactions from the tethers will not deform or destroy the enclosing bilayer vesicle. Second, an analogue of the rapid solvent exchange protocol for planar tethered bilayers is tested in simulations, suggesting a possible way to assemble these nanocomposites under some fine-tuned solvent condition where lipids form a bilayer vesicle around the core but remain scattered in solution. This special environment could be beneficial when one wants to separate the assembled nanocomposites from the lipid aggregates. Meanwhile, escaping kinetically trapped states in the assembly process may also be achieved in such solvent condition, since the exchange of lipids between the membrane vesicle around the tethers and other lipids in the bulk or in free membrane patches might happen more easily.

Thermal response

Many further questions regarding this design of polymer-tethered membrane-nanoparticle structure may be investigated following the current study. One especially interesting one concerns a potential strategy to release the drug payload utilizing external thermal input.

Suppose the complete membrane-nanoparticle structure can be prepared using lipids which stay in the gel phase under physiological conditions. Then, upon the increase of the local temperature around the particles, *e.g.* by utilizing enhanced surface plasmon resonance [PB11], the membrane and the polymer chains would behave very differently: On the one hand, the increase in temperature may drive the lipids over the phase transition

from the gel phase into the fluid phase, during which the surface area of the vesicle *expands* normally by 10 to 30%[NE88, NTN00]. On the other hand, the polymer chains would tend to *contract* more strongly due to the enhanced entropic effect.⁴ As a consequence of these two types of responses in the opposite directions, one might hope that the membrane vesicle ruptures, and releases the drug payload.⁵

⁴This is the same effect that makes rubber contract upon heating.

⁵Series of research have been devoted to developing temperature-dependent drug release liposomes [NAKD00, ND01, NPWT13]. Ideally, one can implement such optimized membrane formulations in our nanocomposites. Then the additional stress from the polymer chains may further improve the release mechanism.

Appendix

Appendix A

Notes on Data Analysis

After the design and implementation of simulations, data analysis is a crucial step leading to sound conclusions and enabling meaningful discussions. It involves much more than simply calculating averages and feeding numbers into your favorite fitting software. In this appendix, I will outline those aspects of data analysis that are the most relevant ones to my day-to-day research, in an order that is similar to the typical work-flow.

First, after investing hundreds of CPU hours, we need to extract measurements with *reliable errors* out of our simulation trajectories. The blocking method, nicely described by Flyvbjerg and Peterson [FP89], provides an accurate estimate of the variance of the original data even in the presence of correlations between consecutive data points. This method also warns the user when such estimates are unavailable based on the current data set, and thus longer simulations are needed. A general procedure for this method will be explained in Section A.1.

Second, *fitting* is also a key step of any analysis that aims to extract some physical quantities of a theoretical model that purports to explain these data. For this, a short overview of weighted least square regression is described in Section A.2, covering both linear and nonlinear regressions.

Third, to estimate the errors on the fitting parameters, the Monte Carlo resampling technique is almost universally applicable and nevertheless straightforward to implement. As described in Section A.3, this technique does not require one to analytically carry out complicated error propagation (an endeavor that is anyways almost never pushed beyond linear order). At the same time, much more information regarding the fits can be learned through this method.

A.1 Blocking Analysis

Generally, the output of our MD simulations consists of various physical quantities, such as energies, forces, and pressures of the simulated system, in the form of a time series. Because having more data points helps to obtain better statistics, and thus make better use of the trajectories, it is tempting to generate output data as frequently as possible. However, this brings in a new problem one now needs to solve: The commonly used quantity, the (naively calculated) standard error of the mean, *underestimates* the real error on the series average, because it overlooks correlations between neighboring data points.

A classical remedy for this situation is to calculate the correlation function, from which one can calculate the correlation time of the series of data points, and this permits one to calculate correction factors to the naive (and too small) error of the mean. Yet, the blocking method, which will be outlined in this section, has been proven to be both more rigorous and computationally less demanding. For more details, the reader is encouraged to consult the very lucid paper by Flyvbjerg and Peterson [FP89].

Consider a system in equilibrium, thus the *unknown* probability distribution of a quantity x , $p(x)$, will be independent of time. Let x_i be a set of measurements of x , where $i = 1 \dots n$ indicate the order of the measurement, which we will assume to have been taken at regular time increments. The expectation value of some function $f(x)$ is then

$$\langle f \rangle \equiv \int dx p(x) f(x), \quad (\text{A.1})$$

while the sample average \bar{f} is

$$\bar{f} \equiv \frac{1}{n} \sum_{i=1}^n f(x_i). \quad (\text{A.2})$$

The former expression, $\langle \dots \rangle$, is a theoretical quantity based on the *unknown* probability distribution function $p(x)$, whereas the latter one, $\overline{\dots}$, is calculated from the finite sample of measurements $\{x_i | i = 1 \dots n\}$.

Assuming ergodicity, \bar{x} is then an unbiased estimator of $\langle x \rangle$, and it will become arbitrarily accurate in the limit of infinite sample size. But in reality, only finite sample sizes are available, thus we need a good estimate of the error on \bar{x} . More specifically, we want to estimate the variance of $m \equiv \bar{x} = \frac{1}{n} \sum_{i=1}^n x_i$, *i.e.*

$$\sigma^2(m) = \langle m^2 \rangle - \langle m \rangle^2. \quad (\text{A.3})$$

Note that the “naive” sample variance

$$c_0 \equiv \frac{1}{n} \sum_{k=1}^n (x_k - \bar{x})^2 \quad (\text{A.4})$$

is not the real variance, since the data are correlated.

The blocking method provides a rigorous estimate of $\sigma^2(m)$. It relies on the following linear transformation: Let $\{x'\}$ be the transformed data set with

$$x'_i = \frac{1}{2}(x_{2i-1} + x_{2i}), \quad (\text{A.5})$$

$$n' = \frac{1}{2}n. \quad (\text{A.6})$$

This means every two consecutive data points are averaged into one “new” data points. In case that the number of data points is odd, the last point would be dropped.

It is clear that $\overline{x'} = \bar{x}$ due to the linearity. Flyvbjerg and Peterson point out two more properties of the blocking transformation [FP89]:

1. $\sigma^2(m)$ stays invariant through this transformation, *i.e.* $\sigma^2(m') = \sigma^2(m)$. Thus, all information we want to obtain about $\sigma^2(m)$ is kept after the blocking transformation.
2. As one repeats the blocking again and again, the system approaches a fixed point, at which

$$\sigma^2(m) = \left\langle \frac{c_0}{n-1} \right\rangle. \quad (\text{A.7})$$

As a consequence, to obtain $\sigma^2(m)$, one keeps applying the blocking transformation Eq. (A.5) until $n' = 2$. After each round of transformation, calculate

$$\sigma(m) \approx \sqrt{\frac{c'_0}{n'-1}} \left(1 \pm \frac{1}{\sqrt{2(n'-1)}} \right). \quad (\text{A.8})$$

When $\sigma(m)$ reaches a plateau within error bars, the system is at the fixed point. Then, Eq. (A.8) gives a good estimate of $\sigma(m)$.

If, unfortunately, no plateau is found, this means that the current sample size is insufficient for the system to arrive at the fixed point. This should be taken as a warning: a larger sample size, *i.e.* a longer simulation, is needed. Meanwhile, Eq. (A.8) at least constitutes a lower bound of $\sigma(m)$.

The advantages of the blocking method include, but are not limited to:

- computational efficiency: the total number of operations is $\mathcal{O}(n \ln n)$, and
- possibility of automation: for example, one can compare the estimated error $\sigma(m')$ from one round of blocking with the error $\sigma(m)$ from the previous round in order to determine whether the plateau is reached, and output the value of $\sigma(m)$ when it is converged.

In this thesis, the blocking method is applied to all possible cases when an accurate error of a physical quantity is needed from a time series.

A.2 Least Square Curve Fitting

From the blocking analysis described in the previous section, one obtains meaningful errors σ_i associated with each measurement y_i , thus our data points can be denoted as $\{x_i, y_i \pm \sigma_i\}$, $i = 1 \dots n$. Note that we assume no error is associated with the independent variables x_i . If this assumption does not hold, instead of the weighted least square regression model described here, other fitting models, for instance the errors-in-variables models [RPL81], should be adopted.

The purpose of reviewing some basics of the weighted least square regression is to provide a better understanding of the fitting process. Then, one can easily code it into scripts, so that repeating the fitting for a large amount of times becomes possible, as required by the resampling techniques which will be described in the next section.

The general aim of fitting is to obtain a set of optimal fitting parameters $\boldsymbol{\beta}^* = (\beta_1, \beta_2, \dots, \beta_p)'$ (denoted by the superscript *) in the fitting function $f(x; \boldsymbol{\beta})$ which “fit” the data set best.¹ Within least square methods, the best fit is found by minimizing the weighted sum of squared residuals \mathcal{S} as a function of $\boldsymbol{\beta}$:

$$\min_{\boldsymbol{\beta}=(\beta_1, \dots, \beta_p)'} \mathcal{S}(\{x_i\}; \boldsymbol{\beta}) = \min_{\boldsymbol{\beta}} \sum_{i=1}^n w_i [y_i - f(x_i; \boldsymbol{\beta})]^2, \quad (\text{A.9})$$

where the weights are $w_i = 1/\sigma_i^2$ for uncorrelated errors $\{\sigma_i\}$. This is equivalent of maximizing the likelihood of the data given the fit, under the assumption that all data points follow Gaussian distributions with mean y_i and standard deviation σ_i .

A *linear* fit assumes the fitting function $f(x; \boldsymbol{\beta})$ is a linear combination of certain functions that are independent of $\boldsymbol{\beta}$, *i.e.*

$$f(x; \boldsymbol{\beta}) = \sum_{j=1}^p \beta_j f_j(x). \quad (\text{A.10})$$

Notice, $f_j(x)$ does *not* need to be linear in x : For instance, in polynomial regression, $f_j(x) = x^j$. However, $f_j(x)$ has to be independent of $\boldsymbol{\beta}$. So $f_j(x) = \exp(\beta_j x)$ is in fact a *nonlinear* fit.

Linear fitting is deterministic and requires no initial guess on $\boldsymbol{\beta}$, while nonlinear fitting normally uses iterative numerical solvers to refine an initial guess $\boldsymbol{\beta}_0$. This difference originates from the distinct dependence on $\boldsymbol{\beta}$: For linear models, $\partial f(x; \boldsymbol{\beta})/\partial \beta_k = f_k(x)$ is constant, given the data x . On the other hand, a nonlinear model may have a complicated $\boldsymbol{\beta}$ dependency. The following two subsections will discuss corresponding strategies for solving linear and nonlinear problems.

A.2.1 Linear Least Square Regression

The linear dependence of $f(x)$ on $\boldsymbol{\beta}$, Eq. (A.10), makes it possible to analytically solve the minimization problem of Eq. (A.9) by calculating the partial derivatives of \mathcal{S} with respect to the fitting parameters:

$$0 \stackrel{!}{=} \frac{\partial \mathcal{S}}{\partial \beta_m} = \sum_i 2 [w_i (y_i - f(x_i; \boldsymbol{\beta}))] \left[-\frac{\partial}{\partial \beta_m} f(x_i; \boldsymbol{\beta}) \right] \quad (\text{A.11})$$

$$= -2 \sum_i \left[w_i (y_i - \sum_j \beta_j f_j(x_i)) \right] f_m(x_i) \quad (\text{A.12})$$

Denote $W_{ij} \equiv \delta_{ij} \sigma_i^{-2}$, $X_{ij} \equiv f_j(x_i)$ and $\mathbf{y} \equiv (y_1, \dots, y_n)'$. Now, \mathbf{W} is an $n \times n$ matrix, \mathbf{X} an $n \times p$ matrix, and \mathbf{y} an n -dimensional column vector. Then, Eq. (A.12) can be written into matrix form as

$$\mathbf{X}' (\mathbf{W} (\mathbf{y} - \mathbf{X} \boldsymbol{\beta})) = 0, \quad (\text{A.13})$$

¹The prime in $\boldsymbol{\beta}$ means $\boldsymbol{\beta}$ is a column vector.

which leads to the normal equation:

$$\mathbf{X}'\mathbf{W}\mathbf{X}\boldsymbol{\beta} = \mathbf{X}'\mathbf{W}\mathbf{y}. \quad (\text{A.14})$$

If the $n \times n$ matrix $(\mathbf{X}'\mathbf{W}\mathbf{X})$ is invertable, we obtain the unique solution of the fitting parameters

$$\boldsymbol{\beta}^* = (\mathbf{X}'\mathbf{W}\mathbf{X})^{-1} \mathbf{X}'\mathbf{W}\mathbf{y}. \quad (\text{A.15})$$

Nowadays, most of the scientific computing packages contain modules for linear least square fitting, so it is unnecessary to code the fitting kernel by hand. Yet, some high performance packages, such as the GNU Scientific Library `GSL`,² require users to provide input data in the format of \mathbf{X} , \mathbf{y} , \mathbf{W} . Thus, for implementation, one needs to understand the basic concepts in Eq. (A.9 – A.15).

A.2.2 Nonlinear Least Square Regression

For nonlinear least square problems, the partial derivative $\frac{\partial}{\partial \beta_m} f(x_i; \boldsymbol{\beta})$ is no longer equal to $f_m(x_i)$, but becomes a function of $\boldsymbol{\beta}$. This extra complication eliminates the simple solutions à la Eq. (A.15).

To find $\boldsymbol{\beta}^*$, we rewind to a multidimensional minimization problem as described in Eq. (A.9). Fortunately, most of the scientific packages also contain optimization modules. Elaborating on optimization methods is beyond the scope of this appendix. But, generally speaking, the input should contain

- A target function $\mathcal{S}(\boldsymbol{\beta}; \{x_i\})$,³
- A set of initial parameter $\boldsymbol{\beta}_0$ to start with, and sometimes
- The dependence of \mathcal{S} on $\boldsymbol{\beta}$, *i.e* the Jacobian $\left| \frac{\partial \mathcal{S}}{\partial \boldsymbol{\beta}} \right|$.

After feeding the package with the data in the required format, we can find the fitting parameters $\boldsymbol{\beta}$ as outputs of the minimization modules.

It is important to realize that the quest for a minimum of \mathcal{S} need not have a unique solution, because the problem is nonlinear. Multiple solutions could exist, and these can vary substantially in “quality”. Arriving at a “good” one often depends quite crucially on how well one guessed the initial parameter set $\boldsymbol{\beta}_0$. To find better fits, one can sample various initial $\boldsymbol{\beta}_0$ and pick the results with a minimum weighted sum of square residual \mathcal{S} .

A.3 Monte Carlo Data Resampling

In addition to the values of the fitting parameters, we would like to know the errors and sometimes even the distributions of these parameters or their cross-correlations. One

²<http://www.gnu.org/software/gsl/>

³Note that \mathcal{S} is a function of $\boldsymbol{\beta}$ here, not of $\{x_i\}$.

intuitive method is to divide the data set into smaller subsets (or equivalently, try to obtain more data sets), fit each individual set, and study the “ensemble” of each parameter. However, in real life obtaining more data is always limited by the available computational resources.

Another less expensive method is to resample the original data set many times based on the variance of the data, and treat the resampled sets as “new” data sets. The logic is, if our original data set follows an *unknown* population distribution, then the resampled sets will follow the same distribution.

To resample the data $\{x_i, y_i \pm \sigma_i\}$, ideally we should draw “new” points $\{x_i, y'_i \pm \sigma_i\}$ according to the probability distributions of the original measurements $\{y_i\}$. Since these distributions are generally unknown, we normally assume normality, *i.e.* $y_i \sim \mathcal{N}(y_i, \sigma_i)$. Here, $\mathcal{N}(\mu, \sigma)$ denotes a Gaussian distribution with mean μ and standard deviation σ . This assumption is often (but of course not always) endorsed by the central limit theorem.

The general procedure is as follows:

1. Create an artificial shift δy_i for each y_i with $\delta y_i \sim \mathcal{N}(0, \sigma_i)$, thus the “new” data point $y'_i = y_i + \delta y_i \sim \mathcal{N}(y_i, \sigma_i)$;
2. Fit the newly generated data set, $\{x_i, y'_i \pm \sigma_i\}$, and record the results β' ;
3. Repeat step 1 and 2 sufficiently often (say, more than 1000 times), and obtain $\{\beta^{(0)}, \beta^{(1)}, \dots, \beta^{(R)}\}$, where $\beta^{(r)}$ denotes the result β' from the r^{th} resampled set; and
4. Analyze $\{\beta^{(0)}, \beta^{(1)}, \dots, \beta^{(R)}\}$ to get the statistics of β .

This resampling technique tries to exploit the maximum information embedded in the original data set; Instead of a single result β^* , now we have an ensemble of β at hand, which presumably follows the probability distribution implied by in the original data for the model parameters. Essentially, we are exploring the possibilities in the sample space allowed by the original data.

A closely related resampling method is the Bootstrap Method [Efr79].⁴ In bootstrapping, one resamples the data by drawing the same number of data points from the original data set with *replacement*, so it is possible that some data points appear multiple times in the resampled set. Except for the way in which the data is resampled, the Bootstrap method shares all other aspects with the MC resampling method described here in this section. Since bootstrapping has been studied for decades, we can borrow many analysis methods and apply them to our resampling.⁵ A key difference between bootstrapping and MC resampling is the former does not work effectively if the size of the data set is too small, since one is always choosing the same data.

⁴The name originated from the saying “pulling oneself up by bootstraps”, because one is generating more “new” data out of the old data.

⁵More details with the Bootstrap Method and resampling can be found in Ref. [ET94].

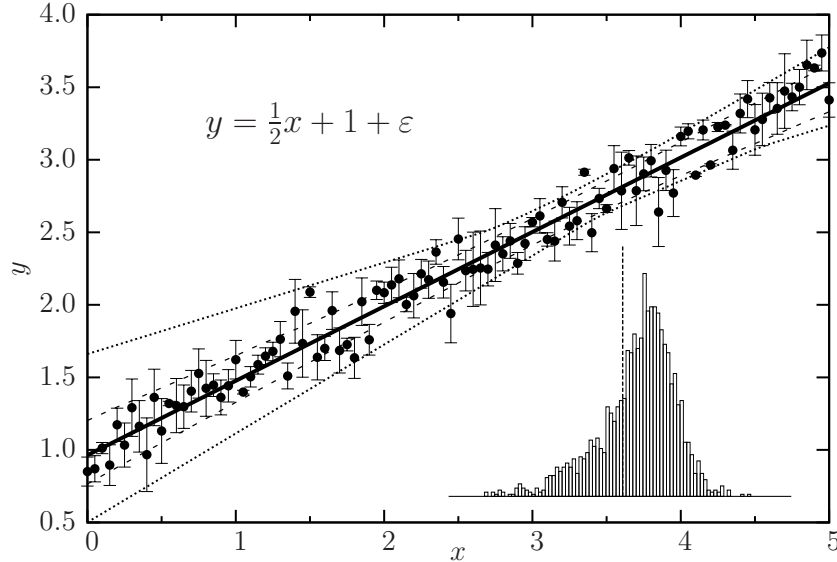


Figure A.1: Resampling results of an artificial data set is shown. Closed circles denote the original data. The thick solid curve is the averaged fit over resampled results. Dashed curves show the 95% confidence interval of the fitted curve, while dotted ones envelope all resampled fitting results. The inset shows the histogram of the fitting parameter β_1 , with real value $\beta_1 = 0.5$ plotted as the vertical dashed line.

The error on the fitting parameters β can be approximated by the standard deviation of β from the set $\{\beta^{(0)}, \beta^{(1)}, \dots, \beta^{(R)}\}$. In addition, the confidence interval of β can be estimated from the empirical quantiles of the set. In case β follows a non-Gaussian distribution, especially a nonsymmetric one, the confidence interval contains more information than the standard deviation.

Besides the knowledge on β , resampling also provides access to the “confidence interval” of the *fitted curve* $f(x; \beta^*)$ on the graph, which indicates the region where the curve could possibly locate with some probability, say 95%. This can be implemented by inserting an extra step after step 2 in the previous procedure:

- 2'. Calculate and keep the values of the fitting function $f(x; \beta^{(r)})$ at a fixed set of grid points $\{X_k\}$, $k = 1 \dots K$. Denote $F_{k,r} = f(X_k; \beta^{(r)})$ for the function value at grid point k in resampled set r .

After completing all resampling, one sorts the matrix $\mathbf{F} = \|F_{k,r}\|$ by columns, *i.e.* by grid points X_k , to obtain the empirical quantiles (say, the 2.5%- and 97.5%-quantiles) and thus the confidence interval at $x = X_k$.

As a demonstration, an artificial data set was created, shown in Fig. A.1. These data follow

$$y = \hat{\beta}_1 x + \hat{\beta}_0 + \varepsilon, \quad (\text{A.16})$$

with $\hat{\beta}_1 = 1/2$, $\hat{\beta}_0 = 1$, and ε being a term for random noise . Using the aforementioned resampling method, the following statistics are obtained from 2000 resamplings:

$$\beta_1 = 0.513 \pm 0.034, \text{ and } \beta_0 = 0.963 \pm 0.109.$$

Within error bars, we successfully rediscover the true parameters of the original distribution.

Moreover, the best fit (solid curve) with confidence interval (dashed) is plotted in Fig. A.1, as well as the extrema of the resampled fits (dotted). These curves provide an excellent picture of where the fit could be.

Even better is the access to the distribution of each fitting parameter. Exemplified by the inset of Fig. A.1, the slope of the line, β_1 , does not peak around its true value 0.5, but slightly higher. In addition, the distribution is asymmetric. In this case, the fact that the noise ε depends in some nontrivial way on x leads to the observed skewness.

All information discussed so far could deepen the understanding of the system studied, and the computational cost is economic, too. Using a Perl implementation on a single core, the 2000 resamplings took less than one minute.⁶ With other scientific programming languages that have better support in parallelization, *e.g.* C/C++, this cost can be further reduced significantly by distributing the resamplings to multiple cores; Each resampling process is independent of the others, thus the method trivially parallelizes.

⁶Note that our artificial data set consists of 100 points, while in real cases this number is normally much smaller. Thus, the program will work much faster.

List of Figures

1.1	Structure of the proposed membrane-nanoparticle composite	5
2.1	The potentials used in the Cooke model	16
2.2	Tuning the aspect ratio in the Cooke model	22
2.3	Tuning the energy scales in the Cooke model	23
2.4	Tuning the length and energy scales together	24
2.5	Schematics of the CG linker and lipid	25
2.6	Tuning the persistence length ℓ_p of the spacers	27
3.1	Force-extension relation for a single CG spacer chain	37
3.2	Compare different predictions on brush heights	45
3.3	Osmotic pressure for two example systems	46
3.4	Single-chain force-extension curve	48
4.1	Illustration of the geometry of a buckle	52
4.2	Sketches of the series expansions in buckling theory	54
4.3	Snapshots of two buckled membranes	58
4.4	Stress-strain relation of a buckled membrane	59
4.5	Buckling energy versus free energy	64
4.6	Temperature dependence of κ	65
5.1	Example snapshots of the vesiculation process	73
5.2	The probability of patch-closure for an example system	76
5.3	Sketches of the “groove” and the “sandwich” constraints	80
5.4	Time-evolution of the shape anisotropy index κ_s^2	82
5.5	Elastic ratio versus lipid spontaneous curvature	86
5.6	Lateral stress profiles of MARTINI PC lipids	89
5.7	The integrand of the second moment of MARTINI PC lipids	90
5.8	Bilayer elastic ratio versus bending modulus	92
6.1	tBLM formed using rapid solvent exchange	101
6.2	tBLM formed using vesicle fusion	102
6.3	tBLM height versus tether fraction	104
6.4	Diffusion constants versus tether fraction	105
6.5	Destabilization of membranes due to long tethers	107

List of Figures

7.1	Force-extension curve for a spherical brush	117
7.2	Assembly of the proposed membrane-nanoparticle composites	119
7.3	Radial density profile of a membrane-NP composite	120
7.4	Solvent quality in the assembly of the proposed nanocomposite	122
7.5	Schultz distribution function for polydisperse chains	124
A.1	Example of data resampling	135

List of Tables

2.1	Parameters to tune the aspect ratio in the Cooke model	22
2.2	Interaction parameters	29
4.1	Summary of the results from the buckling method	60
4.2	Coefficients for the series expansions in the buckling theory	68
4.3	Properties of the systems studied using the buckling method	69
5.1	List of all simulated systems using the patch-closure method	95
5.2	Elastic parameters of MARTINI lipids from stress profiles	96

List of Technical Notes

3.1	Relation between κ and ℓ_p	35
4.1	Thermodynamic integration	63
5.1	Gauss-Bonnet theorem	72
5.2	Shape anisotropy indexes	81

Bibliography

- [AC04] T. M. Allen and P. R. Cullis, *Drug Delivery Systems: Entering the Mainstream*, *Science* **303**, 1818–1822 (2004).
- [AC13] T. M. Allen and P. R. Cullis, *Liposomal drug delivery systems: From concept to clinical applications*, *Advanced Drug Delivery Reviews* **65**, 36–48 (2013).
- [AFtW06] R. J. Allen, D. Frenkel and P. R. ten Wolde, *Forward flux sampling-type schemes for simulating rare events: Efficiency analysis*, *The Journal of Chemical Physics* **124**, 194111 (2006).
- [AJK11] W. T. Al-Jamal and K. Kostarelos, *Liposomes: From a Clinically Established Drug Delivery System to a Nanoparticle Platform for Theranostic Nanomedicine*, *Accounts of Chemical Research* **44**, 1094–1104 (2011).
- [Ale77] S. Alexander, *Adsorption of chain molecules with a polar head a scaling description*, *Journal de Physique* **38**, 983–987 (1977).
- [All94] T. M. Allen, *Long-circulating (sterically stabilized) liposomes for targeted drug delivery*, *Trends in Pharmacological Sciences* **15**, 215–220 (1994).
- [AS72] M. Abramowitz and I. A. Stegun, *Handbook of mathematical functions: with formulas, graphs and mathematical tables*, Dover, New York (1972).
- [AT89] M. P. Allen and D. J. Tildesley, *Computer simulation of liquids*, Clarendon Press ; Oxford University Press, Oxford [England]; New York (1989).
- [ATC12] A. Albanese, P. S. Tang and W. C. Chan, *The Effect of Nanoparticle Size, Shape, and Surface Chemistry on Biological Systems*, *Annual Review of Biomedical Engineering* **14**, 1–16 (2012).
- [AV02] G. Ayton and G. A. Voth, *Bridging Microscopic and Mesoscopic Simulations of Lipid Bilayers*, *Biophysical Journal* **83**, 3357–3370 (2002).
- [AYS08] A. Arkhipov, Y. Yin and K. Schulten, *Four-scale description of membrane sculpting by BAR domains*, *Biophysical Journal* **95**, 2806–2821 (2008).
- [BB03] G. Brannigan and F. L. H. Brown, *Solvent-free simulations of fluid membrane bilayers*, *The Journal of Chemical Physics* **120**, 1059–1071 (2003).

- [BB05] G. Brannigan and F. L. H. Brown, *Composition dependence of bilayer elasticity*, The Journal of Chemical Physics **122**, 074905–074905–11 (2005).
- [BBS⁺11] E. G. Brandt, A. R. Braun, J. N. Sachs, J. F. Nagle and O. Edholm, *Interpretation of Fluctuation Spectra in Lipid Bilayer Simulations*, Biophysical Journal **100**, 2104–2111 (2011).
- [BCOY93] D. Brown, J. H. Clarke, M. Okuda and T. Yamazaki, *A domain decomposition parallelization strategy for molecular dynamics simulations on distributed memory machines*, Computer Physics Communications **74**, 67–80 (1993).
- [BDWJ05] T. Baumgart, S. Das, W. W. Webb and J. T. Jenkins, *Membrane elasticity in giant vesicles with fluid phase coexistence*, Biophysical Journal **89**, 1067–1080 (2005).
- [BEJ97] O. Berger, O. Edholm and F. Jähnig, *Molecular dynamics simulations of a fluid bilayer of dipalmitoylphosphatidylcholine at full hydration, constant pressure, and constant temperature*, Biophysical Journal **72**, 2002–2013 (1997).
- [Bin02] K. Binder, *Scaling concepts for polymer brushes and their test with computer simulation*, The European Physical Journal E - Soft Matter **9**, 293–298 (2002).
- [BM84] A. A. Brian and H. M. McConnell, *Allogeneic stimulation of cytotoxic T cells by supported planar membranes*, Proceedings of the National Academy of Sciences **81**, 6159–6163, PMID: 6333027 (1984).
- [BM12] K. Binder and A. Milchev, *Polymer brushes on flat and curved surfaces: How computer simulations can help to test theories and to interpret experiments*, Journal of Polymer Science Part B: Polymer Physics **50**, 1515–1555 (2012).
- [BMT12] S. Baoukina, S. J. Marrink and D. P. Tieleman, *Molecular Structure of Membrane Tethers*, Biophysical Journal **102**, 1866–1871 (2012).
- [BMT13] G. Bao, S. Mitragotri and S. Tong, *Multifunctional Nanoparticles for Drug Delivery and Molecular Imaging*, Annual Review of Biomedical Engineering **15**, 253–282 (2013).
- [BP11] Y. H. Bae and K. Park, *Targeted drug delivery to tumors: Myths, reality and possibility*, Journal of Controlled Release **153**, 198–205 (2011).
- [BR92] D. H. Boal and M. Rao, *Topology changes in fluid membranes*, Physical Review A **46**, 3037–3045 (1992).

- [BSW65] A. Bangham, M. Standish and J. Watkins, *Diffusion of univalent ions across the lamellae of swollen phospholipids*, Journal of Molecular Biology **13**, 238–252 (1965).
- [BW89] L. Bo and R. E. Waugh, *Determination of bilayer membrane bending stiffness by tether formation from giant, thin-walled vesicles*, Biophysical Journal **55**, 509–517 (1989).
- [BZM94] R. Bar-Ziv and E. Moses, *Instability and "Pearling" States Produced in Tubular Membranes by Competition of Curvature and Tension*, Physical Review Letters **73**, 1392–1395 (1994).
- [Car76] M. P. d. Carmo, *Differential geometry of curves and surfaces*, Prentice-Hall, Englewood Cliffs, N.J (1976).
- [CBMK⁺97] B. A. Cornell, V. L. B. Braach-Maksvytis, L. G. King, P. D. J. Osman, B. Raguse, L. Wiczorek and R. J. Pace, *A biosensor that uses ion-channel switches*, Nature **387**, 580–583 (1997).
- [CC07] B. D. Chithrani and W. C. W. Chan, *Elucidating the Mechanism of Cellular Uptake and Removal of Protein-Coated Gold Nanoparticles of Different Sizes and Shapes*, Nano Letters **7**, 1542–1550 (2007).
- [CD05] I. R. Cooke and M. Deserno, *Solvent-free model for self-assembling fluid bilayer membranes: Stabilization of the fluid phase based on broad attractive tail potentials*, The Journal of Chemical Physics **123**, 224710 (2005).
- [CDBN05] D. Cuvelier, I. Derényi, P. Bassereau and P. Nassoy, *Coalescence of membrane tethers: experiments, theory, and applications*, Biophysical Journal **88**, 2714–2726 (2005).
- [CG06] M. Christen and W. F. v. Gunsteren, *Multigraining: An algorithm for simultaneous fine-grained and coarse-grained simulation of molecular systems*, The Journal of Chemical Physics **124**, 154106 (2006).
- [CGC06] B. D. Chithrani, A. A. Ghazani and W. C. W. Chan, *Determining the Size and Shape Dependence of Gold Nanoparticle Uptake into Mammalian Cells*, Nano Letters **6**, 662–668 (2006).
- [CGFF11] M. Cavadas, A. González-Fernández and R. Franco, *Pathogen-mimetic stealth nanocarriers for drug delivery: a future possibility*, Nanomedicine: Nanotechnology, Biology and Medicine **7**, 730–743 (2011).
- [CGS03] R. Capovilla, J. Guven and J. A. Santiago, *Deformations of the geometry of lipid vesicles*, Journal of Physics A: Mathematical and General **36**, 6281 (2003).

- [CK10] P. S. Coppock and J. T. Kindt, *Determination of Phase Transition Temperatures for Atomistic Models of Lipids from Temperature-Dependent Stripe Domain Growth Kinetics*, *The Journal of Physical Chemistry B* **114**, 11468–11473 (2010).
- [CKD05] I. R. Cooke, K. Kremer and M. Deserno, *Tunable generic model for fluid bilayer membranes*, *Physical Review E* **72**, 011506 (2005).
- [CKL⁺05] N. Chu, N. Kučerka, Y. Liu, S. Tristram-Nagle and J. F. Nagle, *Anomalous swelling of lipid bilayer stacks is caused by softening of the bending modulus*, *Physical Review E* **71**, 041904 (2005).
- [CLLC12] K. Y. Choi, G. Liu, S. Lee and X. Chen, *Theranostic nanoplatfoms for simultaneous cancer imaging and therapy: current approaches and future perspectives*, *Nanoscale* **4**, 330–342 (2012).
- [DB12] T. L. Doane and C. Burda, *The unique role of nanoparticles in nanomedicine: imaging, drug delivery and therapy*, *Chemical Society Reviews* **41**, 2885–2911 (2012).
- [DBCC98] C. Dellago, P. G. Bolhuis, F. S. Csajka and D. Chandler, *Transition path sampling and the calculation of rate constants*, *The Journal of Chemical Physics* **108**, 1964 (1998).
- [DC82] M. Daoud and J. Cotton, *Star shaped polymers : a model for the conformation and its concentration dependence*, *Journal de Physique* **43**, 531–538 (1982).
- [DCS08] M. E. Davis, Z. G. Chen and D. M. Shin, *Nanoparticle therapeutics: an emerging treatment modality for cancer*, *Nature Reviews Drug Discovery* **7**, 771–782 (2008).
- [Des09] M. Deserno, *Mesoscopic Membrane Physics: Concepts, Simulations, and Selected Applications*, *Macromolecular Rapid Communications* **30**, 752–771 (2009).
- [dG79] P.-G. de Gennes, *Scaling concepts in polymer physics*, Cornell University Press, Ithaca, N.Y. (1979).
- [dG80] P. G. de Gennes, *Conformations of Polymers Attached to an Interface*, *Macromolecules* **13**, 1069–1075 (1980).
- [dG87] P.-G. de Gennes, *Polymers at an interface; a simplified view*, *Advances in Colloid and Interface Science* **27**, 189–209 (1987).
- [DH76] H. Deuling and W. Helfrich, *Red blood cell shapes as explained on the basis of curvature elasticity*, *Biophysical Journal* **16**, 861–868 (1976).

-
- [DID] P. Diggins IV and M. Deserno, in preparation .
- [DJHK⁺08] W. H. De Jong, W. I. Hagens, P. Krystek, M. C. Burger, A. J. Sips and R. E. Geertsma, *Particle size-dependent organ distribution of gold nanoparticles after intravenous administration*, *Biomaterials* **29**, 1912–1919 (2008).
- [dOS07a] W. den Otter and S. Shkulipa, *Intermonolayer Friction and Surface Shear Viscosity of Lipid Bilayer Membranes*, *Biophysical Journal* **93**, 423–433 (2007).
- [DOS⁺07b] D. E. Discher, V. Ortiz, G. Srinivas, M. L. Klein, Y. Kim, D. Christian, S. Cai, P. Photos and F. Ahmed, *Emerging applications of polymersomes in delivery: From molecular dynamics to shrinkage of tumors*, *Progress in Polymer Science* **32**, 838–857 (2007).
- [DP10] J. M. DeSimone and R. A. Petros, *Strategies in the design of nanoparticles for therapeutic applications*, *Nature Reviews Drug Discovery* **9**, 615–627 (2010).
- [DTM12] H.-m. Ding, W.-d. Tian and Y.-q. Ma, *Designing Nanoparticle Translocation through Membranes by Computer Simulations*, *ACS Nano* **6**, 1230–1238 (2012).
- [DV13] R. Duncan and M. J. Vicent, *Polymer therapeutics-prospects for 21st century: The end of the beginning*, *Advanced Drug Delivery Reviews* **65**, 60–70 (2013).
- [EB] http://en.wikipedia.org/wiki/Encyclop%C3%A6dia_Britannica.
- [Efr79] B. Efron, *Bootstrap Methods: Another Look at the Jackknife*, *The Annals of Statistics* **7**, 1–26 (1979).
- [EKB82] E. Eisenriegler, K. Kremer and K. Binder, *Adsorption of polymer chains at surfaces: Scaling and Monte Carlo analyses*, *The Journal of Chemical Physics* **77**, 6296–6320 (1982).
- [ET94] B. Efron and R. J. Tibshirani, *An Introduction to the Bootstrap*, 1 ed., Chapman and Hall/CRC (1994).
- [Far03] O. Farago, *“Water-free” computer model for fluid bilayer membranes*, *The Journal of Chemical Physics* **119**, 596–605 (2003).
- [FC99] E. G. Flekkøy and P. V. Coveney, *From Molecular Dynamics to Dissipative Particle Dynamics*, *Physical Review Letters* **83**, 1775–1778 (1999).
- [FC08] D. B. Fenske and P. R. Cullis, *Liposomal nanomedicines*, *Expert Opinion on Drug Delivery* **5**, 25–44 (2008).

- [Fer08] M. Ferrari, *Nanogeometry: Beyond drug delivery*, Nature Nanotechnology **3**, 131–2 (2008).
- [Fey60] R. P. Feynman, *There's Plenty of Room at the Bottom: An invitation to enter a new field of physics*, Caltech Engineering and Science **23**, 22–36 (1960).
- [FHKvdV09] D. Fritz, C. R. Herbers, K. Kremer and N. F. A. van der Vegt, *Hierarchical modeling of polymer permeation*, Soft Matter **5**, 4556 (2009).
- [FK73] M. Fixman and J. Kovac, *Polymer conformational statistics. III. Modified Gaussian models of stiff chains*, The Journal of Chemical Physics **58**, 1564–1568 (1973).
- [Flo53] P. J. Flory, *Principles of polymer chemistry*, The George Fisher Baker non-resident lectureship in chemistry at Cornell University, Cornell University Press, (1953).
- [Flo12] A. T. Florence, *“Targeting” nanoparticles: The constraints of physical laws and physical barriers*, Journal of Controlled Release **164**, 115–124 (2012).
- [FM11] M. Fuhrmans and S. J. Marrink, *Molecular View of the Role of Fusion Peptides in Promoting Positive Membrane Curvature*, Journal of the American Chemical Society **134**, 1543–1552 (2011).
- [FP89] H. Flyvbjerg and H. G. Petersen, *Error estimates on averages of correlated data*, The Journal of Chemical Physics **91**, 461 (1989).
- [FPBMM94] L. Fernandez-Puente, I. Bivas, M. D. Mitov and P. Méléard, *Temperature and Chain Length Effects on Bending Elasticity of Phosphatidylcholine Bilayers*, Europhysics Letters **28**, 181 (1994).
- [Fro83] P. Fromherz, *Lipid-vesicle structure: Size control by edge-active agents*, Chemical Physics Letters **94**, 259–266 (1983).
- [FW78] P. F. Fahey and W. W. Webb, *Lateral diffusion in phospholipid bilayer membranes and multilamellar liquid crystals*, Biochemistry **17**, 3046–3053 (1978).
- [GCHT85] S. M. Gruner, P. R. Cullis, M. J. Hope and C. P. S. Tilcock, *Lipid Polymorphism: The Molecular Basis of Nonbilayer Phases*, Annual Review of Biophysics and Biophysical Chemistry **14**, 211–238 (1985).
- [GG05] A. K. Gupta and M. Gupta, *Synthesis and surface engineering of iron oxide nanoparticles for biomedical applications*, Biomaterials **26**, 3995–4021 (2005).

-
- [GGL99] R. Goetz, G. Gompper and R. Lipowsky, *Mobility and Elasticity of Self-Assembled Membranes*, Physical Review Letters **82**, 221–224 (1999).
- [GK86] G. S. Grest and K. Kremer, *Molecular dynamics simulation for polymers in the presence of a heat bath*, Physical Review A **33**, 3628–3631 (1986).
- [GK92] G. Gompper and S. Klein, *Ginzburg-Landau theory of aqueous surfactant solutions*, Journal de Physique II **2**, 1725–1744 (1992).
- [GKDP13] C. Globisch, V. Krishnamani, M. Deserno and C. Peter, *Optimization of an Elastic Network Augmented Coarse Grained Model to Study CCMV Capsid Deformation*, PLoS ONE **8**, e60582 (2013).
- [GL98] R. Goetz and R. Lipowsky, *Computer simulations of bilayer membranes: Self-assembly and interfacial tension*, The Journal of Chemical Physics **108**, 7397–7409 (1998).
- [Goh13] H. Z. Goh, *Solid-Supported Lipid Membranes: Formation, Stability and Applications*, Ph.D., Carnegie Mellon University, United States – Pennsylvania (2013).
- [Gre73] G. Gregoriadis, *Drug entrapment in liposomes*, FEBS Letters **36**, 292–296 (1973).
- [Gre76a] G. Gregoriadis, *The Carrier Potential of Liposomes in Biology and Medicine*, New England Journal of Medicine **295**, 704–710 (1976).
- [Gre76b] G. Gregoriadis, *The Carrier Potential of Liposomes in Biology and Medicine*, New England Journal of Medicine **295**, 765–770 (1976).
- [Gre81] G. Gregoriadis, *Targeting of drugs: Implications in medicine*, The Lancet **318**, 241–247 (1981).
- [Gre10] K. Greish, *Enhanced Permeability and Retention (EPR) Effect for Anti-cancer Nanomedicine Drug Targeting*, in S. R. Grobmyer and B. M. Moudgil (eds.), *Cancer Nanotechnology*, no. 624 in Methods in Molecular Biology, 25–37, Humana Press (2010).
- [GZ92] G. Gompper and S. Zschocke, *Ginzburg-Landau theory of oil-water-surfactant mixtures*, Physical Review A **46**, 4836–4851 (1992).
- [Ham86] R. W. Hamming, *Numerical methods for scientists and engineers*, Dover, New York (1986).
- [HBD12] M. Hu, J. J. Briguglio and M. Deserno, *Determining the Gaussian Curvature Modulus of Lipid Membranes in Simulations*, Biophysical Journal **102**, 1403–1410 (2012).

- [HD06] V. A. Harmandaris and M. Deserno, *A novel method for measuring the bending rigidity of model lipid membranes by simulating tethers*, The Journal of Chemical Physics **125**, 204905 (2006).
- [HDD13] M. Hu, P. Diggins and M. Deserno, *Determining the bending modulus of a lipid membrane by simulating buckling*, The Journal of Chemical Physics **138**, 214110 (2013).
- [Hel73] W. Helfrich, *Elastic properties of lipid bilayers: theory and possible experiments*, Zeitschrift Für Naturforschung. Teil C: Biochemie, Biophysik, Biologie, Virologie **28**, 693–703 (1973).
- [Hel74] W. Helfrich, *The size of bilayer vesicles generated by sonication*, Physics Letters A **50**, 115–116 (1974).
- [Hel81] W. Helfrich, *Amphiphilic mesophases made of defects*, in R. Balian, M. Kléman and J. P. Poirier (eds.), *Physics of Defects*, 715–755, North-Holland, Amsterdam (1981).
- [Hel94] W. Helfrich, *Lyotropic Lamellar Phases*, Journal of Physics: Condensed Matter **6**, A79–A92 (1994).
- [Hig61] T. Higuchi, *Rate of release of medicaments from ointment bases containing drugs in suspension*, Journal of Pharmaceutical Sciences **50**, 874–875 (1961).
- [HJMD13] M. Hu, D. H. d. Jong, S. J. Marrink and M. Deserno, *Gaussian curvature elasticity determined from global shape transformations and local stress distributions: a comparative study using the MARTINI model*, Faraday Discussions **161**, 365–382 (2013).
- [HKvdSL08] B. Hess, C. Kutzner, D. van der Spoel and E. Lindahl, *GROMACS 4: Algorithms for Highly Efficient, Load-Balanced, and Scalable Molecular Simulation*, Journal of Chemical Theory and Computation **4**, 435–447 (2008).
- [HNPA12] L. Huynh, C. Neale, R. Pomès and C. Allen, *Computational approaches to the rational design of nanoemulsions, polymeric micelles, and dendrimers for drug delivery*, Nanomedicine: Nanotechnology, Biology and Medicine **8**, 20–36 (2012).
- [HNV⁺09] F. Heinrich, T. Ng, D. J. Vanderah, P. Shekhar, M. Mihailescu, H. Nanda and M. Lösche, *A New Lipid Anchor for Sparsely Tethered Bilayer Lipid Membranes*, Langmuir **25**, 4219–4229 (2009).
- [IK50] J. H. Irving and J. G. Kirkwood, *The Statistical Mechanical Theory of Transport Processes. IV. The Equations of Hydrodynamics*, The Journal of Chemical Physics **18**, 817–829 (1950).

- [Isr91] J. N. Israelachvili, *Intermolecular and surface forces*, 2nd ed. ed., Academic Press London, (1991).
- [Jai99] R. K. Jain, *Transport of Molecules, Particles, and Cells in Solid Tumors*, Annual Review of Biomedical Engineering **1**, 241–263 (1999).
- [JHGL07] M. E. Johnson, T. Head-Gordon and A. A. Louis, *Representability problems for coarse-grained water potentials*, The Journal of Chemical Physics **126**, 144509 (2007).
- [JL93] F. Jülicher and R. Lipowsky, *Domain-induced budding of vesicles*, Physical Review Letters **70**, 2964–2967 (1993).
- [JMM10] S. M. Janib, A. S. Moses and J. A. MacKay, *Imaging and drug delivery using theranostic nanoparticles*, Advanced drug delivery reviews **62**, 1052–1063 (2010).
- [Jor04] W. L. Jorgensen, *The Many Roles of Computation in Drug Discovery*, Science **303**, 1813–1818 (2004).
- [Kaw04] T. Kawakatsu, *Statistical physics of polymers: an introduction*, Advanced texts in physics, Springer, Berlin ; New York (2004).
- [KGV83] S. Kirkpatrick, C. D. Gelatt and M. P. Vecchi, *Optimization by Simulated Annealing*, Science **220**, 671–680 (1983).
- [KHRP13] B. Kollmitzer, P. Heftberger, M. Rappolt and G. Pabst, *Monolayer spontaneous curvature of raft-forming membrane lipids*, Soft Matter **9**, 10877–10884 (2013).
- [KK02] Y. Kozlovsky and M. M. Kozlov, *Stalk Model of Membrane Fusion: Solution of Energy Crisis*, Biophysical Journal **82**, 882–895 (2002).
- [KKO⁺96] B. W. Koenig, S. Krueger, W. J. Orts, C. F. Majkrzak, N. F. Berk, J. V. Silverton and K. Gawrisch, *Neutron Reflectivity and Atomic Force Microscopy Studies of a Lipid Bilayer in Water Adsorbed to the Surface of a Silicon Single Crystal*, Langmuir **12**, 1343–1350 (1996).
- [KLC⁺05] N. Kučerka, Y. Liu, N. Chu, H. I. Petrache, S. Tristram-Nagle and J. F. Nagle, *Structure of Fully Hydrated Fluid Phase DMPC and DLPC Lipid Bilayers Using X-Ray Scattering from Oriented Multilamellar Arrays and from Unilamellar Vesicles*, Biophysical Journal **88**, 2626–2637 (2005).
- [KLHP12] I. K. Kwon, S. C. Lee, B. Han and K. Park, *Analysis on the current status of targeted drug delivery to tumors*, Journal of Controlled Release **164**, 108–114 (2012).

- [KM02] M. Karplus and J. A. McCammon, *Molecular dynamics simulations of biomolecules*, Nature Structural & Molecular Biology **9**, 646–652 (2002).
- [KP49] O. Kratky and G. Porod, *Röntgenuntersuchung gelöster Fadenmoleküle*, Recueil des Travaux Chimiques des Pays-Bas **68**, 1106–1122 (1949).
- [KPK⁺00] F. Kienberger, V. P. Pastushenko, G. Kada, H. J. Gruber, C. Riener, H. Schindler and P. Hinterdorfer, *Static and Dynamical Properties of Single Poly(Ethylene Glycol) Molecules Investigated by Force Spectroscopy*, Single Molecules **1**, 123–128 (2000).
- [Kre91] E. Kreyszig, *Differential geometry*, Dover Publications, New York (1991).
- [KSG⁺03] E. Karatekin, O. Sandre, H. Guitouni, N. Borghi, P. H. Puech and F. Brochard-Wyart, *Cascades of transient pores in giant vesicles: Line tension and transport*, Biophysical Journal **84**, 1734–1749 (2003).
- [LAH⁺11] T. Lammers, S. Aime, W. E. Hennink, G. Storm and F. Kiessling, *Therapeutic Nanomedicine*, Accounts of Chemical Research **44**, 1029–1038 (2011).
- [LAMH06] H. Limbach, A. Arnold, B. Mann and C. Holm, *ESPResSo—an extensible simulation package for research on soft matter systems*, Computer Physics Communications **174**, 704–727 (2006).
- [LCC00] Z. Leonenko, A. Carnini and D. Cramb, *Supported planar bilayer formation by vesicle fusion: the interaction of phospholipid vesicles with surfaces and the effect of gramicidin on bilayer properties using atomic force microscopy*, Biochimica et Biophysica Acta (BBA) - Biomembranes **1509**, 131–147 (2000).
- [LdVMP09] H. Lee, A. H. de Vries, S.-J. Marrink and R. W. Pastor, *A Coarse-Grained Model for Polyethylene Oxide and Polyethylene Glycol: Conformation and Hydrodynamics*, The Journal of Physical Chemistry B **113**, 13186–13194 (2009).
- [LE00] E. Lindahl and O. Edholm, *Spatial and energetic-entropic decomposition of surface tension in lipid bilayers from molecular dynamics simulations*, The Journal of Chemical Physics **113**, 3882–3893 (2000).
- [LE01] E. Lindahl and O. Edholm, *Molecular dynamics simulation of NMR relaxation rates and slow dynamics in lipid bilayers*, The Journal of Chemical Physics **115**, 4938–4950 (2001).
- [Lei86] S. Leibler, *Curvature instability in membranes*, Journal de Physique **47**, 507–516 (1986).

- [LF12] C. Liu and R. Faller, *Conformational, Dynamical. and Tensional Study of Tethered Bilayer Lipid Membranes in Coarse-Grained Molecular Simulations*, *Langmuir* **28**, 15907–15915 (2012).
- [LGZJ77] J. C. Le Guillou and J. Zinn-Justin, *Critical Exponents for the n -Vector Model in Three Dimensions from Field Theory*, *Physical Review Letters* **39**, 95–98 (1977).
- [LKHS10] T. Lammers, F. Kiessling, W. E. Hennink and G. Storm, *Nanotheranostics and Image-Guided Drug Delivery: Current Concepts and Future Directions*, *Molecular Pharmaceutics* **7**, 1899–1912 (2010).
- [LKSP10] W. B. Liechty, D. R. Kryscio, B. V. Slaughter and N. A. Peppas, *Polymers for Drug Delivery Systems*, *Annual Review of Chemical and Biomolecular Engineering* **1**, 149–173 (2010).
- [LL86] L. D. Landau and E. M. Lifshitz, *Theory of Elasticity*, Elsevier (1986).
- [Lou02] A. A. Louis, *Beware of density dependent pair potentials*, *Journal of Physics: Condensed Matter* **14**, 9187 (2002).
- [LRvdGM10] M. Louhivuori, H. J. Risselada, E. van der Giessen and S. J. Marrink, *Release of content through mechano-sensitive gates in pressurized liposomes*, *Proceedings of the National Academy of Sciences* (2010).
- [LS05] O. Lenz and F. Schmid, *A simple computer model for liquid lipid bilayers*, *Journal of Molecular Liquids* **117**, 147–152 (2005).
- [LSH86] S. Lorenzen, R.-M. Servuss and W. Helfrich, *Elastic Torques about Membrane Edges*, *Biophysical Journal* **50**, 565–572 (1986).
- [LVMJP08] H. Lee, R. M. Venable, A. D. MacKerell Jr. and R. W. Pastor, *Molecular Dynamics Studies of Polyethylene Oxide and Polyethylene Glycol: Hydrodynamic Radius and Shape Anisotropy*, *Biophysical Journal* **95**, 1590–1599 (2008).
- [LW75] M. Levitt and A. Warshel, *Computer simulation of protein folding*, *Nature* **253**, 694–698 (1975).
- [LZ06] E. Lyman and D. M. Zuckerman, *Resolution Exchange Simulation with Incremental Coarsening*, *Journal of Chemical Theory and Computation* **2**, 656–666 (2006).
- [Mar06] D. Marsh, *Elastic curvature constants of lipid monolayers and bilayers*, *Chemistry and Physics of Lipids* **144**, 146–159 (2006).

- [Mar13] D. Marsh, *Handbook of lipid bilayers*, 2nd ed., CRC Press, Boca Raton, FL (2013).
- [MBM⁺13] B. Mandal, H. Bhattacharjee, N. Mittal, H. Sah, P. Balabathula, L. A. Thoma and G. C. Wood, *Core-shell-type lipid-polymer hybrid nanoparticles as a drug delivery platform*, *Nanomedicine: Nanotechnology, Biology and Medicine* **9**, 474–491 (2013).
- [MdVM04] S. J. Marrink, A. H. de Vries and A. E. Mark, *Coarse Grained Model for Semiquantitative Lipid Simulations*, *The Journal of Physical Chemistry B* **108**, 750–760 (2004).
- [MF65] J. E. Mark and P. J. Flory, *The Configuration of the Polyoxyethylene Chain*, *Journal of the American Chemical Society* **87**, 1415–1423 (1965).
- [MGP⁺97] P. Méléard, C. Gerbeaud, T. Pott, L. Fernandez-Puente, I. B. Ivas, M. Mitov, J. Dufourcq and P. Bothorel, *Bending elasticities of model membranes: influences of temperature and sterol content*, *Biophysical Journal* **72**, 2616–2629 (1997).
- [MIL91] S. T. MILNER, *Polymer Brushes*, *Science* **251**, 905–914 (1991).
- [MKP⁺08] L. Monticelli, S. K. Kandasamy, X. Periole, R. G. Larson, D. P. Tieleman and S.-J. Marrink, *The MARTINI Coarse-Grained Force Field: Extension to Proteins*, *Journal of Chemical Theory and Computation* **4**, 819–834 (2008).
- [MM86] Y. Matsumura and H. Maeda, *A New Concept for Macromolecular Therapeutics in Cancer Chemotherapy: Mechanism of Tumoritropic Accumulation of Proteins and the Antitumor Agent Smancs*, *Cancer Research* **46**, 6387–6392 (1986).
- [MM01] S. J. Marrink and A. E. Mark, *Effect of Undulations on Surface Tension in Simulated Bilayers*, *The Journal of Physical Chemistry B* **105**, 6122–6127 (2001).
- [MMFC13] A. J. Mieszawska, W. J. M. Mulder, Z. A. Fayad and D. P. Cormode, *Multi-functional Gold Nanoparticles for Diagnosis and Therapy of Disease*, *Molecular Pharmaceutics* **10**, 831–847 (2013).
- [MNK07] E. R. May, A. Narang and D. I. Kopelevich, *Role of molecular tilt in thermal fluctuations of lipid membranes*, *Physical Review E* **76**, 021913 (2007).
- [MPTV10] S. J. Marrink, X. Periole, D. P. Tieleman and A. H. d. Vries, *Comment on “On using a too large integration time step in molecular dynamics simulations of coarse-grained molecular models” by M. Winger, D. Trzesniak, R. Baron and W. F. van Gunsteren*, *Phys. Chem. Chem. Phys.*, 2009, 11, 1934, *Physical Chemistry Chemical Physics* **12**, 2254–2256 (2010).

- [MRM05] S. J. Marrink, J. Risselada and A. E. Mark, *Simulation of gel phase formation and melting in lipid bilayers using a coarse grained model*, Chemistry and Physics of Lipids **135**, 223–244 (2005).
- [MRY⁺07] S. J. Marrink, H. J. Risselada, S. Yefimov, D. P. Tieleman and A. H. de Vries, *The MARTINI Force Field: Coarse Grained Model for Biomolecular Simulations*, The Journal of Physical Chemistry B **111**, 7812–7824 (2007).
- [MS95] J. F. Marko and E. D. Siggia, *Stretching DNA*, Macromolecules **28**, 8759–8770 (1995).
- [mSD] http://en.wikipedia.org/wiki/Secure_Digital.
- [MT13] S. J. Marrink and D. P. Tieleman, *Perspective on the Martini model*, Chemical Society Reviews **42**, 6801–6822 (2013).
- [Mun] R. Munroe, *Purity*, <http://xkcd.com/435/>.
- [MVV⁺07] D. J. McGillivray, G. Valincius, D. J. Vanderah, W. Febo-Ayala, J. T. Woodward, F. Heinrich, J. J. Kasianowicz and M. Lösche, *Molecular-scale structural and functional characterization of sparsely tethered bilayer lipid membranes*, Biointerphases **2**, 21–33 (2007).
- [MWC88a] S. T. Milner, T. A. Witten and M. E. Cates, *A Parabolic Density Profile for Grafted Polymers*, Europhysics Letters **5**, 413 (1988).
- [MWC88b] S. T. Milner, T. A. Witten and M. E. Cates, *Theory of the grafted polymer brush*, Macromolecules **21**, 2610–2619 (1988).
- [Nag13] J. F. Nagle, *Introductory Lecture: Basic quantities in model biomembranes*, Faraday Discussions **161**, 11–29 (2013).
- [NAKD00] D. Needham, G. Anyarambhatla, G. Kong and M. W. Dewhirst, *A New Temperature-sensitive Liposome for Use with Mild Hyperthermia: Characterization and Testing in a Human Tumor Xenograft Model*, Cancer Research **60**, 1197–1201, PMID: 10728674 (2000).
- [ND01] D. Needham and M. W. Dewhirst, *The development and testing of a new temperature-sensitive drug delivery system for the treatment of solid tumors*, Advanced Drug Delivery Reviews **53**, 285–305 (2001).
- [NE88] D. Needham and E. Evans, *Structure and mechanical properties of giant lipid (DMPC) vesicle bilayers from 20.degree.C below to 10.degree.C above the liquid crystal-crystalline phase transition at 24.degree.C*, Biochemistry **27**, 8261–8269 (1988).

- [NG05] H. Noguchi and G. Gompper, *Shape transitions of fluid vesicles and red blood cells in capillary flows*, Proceedings of the National Academy of Sciences of the United States of America **102**, 14159–14164 (2005).
- [NG06] H. Noguchi and G. Gompper, *Dynamics of vesicle self-assembly and dissolution*, The Journal of Chemical Physics **125**, 164908–164908–13 (2006).
- [NLSK04] S. O. Nielsen, C. F. Lopez, G. Srinivas and M. L. Klein, *Coarse grain models and the computer simulation of soft materials*, Journal of Physics: Condensed Matter **16**, R481 (2004).
- [Nog11] H. Noguchi, *Anisotropic surface tension of buckled fluid membranes*, Physical Review E **83**, 061919 (2011).
- [Noi13] W. G. Noid, *Perspective: Coarse-grained models for biomolecular systems*, The Journal of Chemical Physics **139**, 090901 (2013).
- [NPL+02] C. A. Naumann, O. Prucker, T. Lehmann, J. R  he, W. Knoll and C. W. Frank, *The Polymer-Supported Phospholipid Bilayer: Tethering as a New Approach to Substrate-Membrane Stabilization*, Biomacromolecules **3**, 27–35 (2002).
- [NPWT13] D. Needham, J.-Y. Park, A. M. Wright and J. Tong, *Materials characterization of the low temperature sensitive liposome (LTSL): effects of the lipid composition (lysolipid and DSPE-PEG2000) on the thermal transition and release of doxorubicin*, Faraday Discussions **161**, 515–534 (2013).
- [NSM+12] S. Nagarajan, E. E. Schuler, K. Ma, J. T. Kindt and R. B. Dyer, *Dynamics of the Gel to Fluid Phase Transformation in Unilamellar DPPC Vesicles*, The Journal of Physical Chemistry B **116**, 13749–13756 (2012).
- [NT01] H. Noguchi and M. Takasu, *Self-assembly of amphiphiles into vesicles: A Brownian dynamics simulation*, Physical Review E **64**, 041913 (2001).
- [NTN00] J. F. Nagle and S. Tristram-Nagle, *Structure of lipid bilayers*, Biochimica et Biophysica Acta (BBA) - Reviews on Biomembranes **1469**, 159–195 (2000).
- [OE11] M. Orsi and J. W. Essex, *The ELBA Force Field for Coarse-Grain Modeling of Lipid Membranes*, PLoS ONE **6**, e28637 (2011).
- [OHSE08] M. Orsi, D. Y. Haubertin, W. E. Sanderson and J. W. Essex, *A Quantitative Coarse-Grain Model for Lipid Bilayers*, The Journal of Physical Chemistry B **112**, 802–815 (2008).
- [OKS+04] F. Osaki, T. Kanamori, S. Sando, T. Sera and Y. Aoyama, *A Quantum Dot Conjugated Sugar Ball and Its Cellular Uptake. On the Size Effects*

-
- of Endocytosis in the Subviral Region*, Journal of the American Chemical Society **126**, 6520–6521 (2004).
- [OL00] S. M. Oversteegen and F. A. M. Leermakers, *Thermodynamics and mechanics of bilayer membranes*, Physical Review E **62**, 8453–8461 (2000).
- [OME10] M. Orsi, J. Michel and J. W. Essex, *Coarse-grain modelling of DMPC and DOPC lipid bilayers*, Journal of Physics: Condensed Matter **22**, 155106 (2010).
- [ONK03] H. Otsuka, Y. Nagasaki and K. Kataoka, *PEGylated nanoparticles for biological and pharmaceutical applications*, Advanced Drug Delivery Reviews **55**, 403–419 (2003).
- [ORKV07] O. H. S. Ollila, T. Róg, M. Karttunen and I. Vattulainen, *Role of sterol type on lateral pressure profiles of lipid membranes affecting membrane protein functionality: Comparison between cholesterol, desmosterol, 7-dehydrocholesterol and ketosterol*, Journal of Structural Biology **159**, 311–323 (2007).
- [ORL⁺09] O. H. S. Ollila, H. Risselada, M. Louhivuori, E. Lindahl, I. Vattulainen and S. J. Marrink, *3D Pressure Field in Lipid Membranes and Membrane-Protein Complexes*, Physical Review Letters **102**, 078101 (2009).
- [OV10] O. H. S. Ollila and I. Vattulainen, *Chapter 2. Lateral Pressure Profiles in Lipid Membranes: Dependence on Molecular Composition*, in M. S. P. Sansom and P. C. Biggin (eds.), *Molecular Simulations and Biomembranes*, 26–55, Royal Society of Chemistry, Cambridge (2010).
- [PB11] M. R. Preiss and G. D. Bothun, *Stimuli-responsive liposome-nanoparticle assemblies*, Expert Opinion on Drug Delivery **8**, 1025–1040 (2011).
- [PC08] K. F. Pirollo and E. H. Chang, *Does a targeting ligand influence nanoparticle tumor localization or uptake?*, Trends in Biotechnology **26**, 552–558 (2008).
- [Pep13] N. A. Peppas, *Historical perspective on advanced drug delivery: How engineering design and mathematical modeling helped the field mature*, Advanced Drug Delivery Reviews **65**, 5–9 (2013).
- [Pin76] P. Pincus, *Excluded Volume Effects and Stretched Polymer Chains*, Macromolecules **9**, 386–388 (1976).
- [PK09] C. Peter and K. Kremer, *Multiscale simulation of soft matter systems – from the atomistic to the coarse-grained level and back*, Soft Matter **5**, 4357–4366 (2009).

- [PKH⁺07] D. Peer, J. M. Karp, S. Hong, O. C. Farokhzad, R. Margalit and R. Langer, *Nanocarriers as an emerging platform for cancer therapy*, *Nature Nanotechnology* **2**, 751–760 (2007).
- [PKT09] R. Phillips, J. Kondev and J. Theriot, *Physical biology of the cell*, Garland Science, New York (2009).
- [PL03] J. Panyam and V. Labhasetwar, *Biodegradable nanoparticles for drug and gene delivery to cells and tissue*, *Advanced Drug Delivery Reviews* **55**, 329–347 (2003).
- [PLLS13] S. Piana, K. Lindorff-Larsen and D. E. Shaw, *Atomic-level description of ubiquitin folding*, *Proceedings of the National Academy of Sciences* 201218321 (2013).
- [PMS12] S. Parveen, R. Misra and S. K. Sahoo, *Nanoparticles: a boon to drug delivery, therapeutics, diagnostics and imaging*, *Nanomedicine: Nanotechnology, Biology and Medicine* **8**, 147–166 (2012).
- [PSH⁺06] M. Przybylo, J. Sýkora, J. Humpolíčková, A. Benda, A. Zan and M. Hof, *Lipid Diffusion in Giant Unilamellar Vesicles Is More than 2 Times Faster than in Supported Phospholipid Bilayers under Identical Conditions*, *Langmuir* **22**, 9096–9099 (2006).
- [PSK08] M. Praprotnik, L. D. Site and K. Kremer, *Multiscale Simulation of Soft Matter: From Scale Bridging to Adaptive Resolution*, *Annual Review of Physical Chemistry* **59**, 545–571 (2008).
- [PST91] C. L. Poglitsch, M. T. Sumner and N. L. Thompson, *Binding of IgG to MoFc.gamma.RII purified and reconstituted into supported planar membranes as measured by total internal reflection fluorescence microscopy*, *Biochemistry* **30**, 6662–6671 (1991).
- [PTNKN08] J. Pan, S. Tristram-Nagle, N. Kučerka and J. Nagle, *Temperature Dependence of Structure, Bending Rigidity, and Bilayer Interactions of Dioleoylphosphatidylcholine Bilayers*, *Biophysical Journal* **94**, 117–124 (2008).
- [PWJ⁺09] S. D. Perrault, C. Walkey, T. Jennings, H. C. Fischer and W. C. W. Chan, *Mediating Tumor Targeting Efficiency of Nanoparticles Through Design*, *Nano Letters* **9**, 1909–1915 (2009).
- [RAG12] S. Riniker, J. R. Allison and W. F. v. Gunsteren, *On developing coarse-grained models for biomolecular simulation: a review*, *Physical Chemistry Chemical Physics* **14**, 12423–12430 (2012).

- [RBB06] R. P. Richter, R. Bérat and A. R. Brisson, *Formation of Solid-Supported Lipid Bilayers: An Integrated View*, *Langmuir* **22**, 3497–3505 (2006).
- [RBMC⁺98] B. Raguse, V. Braach-Maksvytis, B. A. Cornell, L. G. King, P. D. J. Osman, R. J. Pace and L. Wiczorek, *Tethered Lipid Bilayer Membranes: Formation and Ionic Reservoir Characterization*, *Langmuir* **14**, 648–659 (1998).
- [RBMR12] S. Rana, A. Bajaj, R. Mout and V. M. Rotello, *Monolayer coated gold nanoparticles for delivery applications*, *Advanced Drug Delivery Reviews* **64**, 200–216 (2012).
- [RCF10] P. Ruenraroengsak, J. M. Cook and A. T. Florence, *Nanosystem drug targeting: Facing up to complex realities*, *Journal of Controlled Release* **141**, 265–276 (2010).
- [RD08] B. Reynwar and M. Deserno, *Membrane composition-mediated protein-protein interactions*, *Biointerphases* **3**, FA117–FA124 (2008).
- [RHMM03] A. Rosa, T. X. Hoang, D. Marenduzzo and A. Maritan, *Elasticity of Semiflexible Polymers with and without Self-Interactions*, *Macromolecules* **36**, 10095–10102 (2003).
- [RIH⁺07] B. J. Reynwar, G. Illya, V. A. Harmandaris, M. M. Müller, K. Kremer and M. Deserno, *Aggregation and vesiculation of membrane proteins by curvature-mediated interactions*, *Nature* **447**, 461–464 (2007).
- [RM08] H. J. Risselada and S. J. Marrink, *The molecular face of lipid rafts in model membranes*, *Proceedings of the National Academy of Sciences* **105**, 17367–17372 (2008).
- [RMG96] M. Rogošić, H. Mencer and Z. Gomzi, *Polydispersity index and molecular weight distributions of polymers*, *European Polymer Journal* **32**, 1337–1344 (1996).
- [RMM08] H. J. Risselada, A. E. Mark and S. J. Marrink, *Application of Mean Field Boundary Potentials in Simulations of Lipid Vesicles*, *The Journal of Physical Chemistry B* **112**, 7438–7447 (2008).
- [RPL81] P. M. Reilly and H. Patino-Leal, *A Bayesian Study of the Error-in-Variables Model*, *Technometrics* **23**, 221–231 (1981).
- [RSdM⁺12] J. M. Rodgers, J. Sørensen, F. J.-M. de Meyer, B. Schiøtt and B. Smit, *Understanding the Phase Behavior of Coarse-Grained Model Lipid Bilayers through Computational Calorimetry*, *The Journal of Physical Chemistry B* **116**, 1551–1569 (2012).

- [RSG⁺10] A. J. Rzepiela, L. V. Schäfer, N. Goga, H. J. Risselada, A. H. De Vries and S. J. Marrink, *Reconstruction of atomistic details from coarse-grained structures*, Journal of Computational Chemistry **31**, 1333–1343 (2010).
- [RSL⁺09] K. Riehemann, S. W. Schneider, T. A. Luger, B. Godin, M. Ferrari and H. Fuchs, *Nanomedicine-Challenge and Perspectives*, Angewandte Chemie International Edition **48**, 872–897 (2009).
- [Sac96] E. Sackmann, *Supported Membranes: Scientific and Practical Applications*, Science **271**, 43–48, PMID: 8539599 (1996).
- [SBL91] U. Seifert, K. Berndl and R. Lipowsky, *Shape transformations of vesicles: Phase diagram for spontaneous-curvature and bilayer-coupling models*, Physical Review A **44**, 1182–1202 (1991).
- [SCGH⁺11] T. Schlick, R. Collepardo-Guevara, L. A. Halvorsen, S. Jung and X. Xiao, *Biomolecular modeling and simulation: a field coming of age*, Quarterly Reviews of Biophysics **44**, 191–228 (2011).
- [Sch09] F. Schmid, *Toy amphiphiles on the computer: What can we learn from generic models?*, Macromolecular Rapid Communications **30**, 741–751 (2009).
- [SGB96] J. Salafsky, J. T. Groves and S. G. Boxer, *Architecture and Function of Membrane Proteins in Planar Supported Bilayers: A Study with Photosynthetic Reaction Centers[†]*, Biochemistry **35**, 14773–14781 (1996).
- [Shk06] S. A. Shkulipa, *Computer simulations of lipid bilayer dynamics*, Ph.D. thesis, University of Twente, Enschede, The Netherlands (2006).
- [Sie99] D. P. Siegel, *The Modified Stalk Mechanism of Lamellar/Inverted Phase Transitions and Its Implications for Membrane Fusion*, Biophysical Journal **76**, 291–313 (1999).
- [Sie06] D. P. Siegel, *Determining the ratio of the Gaussian curvature and bending elastic moduli of phospholipids from Q_{II} phase unit cell dimensions*, Biophysical Journal **91**, 608–618 (2006).
- [Sie08] D. P. Siegel, *The Gaussian curvature elastic energy of Intermediates in Membrane Fusion*, Biophysical Journal **95**, 5200–5215 (2008).
- [SJH⁺11] L. V. Schäfer, D. H. d. Jong, A. Holt, A. J. Rzepiela, A. H. d. Vries, B. Poolman, J. A. Killian and S. J. Marrink, *Lipid packing drives the segregation of transmembrane helices into disordered lipid domains in model membranes*, Proceedings of the National Academy of Sciences **108**, 1343–1348 (2011).

- [SK01] E.-K. Sinner and W. Knoll, *Functional tethered membranes*, Current Opinion in Chemical Biology **5**, 705–711 (2001).
- [SK04] D. P. Siegel and M. M. Kozlov, *The Gaussian curvature elastic modulus of N-monomethylated dioleoylphosphatidylethanolamine: Relevance to membrane fusion and lipid phase behavior*, Biophysical Journal **87**, 366–374 (2004).
- [SKBS⁺90] I. Szleifer, D. Kramer, A. Ben-Shaul, W. M. Gelbart and S. A. Safran, *Molecular theory of curvature elasticity in surfactant films*, The Journal of Chemical Physics **92**, 6800–6817 (1990).
- [SL93] U. Seifert and S. A. Langer, *Viscous Modes of Fluid Bilayer Membranes*, Europhysics Letters **23**, 71 (1993).
- [SMF⁺10] S. Shenoy, R. Moldovan, J. Fitzpatrick, D. J. Vanderah, M. Deserno and M. Lösche, *In-plane homogeneity and lipid dynamics in tethered bilayer lipid membranes (tBLMs)*, Soft Matter **6**, 1263 (2010).
- [SN11] H. Shiba and H. Noguchi, *Estimation of the bending rigidity and spontaneous curvature of fluid membranes in simulations*, Physical Review E **84**, 031926 (2011).
- [SS08] J. Siepmann and F. Siepmann, *Mathematical modeling of drug delivery*, International Journal of Pharmaceutics **364**, 328–343 (2008).
- [ST93] J. M. Seddon and R. H. Templer, *Cubic Phases of Self-Assembled Amphiphilic Aggregates*, Philosophical Transactions of the Royal Society of London. Series A: Physical and Engineering Sciences **344**, 377–401 (1993).
- [TB08] A. Tian and T. Baumgart, *Sorting of Lipids and Proteins in Membrane Curvature Gradients*, Biophysical Journal **96**, 2676–2688 (2008).
- [TDGBS04] S. Tzlil, M. Deserno, W. M. Gelbart and A. Ben-Shaul, *A Statistical-Thermodynamic Model of Viral Budding*, Biophysical Journal **86**, 2037–2048 (2004).
- [TdOB04a] T. V. Tolpekina, W. K. den Otter and W. J. Briels, *Nucleation free energy of pore formation in an amphiphilic bilayer studied by molecular dynamics simulations*, The Journal of Chemical Physics **121**, 12060–12066 (2004).
- [TdOB04b] T. V. Tolpekina, W. K. den Otter and W. J. Briels, *Simulations of stable pores in membranes: System size dependence and line tension*, The Journal of Chemical Physics **121**, 8014–8020 (2004).
- [TKS98] R. H. Templer, B. J. Khoo and J. M. Seddon, *Gaussian curvature modulus of an amphiphilic monolayer*, Langmuir **14**, 7427–7434 (1998).

- [TL07] A.-L. Troutier and C. Ladavière, *An overview of lipid membrane supported by colloidal particles*, *Advances in Colloid and Interface Science* **133**, 1–21 (2007).
- [TM85] L. Tamm and H. McConnell, *Supported phospholipid bilayers*, *Biophysical Journal* **47**, 105–113 (1985).
- [TM12] W.-d. Tian and Y.-q. Ma, *Theoretical and computational studies of dendrimers as delivery vectors*, *Chemical Society Reviews* **42**, 705–727 (2012).
- [TS85] D. N. Theodorou and U. W. Suter, *Shape of unperturbed linear polymers: polypropylene*, *Macromolecules* **18**, 1206–1214 (1985).
- [TS05] M. Tanaka and E. Sackmann, *Polymer-supported membranes as models of the cell surface*, *Nature* **437**, 656–663 (2005).
- [TT10] N. M. Toan and D. Thirumalai, *Theory of Biopolymer Stretching at High Forces*, *Macromolecules* **43**, 4394–4400 (2010).
- [TV05] H. L. Tepper and G. A. Voth, *A coarse-grained model for double-helix molecules in solution: Spontaneous helix formation and equilibrium properties*, *The Journal of Chemical Physics* **122**, 124906 (2005).
- [vGB90] W. F. van Gunsteren and H. J. C. Berendsen, *Computer Simulation of Molecular Dynamics: Methodology, Applications, and Perspectives in Chemistry*, *Angewandte Chemie International Edition in English* **29**, 992–1023 (1990).
- [vK07] N. G. van Kampen, *Stochastic Processes in Physics and Chemistry*, 3 ed., Elsevier, Amsterdam (2007).
- [VOR⁺08] I. K. Vockenroth, C. Ohm, J. W. F. Robertson, D. J. McGillivraya, M. Lösche and I. Köper, *Stable insulating tethered bilayer lipid membranes*, *Biointerphases* **3**, FA68–FA73 (2008).
- [Vot09] G. A. Voth (ed.), *Coarse-graining of condensed phase and biomolecular systems*, CRC Press, Boca Raton (2009).
- [VRL05] J. K. Vasir, M. K. Reddy and V. D. Labhasetwar, *Nanosystems in Drug Targeting: Opportunities and Challenges*, *Current Nanoscience* **1**, 47–64 (2005).
- [WD10] Z.-J. Wang and M. Deserno, *A Systematically Coarse-Grained Solvent-Free Model for Quantitative Phospholipid Bilayer Simulations*, *The Journal of Physical Chemistry B* **114**, 11207–11220 (2010).
- [WdOEB06] J. Wohler, W. K. den Otter, O. Edholm and W. J. Briels, *Free energy of a trans-membrane pore calculated from atomistic molecular dynamics simulations*, *The Journal of Chemical Physics* **124**, 154905 (2006).

- [WE06] J. Wohlert and O. Edholm, *Dynamics in atomistic simulations of phospholipid membranes: Nuclear magnetic resonance relaxation rates and lateral diffusion*, The Journal of Chemical Physics **125**, 204703 (2006).
- [WE09] Q. Waheed and O. Edholm, *Undulation contributions to the area compressibility in lipid bilayer simulations*, Biophysical Journal **97**, 2754–2760 (2009).
- [WF05] Z.-J. Wang and D. Frenkel, *Modeling flexible amphiphilic bilayers: A solvent-free off-lattice Monte Carlo study*, The Journal of Chemical Physics **122**, 234711 (2005).
- [WHZ12] H. Wang, D. Hu and P. Zhang, *Measuring the Spontaneous Curvature of Bilayer Membranes by Molecular Dynamics Simulations*, Communications in Computational Physics (2012).
- [WJK09] H. Wang, C. Junghans and K. Kremer, *Comparative atomistic and coarse-grained study of water: What do we lose by coarse-graining?*, The European Physical Journal E **28**, 221–229 (2009).
- [WP86] T. A. Witten and P. A. Pincus, *Colloid stabilization by long grafted polymers*, Macromolecules **19**, 2509–2513 (1986).
- [WPWB11] M. C. Watson, E. S. Penev, P. M. Welch and F. L. H. Brown, *Thermal fluctuations in shape, thickness, and molecular orientation in lipid bilayers*, The Journal of Chemical Physics **135**, 244701–244701–22 (2011).
- [WT00] M. Wagner and L. Tamm, *Tethered Polymer-Supported Planar Lipid Bilayers for Reconstitution of Integral Membrane Proteins: Silane-Polyethyleneglycol-Lipid as a Cushion and Covalent Linker*, Biophysical Journal **79**, 1400–1414 (2000).
- [XA06] T.-X. Xiang and B. D. Anderson, *Liposomal drug transport: A molecular perspective from molecular dynamics simulations in lipid bilayers*, Advanced Drug Delivery Reviews **58**, 1357–1378 (2006).
- [ZG96] A. G. Zilman and R. Granek, *Undulations and Dynamic Structure Factor of Membranes*, Physical Review Letters **77**, 4788–4791 (1996).
- [ZLL⁺09] S. Zhang, J. Li, G. Lykotrafitis, G. Bao and S. Suresh, *Size-Dependent Endocytosis of Nanoparticles*, Advanced Materials **21**, 419–424 (2009).
- [ZPY⁺13] G. Zhao, J. R. Perilla, E. L. Yufenyuy, X. Meng, B. Chen, J. Ning, J. Ahn, A. M. Gronenborn, K. Schulten, C. Aiken and P. Zhang, *Mature HIV-1 capsid structure by cryo-electron microscopy and all-atom molecular dynamics*, Nature **497**, 643–646 (2013).

- [ZTD⁺12] G. H. Zan, C. Tan, M. Deserno, F. Lanni and M. Lösche, *Hemifusion of giant unilamellar vesicles with planar hydrophobic surfaces: a fluorescence microscopy study*, *Soft Matter* **8**, 10877–10886 (2012).
- [ZVC93] J. Zimmerberg, S. S. Vogel and L. V. Chernomordik, *Mechanisms of Membrane Fusion*, *Annual Review of Biophysics and Biomolecular Structure* **22**, 433–466 (1993).
- [ZYG⁺11] L. S. Zheng, Y. Q. Yang, X. D. Guo, Y. Sun, Y. Qian and L. J. Zhang, *Mesoscopic simulations on the aggregation behavior of pH-responsive polymeric micelles for drug delivery*, *Journal of Colloid and Interface Science* **363**, 114–121 (2011).